

Alexander Bock

## **Generation and Analysis of Plasmas with Centrally Reduced Helicity in Full-Tungsten ASDEX Upgrade**

**IPP 1/357**  
**Juni, 2016**

---

# Generation and Analysis of Plasmas with Centrally Reduced Helicity in Full-Tungsten ASDEX Upgrade

Alexander Bock

---

München 2016





# Generation and Analysis of Plasmas with Centrally Reduced Helicity in Full-Tungsten ASDEX Upgrade

Dissertation zur Erlangung des akademischen Grades eines  
**Doktors der Naturwissenschaften (Dr. rer. nat.)**  
an der Fakultät für Physik der Ludwig-Maximilians-Universität  
München

durchgeführt am  
Max-Planck-Institut für Plasmaphysik, Garching bei München

vorgelegt von  
**Alexander Bock**  
geboren am 13. Juni 1987 in Bukarest

München, den 1. März 2016

Erstgutachter: PD Dr. Jörg Stober

Zweitgutachter: Prof. Dr. Gregor Morfill

Tag der mündlichen Prüfung: 2016-05-25

---

## Zusammenfassung

Die vielversprechendsten Konzepte zur Nutzbarmachung der Kernfusion sind toroidale Maschinen wie Tokamaks, in denen ein Plasma durch helikal gewundene Magnetfeldlinien eingeschlossen wird. Um die Feldlinien zu verdrillen wird im Tokamak ein toroidaler Plasmastrom benötigt, welcher größtenteils durch einen Transformator induziert wird, weswegen konventionelle Tokamaks auf gepulsten Betrieb beschränkt sind. Außerdem macht dieser Strom das Plasma anfällig für eine Vielzahl von den Einschluss verringernden magnetohydrodynamischen (MHD) Instabilitäten, die an Orten mit rationaler Feldlinienhelizität  $q$  auftreten können — Sägezähne bei  $1/1$ , neoklassische Tearingmoden (NTMs) beispielsweise bei  $3/2$  oder  $2/1$ .

Diese Arbeit präsentiert Untersuchungen von Plasmen mit durch externen Stromtrieb zentral angehobenen  $q$ -Profilen unter stationären Bedingungen im voll-Wolfram Tokamak ASDEX Upgrade. Ohne das üblicherweise monotone  $q$ -profil verschwinden Instabilitäten mit niedriger Helizität, was die Plasmastabilität verbessert. Außerdem erhöht das Anheben von  $q$  den sog. Bootstrap-Strom, den das Plasma in der Gegenwart von Druckgradienten selbst treibt, was es unabhängiger vom Transformator macht. Im besten Fall könnte ein „Advanced Tokamak“ (AT) stationär betrieben werden. Zusätzlich sollte ein angehobenes und dadurch flaches/leicht invertiertes  $q$ -Profil auch den Einschluss durch Behinderung von Turbulenz verbessern.

Die Rekonstruktion des erzeugten  $q$ -Profils wird mit dem neuen Gleichgewichtscodex IDE und Messungen einer Schlüsseldiagnostik, die auf dem Motional Stark Effect aufbaut, bewerkstelligt. Während dieser Arbeit wurde entdeckt, dass die Diagnostik durch polarisiertes Hintergrundlicht gestört wird. Ein Prototyp zur Korrektur wurde erfolgreich getestet. Außerdem wurden Nichtlinearitäten im optischen System der Diagnostik gefunden und ein Kalibrationsschema zur Kompensation entworfen.

Es wurden sowohl die konventionelle Herangehensweise an AT-Studien, bei denen ein Plasma früh geheizt wird um die Relaxation des anfangs angehobenen  $q$ -Profils zu verzögern, als auch ein neuer Ansatz bei dem ein relaxiertes  $q$ -Profil verändert wird, untersucht. Ersteres wurde als für nichtinduktiven Betrieb geeignet befunden, blieb aber anfällig für  $2/1$ -NTMs. Letzteres erlaubte den nichtinduktiven Betrieb bei hohem Plasmadruck unter reaktorrelevanten Bedingungen ohne Verringerung des Einschlusses oder starke MHD Instabilitäten.

Der Wärmetransport im Plasma wurde in stationären Phasen mit erhöhtem  $q$  mithilfe des numerischen Simulationscodes TGLF modelliert. Ohne Scherflüsse durch ein radiales elektrisches Feld sind die Vorhersagen von TGLF für den Wärmetransport jenseits der experimentellen Beobachtungen. Mit solchen Flüssen werden die experimentell beobachteten Temperaturen signifikant übertroffen, der Transport also unterschätzt.

Die Ergebnisse dieser Arbeit zeigen, dass der attraktive nichtinduktive Betrieb mit hohem Einschluss in ASDEX Upgrade erreicht werden kann. Dementsprechend können weitere AT-Studien durchgeführt werden.



---

## Abstract

The most promising concepts for harnessing nuclear fusion are toroidal devices like tokamaks, where a plasma is confined by helically twisted magnetic field lines. To provide the twisting of the field lines, a tokamak relies on a toroidal current in the plasma, which is largely generated by a transformer. As such, conventional tokamaks are limited to pulsed operation. Moreover, this current makes tokamak plasmas prone to numerous confinement degrading magnetohydrodynamic (MHD) instabilities that can emerge at locations where the field line helicity  $q$  takes on rational values like  $1/1$ ,  $3/2$  or  $2/1$ , i.e. sawteeth or neoclassical tearing modes (NTMs).

This thesis presents studies of plasmas with centrally elevated  $q$ -profiles created by external electron-cyclotron and neutral beam current drive (ECCD/NBCD) under steady-state conditions in the full-tungsten tokamak ASDEX Upgrade. Without the usually monotonic  $q$ -profile, instabilities of low helicity disappear, thereby improving the plasma stability. Furthermore, elevating  $q$  increases the amount of so-called (toroidal) bootstrap current, which the plasma drives by itself in the presence of pressure gradients, thereby reducing the reliance on the transformer. In the best case, an advanced tokamak (AT) could thus run in steady state. Additionally, an elevated and thus flat/slightly reversed  $q$ -profile is thought to improve confinement by impeding turbulent transport.

Reconstruction of the tailored  $q$ -profile is accomplished with the new integrated data equilibrium (IDE) code and information from a key diagnostic that is based on the Motional Stark Effect (MSE). During the course of this work it was discovered that the MSE diagnostic suffers from interference from polarised background light. A prototype mitigation system was successfully tested. Also, non-linearities in the diagnostic's optical relay system were found and a calibration scheme devised to take them into account.

Both the conventional approach of AT-studies where the plasma is heated early in the discharge to delay the relaxation of the initially elevated  $q$ -profiles as well as a new approach of manipulating an already equilibrated  $q$ -profile have been explored. The former was found to be suitable for non-inductive operation but remained susceptible to  $2/1$ -NTMs. The latter allowed non-inductive operation at high plasma pressure under reactor-relevant conditions to be achieved without confinement degradation or any strong MHD instabilities.

The plasma heat transport in steady-state phases with elevated  $q$  was modelled using the numerical simulation code TGLF. Without shear flows due to a radial electric field TGLF's predictions for the ion heat transport are beyond the experimental observation, which may be due to TGLF not considering stabilising effects of fast ions. With such shear flows the TGLF temperature predictions exceed the experimental observations significantly, i.e. heat transport is underestimated.

The findings of this work show that the attractive non-inductive operation with high confinement can be achieved in ASDEX Upgrade. As such, further AT-studies are possible.





---

*«Un bon mot ne prouve rien.»*  
—Voltaire, 1767

# Contents

<b>1</b>	<b>Introduction</b>	<b>1</b>
1.1	Thermonuclear Fusion . . . . .	1
1.2	This Thesis . . . . .	3
<b>2</b>	<b>Theory and Background</b>	<b>5</b>
2.1	Plasma Equilibrium . . . . .	5
2.1.1	The Grad-Shafranov Equation . . . . .	7
2.1.2	The Safety-Factor $q$ . . . . .	9
2.2	Classical and Neoclassical Plasma Transport . . . . .	11
2.2.1	Diffusion . . . . .	12
2.2.2	Plasma Drifts . . . . .	13
2.2.3	Neoclassical Transport . . . . .	14
2.2.4	Neoclassical Bootstrap Current . . . . .	16
2.3	Anomalous Transport . . . . .	17
2.3.1	Micro-Instabilities . . . . .	17
2.3.2	Macroscopic Critical Gradients . . . . .	21
2.3.3	Critical Gradient Parameter Dependences . . . . .	24
2.3.4	TGLF and ASTRA . . . . .	29
2.4	The H-Mode . . . . .	30
2.5	Internal Instabilities . . . . .	33
2.5.1	Sawtooth Instability . . . . .	33
2.5.2	Neoclassical Tearing Modes . . . . .	35
2.6	Improving the H-Mode . . . . .	37
<b>3</b>	<b>Experimental Setup</b>	<b>45</b>
3.1	ASDEX Upgrade . . . . .	45
3.2	Plasma Diagnostics and Heating Systems . . . . .	46
3.2.1	External Magnetic Measurements . . . . .	46
3.2.2	Temperature Measurements (ECE, TS) . . . . .	47
3.2.3	Density Measurements (DCN) . . . . .	50
3.2.4	Integrated Data Analysis (IDA) . . . . .	52
3.2.5	Internal Magnetic Measurements . . . . .	53
3.3	Heating and Current Drive Systems . . . . .	55
3.3.1	Electron-Cyclotron Heating/Current Drive . . . . .	55
3.3.2	Neutral Beam Injection (NBI) . . . . .	60

<b>4</b>	<b>The MSE Diagnostic</b>	<b>63</b>
4.1	Introduction . . . . .	63
4.2	Interference from Polarised Background Light . . . . .	68
4.2.1	Identification of the Polarised Background . . . . .	69
4.2.2	Polarised Background Correction . . . . .	74
4.3	Absolute Calibration . . . . .	76
<b>5</b>	<b>Equilibrium Reconstruction</b>	<b>83</b>
5.1	General Approach . . . . .	83
5.2	Accuracy and Internal Constraints . . . . .	87
5.2.1	Statistical Errors . . . . .	87
5.2.2	Systematic Errors . . . . .	91
<b>6</b>	<b>Experimental and Modelling Results</b>	<b>93</b>
6.1	Early Heating . . . . .	94
6.1.1	Starting Point . . . . .	95
6.1.2	Iterative Improvements . . . . .	98
6.1.3	Latest Result . . . . .	99
6.2	Late Heating with Narrow Counter-ECCD . . . . .	105
6.2.1	Steady State Internal Transport Barrier . . . . .	107
6.2.2	Transport Modelling with TGLF . . . . .	108
6.3	Late Heating with Broad Counter-ECCD . . . . .	114
6.3.1	Steady State Operation with High Bootstrap Fraction . . . . .	119
6.3.2	Transport Modelling with TGLF . . . . .	124
<b>7</b>	<b>Summary and Outlook</b>	<b>133</b>
<b>8</b>	<b>Bibliography</b>	<b>137</b>
	<b>Acknowledgements</b>	<b>145</b>



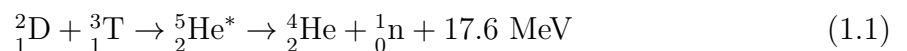
# 1 Introduction

Modern civilisation depends on cheap, abundant energy like never before in history. The bulk of this energy comes from the extraction and combustion of fossil fuels. With the world finally waking up to both the finiteness of these fuels and their negative consequences on the environment, other, cleaner and more sustainable means of power generation begin to attract more and more notice.

## 1.1 Thermonuclear Fusion

One solution to supply the ever-growing demand for power that has been pursued for several decades now is thermonuclear fusion, the mechanism that powers stars such as the Sun. In the Sun, hydrogen is fused over several stages into helium. For this process to occur, enormous pressure in the star's core is necessary, which the star's sheer mass and gravitational attraction can sustain. Even if reliably recreating these conditions on Earth were possible, the necessary conversion of protons into neutrons using the weak interaction with its small cross section would make terrestrial fusion unviable.

Fortunately, the fusion reaction between two isotopes of hydrogen, deuterium (D) and tritium (T) with one and two neutrons, respectively, has a much larger cross section since all nucleons are already present and because of the existence of an excited intermediate state of Helium:



The reaction releases 4/5 of its energy through the neutron. In addition to heating a fluid to drive turbines and generate electricity, it can also be used to breed lithium into tritium, which doesn't occur naturally due to its radioactivity and short half-life, allowing a future fusion power plant to breed its own fuel while only receiving deuterium and lithium from the outside, which are abundant and — in comparison to classical nuclear fuels — harmless.

While the DT reaction is much more likely to occur than the ordinary pp-reaction of the Sun, a set of conditions must still be met for a viable terrestrial fusion power plant. Specifically, the temperature  $T$  must be high enough for the particles to be able to overcome the Coulomb-barrier while the particle density  $n$  and so-called energy confinement time  $\tau_E$  must be sufficiently high to allow for enough fusion interactions to take place in the

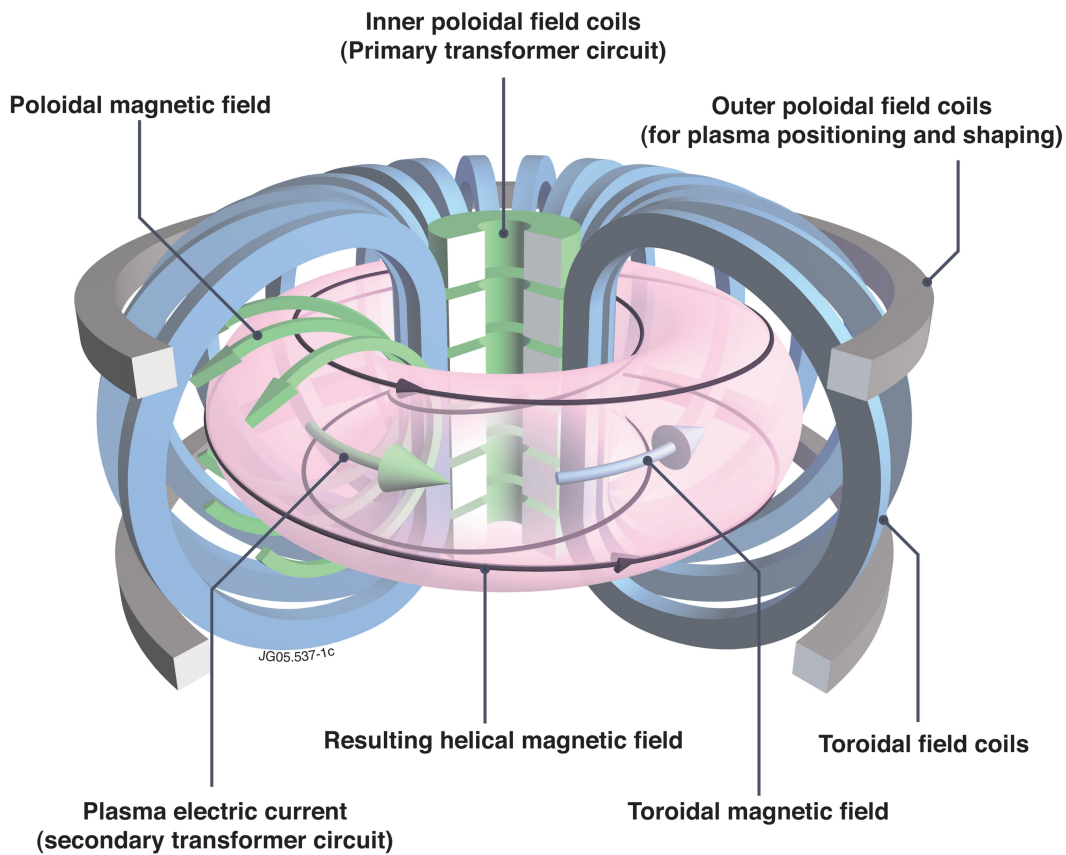


**Figure 1.1:** Tokamak principle: toroidal field coils (blue) and toroidal plasma current generate helical magnetic field. Plasma current is induced by the transformer (green). Poloidal field coils (gray) are used for shaping and positioning. [2]

presence of the still much more likely Coulomb collisions. Generally, the fuel will exist in the plasma-state at these conditions where electrons and ions can move freely and are not directly bound to each other. Here, the energy confinement time is the stored energy of the fusion plasma divided by the total emitted power, not including the neutrons. For the fusion reaction to be self-sustaining, that emitted power must be wholly compensated by the fusion reactions. This can be expressed in a Lawson-criterion-like form [1]:

$$nT\tau_E \geq 5 \times 10^{21} \text{ keV s m}^{-3} \quad (1.2)$$

Magnetic confinement fusion (MCF) has emerged as the most likely concept to meet this criterion. Charged particles can move freely only along magnetic field lines and, accordingly, MCF exploits this to confine a fusion plasma using magnetic fields. Various kinds of magnetic confinement devices have been studied over the years, culminating in toroidal devices with a helical magnetic field geometry that have demonstrated the best ability to adequately contain a fusion-relevant plasma. There are two main designs for

such devices: stellarators that create the magnetic field solely with external coils, and tokamaks that use external coils for the toroidal magnetic field and a toroidal current in the plasma to generate a poloidal field which combines with the applied field to form the necessary helical field. This work focuses only on tokamaks.

The tokamak concept was developed in the mid-20th century in the Soviet Union. The bulk of the magnetic field cage holding the plasma is generated by toroidal field coils (see figure 1.1). The helical twisting of the field lines is added using a current flowing in toroidal direction through the plasma. This current is inductively driven using a transformer, meaning that a conventional tokamak is always limited to pulsed operation. Further toroidal currents flow through additional outer poloidal field coils, which are used for shaping and positioning of the plasma.

## 1.2 This Thesis

This thesis explores the possibilities of improving the confinement and stability of the standard high confinement operation regime in tokamaks as well as decreasing its reliance on inductive current drive by manipulating the helicity  $q$  of the magnetic field configuration.

In chapter 2 the background including theory is introduced. After having presented the prerequisites, it ends with an in-depth motivation for this work in section 2.6, where this work is also put into the wider context of previously conducted studies.

The tokamak ASDEX Upgrade (AUG) and the experimental setup used for this work are described in chapter 3 while the overhaul of the MSE diagnostic, which is crucial for determining the  $q$ -profile inside the plasma, is reported in chapter 4. The data are used to constrain the reconstruction of the plasma equilibrium, including its internal structure, in particular its helicity profile. This is discussed in chapter 5.

The experimental observations and the modelling results are presented in chapter 6. Finally, a summary and conclusions are given in chapter 7.





## 2 Theory and Background

A plasma consists of charged particles, ions and electrons. It can be manipulated using magnetic fields, which turn it into a magnetised plasma. For the purpose of describing a plasma equilibrium existing under conditions typically present in contemporary fusion experiments, it can be treated as a single fluid whose behaviour is described by Magnetohydrodynamics (MHD) [1, 3].

From MHD, two important timescales for processes occurring in magnetised plasmas are derived. They are the Alfvén timescale  $\tau_A$  for waves affecting the magnetic field lines and the resistive timescale  $\tau_R$  for diffusive and dissipative processes affecting plasma currents.

$$\begin{aligned}\tau_A &= \frac{L}{v_A} = \frac{L\sqrt{\mu_0\rho}}{B} \\ \tau_R &= \mu_0\sigma L\end{aligned}\tag{2.1}$$

Here,  $L$  denotes the system size (e.g. the minor radius of a tokamak, see figure 2.2),  $\rho$  the mass density and  $\sigma$  the conductivity (e.g. Spitzer conductivity  $\sigma \propto T^{-3/2}$ ). The resistive timescale is much longer than its Alfvénic counterpart  $\tau_R \gg \tau_A$ . In a device like ASDEX Upgrade, the former is typically of the order of seconds for the entire plasma and up to hundreds of milliseconds for localised phenomena, while the latter does not exceed the microsecond range.

### 2.1 Plasma Equilibrium

In modern magnetic confinement devices, the confined plasma is suspended without contact to the surrounding vacuum vessel using a tailored helical magnetic field. This is known as the divertor-configuration in which the magnetic field of an external coil diverts the field lines to separate the magnet field cage in two regions: one with closed field lines separated from the open field lines by the so-called separatrix (cf. section 3.1 on page 45). This is shown in figure 2.1a. The open field lines are channeled into the so-called divertor where they make primary contact to the wall on the strike-points (red). In the alternative limiter-configuration (figure 2.1b) the confined plasma column directly touches the wall at a limiter. The topological separation of the divertor configuration allows higher plasma performance and reduces the amount of impurities in the plasma

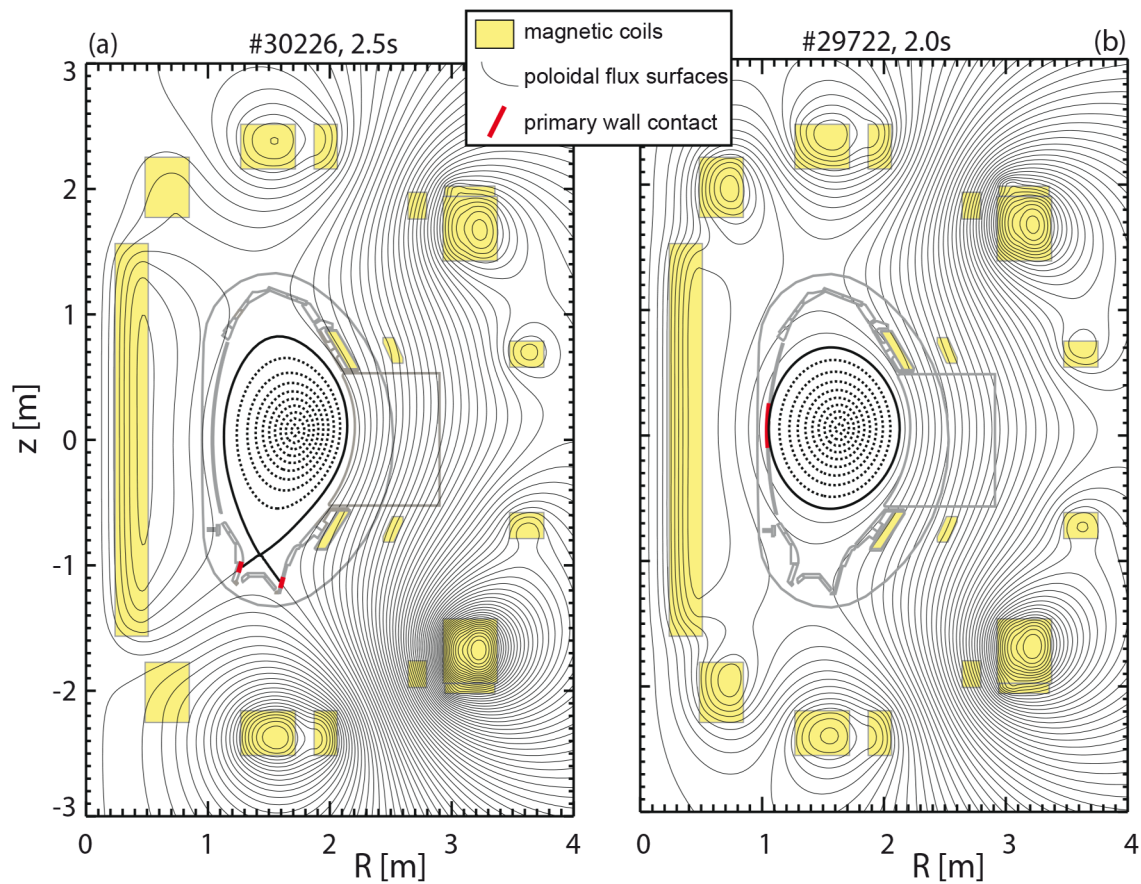


**Figure 2.1:** Equilibria of two ASDEX Upgrade plasmas in a) divertor configuration and b) limiter configuration. Contours of constant poloidal magnetic flux are marked. The closed flux surfaces (dashed lines) are separated from open ones (thin solid lines) by the separatrix/last closed flux surface (thick black lines). They are generated by currents in the plasma and in the coils. Figure reproduced from [4].

compared to the limiter configuration, making it the preferred confinement setup for modern day experiments.

In equilibrium, the kinetic pressure of a plasma is balanced by the magnetic pressure caused by the forces generated by the field acting on the charged particles:

$$\vec{j} \times \vec{B} = \nabla p \quad (2.2)$$

The plasma is constantly undergoing changes, which are generally slower than the aforementioned  $\tau_A$  on which the magnetic field responds to changes. Thus, since these changes are not happening too quickly, the plasma can be considered to evolve as a series of equilibria. The specific properties of this equilibrium state — generally referred to as “magnetic equilibrium” — have not only profound influence on the confinement and sta-

bility of the plasma, but are also crucial for control of the plasma during operation with improved confinement.

It is necessary to choose a suitable coordinate system for describing the equilibrium state and the discussion of the subsequent studies. A straightforward approach is to view the torus as a quasi-cylinder with its toroidal extent (i.e.  $2\pi R$ , cf. figure 2.2) being the equivalent of the cylinder's length. In addition, since a tokamak is axisymmetric, the vast majority of phenomena can be described using only a poloidal plane through the tokamak. This plane can be spanned by a unit vector in direction of the torus' major radius  $\vec{u}_R$  and one in the vertical direction  $\vec{u}_z$  while the toroidal coordinate is understood as a toroidal angle  $\phi/\vec{u}_\phi$ . This representation is particularly useful for applications that need to consider the outside of the plasma. Alternatively, the poloidal plane can also be covered by a coordinate along the minor radius of the torus and a poloidal angle  $\theta$ .

An equilibrium's effectiveness at confining a plasma is quantified by normalising the average thermal pressure to the magnetic pressure:

$$\beta = \frac{\langle p \rangle}{B^2/2\mu_0} \quad (2.3)$$

In general the magnetic field  $B$  in the expression is the total field on the axis. A related quantity  $\beta_{\text{pol}}$  relates the thermal pressure to only the average poloidal magnetic field  $B_{\text{pol}}$  at the plasma edge. Typical values of  $\beta$  for conventional tokamaks are in the range of single digit percentages and generally given as such for convenience, e.g.  $\beta = 2.0$  for 2.0%.

### 2.1.1 The Grad-Shafranov Equation

A tokamak is axisymmetric ( $\partial/\partial\phi = 0$ ), which allows the entire equilibrium to be described in a 2D plane  $(R, z)$ . It must satisfy the Grad-Shafranov-equation (GSE):

$$\begin{aligned} -\Delta^*\psi &= \mu_0 R^2 \frac{\partial p}{\partial\psi} + f \frac{\partial f}{\partial\psi} \\ &= \mu_0 R^2 p'(\psi) + f f'(\psi) = \mu_0 R j_{\text{tor}} \end{aligned} \quad (2.4)$$

Here,  $\Delta^*$  is the Stokes operator in cylindrical coordinates. The equation describes a set of nested surfaces of constant magnetic flux  $\psi$  and (when neglecting toroidal rotation) equal pressure  $p$  (see figure 2.2 on the next page). In general, it is not analytically solvable and finding a solution requires an iterative approach (see chapter 5).

As many derivations of the GSE are available, e.g. in [5–7], a derivation will be omitted here. Instead, an introduction of the individual terms is given:

$\psi(\mathbf{R}, \mathbf{z})$  The poloidal flux is a 2D scalar field containing all magnetic flux contributions from the plasma itself and the surrounding coils (see figure 2.1 on the facing page).

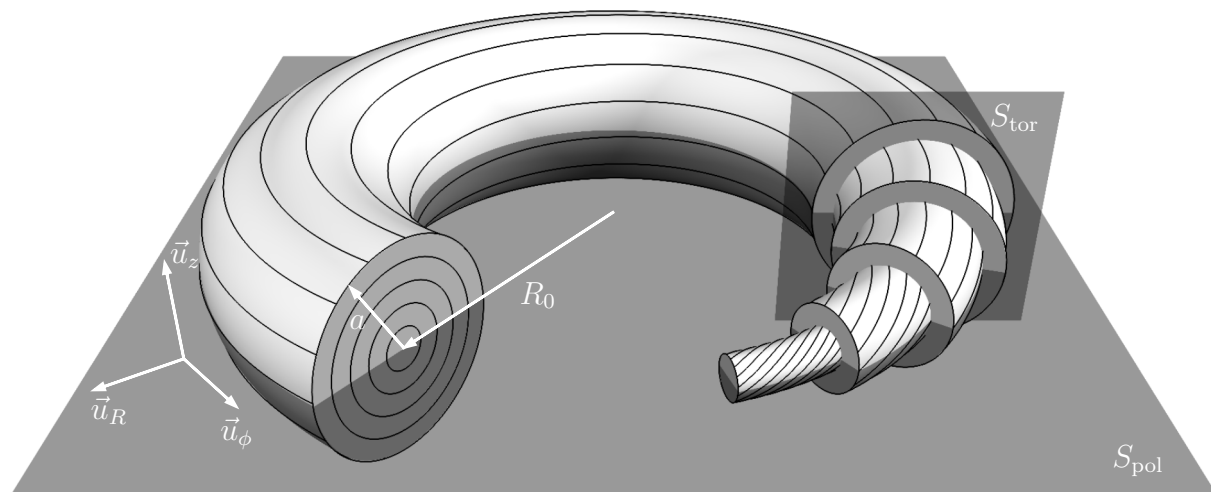


**Figure 2.2:** Coordinate system for toroidal magnetic confinement devices with major radius  $R = R_0$  and minor radius  $r = a$ . Five example nested flux surfaces are shown; helicities are exaggerated for easier visualisation. Shaded planes indicate surfaces used to define toroidal and poloidal flux ( $S_{\text{tor}}$ ,  $S_{\text{pol}}$ ).

Thus, the GSE must be satisfied at any point  $(R, z)$ . It is obtained by integrating the magnetic field over a surface  $S_{\text{pol}}$  as indicated in figure 2.2:

$$\psi(R, z) = \int_{S_{\text{pol}}} \vec{B} \cdot d\vec{S} \quad (2.5)$$

The most obvious  $S_{\text{pol}}$  to perform this integration is a circle of radius  $R$  centred on  $R = 0$  in some plane  $z = z'$ . Similarly, for the toroidal flux  $\phi$  the most obvious surface is a poloidal cut as indicated in figure 2.2, centred on  $r = 0$ .

The magnetic fields in the poloidal plane are obtained from:

$$\begin{aligned} B_R &= -\frac{1}{2\pi R} \frac{\partial \psi(R, z)}{\partial z} \\ B_z &= \frac{1}{2\pi R} \frac{\partial \psi(R, z)}{\partial R} \end{aligned} \quad (2.6)$$

Using coils, the total magnetic flux at the coil location can be measured directly, although not in the plasma core. This information is the main measurement used in equilibrium reconstruction.

- $\mathbf{p}'$  The pressure gradient  $p' = \partial p / \partial \psi$  is purely perpendicular to the flux surfaces and — just like the pressure itself — a flux surface quantity. The pressure is measured, including inside the plasma, by determining temperature  $T$  and density  $n$  separately and combining them as  $p = nT$ . The information is used to constrain equilibrium reconstruction further.

- $f$**  The poloidal current flux function  $f(\psi) = RB_{\text{tor}} = \mu_0 I_{\text{pol}}(2\pi)^{-1}$  is also a flux surface quantity that reflects the influence of poloidal currents in the plasma and in the surrounding toroidal field coils (not shown in figure 2.1). It, too, can be measured using magnetic coils, although not in the plasma.
- $j_{\text{tor}}$**  The toroidal current density describes the currents in toroidal direction. It is not a flux surface quantity, although it is often given as a flux surface average. In the plasma core,  $j_{\text{tor}}$  is only accessible using advanced diagnostics like MSE (see chapter 4). The toroidal current density is very important as it determines the poloidal magnetic field  $B_{\text{pol}}$  and, by extension, the helicity of the magnetic field lines by combining  $B_{\text{pol}}$ , toroidal magnetic field  $B_{\text{tor}}$  and the flux surface geometry. Unlike  $B_{\text{pol}}$ , the toroidal field is well known, and scales inversely with the major radius  $B_{\text{tor}} \propto 1/R$ .

Any solution to the GSE consists of a self-consistent set of  $\psi(R, z)$ ,  $p(\psi)$  and  $f(\psi)$  which can be interpreted as an infinite number of nested surfaces of constant flux, pressure and poloidal current density.

This geometry is common to all tokamaks. To make results comparable across scenarios and machines, a normalised coordinate system based on the flux is introduced. Common flux labels are the normalised poloidal flux  $\Psi_N$  and  $\rho_{\text{pol}}$ :

$$\begin{aligned}\Psi_N &= \frac{\psi - \psi_{\text{axis}}}{\psi_{\text{separatrix}} - \psi_{\text{axis}}} \\ \rho_{\text{pol}} &= \sqrt{\Psi_N}\end{aligned}\tag{2.7}$$

Of course, an equivalent label can be generated from the toroidal flux  $\phi$  instead of  $\psi$ . However, as the toroidal flux requires a closed surface to be defined,  $\phi$  and thus  $\rho_{\text{tor}}$  are only valid up to the separatrix, whereas  $\rho_{\text{pol}}$  extends into the scrape-off layer. In practice,  $\rho_{\text{pol}}$  is often used for edge physics whose phenomena extend across the separatrix while  $\rho_{\text{tor}}$  is only used for core physics.

### 2.1.2 The Safety-Factor $q$

The poloidal and toroidal magnetic fluxes are used together to determine the helicity of the field lines forming a given flux surface. The helicity is commonly expressed as the safety factor:

$$q = -\frac{d\phi}{d\psi}\tag{2.8}$$

For small inverse aspect ratios  $\epsilon = r/R \ll 1$  the safety factor can also be approximated by equation 2.9 on the following page [1]:

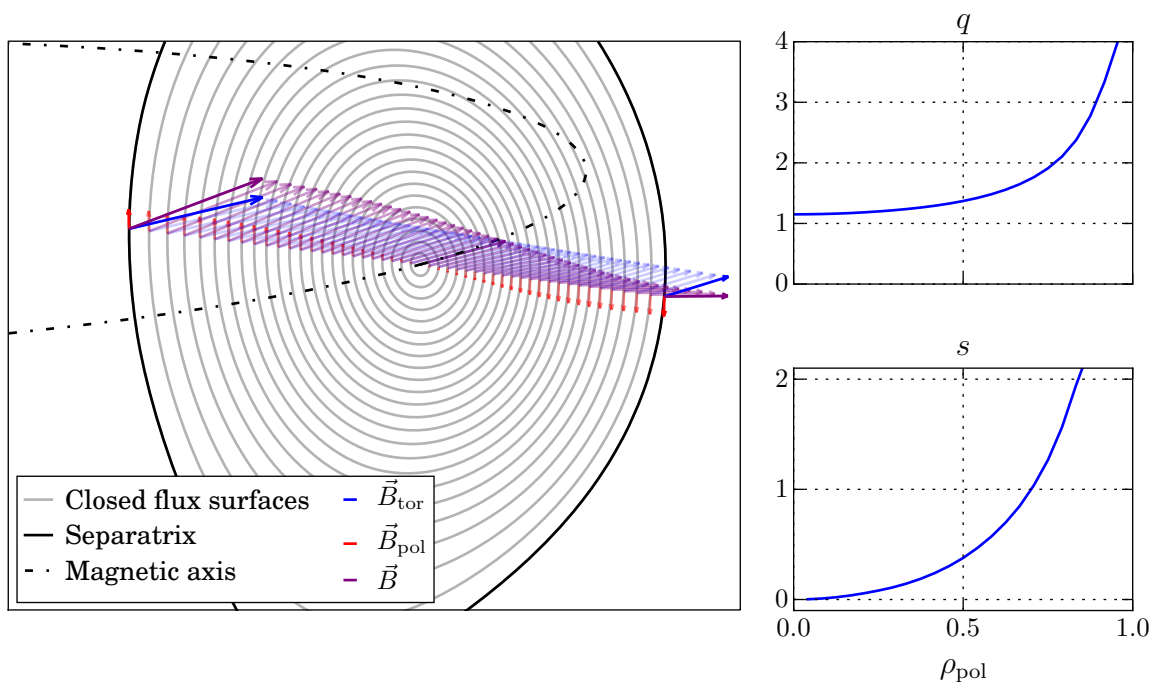


**Figure 2.3:** Left: 3D view of a poloidal cross-section through a standard ASDEX Upgrade equilibrium (generated with CLISTE [8] for #32232 at  $t = 3.5$  s) including magnetic field vectors in the midplane. Right: profiles of safety factor  $q$  and flux-surface-averaged normalised shear  $s$ .

$$q \approx \frac{r B_{\text{tor}}}{R B_{\text{pol}}} \quad (2.9)$$

Here, all quantities are averages over the flux surface in question. An example  $q$ -profile is shown in figure 2.3. In conventional tokamak discharges,  $q$  is close to unity near the magnetic axis and grows towards the edge. In divertor configuration, the imposition of an X-point causes a divergence of  $q$  at the separatrix as the poloidal field becomes zero in the X-point itself, even though a finite  $B_{\text{pol}}$  is present in the rest of the separatrix. This is why the global safety factor is often given by the safety factor at 95% of normalised poloidal flux  $\Psi_N$ , i.e.  $q_{95}$ .

In the 3D plot, the magnetic field across the midplane is shown. It is dominated by the toroidal magnetic field, which declines with  $B_{\text{tor}} \propto 1/R$ .  $B_{\text{pol}}$ , however, is given primarily by the plasma current, i.e. [1]:

$$B_{\text{pol}}(r) = \frac{\mu_0}{2\pi r} \int_0^r j_{\text{tor}}(r') r' dr' \quad (2.10)$$

As a result, the  $q$ -profile is closely connected to the current profile, i.e.  $q$  reflects the current enclosed in a flux surface. However, due to its dependence on the plasma geometry, it is not just a reflection of the poloidal field: while the field has a maximum inside the plasma and then begins to drop as the minor radius grows faster than the enclosed current (see 3D view in figure 2.3 on the facing page), the  $q$ -profile rises continuously (even without the X-point's influence). The  $q$ -profile, being a flux surface quantity, is not interchangeable with any local quantity. That also means that it cannot be directly measured and can only be obtained through reconstruction of the entire plasma equilibrium. Information about the local orientation and magnitude of the magnetic field can, however, constrain and thus improve the reconstruction (see chapter 4).

Another important flux surface quantity is the (normalised) magnetic shear, which is defined as [1]:

$$s = \frac{r}{q} \frac{dq}{dr} \quad (2.11)$$

$s$  is also shown in figure 2.3. Here the geometric effects are more easily visible. Near the plasma edge, the poloidal magnetic field does not change much, but  $q$  and  $s$  both still change substantially.

Both  $q$  and  $s$  influence physical processes in the plasma. For instance, flux surfaces with rational values of  $q = m/n$ , where  $m, n \in \mathbb{N}$ , are of special importance because they are prone to certain instabilities (see section 2.5). This is because on these surfaces, a field line closes on itself after  $m$  toroidal and  $n$  poloidal turns, which allows periodic perturbations to grow there. Furthermore, both magnetic shear and safety factor influence the transport processes inside the plasma (see section 2.3).

## 2.2 Classical and Neoclassical Plasma Transport

This section introduces the fundamentals of plasma transport. Readers familiar with tokamak transport physics may skip it but are still encouraged to at least skim through subsection 2.2.4 on page 16 where the neoclassical bootstrap current and its parameter dependences are described.

A plasma in a tokamak is characterised by various properties, such as temperature, rotation velocity or particle density. Gradients of these properties give rise to heat, momentum and particle transport fluxes. The understanding of the underlying transport processes is crucial for the further development of nuclear fusion power plants. This section is roughly based on [6, 9].

$$\frac{\partial w}{\partial t} = -\nabla \vec{q} + P \quad (2.12)$$



Equation 2.12 is the continuity equation for the energy density  $w$  [ $\text{Jm}^{-3}$ ]. Its change over time is balanced by the heat flux  $\vec{q}$  [ $\text{Wm}^{-2}$ ] and possible power sources or sinks  $P$  [ $\text{Wm}^{-3}$ ]. In a fusion plasma, the latter can be caused by ionisation, external heating or fusion processes. The further discussion will focus on the fluxes that are forming the basis for plasma transport, i.e.  $\vec{q}$ .

A common ansatz for the heat flux is:

$$\vec{q} = -n\chi\vec{\nabla}T \quad (2.13)$$

The density as well as the temperature and its gradient can be experimentally determined. The diffusion coefficient  $\chi$  can also be determined by doing a power balance analysis: in steady state ( $\partial w/\partial t = 0$ ,  $\partial T/\partial t = 0$ ), the power losses must be compensated by the power source, which allows solving equations 2.12 and 2.13 for  $\chi$ . Predicting  $\chi$  from the plasma properties, however, requires an appropriate understanding of the underlying transport processes.

### 2.2.1 Diffusion

In a homogeneously magnetised plasma particles can move freely along the magnetic field lines but are restricted to a gyrating motion in perpendicular direction. Accordingly, it is obvious to assume that transport perpendicular to the magnetic field lines can only occur through collisions. A suitable description of this motion is the so-called random walk: in the simplest model, a particle can move by  $\pm\Delta x$  after every collision, which happens, on average, every time interval  $\Delta t$ . After  $N$  collisions, the mean displacement of the moving particle will be  $\Delta = 0$  since the binomial distribution has a mean value of 0. However, the standard deviation is  $\sigma = 1/2\sqrt{N}$ , so the mean excursion of the particle will be  $\Delta \propto \sqrt{N}\Delta x$  over a time  $\tau = N\Delta t$ . Thus, a diffusion coefficient  $D$  can be written:

$$D = \frac{\Delta^2}{\tau} \propto \frac{\Delta x^2}{\Delta t} \quad (2.14)$$

For a magnetised plasma where the gyration has a so-called Larmor radius  $r_L = mv_{\perp}/(qB)$  with collision frequency  $\nu$  the diffusion coefficient becomes  $D = r_L^2\nu$ . For a flux to arise from this diffusion, a non-vanishing density gradient is required. Note that there cannot be a net particle transport if the both colliding particles are of the same type, since they would simply switch places. This is not the case for heat transport with heat conductivity  $\chi = r_L^2\nu$  as long as the colliding particles have differing kinetic energies/temperatures, i.e. as long as there is a non-vanishing temperature gradient. For a given species of particles  $s$  the Larmor radius is  $r_{L,s} = m_s v_{\perp}/(q_s B)$ , so for the classical heat conductivity is far higher for ion-ion collisions:

$$\chi_{ee} \approx \chi_{ei,ie} \approx \sqrt{\frac{m_e}{m_i}} \chi_{ii} \quad (2.15)$$

For typical values of  $T = 10$  keV and  $n = 1 \times 10^{20} \text{ m}^{-3}$  which lead to  $r_{L,e} \approx 100 \text{ } \mu\text{m}$  and  $\tau_{ee} \approx 300 \text{ } \mu\text{s}$  one arrives at  $D \approx \chi \approx 10^{-5} - 10^{-4} \text{ m}^2 \text{ s}^{-1}$ . In contrast, experimental observation leads to values of  $\chi \approx 1 \text{ m}^2 \text{ s}^{-1}$  and  $D \approx 0.1 \text{ m}^2 \text{ s}^{-1}$ .

The discrepancy between the classically calculated transport coefficients and the experimentally measured ones suggests that the most important channels of perpendicular transport are not described by the classic collision model described above. Further investigation therefore focuses on increasing the step size beyond the Larmor radius.

### 2.2.2 Plasma Drifts

In addition to diffusive transport, convective transport caused by auxiliary forces also has to be considered. In naturally occurring plasmas like the Ionosphere this can be gravity, which has negligible impact on artificial fusion plasmas. Instead, for homogenous magnetic fields (homogeneous) electric fields lead to drifts:

$$\vec{v} = \frac{1}{q} \frac{\vec{F} \times \vec{B}}{B^2} = \frac{\vec{E} \times \vec{B}}{B^2} \quad (2.16)$$

Note that while an electric field accelerates opposite charges in opposite direction, this drift velocity is in the same direction and with the same absolute value both for ions and electrons.

Even though the  $E \times B$ -drift cannot make up for the discrepancy in diffusion coefficients mentioned above, it does play an important role, especially for turbulent processes in the plasma (see section 2.3).

Another important drift is driven by the pressure gradient which has an effect when averaging over an ensemble of particles that forms a fluid. Gyration motions in areas of higher pressure, when overlapping with regions of lower pressure, yield a net velocity:

$$\vec{v}_{\text{diamagnetic}} = -\frac{\nabla p \times \vec{B}}{qnB^2} \quad (2.17)$$

In contrast to the  $E \times B$ -drift, the diamagnetic drift is charge dependent and thus different for electrons and ions.

Finally, inhomogeneity of the magnetic fields also causes drifts, namely curvature and  $\nabla B$  drifts:

$$\begin{aligned}
 \vec{v}_D &= \vec{v}_{D,\text{curv}} + \vec{v}_{D,\nabla B} = -\frac{mv_\perp^2}{2qB^3}\nabla B \times \vec{B} - \frac{mv_\parallel^2}{qB^3}\nabla B \times \vec{B} \\
 &= -\frac{m}{qB^3}\left(\frac{1}{2}v_\perp^2 + v_\parallel^2\right)\nabla B \times \vec{B} \propto -\frac{T}{qB^3}\nabla B \times \vec{B}
 \end{aligned}
 \tag{2.18}$$

This becomes particularly important for the first expansion of classical transport towards neoclassical transport.

### 2.2.3 Neoclassical Transport

In addition to diffusion and convection due to drifts, the inhomogeneous magnetic field induces transport. The total magnetic field is dominated by its toroidal component and decreases with larger major radius  $B_{\text{tor}} \propto 1/R$ , hence the designations high field side (HFS) and low field side (LFS) to distinguish both sides of the magnetic axis.

The magnetic moment of a particle  $\mu = \frac{1}{2}mv_\perp^2/B$  is invariant as  $B$  slowly changes along the path of a plasma particle. Thus, its velocity perpendicular to the magnetic field lines  $v_\perp$  must also slowly change. Since the kinetic energy of the particle is also conserved, the parallel velocity  $v_\parallel$  is changing as well. If the so-called mirror condition

$$\frac{v_\parallel^2(R_0 + r)}{v_\perp^2(R_0 + r)} < \frac{B_{\text{max}}}{B_{\text{min}}} - 1
 \tag{2.19}$$

is fulfilled, the particle becomes trapped, i.e. is reflected when the parallel velocity vanishes. Here,  $R_0$  denotes the major radius of the magnetic axis and  $r$  the minor radius of the flux surface on which the particle is travelling while  $B_{\text{max}}/B_{\text{min}}$  denote the maximum and minimum magnetic field encountered along the path of the trapped particle. For small inverse aspect ratio  $\epsilon = r/R \ll 1$  the mirror condition can be simplified to:

$$\left| \frac{v_\parallel}{v_\perp} \right| < \sqrt{2\epsilon}
 \tag{2.20}$$

Assuming a Maxwell-distribution for the particle velocities, the share of trapped particles can be estimated to be  $n_t/n = \sqrt{2\epsilon}$ . The trapping itself only leads to a movement back and forth along a magnetic field line. However, the toroidal geometry and inhomogeneity impose additional drifts on the particles, notably the curvature- and  $\nabla B$ -drift (see previous section).

Depending on the sign of the poloidal field and the particles charge, these drifts push the particle up- and downwards when moving from the HFS to the LFS while doing the opposite when the particle moves in the opposite direction, resulting in a characteristic banana-shaped orbit when projecting the particle's trajectory into a poloidal plane. In

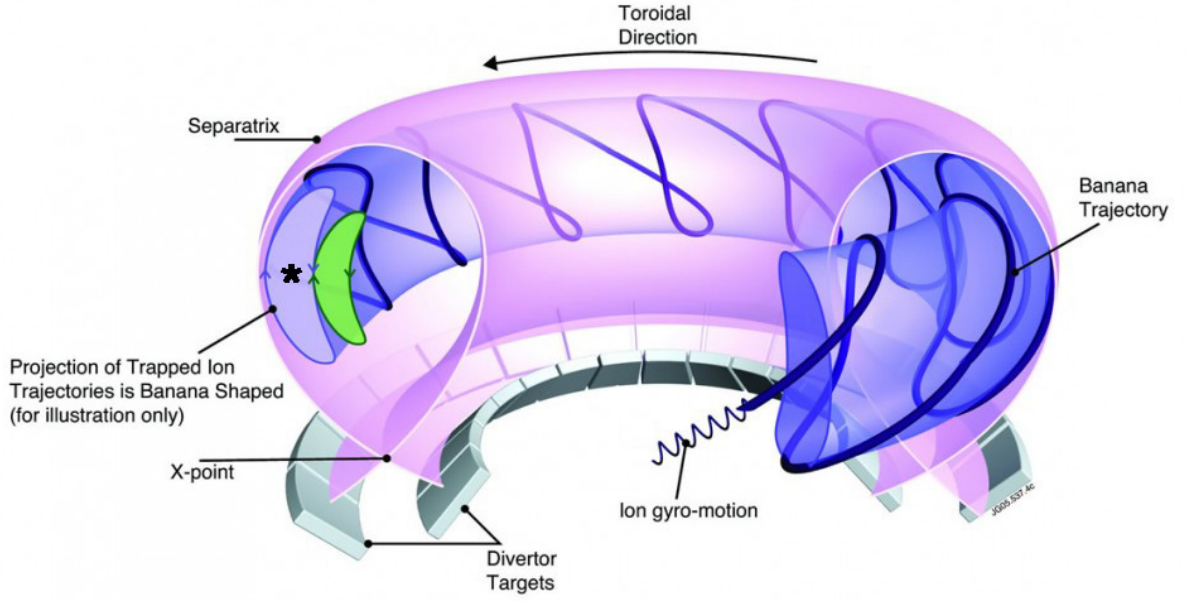


**Figure 2.4:** Movement of charged particles in a tokamak. The precession in toroidal direction is clearly visible. The asterisk highlights where two banana orbits overlap to result in a net bootstrap current. More details are given in the text. Image adapted from [10].

addition, the  $\nabla B$ -drift caused by the poloidal component of the magnetic field  $\nabla B \times \vec{B}_p$  imposes a slow precession of the trajectory in toroidal direction (see figure 2.4).

The width of a banana orbit, which is typically significantly larger than the Larmor radius, is now used to estimate diffusion coefficients in the same fashion as for the classical transport. The maximum banana width is given by barely trapped particles on a trajectory that experiences reflection at the innermost point of a flux surface, which requires  $\Delta t = qr\pi/v_{\parallel}$  time for one completed orbit. Together with  $\epsilon = a/R_0$  as the inverse aspect ratio and the Larmor radius  $r_L = mv_{\perp}/(qB)$ , this yields:

$$w_B = |\vec{v}_D|\Delta t \approx r_L \frac{q}{\sqrt{\epsilon}} \quad (2.21)$$

On top of the wider step size, the collision frequency also increases to the effective collision frequency of  $\nu_{\text{eff}} = \frac{\nu}{2\epsilon}$ . The increase compared to classical particle transport comes from the fact that only collisions that free a trapped particle are of interest as only freed particles change their radial location whereas trapped ones continue to drift in and out of their respective flux surface.

The neoclassical diffusion coefficient for trapped portion of all particles can now be written as:

$$D_{\text{neo}} = w_{\text{B}}^2 \nu_{\text{eff}} \frac{n_{\text{t}}}{n} = r_{\text{L}}^2 \frac{q^2 \nu}{2\epsilon^2} \sqrt{2\epsilon} \approx \frac{q^2}{\epsilon^{3/2}} D_{\text{classic}} \quad (2.22)$$

For a particle at mid-(minor-)radius in a typical fusion plasma, i.e. with  $r \approx R/10$  and  $q \approx 2$ , we arrive at  $D_{\text{neo}} \approx 100 D_{\text{classic}}$  which is still about up to one order of magnitude below experimentally observed values for particle transport [1]. For electron heat transport, the discrepancy is still two orders of magnitude while it is only between 1–10 times lower than observed ion heat transport values [1]. This means that neoclassical effects could at least already play a non-negligible role in the latter, while the former are still dominated by another mechanism known as anomalous transport (see section 2.3).

## 2.2.4 Neoclassical Bootstrap Current

Transport is not the only aspect affected by neoclassical effects. In the presence of pressure gradients, particles on banana orbits closer to the magnetic axis are hotter and denser than those further outside. Overlapping orbits as sketched in figure 2.4 on the preceding page therefore can result in a net current in mostly toroidal direction. According to [11], if  $\epsilon \ll 1$  and the probability for collisions during a banana orbit is small, that is  $1 \gg \nu^* = \nu_{\text{eff}} \Delta t = \nu q R / (2\epsilon v_{\parallel})$ , then the so-called bootstrap current density  $j_{\text{bs}}$  is given by:

$$j_{\text{bs}} = \frac{\sqrt{\epsilon} k_{\text{B}}}{B_{\text{pol}}} \left[ 2.44(T_{\text{e}} + T_{\text{i}}) \frac{dn}{dr} + 0.69n \frac{dT_{\text{e}}}{dr} - 0.42n \frac{dT_{\text{i}}}{dr} \right] \quad (2.23)$$

The dependency on the inverse aspect ratio  $\epsilon$  is clear because bootstrap current requires trapped particles, whose fraction can be approximated by  $\sqrt{2\epsilon}$  [1], while the aforementioned drifts contribute the  $B_{\text{pol}}$  dependence. The inverse dependence on  $B_{\text{pol}}$  can also be interpreted as an approximately proportional dependence with  $q$ , so the bootstrap current increases with higher  $q$ . Furthermore,  $j_{\text{bs}}$  varies with the kinetic profiles, whose exact contributions vary with the plasma conditions as explained in [12, 13], where a more comprehensive expression for the bootstrap current is presented:

$$\langle j_{\text{bs}} B \rangle = -I(\psi) p_{\text{e}} \times \left[ \mathcal{L}_{31} \frac{p_{\text{e}}}{p} \frac{\partial \ln p}{\partial \psi} + \mathcal{L}_{32} \frac{\partial \ln T_{\text{e}}}{\partial \psi} + \mathcal{L}_{34} \alpha \frac{1 - R_{\text{pe}}}{R_{\text{pe}}} \frac{\partial \ln T_{\text{i}}}{\partial \psi} \right] \quad (2.24)$$

Here,  $I = RB_{\text{tor}}$  is the poloidal current and  $R_{\text{pe}} = p_{\text{e}}/p$  the ratio of electron pressure to total pressure. The factors  $\mathcal{L}_{xx}$  and  $\alpha$  depend on the plasma parameters and can change by up to an order of magnitude, with  $\mathcal{L}_{32}$  rarely even changing its sign. Their exact expressions (and visualisation) are given in [12] and [13], including some typical values:  $\mathcal{L}_{31} \approx \mathcal{L}_{34} \approx +0.5$ ,  $\mathcal{L}_{32} \approx -0.2$ ,  $\alpha \approx -0.5$ ,  $R_{\text{pe}} \approx 0.5$ .

For the purpose of this work, they are evaluated to calculate the bootstrap current using TRANSP (see section 3.3.2) and/or IDE (see chapter 5).

Under ordinary circumstances in a contemporary tokamak, this additional current can reach several tens of percent of the total toroidal current and must be taken into account. It also opens the possibility of substituting a significant part of the inductively driven current as long as the necessary density and temperature gradients are maintained. If this happens self-consistently, i.e. with the bootstrap current maintaining a magnetic equilibrium that in turn maintains the kinetic gradients, then it would be possible to significantly increase the pulse length of a tokamak (see also section 2.6).

## 2.3 Anomalous Transport

Due to its original elusiveness, all transport exceeding the predictions of (neo)classical theory are called anomalous, although the term “turbulent transport” has become more prominent since turbulence has been identified as its underlying mechanism.

Evidence [6, 14, 15] points towards micro-instabilities that are excited once critical temperature and/or density gradients are exceeded. These micro-instabilities drive macroscopic turbulence eddies which are able to transport particles, heat and momentum across a larger radial extent. The lifetime of such eddies and their size serve as inverse collision frequency and step size for the aforementioned diffusive ansatz.

The following sections introduce the basics of turbulent transport, which dominates transport. Readers who are already familiar with the various micro-instabilities and the critical gradient model may skip ahead to subsection 2.3.3 on page 24 where the parameter dependences of the critical gradients relevant to this work are summarised.

### 2.3.1 Micro-Instabilities

The micro-instabilities relevant to this work can be divided in two groups based on their underlying mechanism:

- Interchange instabilities: ion/electron temperature gradient (ITG/ETG) mode
- Drift-wave instabilities: trapped electron mode, TEM

#### Interchange Instability (ITG, ETG)

Interchange instabilities can be described as pure 2D phenomena similar to the Rayleigh-Taylor instability [16]. They will be discussed in the following paragraphs using the ion-temperature-gradient-driven (ITG) mode as an example. In the linear, electrostatic, adiabatic limit the equivalent ETG mode for electrons follows the same principle with the roles of ions and electrons switched [17]. A major difference is that while the ITG mode’s characteristic scale is the ion Larmor radius, it is the much smaller electron Larmor radius for the ETG mode.

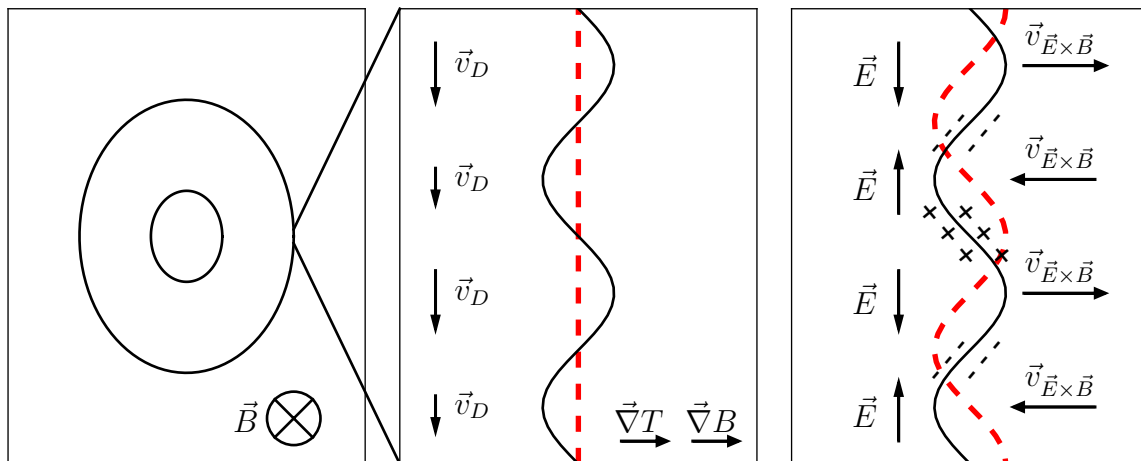


**Figure 2.5:** Simple model of ITG mode emergence.

Left: Equilibrium plasma state with magnetic field pointing into the plane.

Middle: Initial periodic temperature perturbation (black) leads to periodically varying drift velocities.

Right: Varying drift velocities cause periodic accumulation of particles corresponding to a periodic potential (red) whose electric fields lead to a mode-amplifying  $\vec{v}_{\vec{E} \times \vec{B}}$  velocity.

In figure 2.5 a simple model for the emergence of an ITG mode is sketched in a poloidal cross-section of a tokamak core plasma. An initial periodic temperature perturbation on a flux surface affects the drift velocity of the local ions (see equation 2.18): Ions with higher drift velocities from parts with higher temperature move ahead while the slower ones in colder parts fall behind, leading to a periodic aggregation and rarefaction of ions along the flux surface in poloidal direction. This amounts to a periodic perturbation in the ion density, which is — assuming the electrons respond adiabatically — immediately followed by an electron density perturbation so that quasi-neutrality is maintained. Thus, parallel force balance implies the existence of an electrostatic potential  $\phi$  proportional to and in phase with the density perturbation [18]. The electric field  $\vec{E} = -\nabla\phi$  results in an  $\vec{E} \times \vec{B}$  flow that amplifies the original perturbation: colder plasma from the outside is pulled inwards while hot plasma from the inside is pushed outwards, flattening the temperature gradient. This only happens on the low-field side of the tokamak where the magnetic field gradient  $\nabla B$  and the temperature gradient  $\nabla T$  point in the same direction. On the high-field side,  $\nabla B$  remains unchanged in lab coordinates, but  $\nabla T$  is reversed. As a consequence, the  $\vec{E} \times \vec{B}$  flow reduces the perturbation. Thus, the low-field side of the plasma is described as having destabilising ‘bad curvature’ instead of stabilising ‘good curvature’.

Note how the cross-phase [19, 20] between potential and temperature perturbation is exactly  $\delta = \pi/2$  and thus leads to maximum transport whereas it is in phase with the

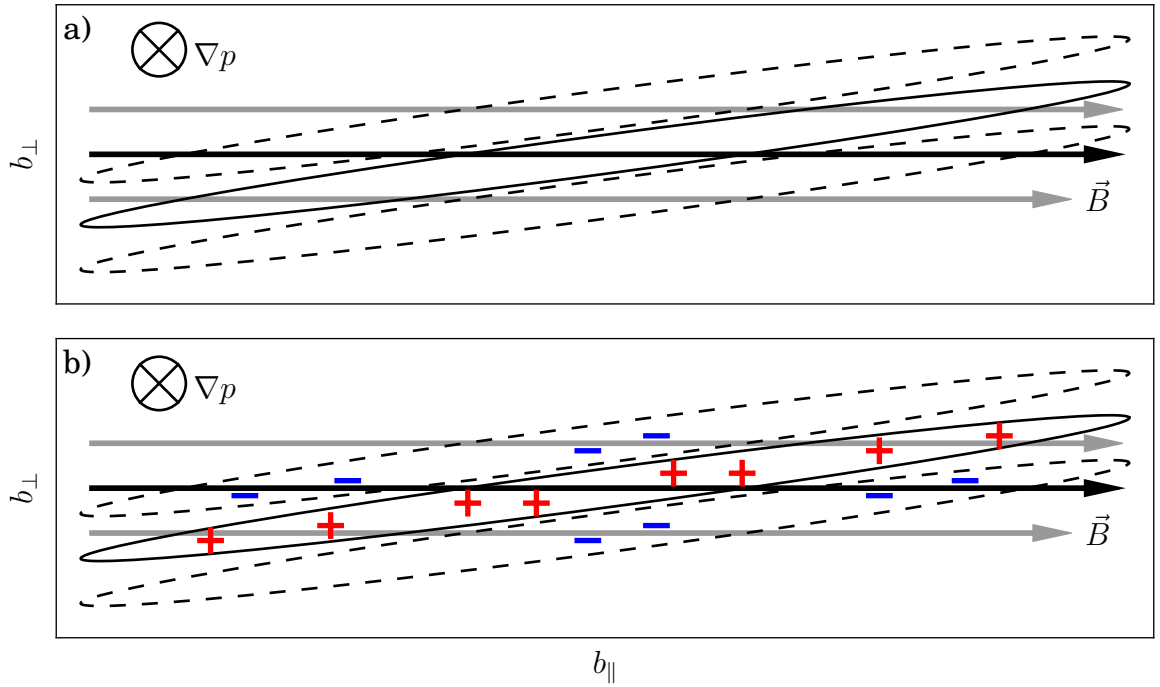


**Figure 2.6:** Cutout of a flux surface on the low-field side.  $b_{\parallel}$  and  $b_{\perp}$  are coordinates parallel and perpendicular to the local magnetic field, respectively.

- a) Initial temperature perturbation; higher pressure in solid ellipse, lower pressure in dashed ellipses.  
 b) Charge separation that causes a downward drift of the mode (see fig. 2.7).

density perturbation and therefore leads to no particle transport. One can, however, construct an analogue model that starts with a density perturbation that is amplified through the electric fields that arise from charge separation which itself is caused by the charge dependence of the drift velocity.

### Drift-Wave Instability (TEM)

The drift-wave instability represents the other important kind of micro-instabilities that are relevant for this work. In contrast to the interchange instability, it requires a 3D description since the initial perturbation and its consequences are best described in two 2D pictures that are perpendicular to one another.

In figure 2.6a an initial perturbation is sketched. Consider a flux surface on which a periodic pressure perturbation is imposed. The surface coincides with the viewing plane with the abscissa pointing along the surface in direction of the magnetic field and the ordinate pointing in poloidal direction, i.e. perpendicular to the magnetic field. This



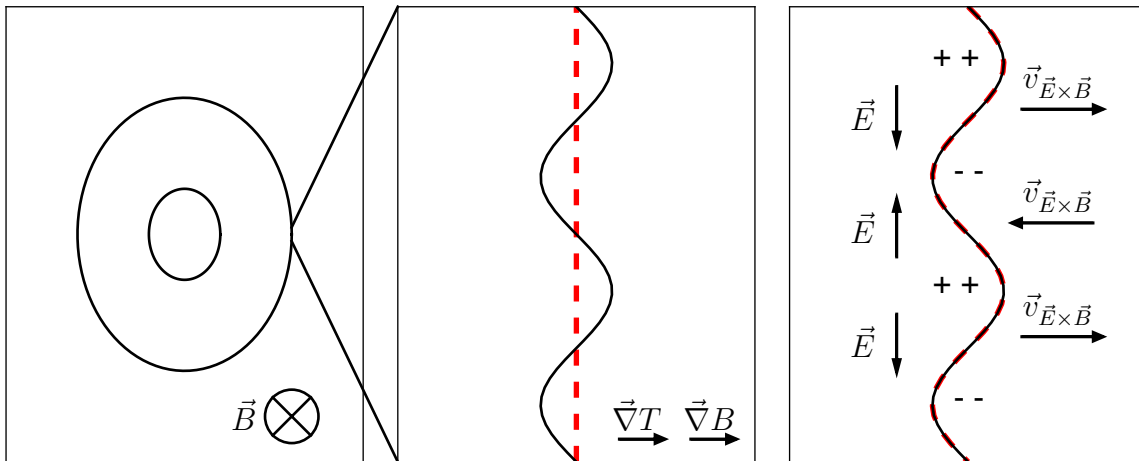


**Figure 2.7:** Simple model of drift-wave instability emergence.

Left: Equilibrium plasma state with magnetic field pointing into the plane.

Middle: Initial periodic pressure perturbation (black).

Right: Varying pressure causes periodic charge separation (see fig. 2.6 on the previous page) corresponding to a periodic potential (red) whose electric fields generate a drift velocity  $\vec{v}_{\vec{E} \times \vec{B}}$ . These drifts lead to the instability advancing downwards along the flux surface.

perturbation can be caused by a perturbation in temperature and/or density, and also has gradients parallel to the magnetic field  $\vec{B}$  — as opposed to the interchange instability, which has no component parallel to the field. In the figure, the solid ellipse is such a region of increased pressure while the dashed ellipses symbolise a corresponding region of reduced pressure.

Assuming the electrons to be adiabatic, they immediately react to the perturbation and escape to regions of lower pressure by flowing along the magnetic field lines, leading to the situation shown in figure 2.6b: positively charged ions are left behind in regions of higher pressure, while regions of lower pressure receive the negatively charged electrons.

In a poloidal plane the same situation occurs only seemingly without a cause, with charges separating into areas of over- and under-pressure as shown on the right-hand side of figure 2.7. The resulting electric fields lead to an  $\vec{E} \times \vec{B}$ -drift like in the interchange case, except now the drift does not amplify the initial perturbation. Instead, it allows the perturbation to travel downwards in the electron diamagnetic drift direction — hence the term drift-wave.

Note that no radial transport occurs since potential and pressure perturbation are in phase, i.e. the cross-phase between them is  $\delta = 0$ .

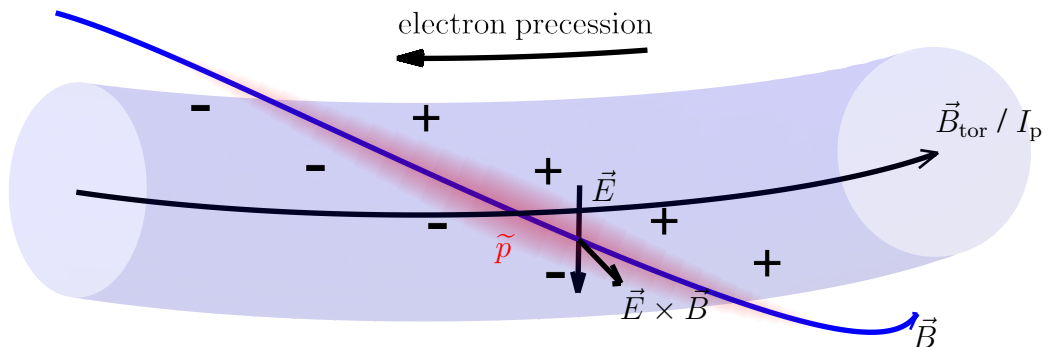


**Figure 2.8:** Charge separation around pressure perturbation  $\tilde{p}$  (red) due to neoclassical electron precession which results in a radial  $\vec{E} \times \vec{B}$ -drift. More details are given in the text.

So far in this description, the electrons were free to flow along the field lines without any additional effects. As a result, the drift-wave did not affect transport. In a tokamak, however, several effects prevent an ideal response. For one, the plasma is resistive and particles are slowed down by collisions. Furthermore, the inhomogeneity of the magnetic field causes neoclassical trapping which also prevents such an ideal reaction. Ultimately, the main consequence for the drift-wave instability comes from the toroidal precession that trapped electrons experience. This is sketched in figure 2.8. As the trapped electrons are precessing toroidally, a charge separation occurs at the pressure perturbation, which causes an electric field with  $\vec{E} \cdot \vec{B} \neq 0$ , resulting in a drift in outwards radial direction at the location of the initial pressure perturbation.

Thus, in a region of already high pressure due to the initial perturbation, the drift-wave instability increases the pressure further by convecting plasma from the high pressure core, which amplifies the initial perturbation.

Trapped electrons do also occur on the high-field side of a toroidal device when their parallel velocity  $v_{\parallel}$  is sufficiently high (see 2.2.3). While only some trapped particles meet that condition, all of them are intermittently present on the low-field side. That makes the trapped electron mode — together with the aforementioned ITG and ETG modes — dominant on the low-field side of a tokamak.

### 2.3.2 Macroscopic Critical Gradients

Turbulent transport allows very high fluxes of at least one order of magnitude above neoclassical predictions [21]. Fortunately for fusion devices, the micro-instabilities be-

hind turbulence are only excited when the kinetic gradients exceed certain threshold values [22]. Above the threshold, turbulence appears and the therefore rapidly increasing fluxes flatten the gradients again until they approach the threshold value, at which point the drive for turbulence vanishes. A quasi-equilibrium state can emerge where, for example, since this work focuses on heat transport, the slopes of a temperature profile remain around a critical gradient that can only be overcome with excessive heating power. Even in that case, the critical value can only be increased by small amounts since the additional heat is immediately transferred out via almost arbitrarily strong turbulent transport. This is known as profile stiffness.

Linear gyrokinetic theory [23] yields that this critical gradient is not just the local temperature gradient  $\nabla T$  but instead the normalised temperature gradient  $R/L_T$  with  $1/L_T = \nabla T/T$  being the inverse temperature gradient length. As a result, the heat conductivity takes a form like [24]:

$$\chi = \chi_0 + C \cdot \left( \frac{1}{L_T} - \frac{1}{L_{T,\text{crit}}} \right) \cdot H \left( \frac{1}{L_T} - \frac{1}{L_{T,\text{crit}}} \right) \quad (2.25)$$

with  $\chi_0$  as the non-turbulent heat conductivity,  $C \gg \chi_0$  as a model-dependent coefficient and  $H$  as the Heaviside step function. The fact that the critical gradient at a given point depends explicitly on the absolute temperature at that point has profound consequences for the attainable temperature profiles.

If  $L_T = L_{T,\text{crit}}$  holds for the whole minor radius, the temperature profile can be approximated using an exponential function [21]:

$$T(r) \approx T(r_{\text{edge}}) e^{(r_{\text{edge}} - r)/L_{T,\text{crit}}} \quad (2.26)$$

As such, the best-case temperature profile depends solely on the edge temperature and the critical gradient across the minor radius, but not on parameters like the applied heating power. Note that this approximation neither describes the necessary flattening at the plasma centre that ensures the smoothness of the profile across the whole plasma cross-section, nor does it provide an in-depth characterisation of the plasma edge, which will be discussed in section 2.4.

In figure 2.9 three examples of such temperature profiles are shown. A reference profile is shown in blue. The red curve shows the effect of a doubled edge temperature: the increased edge value propagates along the entire minor radius. The profile shape does not change and merely scales with the edge temperature. The black profile shows the effect of a 25% increase of the critical temperature gradient. Assuming no change in the density profiles, the change in temperatures will be reflected directly in the plasma pressure. Since fusion power per volume scales with the average plasma pressure  $P_f/V \propto \langle p \rangle^2$  [25], the different temperature profiles will, compared to the reference profile, quadruple the fusion power in the case of doubled edge temperature and roughly double it for the

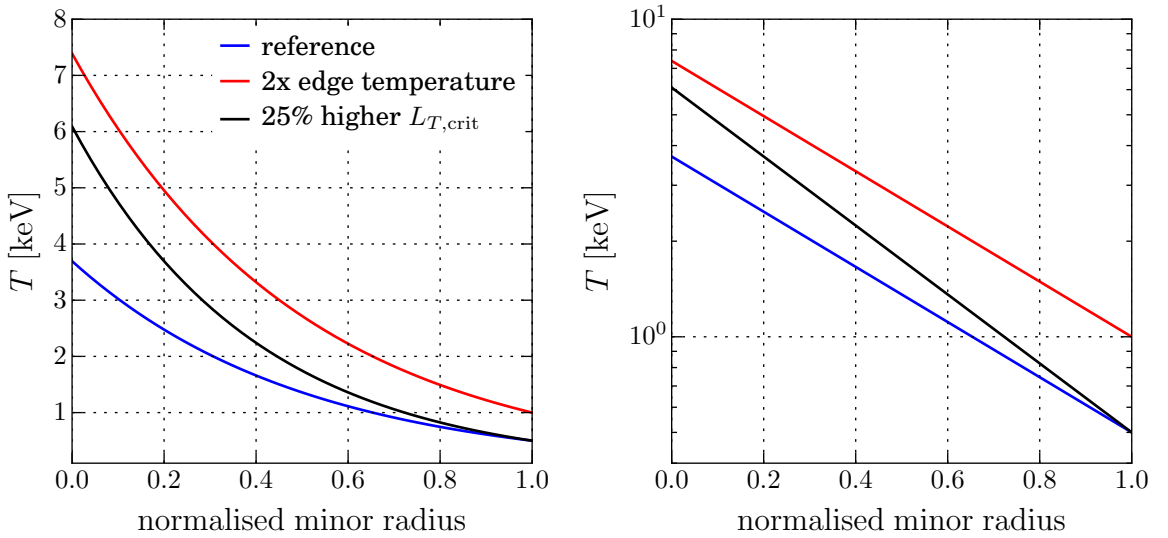


**Figure 2.9:** Example temperature profiles for two different edge temperatures and critical temperature gradients on linear and logarithmic scale.

increased  $L_{T,\text{crit}}$  case. These simple considerations make it self-evident that effective control of temperature profiles is a key ingredient for affordable fusion power.

Due to the profile's exponential character, displaying them on a logarithmic scale yields further insights [26]. It illustrates, for instance, the profile stiffness: for a given critical gradient, the profiles look alike and are only shifted horizontally. At the same time, a change in the critical gradient appears as a change of the slope. When manipulating temperature profiles it is thus useful to turn to such logarithmic plots to isolate changes in the boundary conditions from changes to the transport properties inside the plasma.

A distinct but localised increase of the logarithmic profile slope can be interpreted as a transport barrier. A notable and very strong example is the edge transport barrier (ETB) that is characteristic for high confinement operation (see section 2.4 on page 30). Internal transport barriers [27] (ITBs) are less common and have been found to occur, for instance, due to magnetic shear reversal [28], which is also discussed in the following subsection on critical gradient parameter dependences.

In addition to defining a transport barrier by a locally increased gradient, one can also formulate an equivalent definition that is based on locally reduced transport coefficients. While conceptually very similar, the latter requires a power balance analysis (cf. subsection 2.3.4) to determine an ITB. Lastly, a different definition altogether requires a local reduction of turbulence. Such an approach is used to characterise the ETB using, for example, reflectometric measurements of density fluctuations. This technique is, however, generally not able to reach the plasma core, which is why ITBs are usually characterised by the gradient/coefficient approach.

On the one hand, ITBs are considered advantageous as they increase the plasma confinement and thus its performance. Steep gradients also result in more bootstrap current, which decreases the plasma's reliance on inductive current drive. On the other hand, ITBs may also promote impurity accumulation due to their improved particle confinement and thus affect the performance negatively. This would be particularly problematic for future power plants where the helium ash of the fusion reaction would not be expelled and instead dilute the fusion fuel until the reaction breaks down. In this thesis in particular, ITBs can be problematic when the discharge is already close to the stability limit and an emerging ITB pushes it beyond that limit (cf. section 6.1.3). As such, an ideal ITB would improve heat confinement and therefore allow the external heating to be reduced, but would not affect particle confinement.

The range of achievable edge temperatures and the potential increase of the critical gradient will be discussed in the following sections.

### 2.3.3 Critical Gradient Parameter Dependences

The critical temperature gradient at which micro-instabilities start to grow depends on various parameters. Multiple studies have been carried out in the past to investigate these dependencies, for example [29] give the critical normalised ion temperature gradient for the ITG mode as

$$R/L_{T_{i,\text{crit}}} \propto \frac{4}{3} \left(1 + \frac{T_i}{T_e}\right) \left(1 + 2\frac{s}{q}\right) \quad (2.27)$$

for  $R/L_n < 2 \left(1 + \frac{T_i}{T_e}\right)$  with  $L_n = n/\nabla n$ . The equivalent expression for the ETG mode can be obtained by switching the role of ions and electrons [17]. A more detailed expression is given by [17]. It explicitly includes geometric effects as well as the stabilising effect of peaked density profiles:

$$R/L_{T_{i,\text{crit}}} = \max \left\{ \left(1 + \frac{T_i}{T_e}\right) \left(1.33 + 1.95\frac{s}{q}\right) (1 - 1.5\epsilon) \left(1 + 0.3\epsilon\frac{d\kappa}{d\epsilon}\right), 0.8R/L_n \right\} \quad (2.28)$$

Here,  $\kappa = b/a$  denotes the plasma elongation defined by the ratio of vertical to horizontal extent of the confined plasma. The equation shows that the onset of ITG modes can be delayed by:

- increasing the ion temperature,
- increasing the shear or reducing the safety factor,
- changing the plasma shape,
- peaking the density profile.

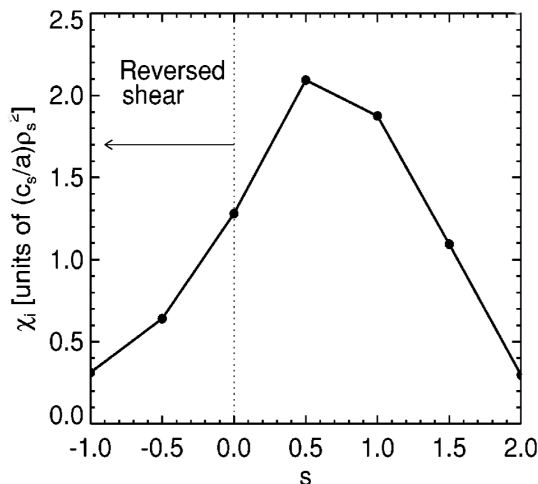


**Figure 2.10:** Normalised heat transport coefficient dependence on normalised magnetic shear. Image reproduced from [32], based on data from [31].

This work focuses on the first two options, i.e. the temperature ratio between ions and electrons and the shear/helicity of the field lines.

There is one important limitation to equation 2.28: it has been derived for  $s > 0.2$ , so cases with no shear or reversed shear are, strictly speaking, not covered by it. Other numerical studies do not expand the given expression for the critical gradient, but they do provide further information on the behaviour of ITG modes [30, 31] or TE modes [30] across different shear values in the form of time averaged heat diffusivities. Specifically, they identify a maximum diffusivity for  $s \approx 0.5$  that drops similarly on either side of that value (see figure 2.10). It has to be noted that the drop towards lower shear  $0.2 < s < 0.5$  is not supported by equation 2.28, while an increase in the critical gradient after  $s \approx 0.5$  is observed, which matches the results obtained with numerical simulations like TGLF (see subsection 2.3.4).

Expressions to estimate the critical gradient of the TEM also exist. One example is given in [33] with  $\epsilon$  as the inverse aspect ratio and  $\nu_{\text{eff}}$  as the effective collision frequency:

$$R/L_{T_e, \text{crit}} = \frac{0.357\sqrt{\epsilon} + 0.271}{\sqrt{\epsilon}} \left[ 4.90 - 1.31 \frac{R}{L_n} + 2.68s + \ln(1 + \nu_{\text{eff}}) \right] \quad (2.29)$$

Due to the  $\epsilon$ -dependence, the critical TEM gradient diverges near the magnetic axis, which is due to the lack of trapped particles at the magnetic axis. This makes the TEM more prominent at larger minor radii. Other than for ITG/ETG mode, a peaked density profile is destabilising for the TEM: this suggests that with peaking density the dominant micro-instability could switch from ITG to TEM. In contrast with this, and similar to the ITG/ETG, an increasing magnetic shear increases the critical gradient. Moreover, collisions interrupt the usual path of trapped particles and thus impede the

charge separation underlying the TEM, which is reflected in a dependence on the collision frequency  $\nu_{\text{eff}}$ .

Further insight has been gained by studies of the parameter dependence of the time averaged diffusivities/fluxes resulting from TEM-triggered turbulence, for example in [34] and [30]. They generally show an increase of the heat fluxes with increasing safety factor  $\chi \propto q$ , a decrease with stronger shear  $\chi \propto -s$  for  $s > 0.5$  and — as opposed to the ITG mode — an increase with higher normalised density gradient  $\chi \propto R/L_n$ . This partially matches the threshold given in equation 2.29, with the exception of the dependence on  $q$ . On top of the opposite density dependence, experimental observations [35] suggest that TEMs are independent of the temperature ratio  $T_e/T_i$  and only weakly dependent on  $q$ , which is in contrast to the theoretical results of [34], and more in line with the threshold given by equation 2.29.

All aforementioned instabilities (ITG/ETG mode, TEM) are expected to occur in the experiment. However, the ITG mode is expected to be dominant [21], which allows the formulation of the following expectations about the heat transport:

- Heat transport will decrease with decreasing  $T_e/T_i$ .
- Heat transport will decrease with increasing  $|s - s_0|$  with  $s_0 \approx 0.5$ .
- Heat transport will increase with increasing  $q$ .

These expectations are guidance for quantitative or even just qualitative analyses of turbulent transport by experimental means. It is, however, also helpful to gain at least some intuitive understanding of the processes that lead to these expectations:

### Temperature Ratio $T_e/T_i$ :

All micro-instabilities are fundamentally based on the different responses of ions and electrons to perturbations. All these reactions are assumed to occur with the respective thermal velocity  $v_{\text{th}} \propto \sqrt{T/m}$  of each particle species. Due to their much lower mass, electrons are able to react faster than ions (hence the adiabatic assumption), which then leads to the emergence of a potential  $\phi$  that causes radial transport when not in phase with the kinetic perturbation. The thermal velocity also depends on each species' temperature, which then gives an intuitive image of how ions can more easily catch up with electrons when they are warmer: as they follow the electrons more easily, the fluctuating potential  $\phi$  decreases and the radial transport is dampened. Obviously this image is only of qualitative use since it neglects all other species-specific characteristics that might affect their ability to respond to a perturbation. However, it does capture the temperature's influence, including the observation that the TEM is largely independent of the temperature ratio: the charge separation that causes  $\phi$  in the TEM case cannot be undone by heating the ions, which will always drift in the opposite direction than the electrons.

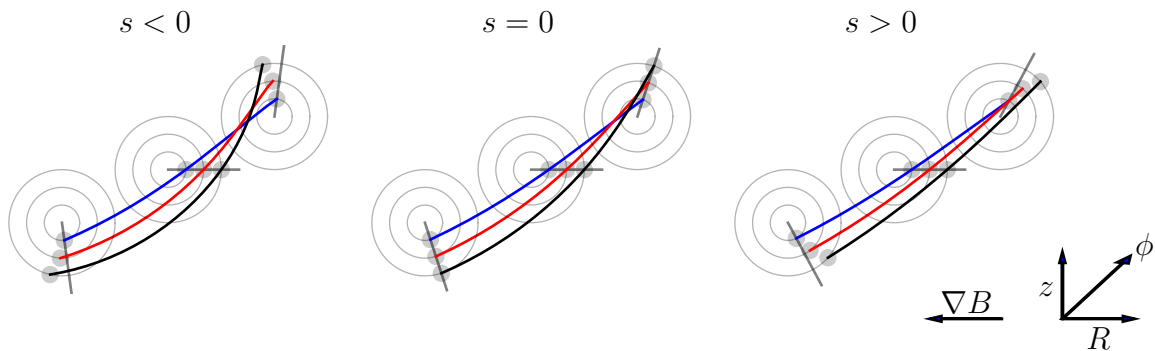


**Figure 2.11:** Simplified picture of the magnetic shear's effect on radially extended mode structures [37]. For  $s \neq 0$ , mode structures are sheared apart and can no longer remain radially aligned as indicated. In addition, for  $s < 0$ , mode structures are bent towards smaller major radius, i.e. towards stabilising good curvature. Cylindrical geometry was chosen for ease of visualisation only. More details, particularly about the  $s = 0$  case, are given in the text and figure 2.12.

### Normalised Magnetic Shear $s$ :

The descriptions of the micro-instabilities make use of a static frame of reference. This is only a simplification. In a real tokamak plasma, the particles and hence the structures occurring during the emergence of an instability move along the field lines. It is evident why a large value of the magnetic shear is therefore stabilising: the radially extending structures are sheared apart before they can grow to become turbulence. Even if they become turbulent, the resulting turbulence eddies are potentially still sheared apart by the magnetic shear and transform into zonal flows [36].

It is straightforward to explain why negative shear has a strong suppressing effect even beyond that of positive shear of the same absolute value. In figure 2.11 three different cases are sketched, one with negative, one with positive, one without magnetic shear. In the case of negative shear, outer field lines are more helically twisted than inner ones, whereas the opposite holds for the positive shear case. Both cases with magnetic shear lead to the radial mode structure being sheared apart. On top of that, in the case of negative shear, one can see how the mode structures are tilted towards the high-field side, which effectively shortens the time they spend in bad curvature on the low-field side and instead extends the time spent on the stabilising high-field side. This effect is not as pronounced in the TEM case, as trapped particles can exist on the high-field side, albeit generally in lower numbers than on the low-field side.

Finally there remains one counter-intuitive characteristic: Why does slightly positive shear appear to lead to the highest radial transport instead of zero shear? First, zero shear is, in fact, the worst configuration with respect to mode stability in a cylindrical plasma. For toroidal geometry, however, more considerations are necessary.



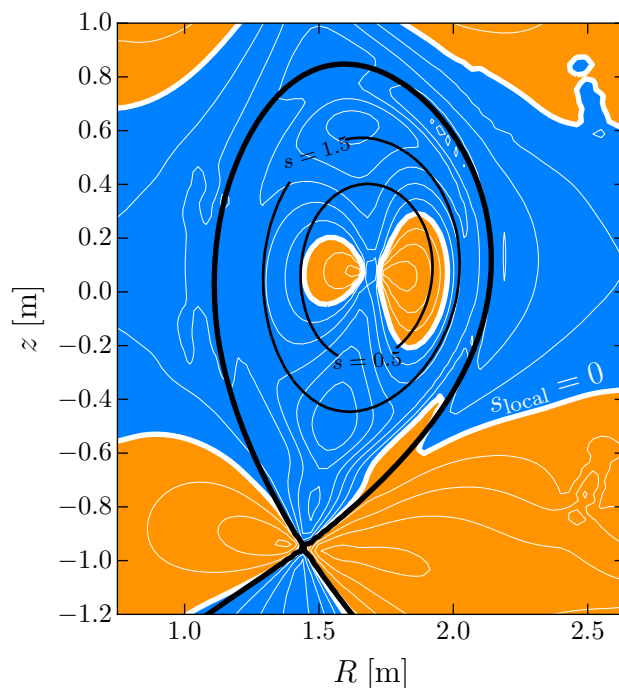


**Figure 2.12:** Local shear in blue/orange (positive/negative), given by  $s_{\text{local}} = \vec{e}_{\perp} \cdot \vec{\nabla} \times \vec{e}_{\perp}$  with  $\vec{e}_{\perp} = \vec{\nabla}\psi / |\vec{\nabla}\psi| \times \vec{B}/B$  [38]. In this example, the local shear becomes zero (white) in the region of bad curvature when flux surface average shear is between  $s = 0.5$  and  $s = 1.5$ . Equilibrium generated with CLISTE [8] for #32232 at  $t = 3.5$  s.

Resolving this seeming contradiction becomes trivial when considering that ITG and ETG modes, and to a lesser extent the TEM, are stable on the high-field side of the given flux surface. The normalised magnetic shear, however, is a flux-surface-averaged quantity, while the instabilities' behaviour is primarily defined by the local shear on the low-field side. For an ordinary tokamak equilibrium, the local shear on the low-field side becomes zero when the normalised magnetic shear is slightly positive as can be seen in figure 2.12. Therefore the highest transport occurs when the shear on the low field side is zero and not when the flux surface averaged shear is zero.

It should be noted that while this section focuses on the dependence of the critical gradient on *magnetic* shear, it is not the only kind of shear that affects turbulent transport. Other effects like  $\vec{E} \times \vec{B}$ -shearing due to a radial electric field may perhaps not directly affect the critical gradient as described by the models introduced earlier, but do have an impact on the resulting turbulent eddies [39]. If they are sheared apart, then turbulent transport can be suppressed even beyond the critical gradient at which micro-instabilities begin to grow.

**Safety Factor  $q$ :**

The safety factor can be approximated by  $q \approx (r/R)(B_{\text{tor}}/B_{\text{pol}})$ . As noted above, higher  $q$  tends to increase radial transport. This is easy to conceptualise by considering the limit of  $q \rightarrow \infty$ . Here, the poloidal magnetic field vanishes  $B_{\text{pol}} \rightarrow 0$ , which would mean that a field line on the low-field side would never reach the high-field side. As a result, no stabilisation due to good curvature occurs and micro-instabilities become unstable.

**2.3.4 TGLF and ASTRA**

TGLF [40] is a transport simulation code with a comprehensive physics model based on the **T**rapped-**G**yro-**L**andau-**F**luid equations [41]. It takes into account trapped particles, the toroidal geometry of a plasma, electron-ion collisions and impurities. It also considers electromagnetic effects, i.e. fluctuations can affect the magnetic field and not just kinetic quantities and the resulting electrostatic potential. Its model provides accurate quasilinear approximations of the linear eigenmodes of gyrokinetic instabilities (including ITG, ETG modes, TEM). Since they are approximations, the results are obtained orders of magnitude faster than in full gyrokinetic simulations like GENE [42, 43] or GYRO [44], from which TGLF is derived.

TGLF takes kinetic profiles and magnetic equilibrium information as an input and generates quasilinear fluxes of energy and particles as output. These fluxes are used to, for example, evolve the input profiles using the transport coefficients calculated by TGLF. Comparisons between experimental measurements and TGLF results serve as benchmarks.

The transport code is embedded in a framework software. Here, this framework is ASTRA, the Automated System for Transport Analysis [9]. ASTRA allows the user to separately provide experimental data and customisable physical models. It is modular, versatile and easily extended, which makes it an ideal environment for analyses with TGLF.

Generally ASTRA is given a set of kinetic profiles, external heating profiles either from pre-calculated profiles or live calculations (e.g. TORBEAM, see section 3.3.1 on page 58), and a boundary in the form of the separatrix of a magnetic equilibrium and a  $q$ -profile. The given profiles are either taken as-is and evaluated to obtain results like the power balance, or, for example with TGLF, evolved using the calculated transport coefficients. Ideally, the simulated evolution of the profiles then matches the experimentally observed behaviour.

TGLF's physics model is sensitive to all aforementioned parameter dependencies, i.e. temperature ratios, safety factor and magnetic shear (as well as  $\vec{E} \times \vec{B}$ -shear). This makes it also sensitive to effects like velocity shearing, which also generates radial electric fields that affect micro-instabilities.

Previous work on ASDEX Upgrade has been able to accurately reproduce electron and ion temperature profiles with TGLF in discharges with both dominant electron heating and dominant ion heating [45]. The latter in particular is to be expected for this work. A major difference is that [45] reports on discharges with monotonic  $q$ -profiles whereas this thesis focuses on elevated and/or even reversed  $q$ -profiles.

Similarly, recent results from DIII-D [46] suggest that it is possible to reproduce temperature profiles in high- $\beta$  steady-state scenarios with TGLF. While DIII-D is also a mid-sized tokamak like ASDEX Upgrade, it is covered with carbon instead of tungsten (cf. chapter 3 on page 45). Moreover, the reported results are achieved by exploiting early heating during the current ramp-up. This is also explored in this thesis (see section 6.1 on page 94) next to late heating scenarios where the starting point is a relaxed current profile (see section 6.2 on page 105 and section 6.3 on page 114). In that sense, this work extends the studies with regard to late heating in a full tungsten machine.

## 2.4 The H-Mode

The significance of the edge kinetic profiles of a fusion plasma for its overall performance was discussed in section 2.3.2. This is the reason why the high-confinement mode (H-mode) is essential for high-performance fusion plasmas [47].

Its main characteristic is the existence of an edge transport barrier caused by suppression of turbulence in the edge, leading to the formation of a pedestal in density and temperature, on top of which the respective stiff profiles extend towards the core. Like its namesake, the pedestal raises the profiles everywhere, resulting in significantly higher

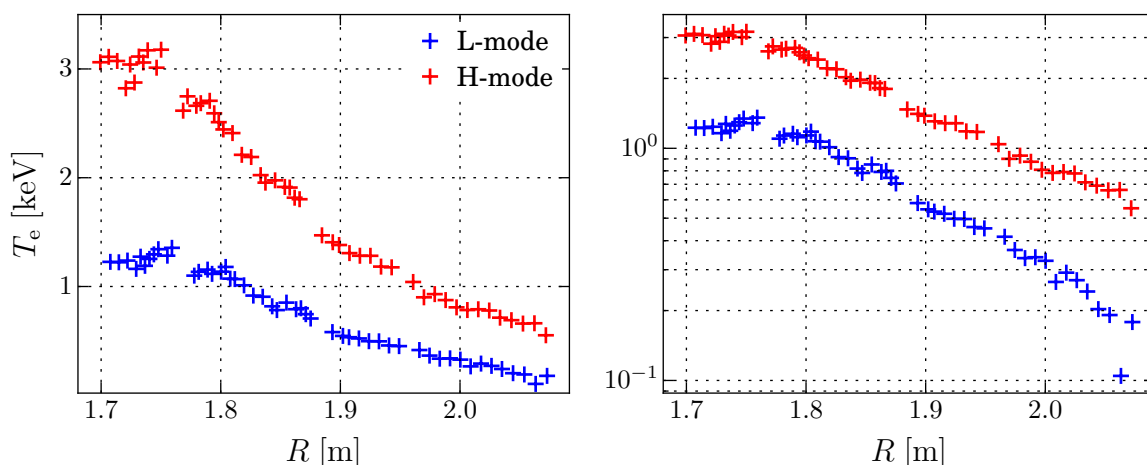


**Figure 2.13:** Electron temperature profiles from ECE (see section 3.2.2 on page 47) in L-mode and H-mode on linear and logarithmic scale. (#32494; 4.9 s, 5.4 s)

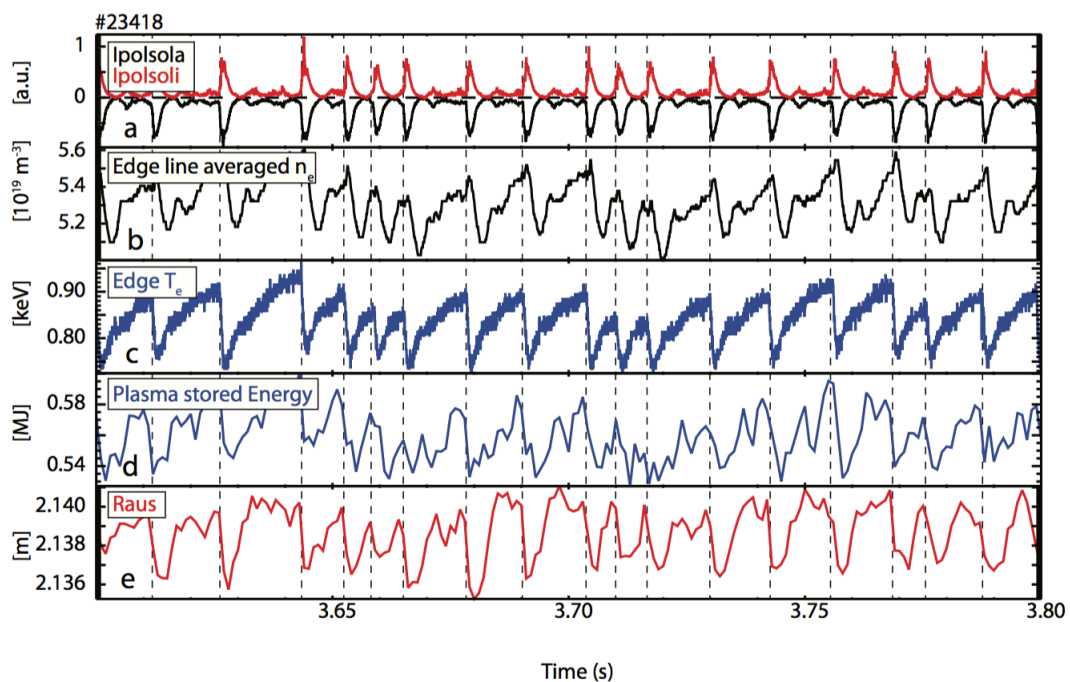


**Figure 2.14:** Time traces of divertor current measurements (a), the edge line averaged electron density (b), the edge electron temperature (c), the plasma stored energy (d) and the position of the outer separatrix (e) in a typical AUG H-mode discharge. Image reproduced from [50].

core pressure. On top of that, as shown in subsection 2.3.2, a higher edge temperatures propagates into the core exponentially through profile stiffness, which leads to otherwise unattainable core temperatures (see figure 2.13).

The edge temperature is limited by MHD instabilities known as Edge Localised Modes (ELMs) [48]. ELMs are quasi-periodical instabilities that collapse the pedestal intermittently when the steep gradients in the edge transport barrier provide enough free energy, i.e. when the plasma state passes over a stability threshold [49]. The crash expels particles and heat from the plasma, flattening the gradients. After the collapse, when the steep gradients are no longer present, the ELM becomes stable again. As the pedestal recovers, the gradients grow again until the next ELM-crash occurs.

During such a crash, hot particles are expelled across the separatrix, leading to drops in the plasma's stored energy — both due to temperature and density loss — and high heat fluxes along the open field lines towards the divertor. Figure 2.14 shows the temporal evolution of various plasma parameters during an H-mode with ELMs.

Note that the stability of ELMs does not depend on the individual density or temperature gradient, but on the pressure gradient they form together  $p \propto nT$ . In order to study heat transport it is beneficial to use low densities since they permit higher edge temperatures before the critical pressure gradients are reached. This means that additional gas

puffing should be kept to a minimum in the experiment if high temperatures are to be achieved. It also constrains the gap between the plasma and the wall since it contributes gas through recycling. However, distance from the walls also means distance from the shaping and positioning coils, which negatively affects plasma stability.

Aside from the pedestal pressure gradient, other quantities affect ELM stability [51, 52]. The width of the pedestal has an influence on ELM stability since wider pedestals allow more MHD phenomena to occur in that region. Recent results from ASDEX Upgrade and JET also indicate a stabilisation of ELMs with increasing  $\beta$  [51, 52]. While the width of the pedestal is not trivial to manipulate,  $\beta$  could in principle be raised by simply increasing the heating power, but also by improving core confinement to allow higher pressure and thus higher  $\beta$  without additional external heating. For this approach the parameters on which the aforementioned critical gradients depend serve as a list of potential levers whose manipulation could improve core confinement.

To judge the global confinement of an H-mode, the energy confinement time  $\tau_E$  is defined as the total stored (thermal) energy divided by the input power [1]:

$$\tau_{E,\text{th}} = \frac{\frac{3}{2} \int (n_i T_i + n_e T_e) dV}{P_{\text{input}}} \quad (2.30)$$

This quantity reflects the plasma's ability to retain energy without requiring any deeper knowledge about the transport processes in the plasma. Strictly speaking, the definition should use the loss power rather than the input power. For experiments in equilibrium where there is negligible fusion power, however, the use of the much more easily obtainable input power is justified as it must match the loss power. This is the case in ASDEX Upgrade.

Due to a lack of first-principle-based understanding of a plasma's global confinement properties and thus its energy confinement time, empirical scalings were created on the basis of large databases of H-mode discharges [53]. One commonly used scaling is IPB98(y,2), which is given by:

$$\tau'_{E,\text{th}} = 0.0562 I^{0.98} B^{0.15} P^{-0.69} n^{0.41} M^{0.19} R_0^{1.97} \epsilon^{0.58} \kappa^{0.78} \quad (2.31)$$

Here,  $I$  is the total plasma current,  $B$  the toroidal magnetic field at major radius  $R_0$ ,  $P$  the loss power,  $n$  the line averaged plasma density,  $M$  the average ion mass,  $\epsilon$  the inverse aspect ratio and  $\kappa$  the plasma elongation.

Moreover, a normalised measure of the confinement quality is introduced, the so-called H-factor. It is obtained by comparing the actual energy confinement time to the confinement time predicted by the scaling, i.e.:

$$H_{98} = \frac{\tau_E}{\tau'_{E,\text{th}}} \quad (2.32)$$

Plasmas with H-factors above unity are exceeding the expectations while values below unity are falling short.

Finally, a normalised plasma  $\beta$  (cf. equation 2.3 on page 7) is introduced:

$$\beta_N = \beta \frac{aB}{I} \quad (2.33)$$

This quantity allows comparing the performance of plasmas with different minor radii, plasma currents and magnetic fields across different devices. The expression was, originally, numerically found to impose an MHD-limit on tokamak plasmas,  $\beta_N \leq 2.8$ . This value is known as the Troyon-limit [54] and gives a threshold for the onset of ideal MHD instabilities [6]. Experimental observations of strongly non-circular plasmas, however, have shown that the limit can be extended [55]. Contemporary results of conventional tokamaks suggest  $\beta_N \leq 3.5$ , while spherical tokamaks have reached values of up to 40 [1]. In any case, to maintain stability at increasing  $\beta$  (i.e. keep  $\beta_N$  fixed), a reduced magnetic field  $B$  and/or an increased plasma current  $I$  are necessary.

## 2.5 Internal Instabilities

ELMs principally affect the edge of the plasma. The loss of heat and particles propagates inwards and affects the core profiles, especially in the case of large ELMs. There are, however, also internal MHD instabilities.

### 2.5.1 Sawtooth Instability

The sawtooth instability is a periodically appearing central instability [56]. Its name stems from the characteristic sawtooth-like time traces of, for example, the central temperature (see figure 2.15 on the following page). The temperature builds up slowly and then drops suddenly, generally on timescales below  $1 \mu\text{s}$ . This drop weakens from the centre towards the edge and inverts at the so-called inversion radius. From there on out the temperature increases suddenly after a sawtooth crash and then slowly drops again afterwards as the heatwave travels outward. The immediate signature of the crash is only visible inside the so-called mixing radius that is further out than the inversion radius. If the expelled heat increases the temperature such that its gradient surpasses the critical gradient, the heat pulse continues to travel towards the plasma edge [57] until it reaches the edge or is dispersed sufficiently among the bulk plasma.

Sawteeth are only observed if the safety factor is below unity, i.e. if the current density is sufficiently peaked. The minor radius of the flux surface with  $q = 1$  then coincides with the inversion radius, which is why it is often used to determine the location of the  $q = 1$  flux surface. Field lines on that surface close on themselves after a single poloidal

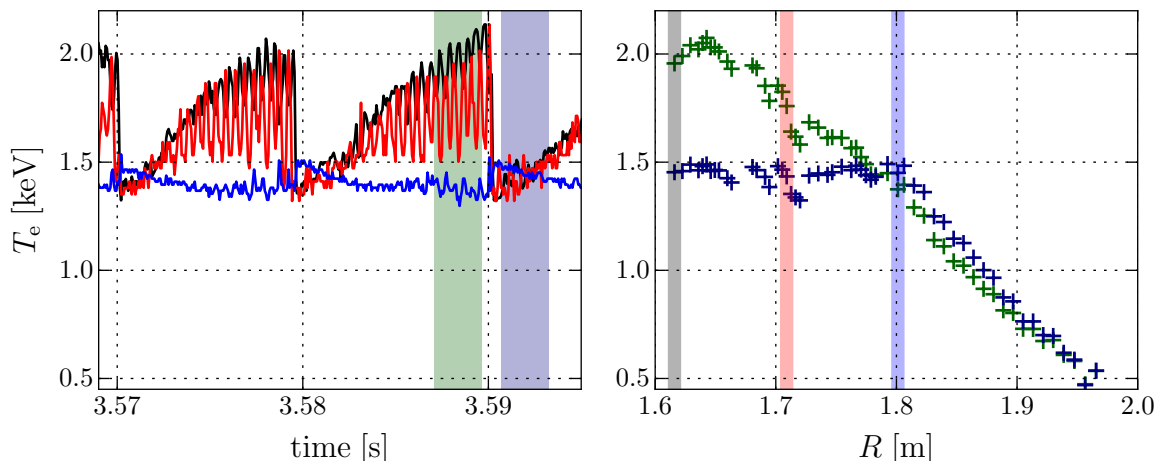


**Figure 2.15:** Select electron temperature time traces (left) and time-averaged profiles for two time intervals (right). The sawtooth-signature is clearly visible in the left plot, including the oscillations of the precursor and its spatial asymmetry. The inversion radius is located at about 1.78m in the right plot. Shaded areas in one plot correspond to data of the same colour in the other plot. (#30693)

and toroidal revolution (see section 2.1.2), which makes the plasma there particularly susceptible to perturbations with the same mode structure, i.e.  $m/n = 1/1$  with  $m$  and  $n$  as the poloidal and toroidal mode numbers, respectively.

In general the instability can be divided into three phases [58]:

**Precondition:** An ideal  $m, n = 1, 1$  kink or a resistive 1, 1 island is present. Ideal means that flux is conserved and the flux surfaces are merely deformed while resistive means that flux is not conserved and that flux surfaces can merge to form island structures [5]. Shortly before the next crash it can appear as steadily increasing oscillations that form a so-called precursor. Evidently, this condition can only be met if  $q \leq 1$  holds because such MHD modes cannot exist otherwise.

**Crash:** The crash is a sudden resistive reconnection event. The exact circumstances that trigger the onset of the resistive reconnection are unknown. What is known is that it suddenly expels heat, particles and possibly also current from inside the inversion radius. In the first widely accepted Kadomtsev<sup>1</sup> model, the helical flux<sup>1</sup> relative to the  $q = 1$  surface is completely redistributed to be monotonic, which sweeps along the particles [56]. That happens on a timescale  $\tau_{\text{crash}} = \sqrt{\tau_A \tau_R}$ . That is, between resistive and Alfvén timescale, fast enough to account for the speed of the crash.

<sup>1</sup>The helical flux is defined analogue to the toroidal or poloidal flux, but in a coordinate system based on a helical field line on the flux surface in question. Details can be found in [5].

**Relaxation:** As the axis region heats up again its conductivity is increasing  $\sigma \propto T^{3/2}$ . Current flows back into the centre until the safety factor drops below unity and the conditions for a crash are again met.

While the Kadomtsev model explains many aspects of sawteeth, it falls short in certain cases. Most notably, it is based on complete reconnection, while experimental evidence points towards only partial reconnection, i.e. the safety factor remaining below unity  $q_0 < 1$  [59, 60]. The equilibrium reconstruction software used for this work (IDE, see chapter 5 on page 83) made use of the Kadomtsev model where applicable, although most analysed phases had  $q > 1$  and thus no sawteeth in the first place.

In any case, the sawtooth instability is generally unwelcome. While it helps with the expelling of unwanted impurities from the plasma core, it also reduces the average core temperature and density, directly reducing the achievable fusion performance. On top of that it can trigger other deleterious phenomena like neoclassical tearing modes. In the worst case, a large sawtooth crash can impose such a big perturbation that a complete loss of plasma confinement is unavoidable. Therefore it is generally considered advantageous to avoid or at least control sawteeth.

## 2.5.2 Neoclassical Tearing Modes

Neoclassical Tearing Modes (NTMs) are another kind of resistive MHD instability. Like the sawtooth instability, they also only exist at flux surfaces that have helicities compatible with the respective mode's helicity. It is, however, not limited to  $q = 1$  but can, in principle, take any rational value where  $q = m/n$  with  $m, n \in \mathbb{N}$ .

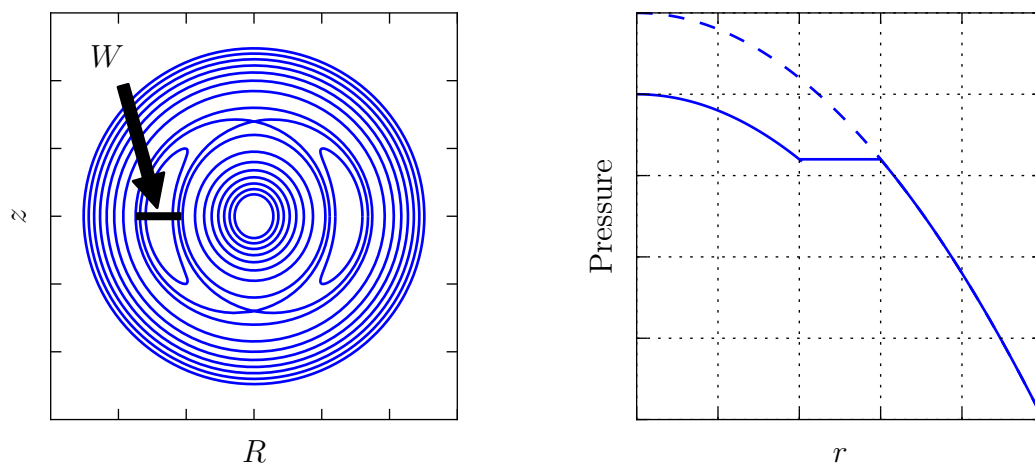


**Figure 2.16:** Sketch of an idealised 2/1-NTM in a cylindrical plasma with width  $W$ .



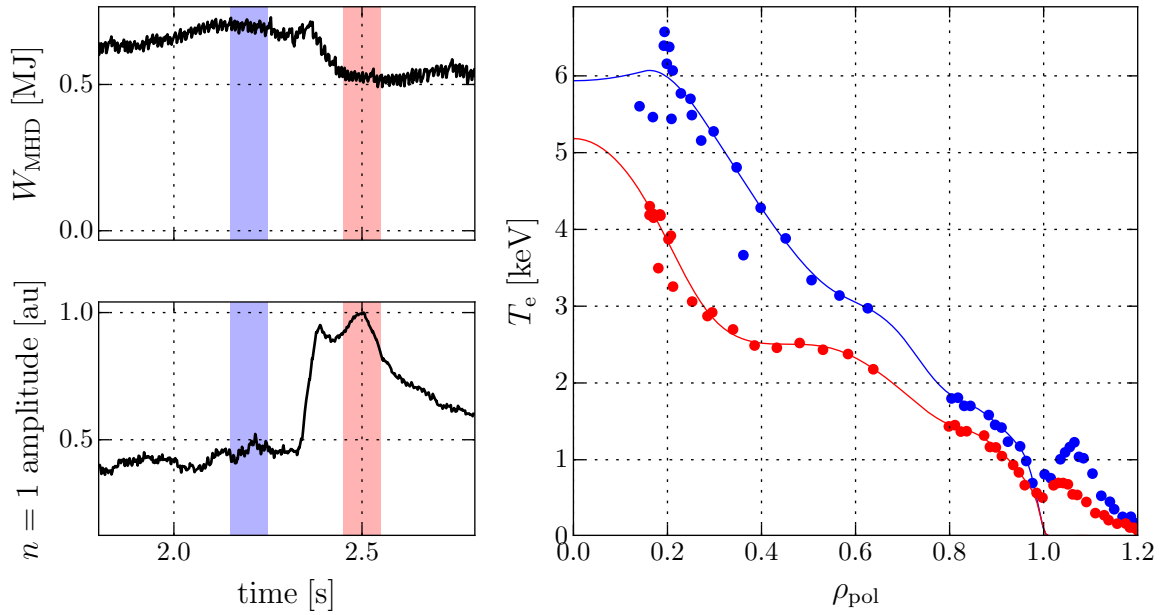


**Figure 2.17:** Stored plasma energy  $W_{\text{MHD}}$  (top left),  $n = 1$  mode amplitude from magnetics (bottom left), electron temperature  $T_e$  profiles before and after NTM emergence (right). Points indicate ECE data (cf. section 3.2.2 on page 47), lines represent IDA reconstruction (cf. section 3.2.4 on page 52). Profiles correspond to shaded time intervals of the same colour. (#32342)

In figure 2.16 an idealised 2,1-NTM is sketched. It shows how the reconnected flux surfaces result in a radial short-circuiting that flattens the pressure across the resulting island with width  $W$ . That is because in the presence of such an island, particles do not need perpendicular transport to cross radial distances. Flows parallel to the island flux surfaces are sufficient with parallel transport being orders of magnitude higher than its perpendicular counterpart, significantly reducing the radial gradients. As a consequence, the core pressure is reduced. An actual example of an NTM's effect is shown in figure 2.17. After its appearance at 2.35 s, the stored plasma energy is reduced significantly from around 0.7 MJ to 0.5 MJ. The flattening of the temperature profile can be seen just inside  $\rho_{\text{pol}} \approx 0.5$ . Moreover, the reduction in stored energy and hence  $\beta$  destabilises the pedestal, whose reduced height propagates inwards as well, causing a reduction in temperature in addition to the NTM's flattening effect.

NTMs are driven by the bootstrap current and therefore by the pressure gradient. An initial flattening of the pressure profile through a so-called seed island — that could be caused by a sawtooth crash, for instance — causes a helical defect in the bootstrap current. This (negative) defect current leads to growth of the island as its magnetic field alters the flux surfaces, further flattening the pressure profile and thus increasing the defect current. As such, it is possible to stabilise NTMs by supplying the defect current

by external means. This can either be accomplished pre-emptively by purposely adding current to a suspected rational flux surface, or by localising and mitigating a mode after its emergence [61, 62].

At best, an NTM reduces the overall performance of a fusion plasma as noted above. At worst, an NTM will grow until it is large enough that it destabilises the whole plasma to the point of disruption by locking with an external error field originating from the wall. Neither the reduced performance, nor the risk of damaging the device are welcome in a future power plant, which is why avoidance or at least control of NTMs is mandatory for large fusion devices.

## 2.6 Improving the H-Mode

The preceding sections have sketched the merits of H-mode operation as well as its principal limits: its performance is determined by the stiffness of the kinetic profiles, it suffers from various instabilities and, like all conventional tokamak operation regimes, it relies on induced current and hence cannot operate in steady state.

It is therefore interesting to study plasmas under conditions that improve on these limitations. This thesis explores one way to do that by manipulating the current profile using external means like ECCD (cf. section 3.3.1). Specifically, it will focus on elevating and flattening the central  $q$ -profile as sketched in figure 2.18 on the following page. This will affect plasma operation in different ways:

**Performance:** The critical temperature gradient is expected to increase as the magnetic shear is moved away from  $s \approx 0.5$ . This should result in steeper gradients at the same heating power, i.e. overall improved performance. The higher  $\beta$  could also help stabilise the pedestal and thus increase performance further by increasing the pedestal height. Ideally, the higher pedestal will raise the core profiles via stiffness, resulting in even higher  $\beta$  and thus even higher pedestals, i.e. a feedback loop whose saturated performance could be significantly higher than in ordinary H-mode.

**Stability:** By raising the  $q$ -profile, instabilities of lower helicity should no longer be able to exist. Due to their requirement of  $q = 1$ , sawteeth are the first to disappear, although with enough correctly applied current drive it should also be possible to eliminate 3,2 and possibly even 2,1 NTMs. In that case, however, NTMs with higher helicity, e.g. 3,1, could still occur and thus limit the achievable performance.

**Pulse length:** Finally, by elevating the  $q$ -profile over a larger extent, the bootstrap current density in that region increases (as an elevated  $q$  coincides with a reduced  $B_{\text{pol}}$  and  $j_{\text{bs}} \propto B_{\text{pol}}^{-1}$ ). Therefore, less ohmic induction or external current drive is necessary to operate the device, resulting in longer pulse duration.

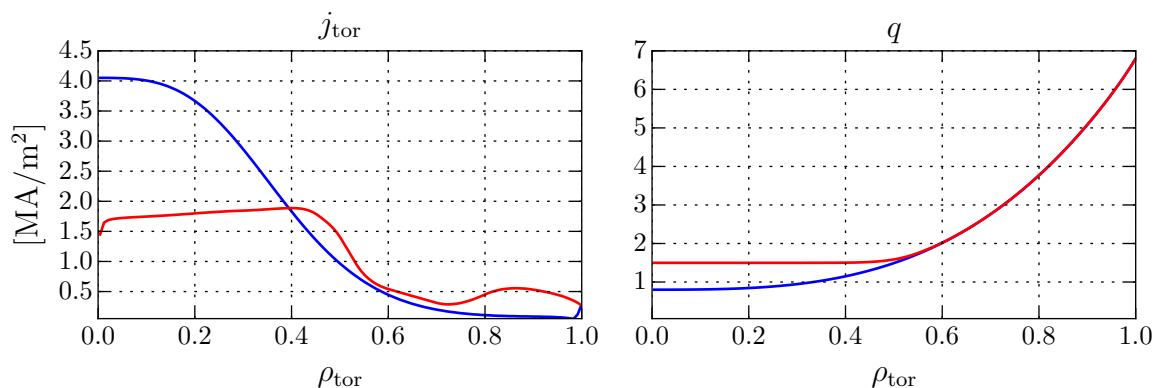


**Figure 2.18:** Toroidal current density profiles for an ordinary (blue) and an elevated (red)  $q$ -profile, generated with ASTRA. To elevate  $q$ , current must be redistributed from the core towards the edge.

Progress on the first two points could allow a better-performing plant to be more compact and/or require less auxiliary heating while a more stable plasma scenario allows more robust operation. Both could help reduce the costs of fusion power.

Increasing the pulse length is of particular interest as pulsed operation is considered unattractive for several reasons. For one thing, for fusion power plants to supply baseload power, they would require systems that bridge the downtime between pulses, making them more expensive. For another thing, pulsed operation induces cyclic stress on the reactor's structure, resulting in a reduced lifetime and increased need for maintenance. Both points would make fusion power more expensive.

By increasing the bootstrap current density, it might be possible to substitute a significant amount of inductive current and thus extend the length of a pulse or even reach a non-inductive regime where bootstrap current and non-inductive external current drive together maintain a steady state plasma.

It has to be noted that while an increase in bootstrap current might be attractive from a steady-state perspective, it could be detrimental to plasma stability as NTMs are driven by defects in the same bootstrap current. Should NTMs become a limiting factor under these circumstances, then an NTM stabilisation scheme might be necessary, which would require further ECCD capacities.

Previous investigations of these issues have been carried out on different tokamaks including AUG, DIII-D, JET and JT-60U. For instance, earlier studies at (then carbon-covered) AUG achieved almost fully non-inductive operation at a total plasma current of 400 kA [63] and  $q_{95} \approx 9$ . This was accomplished without ECCD and led to a slowly decaying plasma current when stopping the induction by the ohmic transformer. Later studies in AUG focused on prolonging the initial relaxation of the  $q$ -profile [64] by early heating, thereby delaying the current diffusion which happens on the resistive timescale

$\tau_R$ . This was done for 1 MA discharges with  $q_{95} \geq 4$ . Here it was found that variations of the start-up have noticeable influence on the resulting relaxed  $q$ -profile, which affects the heat confinement in particular. Like the earlier study, this one was also performed before AUG was converted to a full tungsten machine (cf. chapter 3 on page 45).

Studies performed at JET also point to improved confinement due to  $q$ -profile manipulation [65]. The employed current shaping method is to initially overshoot the ultimately desired plasma current, thereby inducing excess current at the edge, which results in an elevated core  $q$ -profile. Immediately afterwards, heating is applied which again increases  $\tau_R$ . In the reported experiments, MHD activity was still present, but did not result in confinement degradation. In fact, noticeable increases in the ion temperature were observed in the discharges with current profile shaping. Still, the modified current profiles were not stationary and continued to decay; high amounts of bootstrap current were not observed. Furthermore, JET is also not a full tungsten machine.

Experimental investigations at JT-60U focused on creating strongly reversed  $q$ -profiles which resulted in a strong internal transport barrier [66]. This was also accomplished using early heating to exploit the initially elevated  $q$ -profile. The ITB's steep gradients led to high confinement  $H_{98} \approx 1.7$  and substantial amounts of bootstrap current, resulting in almost fully non-inductive operation ( $f_{bs} \approx 0.92$  at  $q_{95} \approx 4.5-6$ ). A big challenge here is to align the ITB's bootstrap current contribution such that is self-consistent with the current profile necessary to maintain the ITB, which would require longer operation. In fact, the upgrade towards a superconducting JT-60SA was strongly motivated by the desire to extend these studies to fully non-inductive operation in steady state.

Finally, recent results from DIII-D indicate fully non-inductive operation at  $q_{95} \approx 5$  with high confinement  $H_{98} \approx 1.4$  [46]. Here again early heating was applied to make use of the initially elevated  $q$ -profile. Co-ECCD was applied on-axis, but due to anomalous current diffusion that was attributed to a 3,2-NTM, the central  $q$  remained above unity.

With this in mind, the purpose of this work is to extend the aforementioned studies in multiple ways:

- Explore early heating schemes that exploit the initially elevated/reversed  $q$ -profile, but also late heating where an equilibrated current profile is manipulated towards the desired shape. If successful, this would make the approach independent of the initial discharge conditions, which are notoriously hard to diagnose.
- Explore central counter-ECCD deposition to raise the central  $q$ -profile. Due to the high core electron temperature, this approach will maximise current drive efficiency. For this approach to be viable in a power plant, the resulting bootstrap current increase must more than compensate the counter-driven current.
- Explore the behaviour of improved H-mode discharges in a full tungsten machine, whose merits are briefly sketched in section 3.1 on page 45.

## Bootstrap Current Estimation

It is possible to use a simple model to estimate what increases to the bootstrap fraction one might expect during such experiments. This model assumes a circular plasma with AUG machine parameters, i.e. minor and major radius  $a/R = 0.5 \text{ m}/1.65 \text{ m}$ , a toroidal magnetic field of 2.5 T and typical AUG kinetic profiles. Since it is circular, it does not capture any effect caused by AUG's elongation  $\kappa = 1.7$ , e.g. the higher  $q \approx \kappa q_{\text{circ}}$ . In equilibrium, the current density profile is given by the sum of ohmic  $j_{\text{oh}}$ , auxiliary external  $j_{\text{aux}}$  and (self-consistently) calculated bootstrap contributions  $j_{\text{bs}}$ .

$$j_{\text{oh}} \propto T_e^{3/2}$$

$$j_{\text{bs}} = \frac{\sqrt{\epsilon} k_B}{B_{\text{pol}}} \left[ A(T_e + T_i) \frac{\partial n}{\partial r} + Bn \frac{\partial T_e}{\partial r} + Cn \frac{\partial T_i}{\partial r} \right]$$

The ohmic current follows Spitzer conductivity, with its proportionality constant (“loop voltage”) chosen to yield a desired total current, e.g. 800 kA. The bootstrap current is given in the form of [11], but does not use the factors  $A$ ,  $B$ ,  $C$  given there. That is because more accurate analysis of the experiments performed for this work using the expressions given in [12] yields significantly different values that attribute more bootstrap current to the temperature gradients such that density and temperature are about equal in their contribution. In any case, the exact numbers are not important since a) such a simple model cannot hope to quantitatively describe a plasma and is therefore only used to explore qualitative rather than quantitative trends — a tool like ASTRA is more suitable for such analyses — and b) changing the three factors only repartitions the bootstrap current contributions among density and temperature, but won't change the overall trends. Therefore, and since it is assumed that  $T_e = T_i$ , the parameters have been set to  $A = B = 1$ ,  $C = 0$ .

The kinetic profiles are assumed to be at fixed critical gradients across the minor radius (see equation 2.26) and end in a parabola that ensures flat profiles at the axis. At the edge, the pedestal is approximated with a boundary value. The pedestal itself is not part of the model. That is because turbulence in that region is suppressed and the kinetic gradient lengths become of the order of the ion gyro-radius, which makes its physics too complex to be captured by the simplified assumptions made above. Since the trends of the bootstrap current in the core plasma are of interest, the omissions of the edge transport barrier is not an issue.

An example of such a modelled plasma is shown in figure 2.19. Its density profile is slightly peaked, its temperature profile is more strongly peaked with a critical gradient of  $R/L_{T_e} = 5$ . At  $\beta_N = 2.6$  it has a bootstrap fraction of  $f_{\text{bs}} = 11.3\%$ . Since the bootstrap current depends not just on the  $B_{\text{pol}}/q$ -profile but also on the kinetic gradients, it is worthwhile to vary the density and temperature profiles at fixed  $\beta_N$  and consider the variation's impact on the bootstrap fraction. The fixed  $\beta_N$  is necessary due to the Troyon limit: plasmas must not exceeded a maximum value of  $\beta_N \leq 3.5$  to remain stable,

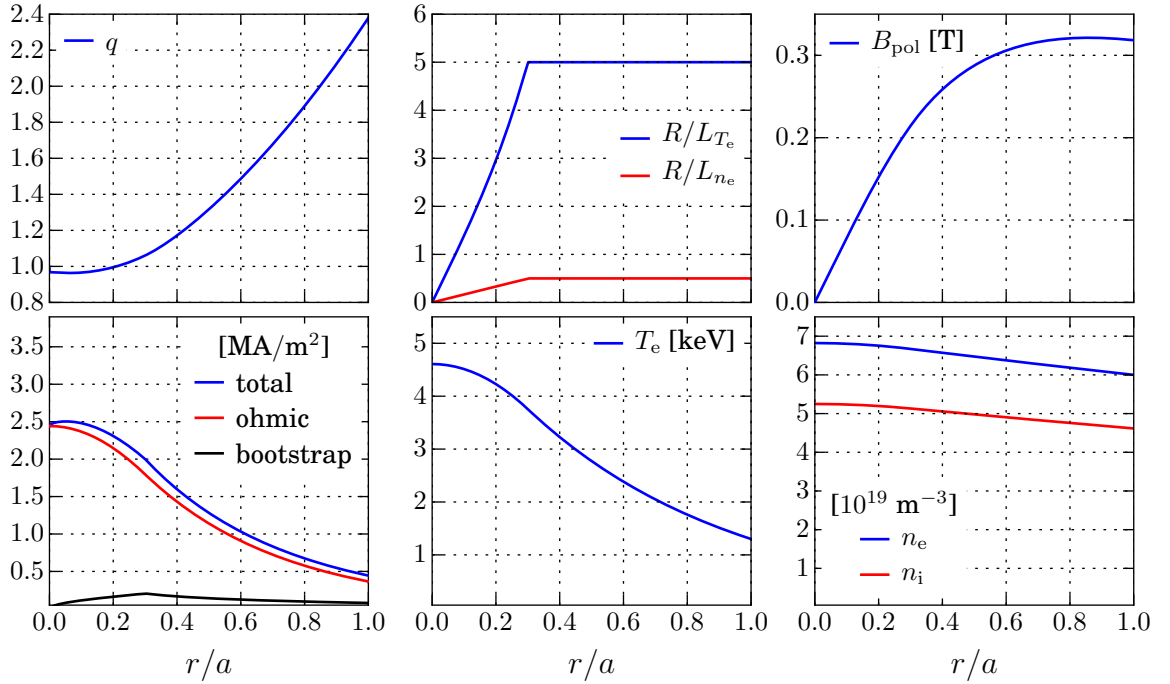


**Figure 2.19:** Example of a circular plasma with typical ASDEX Upgrade parameters ( $B_{\text{tor}} = 2.5$  T,  $I_p = 800$  kA,  $\beta_N = 2.6$ ,  $f_{\text{bs}} = 0.11$ ).

so when steepening kinetic profiles, i.e. increasing  $\beta$ ,  $I_p$  must also increase to keep  $\beta_N$  constant. The chosen  $\beta_N = 2.6$  is routinely achieved in ASDEX Upgrade plasmas and has thus been selected to produce comparable results. The requirement of  $q_{95} > 2$  has been neglected in this variation; it ultimately imposes an upper limit on  $I_p$  and must be taken into account for a comprehensive study.

In figure 2.20 the result of such a variation is shown. The bootstrap fraction varies between 0% with completely flat kinetic profiles to almost 23% in the case of flat temperature and peaked density profiles. Note that the density peaking is significantly weaker than the temperature peaking, as observed in the experiment.

In the case of flat density profiles it can be seen that there exists an optimal temperature profile, in this example at around  $R/L_{T_e} \approx 5$ . At higher or lower gradients, the bootstrap fraction drops. This is due to the competing effects of peaked temperature profiles: on the one hand a temperature gradient contributes to the bootstrap current, on the other hand a peaked temperature profile compels inductive current to diffuse towards the centre, where it increases the overall poloidal field  $B_{\text{pol}}$ , which in turn lowers  $j_{\text{bs}}$ .

If the density now also peaks, the optimal value of  $R/L_{T_e}$  slowly reduces until the optimal temperature profile would be entirely flat. That is also easy to understand: since density gradients only contribute to the bootstrap current but do not drive current towards

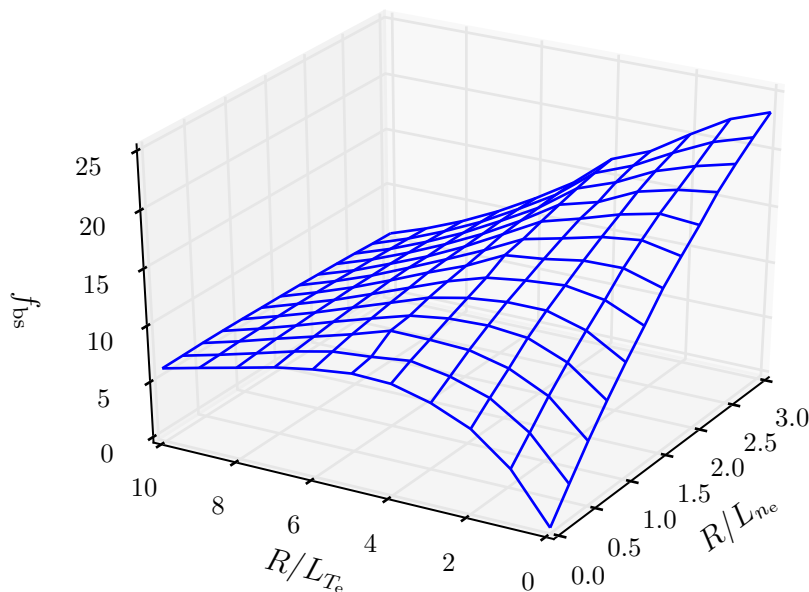


**Figure 2.20:** Bootstrap fraction for different critical temperature/density gradients at fixed  $\beta_N = 2.6$ .

the axis, density peaking can substitute the positive side of temperature peaking until temperature peaking only retains its deleterious effect. At this point, the density gradient maintains the bootstrap current on its own while the temperature gradient only allows current to diffuse towards the axis. Thus, in the case of (unrealistically) high density peaking, it would be optimal to have no temperature gradients at all. Of course, that is not desirable in a fusion reactor as the necessary temperatures would have to be maintained entirely by the pedestal, which is not feasible. Still, a rule of thumb remains: if density is peaking, then temperature profiles should be kept as flat as possible to prevent ohmic current from diffusing towards the axis.

Alternatively one might, as performed in the experiments of this thesis, accept the temperature peaking and simply use external counter-current drive to neutralise the central co-current density, thus retaining only the bootstrap contribution of the peaked temperature. Here the stiffness of the profiles plays into the physicists' hands: electron current drive always comes with electron heating, but since the profiles are stiff, the extra heat would largely be expelled without exacerbating the unwanted diffusion of current towards the axis too much.

One must, however, keep in mind that usefulness of counter-current drive approach is fundamentally dependent on the achievable bootstrap current. The gained bootstrap

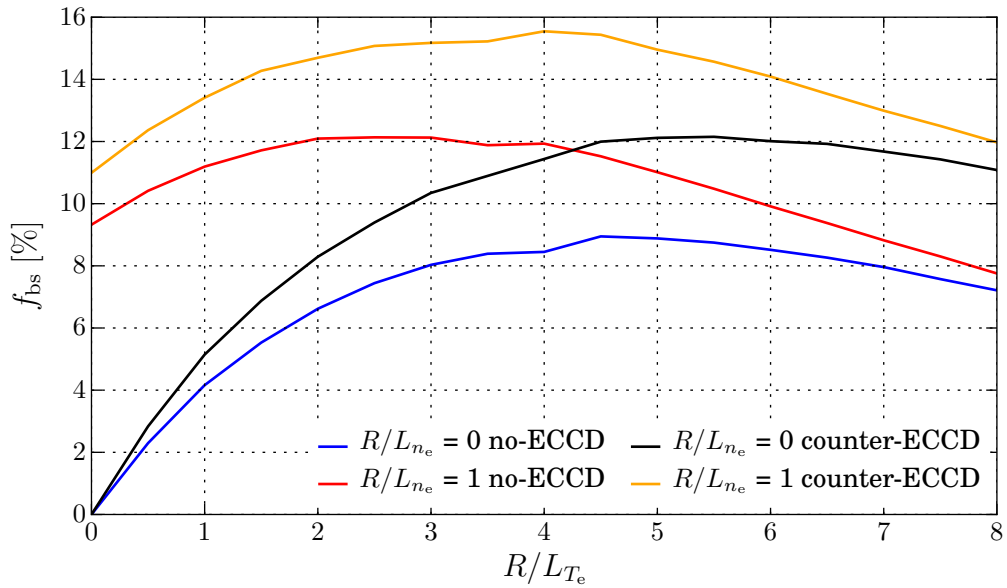


**Figure 2.21:** Bootstrap fraction variation with  $R/L_{T_e}$  for two density profiles with and without central counter-ECCD.

current must over-compensate the loss caused by the counter-current drive to be a viable scenario for a power plant. But even in the worst case, a steady-state manipulation of the  $q$ -profile to study confinement, stability and bootstrap properties is still of interest.

Figure 2.21 shows a variation of the temperature profile for two density profiles with and without central counter-current drive. The modelled ECCD was tuned such that it reduces the current density on axis by 60% and linearly decreases to zero at  $r/a = 0.4$ , leaving the outer current profile unchanged. The total driven current for all points in the figure does not exceed 180 kA, which is close to the upper limit of what ASDEX Upgrade’s ECCD system can achieve for the given plasma conditions, but doesn’t exceed it.

With and without density peaking a similar image is presented: the bootstrap fraction rises and the optimal  $T_e$  gradient is shifted to higher values, i.e. the OH peaking is — as expected — compensated by the current drive to some extent. The achievable bootstrap fraction increases by up to 50% for steeper temperature gradients. Bumps in the curves can be seen near the optimal temperature gradient  $R/L_{T_e} \approx 4$ . In fact, the algorithm calculating the curves is struggling with higher bootstrap fractions as the model’s behaviour becomes strongly non-linear. In extreme cases, the additional off-axis bootstrap current density requires the “loop voltage” to be reduced very strongly to maintain the target plasma current  $I_p$ , which causes a drop in  $B_{\text{pol}}$ , which in turn leads to even more bootstrap current. In the worst case this poses a significant challenge for the convergence of the model’s state.



While such behaviour is unwelcome in numerical simulations, the non-linearity could be beneficial in a real plasma. In this model, a drop of  $B_{\text{pol}}$  has no consequences on density or temperature because transport calculations are too complex to be included. In a real plasma, however, a lack of  $B_{\text{pol}}$  causes a collapse of confinement and therefore a collapse of the kinetic gradients that are needed for the bootstrap current to exist. Hence, there could be a saturated configuration where bootstrap current, poloidal field and kinetic gradients form a delicate (meta-)stable balance that maintains a high bootstrap fraction.

# 3 Experimental Setup

## 3.1 ASDEX Upgrade

All experiments for this work were performed at the tokamak ASDEX Upgrade (AxiSymmetric Divertor Experiment, AUG), located at the Max-Planck-Institute for Plasma Physics in Garching bei München in Germany.

Since 2007, AUG is a full tungsten machine, i.e. its plasma facing components (PFCs) are — where possible — either made of solid tungsten or are graphite coated with tungsten. Tungsten is a very high-Z element and is therefore never fully ionised by the plasma. Consequently, tungsten in the plasma radiates at any location, including the core, which can reduce plasma performance through radiative cooling when the tungsten concentration is too high. In the worst case, accumulating tungsten will radiate so much power that the plasma is lost. One way to mitigate this is central electron heating that can excite ITG turbulence and expel unwanted impurities.

The reason why tungsten is used in AUG is to investigate its suitability for a future fusion power plant. It offers not only superior thermo-mechanical properties but also low erosion under steady state operation conditions [67], which makes it an attractive candidate for the PFCs in a future fusion reactor. On top of that, it has a low fuel retention compared to, for example, carbon, which can chemically react with both deuterium and tritium.

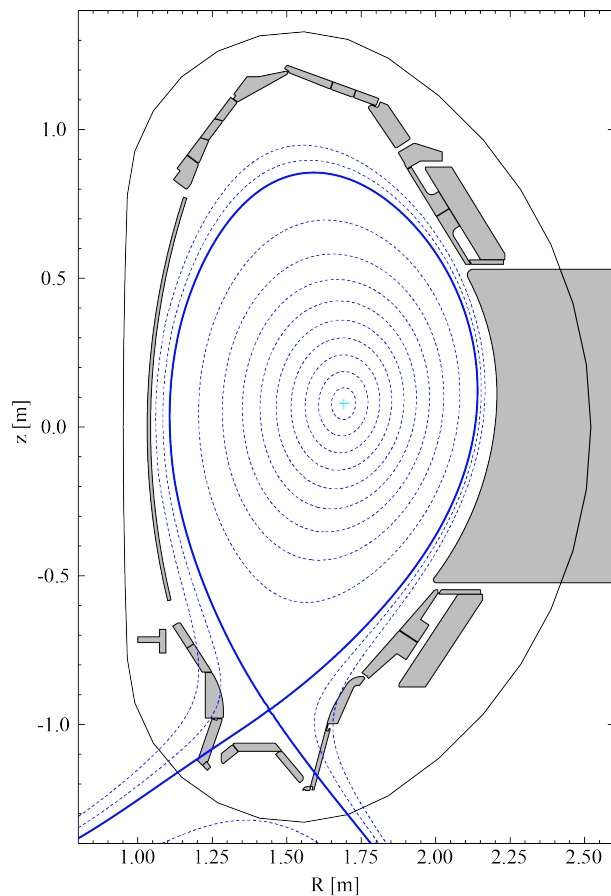


**Figure 3.1:** Example equilibrium in divertor/X-point configuration.

Another significant aspect of ASDEX Upgrade is its divertor (shown in the bottom of figure 3.1, cf. section 2.1 on page 5). Originally proposed for impurity control in stellarators [68], its concept was applied to tokamaks in the form of a bundle divertor [69]. An axisymmetric divertor that spans the entire tokamak toroidally allowed the discovery of the H-mode on AUG's predecessor ASDEX [47]. It has become the default configuration of toroidal fusion devices. By topologically separating the closed magnetic field lines that confine the main plasma from the open field lines that end in the divertor and on other PFCs, the plasma is kept purer than in the limiter configurations where the last closed flux surface (LCFS or separatrix) was given by the intersection of the field lines with the PFCs. Instead, the separatrix is generated through additional coils above and below the plasma whose magnetic field together with the plasma's field form a characteristic X-point. The H-mode edge transport barrier forms close to the separatrix.

## 3.2 Plasma Diagnostics and Heating Systems

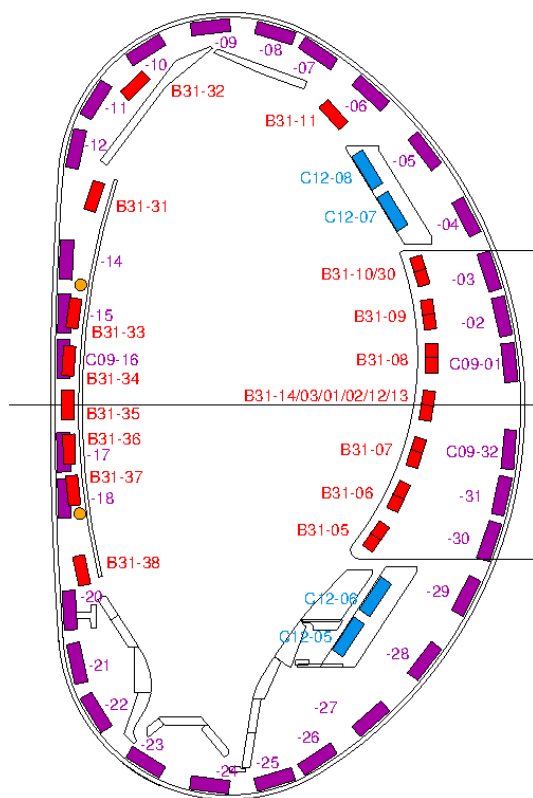


**Figure 3.2:** Coils measuring the poloidal (red), radial magnetic field (purple) and the magnetic field at the passive support loop (blue).

measurements), which allows the detection of fast oscillations that are caused by, for instance,

ASDEX Upgrade is equipped with many measurement systems to accurately diagnose and study the confined plasma. The most important ones for this thesis will be briefly introduced in the following subsection, followed by the heating systems in subsection 3.3 on page 55).

### 3.2.1 External Magnetic Measurements

To determine the state of the magnetic field, ASDEX Upgrade is equipped with a multitude of magnetic probes, mostly coils. A coil with enclosed area  $A$  measures the changes in the magnetic flux as given by:

$$U(t) = -\frac{d\Phi}{dt} = -\frac{d}{dt} \left[ \int \vec{B} \cdot d\vec{A} \right]$$

Time-integrating the voltage  $U$  yields the magnetic flux  $\Phi$ , which is used to reconstruct the magnetic equilibrium (see chapter 5 on page 83). The coils are sampled at a rate of up to 2 MHz (10 kHz for the integrated measurements), which allows the detection of fast oscillations that are caused by, for instance,

rotating neoclassical tearing modes in the range of tens of kHz. The helicity/mode numbers of the observed oscillation can be determined by manually analysing the phases of coils at different poloidal and toroidal positions. Also, a numerical analysis tool has been developed recently. It determines the likelihood of a magnetic signal originating from a phenomenon with a given helicity using a technique based on singular value decomposition [70].

### 3.2.2 Temperature Measurements (ECE, TS)

#### Electron Temperature

The two main techniques to determine the electron temperature  $T_e$  on ASDEX Upgrade are measurements of electron-cyclotron emissions (ECE) and Thomson-scattered (TS) laser light. The location of the respective measurements is shown in figure 3.3.

ECE measurements [71, 72] are enabled by the fact that electrons in a magnetised plasma gyrate and — because of the permanent acceleration — emit radiation with the cyclotron frequency  $\omega_c = eB/m_e$ . Furthermore, the total magnetic field in a tokamak is dominated by the toroidal component, i.e.  $B \approx B_{\text{tor}} \propto 1/R$ . Hence, spectrally resolving ECE measurements amounts to spatially resolving the origin of the radiation.

In general, a fusion plasma is optically thick for all resonant frequencies  $\omega_c$ . That means that virtually all emitted radiation is again absorbed inside the plasma, and in turn, following Kirchoff's law, emitted as black-body radiation. For electrons with a Maxwellian velocity distribution and using the Rayleigh-Jeans approximation, since the photon energy is orders of magnitude small than the electron thermal energy

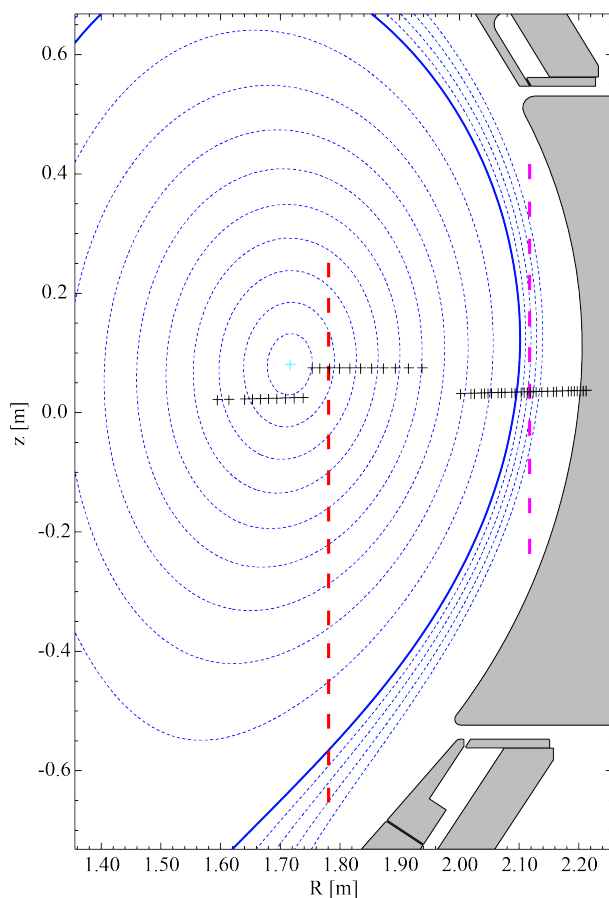


**Figure 3.3:** ECE and TS measurements at AUG. Black: Typical ECE measurement positions. Red/pink: core and edge TS measurement volumes.

( $1 \text{ meV} \approx h\nu \ll kT_e \lesssim 1 \text{ keV}$ ), the measured intensities  $I_{\text{BB}}$  are directly related to the electron temperature:

$$I_{\text{BB}} = \frac{\omega_c^2(R)}{4\pi^2 c^3} k_B T_e \quad (3.1)$$

ECE measurements at ASDEX Upgrade have an accuracy of 7% and are sampled at up to 1 MHz. Up to 60 frequencies can be recorded simultaneously, allowing — in principle — complete coverage of AUG’s 60 cm minor radius with a spatial resolution of 1 cm. The ECE configuration used for the experiments in this thesis is indicated in figure 3.3 on the preceding page by the black crosses: one of the three mixers is dedicated to the edge to accurately resolve the pedestal while the other two mixers are configured to pick up radiation from the core plasma. This leaves a gap of  $\Delta\rho_{\text{pol}} \approx 0.15$  just inside the outer mixer’s location. The gap does not pose a significant problem for acquiring the overall temperature profile, but it does create a dead spot in which NTM localisation is not possible [61, 62].

In cases where the requirement of optical thickness is not met, ECE measurements can be contaminated with so-called shine-through, that is radiation erroneously attributed to the wrong radial position. This is corrected using integrated data analysis (IDA), which is discussed in subsection 3.2.4 on page 52.

In contrast to ECE, TS is an active measurement [73]. High-intensity Nd-YAG laser light passes vertically through the plasma at two locations, one near the centre and one near the edge of the plasma. Part of the light is scattered by the plasma electrons and observed through several lines of sight perpendicular to the laser beam. Using optical fibres, the light is relayed to a polychromator that measures both the spectral broadening of the scattered laser light due to averaged Doppler shifts from many electrons with different velocity vectors as well as its overall intensity. For electrons with a Maxwellian velocity distribution the broadening results in a Gaussian whose width yields the temperature  $T_e \propto \text{FWHM}^2$ . The total intensity, i.e. integral over the Gaussian, is proportional to the electron density  $I \propto n_e$ , so TS provides both temperature and density information.

The polychromator is a set of detectors behind interference filters. They are aligned such that every filter transmits only one portion of the spectrum to be measured by the detector and reflects the rest, allowing subsequent probing of the remaining light spectrum at different wavelengths further down the line.

Other than the ECE measurements, which are effectively sampled as fast as the data acquisition system permits, TS sampling is limited by the repetition rate of the lasers. During standard operation,  $2 \times 16$  local measurements are taken at a rate of 80 Hz (core) and 120 Hz (edge). A burst mode with several measurements each 10 ns apart is possible, requiring larger intervals in-between. These data can also be taken into account by IDA.

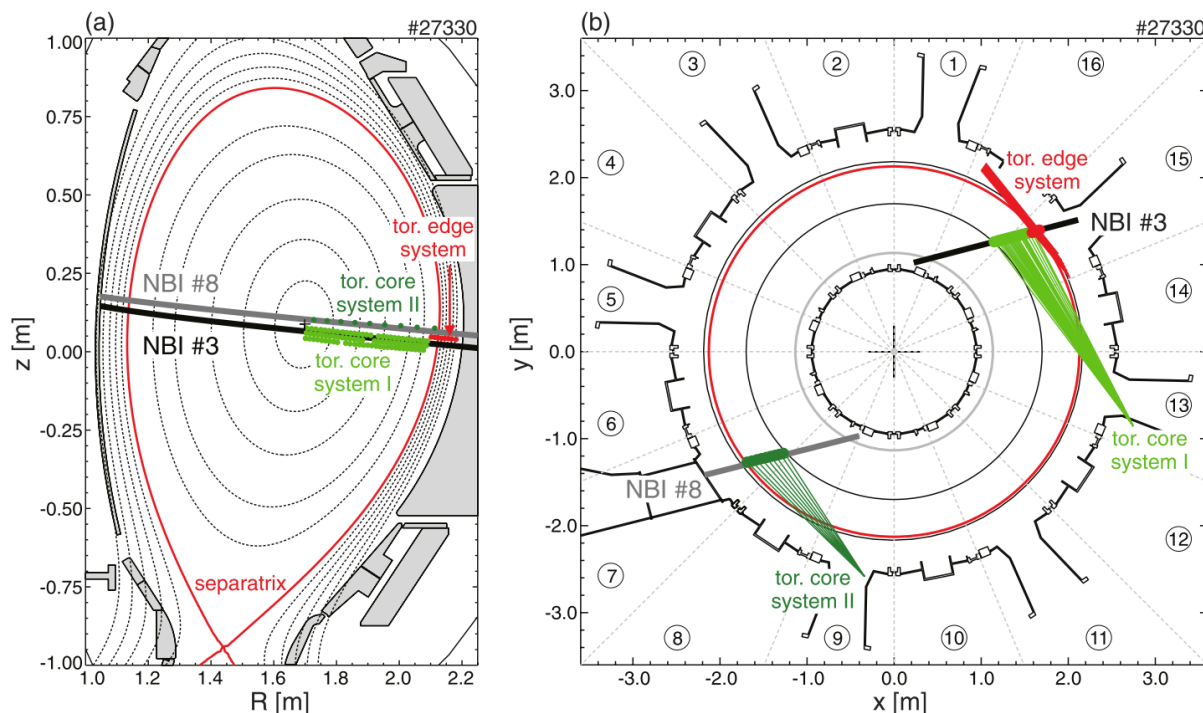


**Figure 3.4:** Geometry of AUG's CXRS diagnostic for ion temperature/velocity measurements. Image reproduced from [74].

### Ion Temperature

ASDEX Upgrade is equipped with several charge exchange recombination spectroscopy (CXRS) systems to measure impurity ion temperatures, velocities and densities [74]. This is accomplished by recording the spectra of emissions generated by charge exchange reactions with neutral atoms using several lines of sight directed at the neutral beam heating systems (see section 3.3.2 on page 60). The collected light is relayed to spectrometers located outside the torus hall using fibre optics.

The recorded spectra are analysed by fitting Gaussians to the known spectral lines. Doppler shifts of the spectral lines are used to determine the rotation velocity, while the broadening of the Gaussian is used to reconstruct the respective impurity ions' temperature. The density of a given impurity can also be determined by modelling the absolute intensity of its line radiation.

Multiple species of impurities can be observed simultaneously. The most common ones are boron, nitrogen and helium, although others like oxygen or neon can be utilised on request, which was not required for this work. The core CXRS systems used for this thesis are shown in figure 3.4. They offer a spatial resolution of about 2.5 cm across the plasma minor radius for  $R \approx 1.65\text{--}2.15$  m. Their typical time resolution for the data used in this thesis is approximately 20 ms, while their accuracy is of the order of 10%.

Even though the measurements typically only characterise impurities, it is generally assumed that all ions are in equilibrium and thus share the same temperature. Equally, they also are assumed to rotate together, and since ions are massive in comparison to electrons, the ion rotation is taken as the overall plasma rotation. The impurity density, however, can obviously not be equated with the overall ion density  $n_i$ . However, the individual impurity measurements can be combined and used to calculate the effective charge of the ion ensemble at various radial locations  $Z_{\text{eff}}$  and thus derive the ion density by exploiting quasi-neutrality. The relationship between all ion species and the electrons is given by:

$$Z_{\text{eff}} = \frac{\sum_j n_j Z_j^2}{n_e} \quad (3.2)$$

In the experiments of this work,  $Z_{\text{eff}}$  is usually slightly above 1 and does not rise above 2 in the plasma centre.

### 3.2.3 Density Measurements (DCN)

Aside from the electron and ion density measurement techniques already introduced in the preceding section on temperature measurements, there also exists a system primarily dedicated to electron density measurements. It is based on interferometry and offers line integrated density measurements along up to five horizontal and three vertical lines of sight [75].

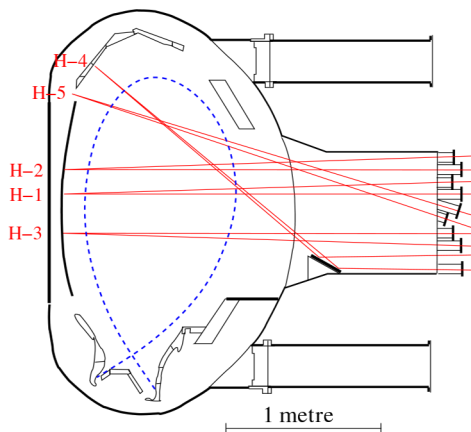


**Figure 3.5:** Geometry of the horizontal DCN interferometry lines of sight. Adapted from [75].

The measurements are taken by passing a laser beam through the lines of sight and then evaluating its phase difference with respect to a reference beam that has not passed through the plasma. In an unmagnetised plasma, the refractive index is given by

$$n = \sqrt{1 - \frac{e^2 n_e}{\epsilon_0 m_e \omega^2}} = \sqrt{1 - \frac{\omega_p^2}{\omega^2}} \leq 1 \quad (3.3)$$

with  $\omega$  being the laser frequency and  $\omega_p$  as the plasma frequency. Note that the refractive index  $n$  is below unity, other than in, for example, glass, leading to an inverted refractive behaviour. This refractive index is the so-called ordinary refractive index  $n_o$  in a magnetised and thus birefringent plasma, i.e. the refractive index for electromagnetic waves that are polarised parallel to the magnetic field lines, along which electrons can travel freely. For

the extraordinary direction (abbreviated by eo or x) perpendicular to  $\vec{B}$ , where electrons are limited to a gyro-motion, the refractive index becomes

$$n_{\text{eo}} = \sqrt{1 - \frac{\omega_{\text{p}}^2 \omega^2 - \omega_{\text{p}}^2}{\omega^2 \omega^2 - \omega_{\text{h}}^2}} \quad (3.4)$$

with  $\omega_{\text{h}}^2 = \omega_{\text{p}}^2 + \omega_{\text{c}}^2$  as the upper hybrid frequency. In the limit of  $\omega_{\text{c}} \rightarrow 0$ , i.e. in an unmagnetised plasma without gyration of the electrons, the extraordinary and ordinary refractive index are the same.

The injected laser light is polarised in the horizontal plane, i.e. almost parallel to the magnetic field, and its reaction to the plasma is thus described using the ordinary refractive index. A simple expression for the phase difference  $\Delta\Phi$  emerges through Taylor expansion and integration of equation 3.3 along the beam path  $s$ :

$$\Delta\Phi = \lambda \frac{e^2}{4\pi\epsilon_0 m_e c^2} \int n_e(s) ds \quad (3.5)$$

Here,  $\lambda$  denotes the laser's wavelength. Since  $\Delta\Phi$  is directly proportional to the laser wavelength and should be maximised to facilitate the measurement, the horizontal system uses a Deuterium-Cyanide (DCN) laser at  $\lambda_{\text{DCN}} = 195 \mu\text{m}$ . Still, at these wavelengths the laser's frequency is still in the THz range and thus outside of any conventional detector's time resolving abilities. By exploiting the heterodyne principle, the signal is downshifted into a beat signal in the 10 kHz range, which allows the interference signature to be sampled by a detector and the phase to be determined. Of course, since sine waves are periodic, only the fractional phase difference is directly measurable while the absolute number of periods in the phase shift must be counted from the beginning of the discharge.

If, for any reason, the detector misses a period, the measurement becomes corrupted. This is often the case during fast changes of the density, for example due to fuel injection via pellets or rotating NTMs that introduce a strong density anisotropy in the plasma. The main reason for the detector missing periods is that the laser beam is momentarily refracted away during these events. Due to the original approach of doing interferometric density measurements by superimposing the probing beam with the reference beam on a screen and literally counting the recorded fringes in the interference pattern, the concept of missing such a fringe has become colloquially known as a "fringe-jump," which has to be corrected during post-processing.

There also exists a vertical system that uses a CO<sub>2</sub> laser at  $\lambda_{\text{CO}_2} = 10.6 \mu\text{m}$ , which offers more robust measurements. Its advantage is that the refraction increases with wavelength squared [76], which makes it less likely to be refracted away from the detector. Unfortunately, as the incurred phase difference depends on the wavelength linearly, its noise level is significantly higher compared to the DCN laser's measurement. In practice, both measurements complement each other.



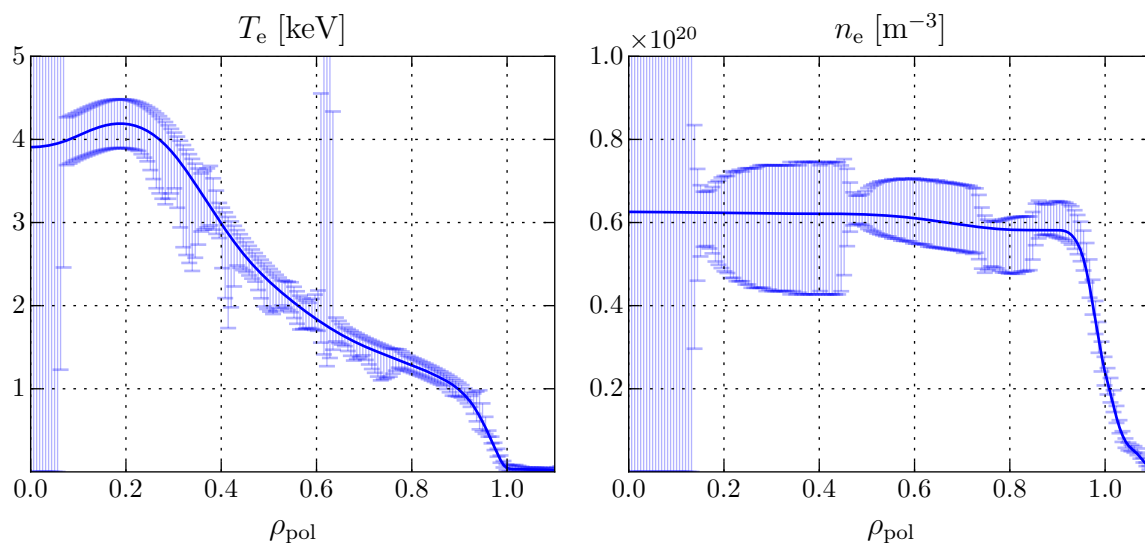


**Figure 3.6:** Electron temperature and density profiles and respective uncertainties, generated with IDA for #32184 at 2.9 s.

The line integrated density by itself is only of limited use. The information of each line of sight is therefore combined in IDA to generate actual density profiles.

### 3.2.4 Integrated Data Analysis (IDA)

IDA coherently combines the data from various diagnostics using Bayesian analysis to yield integrated electron temperature and density profiles [77]. Since the diagnostics do not necessarily all measure at the same location, they are mapped onto a common coordinate system using a magnetic equilibrium (cf. chapter 5).

An example of an IDA result is shown in figure 3.6. The profile depicted as a solid line indicates the result of the forward-model-based Bayesian analysis. The comprehensive forward model includes things like ECE shine-through, which distorts the  $T_e$  measurements when it is not accounted for. The confidence bands surrounding the profile are obtained with a  $\chi^2$  binning method [78]. There the profile in given radial intervals is varied up to the point where  $\chi^2$  increases by 1. As such, these confidence bands are a good indication of the availability of experimental information. For instance, from the density profile of figure 3.6 it is clear that various diagnostics that measure the edge density were taken into account whereas no information was available near the magnetic axis.

Another potential source of errors is the magnetic equilibrium used for the mapping. If it is wrong, then diagnostics may be mapped incorrectly, resulting in artefacts in the

result. For example, the relative drop in  $T_e$  in figure 3.6 near the axis may not actually be real, but merely a consequence of a slightly wrong equilibrium reconstruction.

To tackle this issue, the integrated data equilibrium (IDE, cf. chapter 5) code was developed, which is envisaged to run in conjunction with IDA to ensure consistency and avoid artefacts of that kind.

### 3.2.5 Internal Magnetic Measurements

#### DCN Polarimetry

As mentioned above, the behaviour of waves in a magnetised plasma can be quite complex and depends strongly on the magnetic field applied to the plasma. While the toroidal magnetic field  $\vec{B}_{\text{tor}}$  is well known due to it being dominated by the field of the toroidal field coils, the poloidal field  $\vec{B}_{\text{pol}}$  is, especially deep inside the plasma, largely unknown. Laser light penetrating the plasma is not only affected by the magnetic field perpendicular to its direction  $\vec{k}$ , but also by the parallel magnetic field — which, in the case of the horizontal viewing geometry of the DCN laser, is mostly the poloidal magnetic field  $\vec{k} \parallel \vec{B}_{\text{pol}}$  as  $\vec{k}$  lies in the poloidal plane.

Light travelling through the plasma along a magnetic field incurs so-called Faraday rotation of its direction of polarisation [79]. A linearly polarised wave can be considered as a superposition of two (one left- and one right-) circularly polarised waves. A rotation occurs when the two waves experience different refractive indices. In the case of solid or fluid substances, characterising this effect is complex and usually done empirically in the form of the Verdet constant  $V$ . Then, for a parallel magnetic field  $B$  and a thickness  $d$  the incurred rotation  $\gamma_F$  is given by  $\gamma_F = VBd$ .

In a plasma, a first-principle based derivation is possible [79], beginning with the refractive indices for left- and right-circularly polarised light:

$$\begin{aligned} n_L &= \sqrt{1 - \frac{\omega_p^2/\omega^2}{1 + (\omega_c/\omega)}} \\ n_R &= \sqrt{1 - \frac{\omega_p^2/\omega^2}{1 - (\omega_c/\omega)}} \end{aligned} \tag{3.6}$$

Using the dispersion relation  $k_{L,R}^2 c^2 = \omega^2 n_{L,R}^2$  and the fact that  $\omega \gg \omega_p, \omega_c$ , the difference in wave number for both polarisations can be written as:

$$\Delta k = \frac{1}{2} \frac{\omega_p^2 \omega_c}{\omega^2 c} \tag{3.7}$$

Using this and some trigonometrical identities in the expression for the real part of the electric field of two superimposed left- and right-circularly polarised waves yields that the differential change in polarisation angle is given by  $d\gamma_F/ds = \Delta k$ . Integrating over the beam path  $s$  yields the total incurred rotation in SI units as:

$$\gamma_F = \lambda^2 \frac{e^3}{2\pi m_e^2 c^4} \int n_e(s) B_{\parallel}(s) ds \quad (3.8)$$

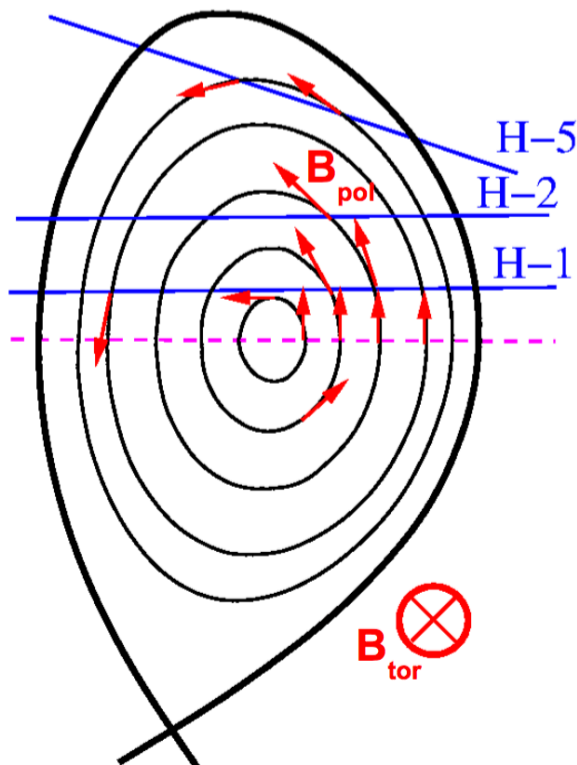


**Figure 3.7:** Examples of lines of sight of the DCN polarimetry at AUG. More details are given in the text. Reproduced from [80].

Since the rotation is caused by the magnetic field along the line of sight, most of the rotation is incurred in a limited volume of the plasma. In figure 3.7 some lines of sight are sketched; H-1, for instance, experiences a strong magnetic field parallel to its beam path only near the axis of the plasma and very little before and after that. This means the measurement yields information mostly about the flux surface the line of sight is tangential to, i.e. it is sensitive to the current enclosed in that surface.

In order to improve the measurement quality, it should be ensured that the line of sight is confined to the poloidal plane. Otherwise it will also be affected by the toroidal

Depending on the line of sight, magnetic field and density, the overall change in rotation for a double pass through the plasma is up to several tens of degrees. Due to the quadratic wavelength dependence, useful polarimetry measurements on AUG are only possible on the DCN laser, whose wavelength is twenty times that of the CO<sub>2</sub> laser. Light from the latter only experiences fractions of degrees of rotation — too little to be resolved given the noise level of the measurement of several tenths of degrees.

The light to be observed for polarimetry is decoupled from the regular density measurement using gold mirrors that obstruct about half of the beam width (FWHM  $w_{\text{laser}} \approx 3$  cm). The direction of its polarisation is then measured using a polariser that rotates with just over 7000 revolutions per minute in front of a detector. In the process of this work, up to two DCN channels (H-2, H-1) became available for polarimetry measurements, where an angular resolution of 0.3° at a time resolution of 50 ms were achieved.

magnetic field, which is about an order of magnitude stronger than the poloidal one. After ensuring that no toroidal field is picked up, or by properly accounting for it, the rotation measurement, together with a density profile, can be fed to equilibrium reconstruction software as an internal constraint. Such constraints will be discussed in section 5 on page 83.

### MSE Polarimetry

Another technique for measuring the magnetic field inside the plasma on ASDEX Upgrade is Motional Stark Effect (MSE) polarimetry. Here, the polarisation of certain spectral lines of neutral beam particles is measured and used to constrain the equilibrium reconstruction. This diagnostic has a crucial role in this work and is therefore discussed in detail in chapter 4 on page 63.

## 3.3 Heating and Current Drive Systems

Ohmic heating using the current driven by the transformer is limited by the fact that the plasma resistivity decreases with increasing temperature. As a result, the temperature plateaus before reaching reactor relevant conditions, and additional heating must be provided.

For this purpose, ASDEX Upgrade is equipped with three different heating systems that can deliver up to around 30 MW of auxiliary heating power. Two of these (ECRH and NBI) were used for this work and will be introduced in the following. The third, ion cyclotron resonance heating, interferes with the MSE measurement and has therefore not been used.

### 3.3.1 Electron-Cyclotron Heating/Current Drive

In section 3.2.2 the ECE diagnostic was introduced. It determines the electron temperature using electron cyclotron emission. The inverse physical process is used to deliver power to the electrons to heat the plasma, so-called electron-cyclotron resonance heating (ECRH). The same fundamental restrictions with respect to wave propagation/cut-off apply to ECRH, but one can choose the most advantageous wave frequencies and orientations for heating whereas ECE has to work with whatever emissions the plasma offers. The explanation of ECRH and its associated current drive will follow [81].

An electromagnetic wave tuned to a harmonic of the resonance frequency of the gyrating electrons  $\omega_c = eB/m_e$  in the plasma is emitted towards it. At the resonance, the wave is absorbed by the electrons, which in turn transfer the absorbed energy via collisions to heat the overall plasma, albeit primarily the electrons.

Specifically, for an injected beam of frequency  $\omega$ , the Doppler-shifted relativistic resonance condition for the  $l$ -th harmonic can be written as:

$$\omega = \frac{l\omega_c}{\gamma} + k_{\parallel}v_{\parallel} \quad (3.9)$$

with  $\gamma$  being the relativistic factor  $\sqrt{1 - v^2/c^2}$  (with  $v^2 = v_{\parallel}^2 + v_{\perp}^2$ ) and  $v_{\parallel}$ ,  $k_{\parallel} = \omega n_{\parallel}/c$  as the electron velocity/beam wave number component parallel to  $\vec{B}$ , respectively. The resonance can be rewritten by defining the relativistic analog of the thermal velocity

$$v_t = c\sqrt{(2T_* + T_*^2)/(1 + 2T_* + T_*^2)} \quad (3.10)$$

using  $T_* = k_B T_e/(mc^2)$ , which becomes  $1/2mv_t^2 = k_B T_e$  for small  $T_e$ . Using also  $w_l = \omega/(l\omega_c)$ , the resonance condition is given by equation 3.11:

$$\frac{v_{\perp}^2}{v_t^2} = (1 - w_l^2) \frac{c^2}{v_t^2} + 2n_{\parallel}w_l^2 \frac{cv_{\parallel}}{v_t^2} - (1 + n_{\parallel}^2w_l^2) \frac{v_{\parallel}^2}{v_t^2} \quad (3.11)$$

This equation describes an ellipse in  $(v_{\parallel}, v_{\perp})$  velocity space, which becomes a circle centred around the origin in the case of  $k_{\parallel} = 0$  (perpendicular injection without a toroidal angle).

This is visualised in figure 3.8 for one point of an injected beam at the resonance. Electrons on the red ellipse can absorb power and thus move in the phase diagram in direction of  $v_{\parallel}$  (blue arrow). Of course, the rotation phase of the electron gyration motion is a distribution that will have an equal number of electrons be accelerated by the wave and an equal number decelerated, i.e. a diffusion in perpendicular direction in  $(v_{\parallel}, v_{\perp})$  phase space that seemingly transfers no energy to the electrons. That image, however, does not take into account the underlying velocity distribution of the electrons, which is generally assumed to be Maxwellian. Thus, similar to Landau damping, if there are more lower- than higher-energy electrons, the diffusion leads to a net reduction of the number of low-energy electrons in favour of more high-energy electrons. The heated electrons thermalise through collisions that convert their excess energy into an overall increased plasma temperature.

Furthermore, the fact that the resonance frequency is Doppler-shifted differently for incoming and outgoing electrons with respect to a wave injected with a toroidal tilt (see  $+k_{\parallel}v_{\parallel}$  in equation 3.9) allows to predominantly heat electrons going in one direction around the torus. In figure 3.8 this is represented by the fact that the red resonance ellipse is not centred on the origin but shifted towards positive  $v_{\parallel}$ . This can be exploited to not just heat the plasma, but also to drive current (ECCD).

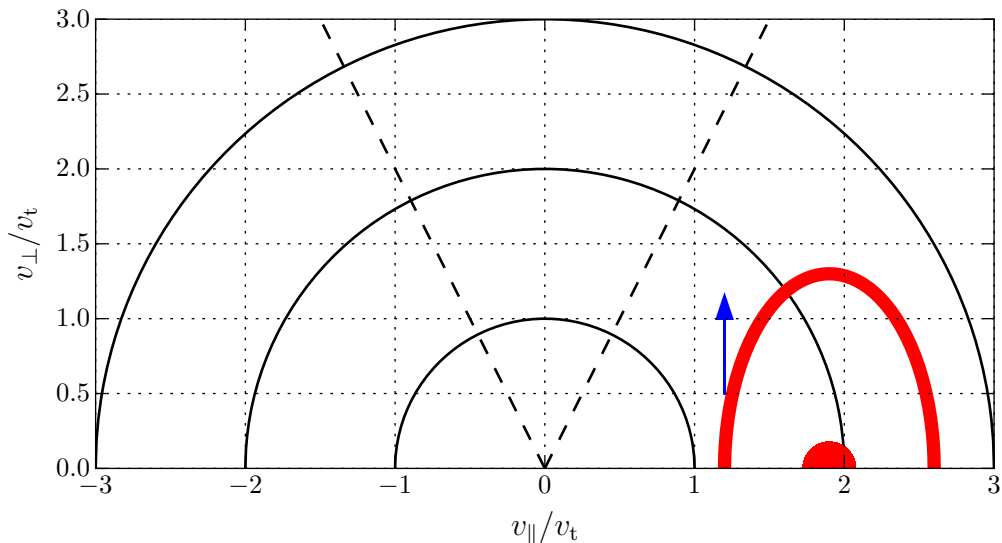


**Figure 3.8:**  $(v_{\parallel}, v_{\perp})$  phase diagram for one resonance point. Black semicircles indicate levels of equal electron energy. Electrons meeting the resonance condition occupy the ellipse highlighted in red and move upwards in direction of  $v_{\perp}$  when they are accelerated (example given as a blue arrow). Dashed lines delimit the region of trapped particles. The size of the red resonance ellipse changes, starting with a point for the first electrons that meet the resonance condition and have no  $v_{\perp}$ , and expanding for later ones until the wave has lost all its energy. Non-perpendicular injection shifts the resonance ellipse horizontally to allow preferential heating of electrons going in one direction  $v_{\parallel}$ .

Two counter-acting mechanisms exist for ECCD:

**Ohkawa current drive:** An accelerated particle that gains perpendicular momentum moves upwards in the phase diagram. If it enters the cone of trapped particles, it can no longer revolve around the torus, effectively subtracting its contribution from the toroidal current. This amounts to a net electron flow in the opposite direction of  $v_{\parallel}$ , also because any de-trapping process will not have a preferential direction [82].

**Fisch-Boozer current drive:** Accelerated particles gain higher  $v$  which leads to a reduced collision rate  $\propto v^{-3}$ . As these electrons now take longer to be slowed down by collisions than their counterparts going in the opposite direction, a net current is driven [83].

These two mechanism oppose each other and could, in principle, cancel each other out under appropriate conditions. In ASDEX Upgrade, most heating and current drive is

applied to the high field side, where the cone of trapped particles vanishes. The same applies to heating near the magnetic axis, on which this work focuses, since the trapped particle fraction scales with  $\sqrt{\epsilon}$  and  $\epsilon(r=0) = 0$ , which is why the Ohkawa mechanism can be neglected here.

ASDEX Upgrade's ECRH system [84, 85] consists of eight gyrotrons located outside the torus hall, four of which can deliver up to 1 MW of power for up to 10 seconds (ECRH2) while another four can deliver 0.5 MW for up to 2 seconds (ECRH1). ECRH2 gyrotrons can generate EC waves at both 105 and 140 GHz, ECRH1 only at 140 GHz. ECRH1 has been shut down in late 2015 and will be replaced by a new system (ECRH3) that will offer similar performance as ECRH2.

ECRH, like the ECE diagnostic, operates on the second or even third harmonic to avoid running into cut-off — which can be more problematic for ECRH, as the reflected power might damage the machine. The beam polarisation can be switched between X- and O-mode (extraordinary and ordinary). For this work, ECRH purely with the second harmonic X-mode at 140 GHz was used.

As ECRH waves are in the millimetre range, they are transmitted from the gyrotrons to the torus quasi-optically using waveguides and mirrors. The mirrors in the torus are steerable, which allows changing the deposition location along the resonance in poloidal and toroidal direction. Certain beam lines allows this even during a discharge using real-time feedback control, for example to mitigate NTMs by pointing the ECRH/ECCD deposition right at them [61, 62].

## TORBEAM

The ECRH deposition location can be calculated using TORBEAM [86]. TORBEAM is a beam tracing code that takes the ECRH configuration, the magnetic equilibrium as well as density and temperature profiles as inputs and determines the path of the injected beam through the plasma until absorption. It returns that path and the deposition profiles of heating  $dP/dV$  and current drive  $j_{\text{ECCD}}$ . An example of TORBEAM's results is shown in figure 3.9. As mentioned earlier in the section on density measurements, the plasma's refractive index is below unity which refracts the beam away from the regions of denser plasma near the centre.

TORBEAM was used for this thesis to plan the on-axis current drive experiments. Since the deposition resonance extends vertically through the plasma, it only intersects the axis in one location, or not at all. This makes on-axis deposition particularly challenging since the magnetic axis (Shafranov-) shifts horizontally with increasing  $\beta$  [87]. That means one must anticipate the expected performance and choose the magnetic field and injection angles such that EC wave, resonance and magnetic axis intersect in space and time.

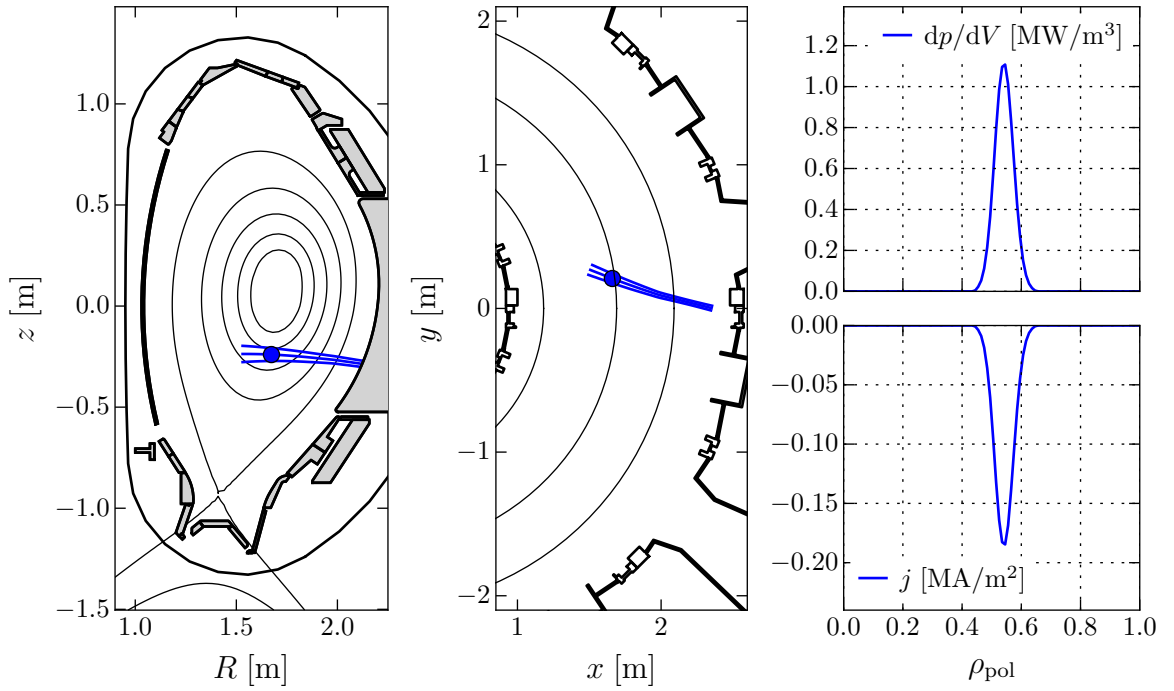


**Figure 3.9:** Example TORBEAM output for Gyrotron 8 in #32303 at 3.2 s.

Left/middle: Poloidal/dorsal cross-section showing beam path.

Right, top/bottom: deposited power/driven current density.

This requires that the deposition of power near the magnetic axis to be accurately calculated in TORBEAM. During this work it was discovered that the assumptions underlying the algorithm generating the deposition profiles (figure 3.9, right) were not appropriate near the magnetic axis, leading to a strong underestimation of deposited power/current on the axis. Thus, a new deposition algorithm was developed and implemented. It operates on a cartesian grid aligned with the beam axis with step size  $dx$  around the deposition location. There, the beam's deposition is evaluated discretely to yield a set of cartesian  $dP/dV_c$  with known  $dV_c = dx^3$ . These discrete contributions are assigned to a flux shell  $d\psi$  and integrated, resulting in  $dP/d\psi$ . Finally, using the equilibrium's volume information  $d\psi/dV$  the individual shells'  $dP/dV$  is calculated. An analogue approach yields  $j = dI/dA$ .

The difference in the calculated deposition profiles is shown in figure 3.10, which depicts two sets of deposition profiles that were both generated with the same input data. While the integrals of both sets of profiles are the same, i.e. the same total power and current were deposited and driven, respectively, their shape has changed. The new algorithm results in a diverging deposition profile on the axis, which is clear as the plasma volume goes to zero as one approaches the axis  $dV \rightarrow 0$ . To ensure that downstream codes relying on TORBEAM do not suffer from this high axial value, it is capped at the



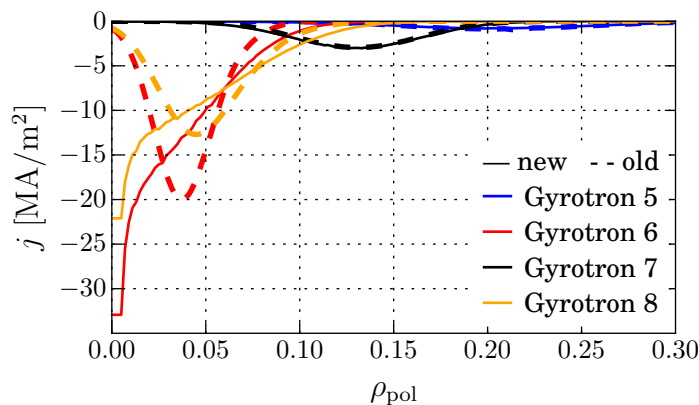


**Figure 3.10:** New and old TORBEAM deposition results near the axis. (#31113, 2.5 s)

second value of the profile. For deposition further away from the axis, old and new algorithm are in agreement.

### 3.3.2 Neutral Beam Injection (NBI)

ASDEX Upgrade’s eight neutral beam injectors are its most powerful heating systems [88]. Together they can deliver up to 20 MW of heating power. They also serve as diagnostic neutral beams for spectroscopic measurements like charge exchange spectroscopy or MSE.

In a neutral beam source, deuterium is ionised by a low power plasma. The ions are then accelerated using a high voltage grid (60 kV for box 1, 90 kV for box 2) before passing through a chamber filled with neutral deuterium to be neutralised again via charge exchange reactions. As there are not only D ions present, but also  $D_2^+$  and  $D_3^+$ , beam particles also occur at 1/2 and 1/3 of the full energy. Ions that have not been neutralised are diverted using a magnetic field while the neutral particles continue onwards to the plasma at a speed of the order of 1–3 Mm/s. Being neutral, the particles are unaffected by the magnetic field and penetrate into the plasma. There, they collide with plasma particles — both ions and electrons, although the cross-sections of these interactions vary with the plasma parameters — and become ionised. Before they thermalise over a characteristic slowing-down time  $\tau_s$  and turn their excess energy into an overall increase of plasma temperature, these supra-thermal/fast ions can have interesting effects on the plasma, for example the stabilisation of sawtooth instabilities [89]. Since fast ions will be naturally produced by the DT-reaction in the form of 3.5 MeV alpha-particles, the study of fast ions and their influence on the plasma is a necessary field in fusion research.

Before they slow down, the fast ions also contribute to the plasma current [90]. Consider beam particles injected from the off-axis sources (see figure 3.11): as they become

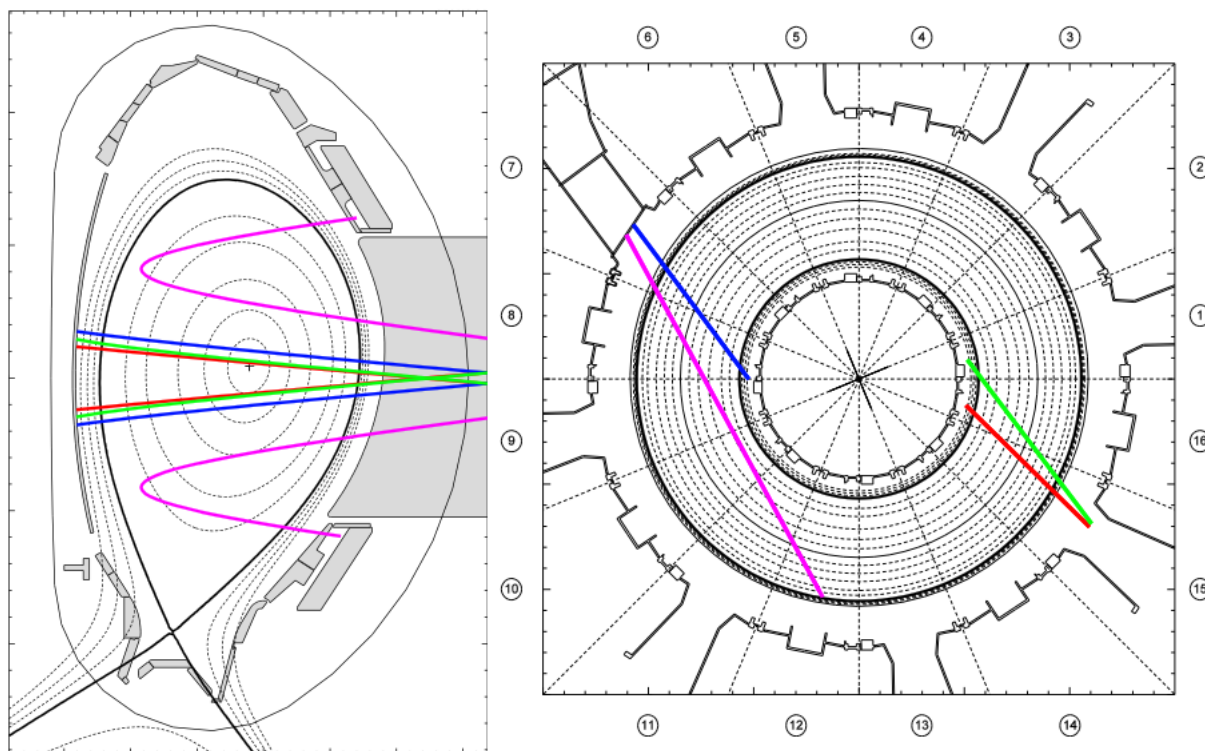


**Figure 3.11:** Poloidal and toroidal projections of the geometry of the NBI boxes (box 1 in sector 15, box 2 in sector 7). Illustrated are two radial sources (red), four tangential sources (green, blue), and two off-axis sources (pink).

ionised, their electrons lose their directional information while the massive nuclei continue onward, resulting in a net-current in beam direction. Existing plasma electrons are pulled along, resulting in a shielding current [90]. Fortunately, trapped electrons cannot participate in this shielding current, allowing the unshielded fast ions to drive a toroidal current during their slowing-down time. The same fundamentally applies to the other sources, but since they are not tilted in toroidal direction for maximum current drive, their contributions is comparably small. All things considered, neutral beam current drive in AUG is of the order of up to 200 kA for typical plasma parameters, increasing with higher temperature and decreasing with higher density.

## TRANSP

A widely used numerical tool for NBI simulation is the TRANSP code [91]. TRANSP is a software suite for comprehensive analysis of tokamak plasmas with a particular focus on transport, that includes the NBI simulation module NUBEAM [92]. NUBEAM uses a Monte-Carlo approach and a comprehensive physical model for the interaction of beam neutrals with plasma. In the simulation, neutrals are injected into the simulated plasma and traced over the slowing-down time. As such, it adds newly ionised neutrals into

a pool of fast ions and, at the same time, removes the ones that have slowed down, keeping an inventory of fast ions available for subsequent physical analyses using codes like TGLF.

This comprehensive NBI simulation yields various relevant quantities, e.g. fast ion density profiles, NBI heating and current deposition profiles or the NBI power loss due to beam shine-through (not to be confused with ECE shine-through that is compensated by IDA). The quality of these results depends on the accuracy of NUBEAM's models as well as its input data, and must therefore be taken with a grain of salt.

# 4 The MSE Diagnostic

Since its first application almost 30 years ago [93], the Motional Stark Effect (MSE) diagnostic has become the de-facto standard for obtaining information about the core plasma equilibrium and, in particular, its  $q$ -profile. Originally installed on AUG in the late 1990s, the diagnostic started suffering from initially inexplicable systematic errors in the 2000s. Part of these errors could be attributed to various optical effects as explained in [94], but some questions concerning spurious, intermittent drifts during discharges and the absolute calibration remained unanswered.

This chapter will first introduce the diagnostic, then report on the progress regarding polarised background light which was found to cause the intra-discharge drifts, and finally discuss the absolute calibration of the diagnostic.

## 4.1 Introduction

The MSE diagnostic yields information about the magnetic fields inside the plasma by measuring the polarisation of light from beam neutrals. This polarisation depends on the magnetic field vector at the point of emission and can be used to constrain equilibrium reconstruction. The explanation of the diagnostic will follow [95] and [96].

The deuterium atoms in the neutral beam emit light when they are excited through plasma interaction. Collecting this light using a view that is non-perpendicular to the beam axis allows the beam emissions to be separated from the emissions of the bulk plasma since the Doppler-effect shifts the beam emissions to other wavelengths (viewing geometry shown in figure 4.2).

An example of an MSE spectrum observed in this manner is shown in figure 4.1. The beam emissions are shifted towards lower wavelength, whereas the bulk plasma emission remains centred albeit broadened around the usual D- $\alpha$ -line. In contrast to the bulk plasma emissions, the beam emissions have a distinct structure caused by the Stark effect, i.e. splitting of the spectral lines in the presence of an electric field. Note that Zeeman-splitting is much weaker and thus neglected.

The particles, as they move through the magnetic field  $\vec{B}$ , experience a strong electric field, i.e. a Lorentz field  $\vec{E}_L = \vec{v}_B \times \vec{B}$ , and any existing background electric field  $\vec{E}_0$ . Since this field appears due to the motion of the particles relative to the static magnetic field, its effect is designated as the *Motional* Stark Effect. The total field reads:

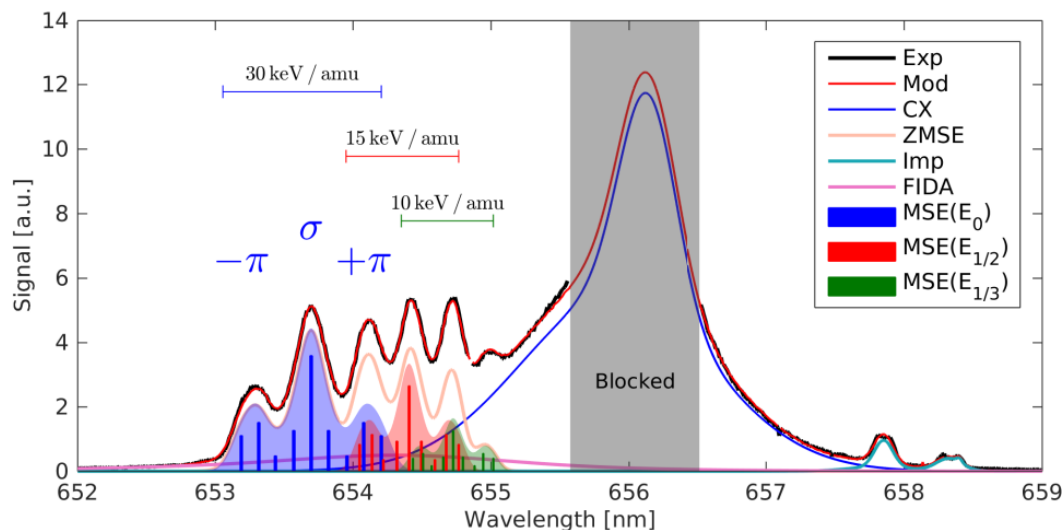


**Figure 4.1:** Typical MSE spectrum reproduced from [96]. The blue-shifted full, half and third energy Stark-split spectral lines are highlighted (between 653 and 655 nm), each consisting of a  $\sigma$ -line flanked by two  $\pi$ -lines on either side.

$$\vec{E} = \vec{v}_B \times \vec{B} + \vec{E}_0 \quad (4.1)$$

Since the beam velocity is far lower than the speed of light  $v_B \ll c$ , relativistic contributions to the expression are neglected. The Stark effect causes the otherwise degenerate Balmer- $\alpha$  transition ( $n = 3 \rightarrow 2$ ) to split into nine distinct spectral lines, illustrated as coloured vertical bars in figure 4.1.

Emissions from these spectral lines are dependent on  $\vec{E}$  in several ways, two of which are of special importance:

- The direction of  $\vec{E}$  determines the polarisation of the light from each spectral line. Emissions from the three middle ones (of one given energy component) are polarised perpendicular to  $\vec{E}$ , which is why they are grouped together as  $\sigma$  (from the German word for perpendicular, senkrecht) whereas the flanking lines emit light polarised parallel to  $\vec{E}$ , i.e.  $\pi$  (see figure 4.1).
- The absolute wavelength of the  $\pi$  lines depends on the strength of the electric field. The distance between  $\pi$  and  $\sigma$  wavelength is proportional to the field.

The fundamental idea behind the MSE diagnostic is to measure the polarisation of  $\sigma$ - and/or  $\pi$ -light emitted from a point and use that information to infer the direction of  $\vec{E}$  and thus  $\vec{B}$  at that point. Specifically, the measured polarisation angle as well as information about the beam geometry and the MSE's line of sight are given to an equilibrium reconstruction code as an internal constraint on the magnetic field vector (see chapter 5 on page 83).

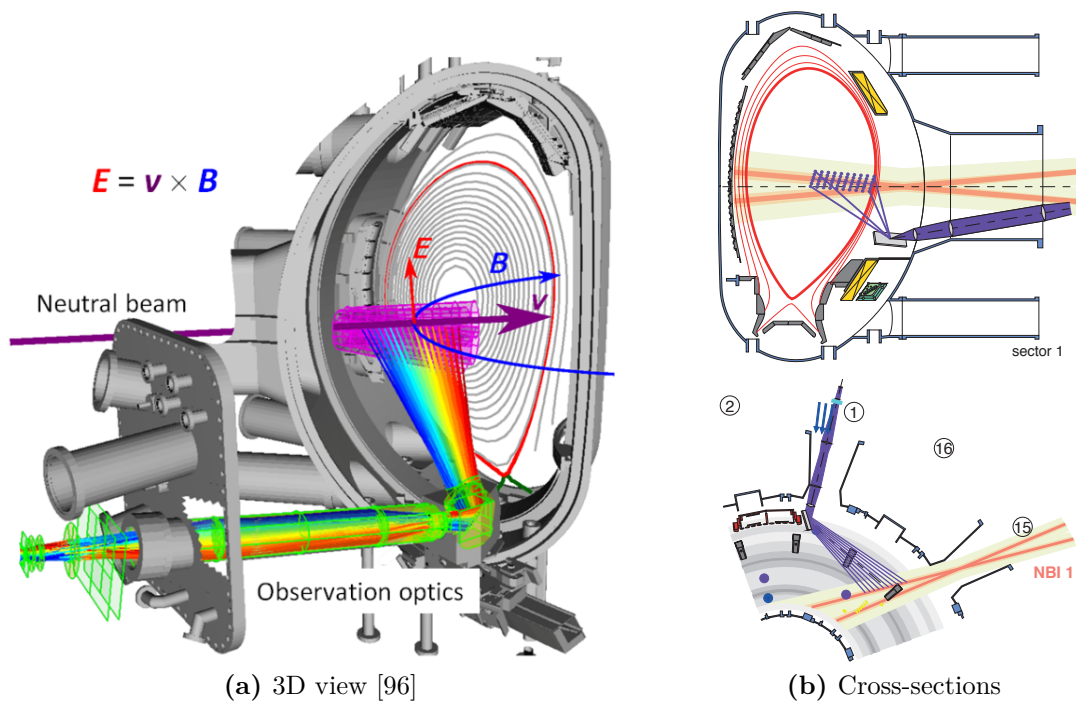


**Figure 4.2:** Observation geometry of the MSE diagnostic. The angle with respect to the neutral beam leads to a blue-shifting of the beam emissions.

For that to be possible, the background electric field  $\vec{E}_0$  must be known, either by inferring it from other measurements or through direct measurements. In this work it is inferred using the dominant toroidal plasma rotation term of the radial force balance  $\vec{E}_0 \approx \vec{v}_{\text{tor}} \times \vec{B}_{\text{pol}}$ . For typical parameters ( $v_B \approx 2$  Mm/s,  $B \approx 2.5$  T) the Lorentz field is of the order of 5 MV/m.  $E_0$  can be up to a tenth of that, which means that it cannot be neglected, especially when using off-axis neutral beam sources which impose a strong toroidal torque on the plasma.

The magnetic field is composed of toroidal and poloidal components,  $\vec{B} = \vec{B}_{\text{tor}} + \vec{B}_{\text{pol}}$ . Since  $\vec{B}_{\text{tor}}$  is well-known, the MSE diagnostic's information mainly constrains  $\vec{B}_{\text{pol}}$ . As such, the MSE ultimately yields information about the toroidal current enclosed in the flux surface on which the observed point lies. To reconstruct a complete toroidal current density profile, several radially distributed measurements are needed.

To accomplish this, the optical system of the MSE diagnostic covers the entire low-field side minor radius of ASDEX Upgrade as shown in figure 4.2. It focuses on the third beam of NBI box 1. Emissions from the other three beams corrupt the measurement and should be avoided since forward-model-based correction schemes like [97] are not routinely available on AUG, which leaves beam box 2 for heating. The beam emissions are reflected by a mirror into an array of lenses that relay the light towards a bundle of 60 optical fibres. The mirror is physically separated from the plasma by a protective

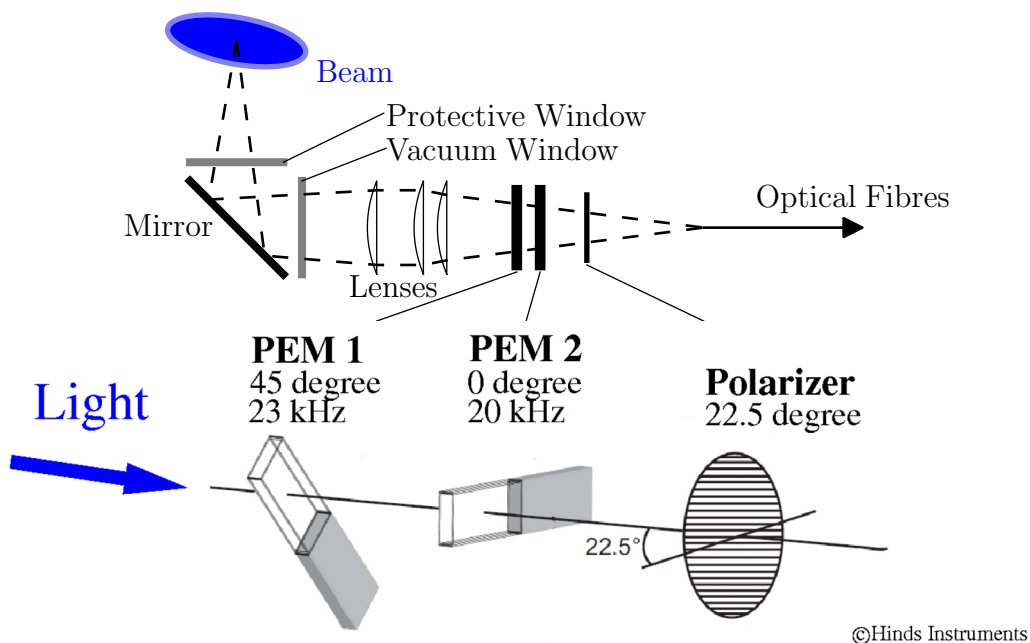


**Figure 4.3:** Schematic view of the MSE optical relay path.

fused silica window. The fibres transmit the light to a data analysis and acquisition system located in a lab outside the torus hall. The fibres are aligned in six rows and ten columns and oriented such that a row is aligned to the beam, allowing measurements at up to ten radial positions. For calibration purposes, three polarised light sources are installed at select locations in the wall segment behind the neutral beam.

Since light does not maintain its polarisation state when transmitted through optical fibres, the information contained in the polarisation angle must be translated into an intensity modulation beforehand. This translation is accomplished using two oscillating photoelastic modulators (PEMs) angled at  $45^\circ$  with respect to each other and a linear polariser after that at  $22.5^\circ$  (shown in figure 4.3). The PEMs are compressed using a piezo crystal, making them periodically birefringent at  $f_1 = 23$  kHz and  $f_2 = 20$  kHz, respectively. The modulated, still polarised light passes through the linear polariser which completes the intensity encoding by transmitting only the component parallel to the polariser. In a simplified picture, the array of PEMs and polariser effectively acts as a polariser rotating in the kHz-range.

This technique is known as Stokes polarimetry [98], as it yields the full 4-component Stokes vector that contains the full state of polarisation, except its phase.

$$\vec{S} = \begin{pmatrix} S_0 \\ S_1 \\ S_2 \\ S_3 \end{pmatrix} = I \begin{pmatrix} 1 \\ p \cos 2\gamma_m \cos 2\chi \\ p \sin 2\gamma_m \cos 2\chi \\ p \sin 2\chi \end{pmatrix} \quad (4.2)$$

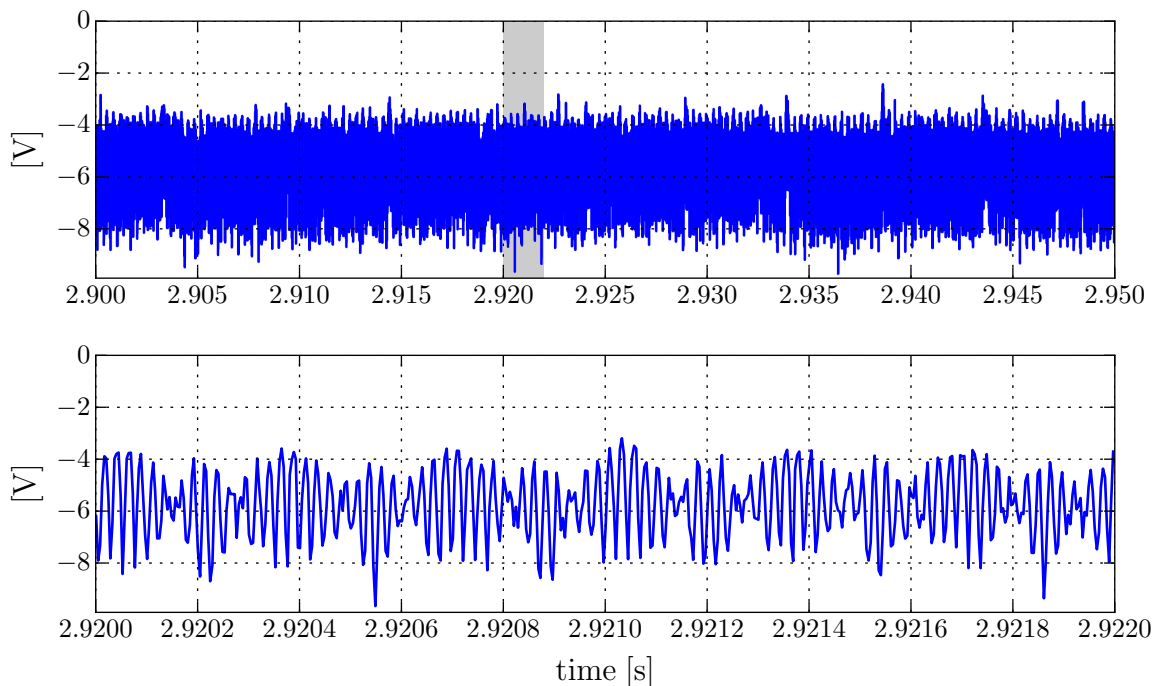


**Figure 4.4:** Example MSE voltages showing an overview (top) and a zoomed in region (bottom), highlighted in the top plot by the shaded area. (#31113, MSE ch. 7)

The Stokes parameters are the total intensity of the light  $I$ , the polarisation fraction  $p$ , the polarisation angle  $\gamma_m$  and the degree of ellipticity  $\chi$ . Even though all parameters are accessible to Stokes polarimetry, only the middle components  $S_1$  and  $S_2$  are of immediate interest to MSE as they depend on the polarisation angle.

$S_1$  and  $S_2$  are proportional to the intensity of the light modulation at the doubled frequencies, respectively, (i.e.  $I_1 = I(2f_1) \propto |S_1|$  and  $I_2 = I(2f_2) \propto |S_2|$ ) which allows to express the measured MSE angle  $\gamma_m$  as:

$$\gamma_m = \frac{1}{2} \arctan \frac{I_2}{I_1} \quad (4.3)$$

Note that the Stokes components can take negative values, whereas intensities cannot. That limits the immediately available range of  $\gamma_m$  to  $[0^\circ, 45^\circ]$ . However, by comparing the phases of each modulation with the reference phase from the respective PEM circuit and choosing the sign accordingly, the range is extended fourfold to a full  $180^\circ$ .

In the lab, the intensities are converted into voltages using photomultipliers and recorded with a data acquisition system sampling at 250 kHz. An example of such data is shown in figure 4.4, where the oscillations are clearly visible. While the sampling rate allows a high time-resolution in theory, in practice one has to always take many oscillation periods



into account to accurately reconstruct the amplitudes, which lowers the time resolution to around 40 Hz or about 25 ms. This is faster than the typical current diffusion times on AUG, which are of the order of hundreds of milliseconds and above. Currently up to 14 photomultipliers are in operation in ASDEX Upgrade's MSE system, using the lines of sight pointed optimally at the neutral beam, radially distributed to cover the largest possible area. Data are obtained with a statistical uncertainty of  $\sigma_{\text{MSE}} \approx 0.2^\circ$ .

To ensure that only light from the wavelengths of interest is picked up, interference filters whose transmission curves are centred on the spectral line of interest and have a FWHM of about 0.2 nm are placed before the photomultipliers. The filters are temperature sensitive, that is their central wavelength depends on the temperature with a shift of  $d\lambda/dT \approx 0.02$  nm/K in the operational range of 30-60°C. This allows finely tuning them for every line of sight by adjusting their temperature using individual ovens. As mentioned before, the  $\pi$  and  $\sigma$  wavelengths change with the beam velocity/observation angle and, in the case of  $\pi$ , also with the magnetic field. While the beam velocity and observation angles are usually stable, different magnetic field strengths are used in AUG experiments. Since no fast adaptive temperature control is installed, the lines of sight measuring the  $\pi$ -line are tuned to function optimally at  $B_0 = 2.5$  T.

The MSE angles are measured in the natural coordinate system of the diagnostic, which has an arbitrary but measurable offset  $\Delta\gamma$  with respect to the torus/plasma coordinate system in which the angles are used to constrain equilibrium reconstruction. The determination of this offset is discussed in section 4.3. Furthermore, the light passing through the protective window in front of the mirror (see figures 4.2 and 4.3) is propagating in toroidal direction. This leads to Faraday rotation by the toroidal magnetic field as explained in section 3.2.5. The effect has been characterised by [94] and the measured angle is corrected accordingly by subtracting the incurred rotation  $\Delta\gamma_{\text{F}}$ . The angle to be used for equilibrium reconstruction thus reads:

$$\gamma_{\text{torus}} = \gamma_{\text{m}} - \Delta\gamma_{\text{F}} + \Delta\gamma \quad (4.4)$$

In summary, the MSE diagnostic provides information on the direction of the magnetic field at a point by measuring the polarisation angle of light emitted from that point. It can be corrupted by emissions from the other neutral beams, which is why the MSE is not used with more than beam three active. Moreover, other sources of polarised light may also corrupt the measurement as discussed in section 4.2.

## 4.2 Interference from Polarised Background Light

This section will report on the influence of polarised background light on the MSE measurement. First, evidence of the background is presented. Then an approach to account for the background interference is introduced.

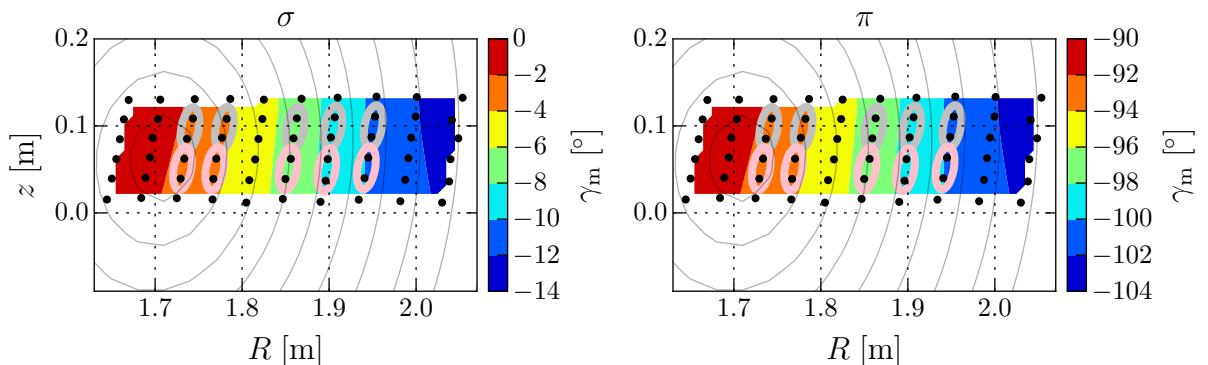


**Figure 4.5:** Contour plot showing expected angles for a given equilibrium on all 60 available views. Also highlighted by ellipses: locations of reconfigured MSE system, using two rows to measure both polarised components simultaneously ( $\pi$  in pink,  $\sigma$  in silver).

Synthetically generated MSE angles are shown in figure 4.5. They are calculated on the basis of a given magnetic equilibrium and show what angle measurements are expected. Over the whole minor radius of the plasma, the angles vary by about  $14^\circ$ . Part of this variation is caused by the lines of sight having a different angle with respect to the magnetic field (up to  $\sim 4^\circ$ ), while the remainder is caused by the magnetic field variation, i.e. the plasma current profile to be diagnosed. Changes in the measurements are expected to be in the range of no more than single degrees, or even fractions of degrees during the flat-top phase in which the total plasma current is kept constant. Changes of up to  $5^\circ$  may occur during large-scale current events like the initial current ramp-up.

Changes exceeding these expectations by several degrees or even tens of degrees are unlikely to be correct and either lead to unphysical results of equilibrium reconstruction or cause the reconstruction to fail altogether as the measured angles cannot be reconciled with other available information. Polarised background light was identified as the main cause for such errors.

### 4.2.1 Identification of the Polarised Background

The identification of the polarised background was accomplished by reconfiguring the MSE system. Originally it used ten lines of sight to observe the beam emissions. They were changed to measure both  $\pi$  and  $\sigma$  light at five locations such that the difference between both angles should amount to  $\Delta\gamma_m = \gamma_\pi - \gamma_\sigma \stackrel{!}{=} 90^\circ$ , neglecting effects from the slightly different measurement locations or the different impact of Faraday rotation in the protective glass. Those changes affect both components in the same way, i.e. even if the difference is not  $90^\circ$ , it should remain constant. This configuration is highlighted by the ellipses in figure 4.5.

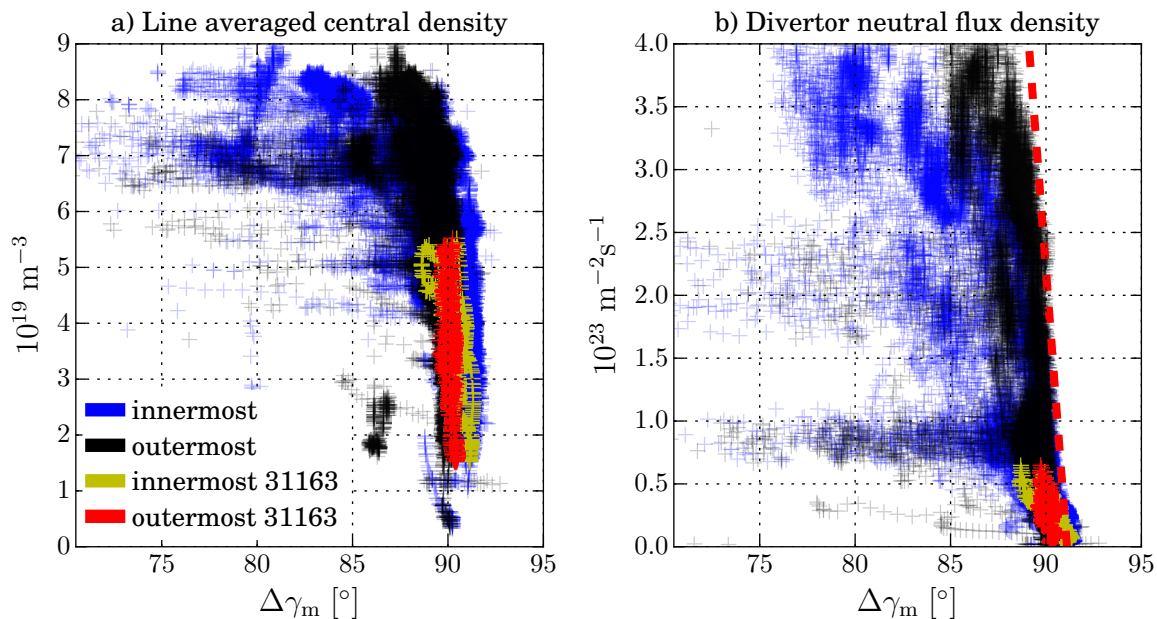


**Figure 4.6:** Difference between innermost and outermost pair of measurements (see figure 4.5) vs. a) line averaged central density (H-1) and b) divertor neutral flux density.

The MSE has been operated in this configuration for most of the 2014 campaign, generating a database of 134 discharges with 66858 samples of valid data. That is,  $B_{\text{tor}} = 2.5 \text{ T}$ , no ICRH, only NBI beam 3 of box 1. The discharges cover a wide range of operational parameters that were included in the database and were subsequently used to find correlations in the data.

Two examples of such correlations are depicted in figure 4.6. The left plot shows how the optimal  $90^\circ$  difference is reduced with higher density. This occurs in both central and edge views, although it is more pronounced in the central one. Such behaviour is due to the neutral beam attenuation: the higher the density, the earlier the neutral beam particles will be ionised, reducing the intensity of the beam emissions the MSE relies on. Thus, the effect of polarised background light is increasing with increasing density.

A similar correlation is observed in the right plot, where higher neutral flux density in the divertor correlates with a reduction of  $\Delta\gamma_m$ . It is particularly noticeable how the increased divertor density creates an upper limit of  $\Delta\gamma_m$  in the form of a solid edge towards the right end of the data distribution (indicated by a dashed red line in figure 4.6b). Here, a similar explanation can be used: the more neutral particles there are in the divertor, the more light they can emit, which in turn can become polarised via reflections. This occurs, for example, during detachment experiments, where neutral gas is injected in the divertor to radiate the power it would otherwise receive. The emitted

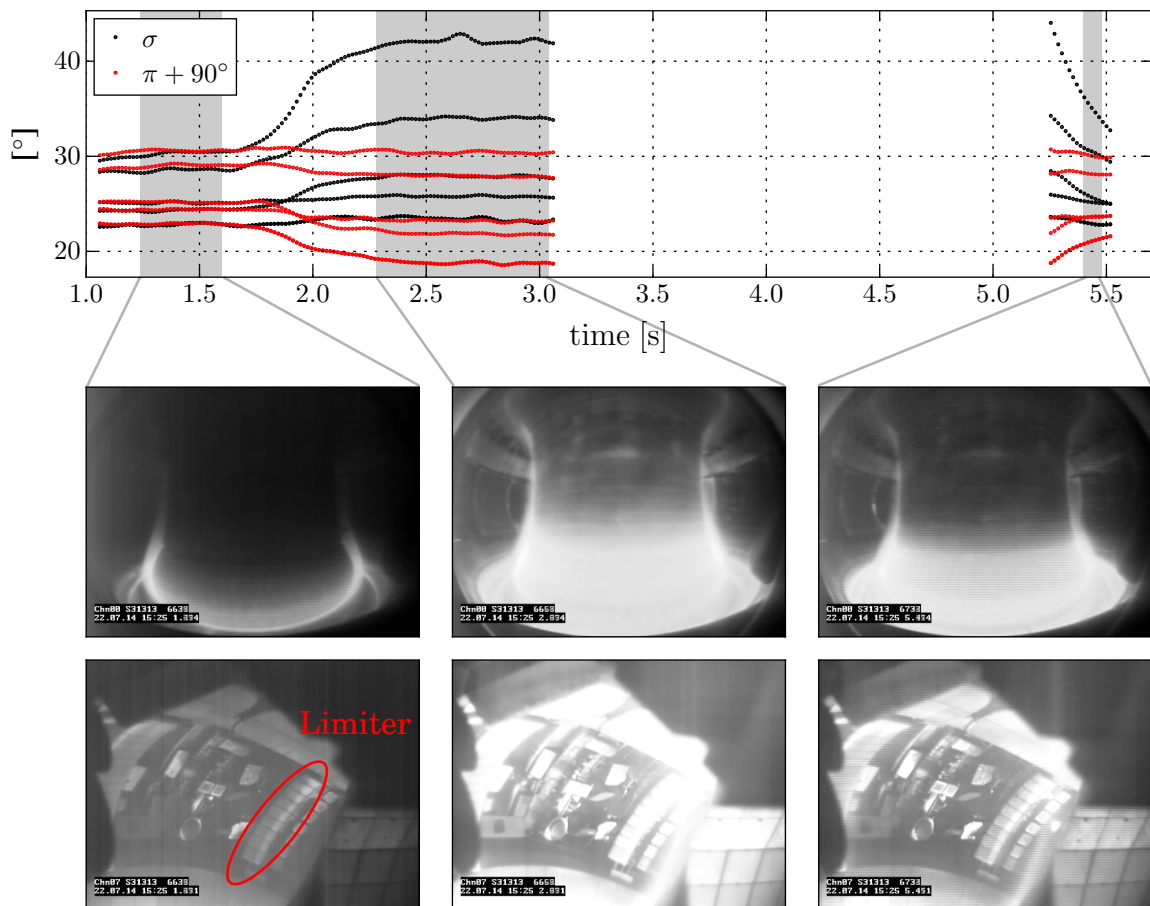


**Figure 4.7:** Evolution of MSE angles and plasma light emission (#31313). For further reference, a limiter is highlighted in the bottom left camera image. Different levels of corruption in the traces result from non-uniformity in the observed view dump as explained in the text.

light, although originally unpolarised, is reflected by the metal plasma facing components — most of which are specular tungsten coated by thin layers of boron and other kinds of plasma deposition — inducing a polarisation through Fresnel reflection. Polarised light reflected into the MSE view by the wall behind the observed neutral beam affects the measurement.

Both plots also include data from discharge #31163, which was performed for the physical part of this work. The distribution shows that while the effect of the polarised background is small  $\Delta\gamma_m \ll 1^\circ$  for the outermost channels, but can be noticeable in the innermost channels  $\Delta\gamma_m \lesssim 1.5^\circ$ . As such, these systematic errors must be expected to affect the equilibrium reconstruction close to the magnetic axis. This is discussed in section 5.2.2 on page 91.

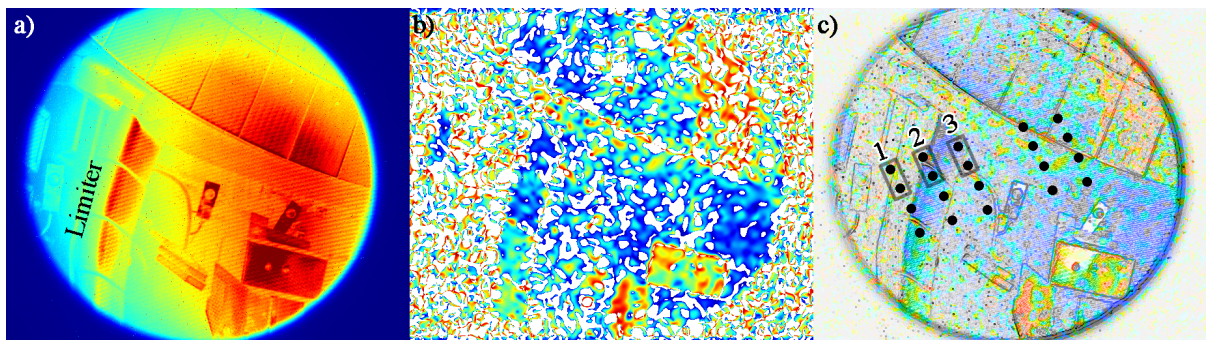


**Figure 4.8:** 200 ms background measurement with a prototype IMSE system using the conventional MSE’s view and one of its filters. Left: raw intensity, showing the fringes. Middle: resulting polarisation angles. Right: combination of both images, including the measurement locations of the conventional MSE in the 2014 campaign.

The phenomenology is shown in figure 4.7. The overview trace shows the evolution of MSE angles. Below are camera images observing the divertor and inner heat shield (first row of images) and a section of the outer wall (second row).

In the beginning until about 1.6 s,  $\pi$  and  $\sigma$  measurements lie  $90^\circ$  apart. The first column of camera pictures (averaged over the first shaded interval) shows a dimly lit torus. After 1.6 s, the heating power is increased and the central density rises from  $5 \cdot 10^{19} \text{ m}^{-3}$  to  $8 \cdot 10^{19} \text{ m}^{-3}$  while the divertor neutral flux density rises strongly from  $0.2 \cdot 10^{23} \text{ m}^{-2}\text{s}^{-1}$  to  $3.4 \cdot 10^{23} \text{ m}^{-2}\text{s}^{-1}$ . The camera images of the second column show a bright plasma from 2.3–3.0 s, during which the innermost MSE angles differ by up to  $10^\circ$  while the outermost deviate by about  $5^\circ$ . From the images of the first row the origin of the increased emissions can be traced back to the high-field side of the torus, down towards the divertor. This region is not directly observed by the MSE diagnostic, yet the measurement is evidently affected by it. This is explained by the camera images of the wall, which is very bright itself, since it reflects the light from the inner heat shield/divertor region.

Between 3.1 and 5.3 seconds, no useful MSE angles can be evaluated as another neutral beam of box 1 is active. After 5.5 s the discharge ends and the emissions decrease. The MSE angles evolve back towards to their expected  $90^\circ$  difference, but do not reach it as beam 3 is turned off prematurely.

The measurements of figure 4.7 on the preceding page are grouped together with three measurements around  $25^\circ$  and another two at around  $30^\circ$  during the unperturbed phase. This is expected since the measurement setup (see ellipses in figure 4.5 on page 69) has a group of three lines of sight further outside and another group of two closer to the axis. When the interference from the polarised background becomes strong, out of the three  $\sigma$  measurements (black in figure 4.7), the first and third remain relatively stable while the middle one increases and even surpasses the third one, suggesting that it is more strongly affected by the interference than the other two, i.e. that the source of the interference is strongly nonuniform — just like the first wall.

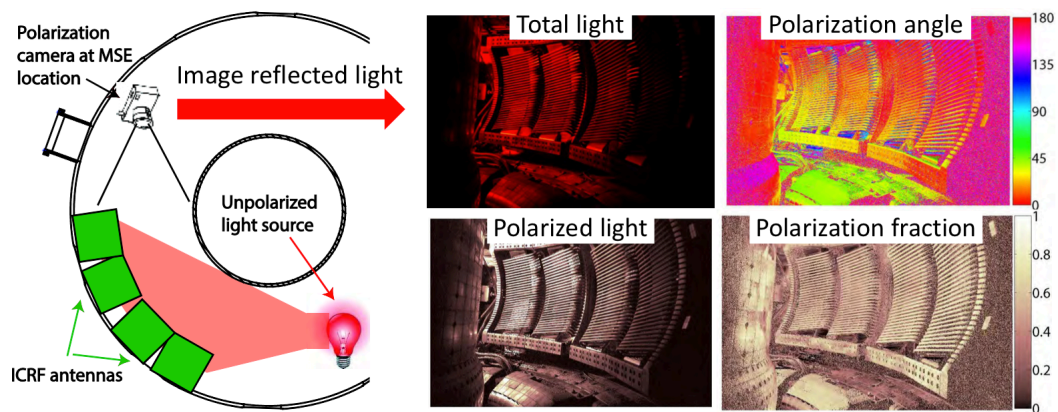


**Figure 4.9:** Polarised reflections recorded at Alcator C-Mod using a polarisation-sensitive camera. Image reproduced from [100]

To capture this non-uniformity, a different, so-called imaging MSE diagnostic was used [99]. The diagnostic, which is currently in development, uses spatial modulation through interference rather than the conventional MSE’s temporal modulation and generates one horizontal and one vertical interference pattern on a camera CCD. The ratio of the contrasts of these fringe patterns also yields the polarisation angle. A prototype of this system has been tested on ASDEX Upgrade in the regular MSE’s place. Figure 4.8 on the facing page shows its measurement during a phase without beam. One can clearly see that without beam a noticeable and non-uniform polarisation is present, especially from structures like the ICRH limiter in the lower left or the protective tiles in the top right.

The MSE measurement locations of the 2014 campaign are overlaid on the right-hand plot 4.8c, with the three views mentioned earlier (each composed of two fibres) being highlighted. This explains why the three adjacent channels mentioned before are not affected equally: the middle one (labeled 2) that experienced the strongest interference sits exactly on the edge of the limiter which results in it receiving the strongest background light.

From these observations it is concluded that the conventional MSE system is suffering from intermittent spurious contamination due to a polarised background primarily caused by reflections.

Similar findings from the tokamak Alcator C-Mod support this conclusion [100]. Its molybdenum walls have similar optical properties as AUG’s tungsten walls, i.e. they, too, have a high reflectivity and cause a polarisation of the reflected light due to diattenuation. Measurements from C-Mod showing this are displayed in figure 4.9. Again, these reflections are highly nonuniform and depend strongly on the wall structure, which is consistent with AUG’s observations.

These findings are also in line with the fact that no background issues were identified on ASDEX Upgrade before it was converted into a full-tungsten machine — the carbon sur-

faces were matte rather than specular and thus only caused diffuse reflections with much lower intensity [96]. This also means that future fusion devices with highly reflective first walls must take these reflections into account when designing an MSE system.

### 4.2.2 Polarised Background Correction

To ensure the viability of MSE under all conditions, a background subtraction scheme must be applied. This is especially important for larger devices like ITER where emissions like bremsstrahlung will be more intense.

One possible scheme is to modulate the neutral beam, measure the background while the beam is off, and subtract an interpolated background from the measurement with beam. This assumes that the plasma will not vary significantly with and without the beam. Unfortunately, since AUG's MSE works on an actual heating beam rather than a pure diagnostic beam with low power, this is not a viable solution. As the beam delivers 2.5 MW of power, turning it off affects the plasma substantially. This is unwelcome for experiments and also casts doubt on the assumption that the plasma does not change significantly due to the beam modulation. Since there is no equivalent beam on the second box, it can also not be intermittently replaced by another beam. For this reason, background subtraction via beam modulation is not a suitable approach for handling the polarised background issue.

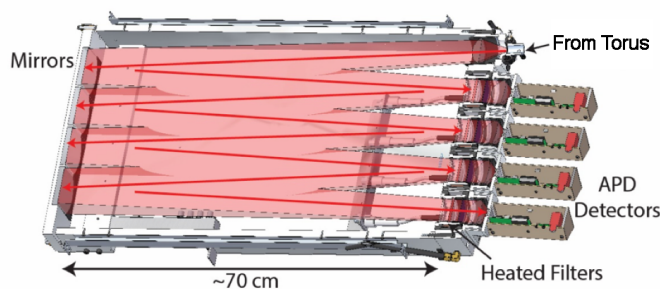


**Figure 4.10:** Schematic view of an MSE polychromator, reproduced from [101].

A technique pioneered at C-Mod uses a polychromator. An MSE polychromator functions fundamentally like a conventional MSE system, except it reflects the light not transmitted by its filter to another filter and detector, and so on. Each filter-detector pair extracts a piece of the spectrum and passes the rest on with a reflectivity of the order of 99%. That allows several parts of the spectrum to be probed simultaneously, which in turn enables

the system to measure the background as well as both  $\pi$  and  $\sigma$  components.

It is assumed that the background is broadband and has a similar polarisation across the whole spectrum such that the measurements of the background can be interpolated at the signal wavelengths and their Stokes components subtracted from each other to correct for the background effect.

A schematic of the polychromator prototype that was loaned to ASDEX Upgrade by C-Mod in late 2015 is shown in figure 4.10. It uses compact avalanche photo diodes instead of photomultipliers and is able to measure at four wavelengths simultaneously.

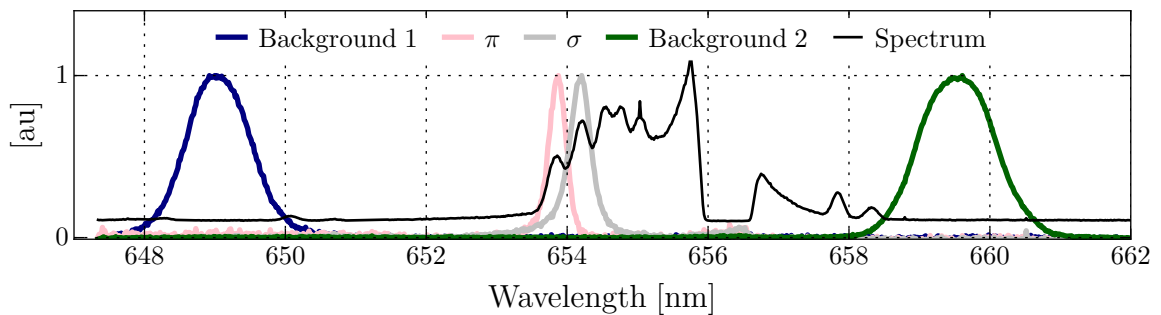


**Figure 4.11:** Intensity of the MSE spectrum and transmissivity of the filters ( $\pi$ ,  $\sigma$  and  $2 \times$  background).

For the first tests, it was installed on the second usable column of MSE views from the centre, where the neutral beam is weak and background emissions relatively strong.

The spectral position of the filters is visualised in figure 4.11. The transmission function of the background filters is significantly wider than the ones measuring  $\pi$  and  $\sigma$  as they receive much less light. Their wavelength should be chosen such that it avoids spectral lines as they violate the assumption of a uniform background. Currently this is only valid for the lower background filter (649 nm) under the condition that no significant nitrogen seeding takes place as there are spectral lines of nitrogen at 648 nm and 650 nm.

From the measurements, a set of Stokes components  $S_1$  and  $S_2$  is generated for each of the four spectral positions. The background Stokes components are interpolated to the  $\pi$  and  $\sigma$  wavelengths and subtracted. The result yields the corrected polarisation angle. A preliminary result of this approach is shown in figure 4.12 on the next page. Here, data from a high density discharge are presented ( $n_e \gtrsim 8 \cdot 10^{19} \text{ m}^{-3}$ ). The intensities of the measurements for each wavelength were relatively calibrated using a polarised light source in the MSE view dump, which has a known intensity distribution but identical polarisation across its whole spectrum. The background measurements set a lower limit for the  $\pi$  and  $\sigma$  measurements as depicted in figure 4.12a, indicating that the assumption of a broadband polarised background is appropriate. Subtracting the Stokes vectors and calculating the angle from the result then yields the corrected  $\sigma$ -angles (figure 4.12b). In the example, the correction generated from the background measurements is around  $1^\circ$ , which is significantly less than the approximately  $10^\circ$  error given in the example shown in figure 4.7. However, it has to be noted that while the density was similarly high, the neutral flux density (cf. figure 4.6b) was only a third ( $\sim 1 \cdot 10^{23} \text{ m}^{-2} \text{ s}^{-1}$  in #32427 instead of  $\sim 3 \cdot 10^{23} \text{ m}^{-2} \text{ s}^{-1}$  in #31313), which is also supported by camera images that show a much darker plasma and thus less stray light that could affect the MSE measurements in the first place.

Note that the  $\pi$  measurement was omitted from the correction above since its filter was mistuned and did not probe the correct part of the spectrum. As the polychromator was



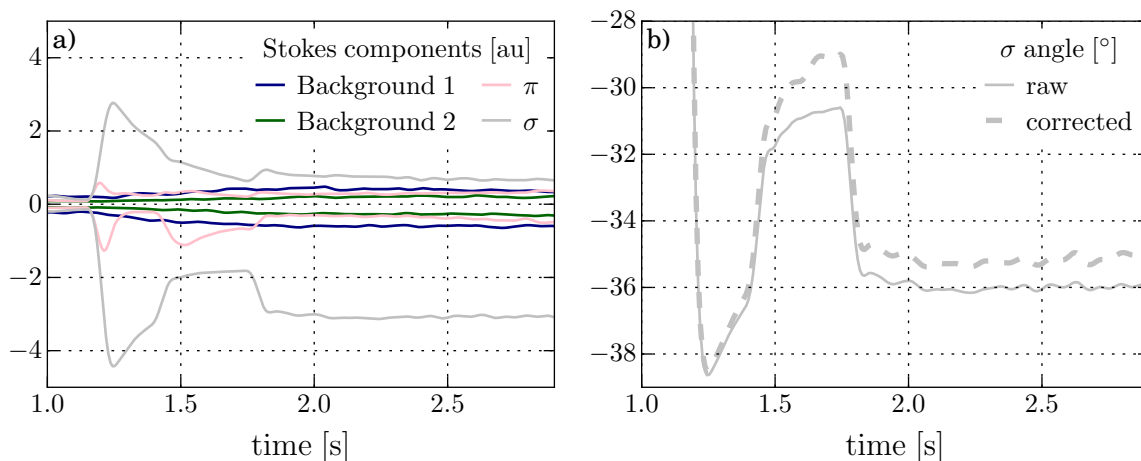


**Figure 4.12:** Stokes components (left, each measurement is split in two traces representing the respective  $S_1$  and  $S_2$ , cf. section 4.1 on page 63) and raw/corrected  $\sigma$ -angle (right) for a high density discharge (#32427).

installed only at the very end of the 2015 deuterium campaign, the mistake could not be corrected in time. A definitive confirmation of this approach’s viability requires both  $\pi$  and  $\sigma$  to ensure that their  $90^\circ$  difference is maintained/restored. Tentatively, however, there is no reason why the positive experiences from C-Mod should not be reproducible on AUG.

The polychromator prototype will be tested further in the 2016 campaign to determine how AUG’s MSE system should be permanently upgraded for background correction.

### 4.3 Absolute Calibration

In section 4.1 it was mentioned that the measurements are inherently taken in the diagnostic’s coordinate system. They need to be translated into the torus coordinate system. Between the two coordinate systems there is a geometric offset due to the PEMs-polariser-array being able to rotate freely along its optical axis. Furthermore, non-geometric differences can also exist, for example non-linearities introduced by optical components that do not perfectly conserve the polarisation.

Without loss of generality, this explanation will use the  $\pi$  measurement. Here, the polarisation is parallel to  $\vec{E}$ , i.e. the MSE effectively measures the projection of  $\vec{E}$  into its coordinate system, which is spanned by two orthogonal vectors  $\vec{x}$  and  $\vec{y}$  (cf. figure 4.13). These  $\vec{x}$  and  $\vec{y}$  are distinct for every line of sight and have been chosen to share a common absolute zero angle. Specifically, for each line of sight  $\vec{s}$ :

$$\begin{aligned}\vec{y} &= \vec{s} \times \vec{u}_\perp \\ \vec{x} &= \vec{s} \times \vec{y}\end{aligned}\tag{4.5}$$

Here,  $\vec{u}_\perp$  is parallel to the six rows of the MSE viewing geometry, i.e. independent of the individual  $\vec{s}$ , which makes it the common “zero polarisation.” With this, the angle in the torus coordinate system is given by:

$$\begin{aligned}\tan \gamma_{\text{torus}} &= \frac{\vec{E} \cdot \vec{y}}{\vec{E} \cdot \vec{x}} \\ \gamma_{\text{torus}} &= \gamma_m - \Delta\gamma_F + \Delta\gamma\end{aligned}\tag{4.6}$$

The Faraday rotation  $\Delta\gamma_F$  in the protective glass is static for a given line of sight at a given magnetic field, so with the characterisation from [94] it can be done analytically. It is also known that a slight non-linearity can be incurred due to a non-perpendicular incidence of the light onto the protective glass. This is known as diattenuation due to Fresnel reflection. Its worst-case magnitude of  $0.03^\circ$  per  $1^\circ$  of change in the input polarisation is, however, well below the MSE’s  $0.2^\circ$  accuracy and will therefore be neglected. Thus, for the remaining  $\Delta\gamma$  a calibration measurement without magnetic field was performed where a known  $\gamma_{\text{torus}}$  was generated and its value subtracted from  $\gamma_m$ :

$$\Delta\gamma = \gamma_{\text{torus}} - \gamma_m\tag{4.7}$$

Note that due to the common zero angle of the coordinate systems, this is a global offset for all lines of sight.

This known polarisation vector  $\vec{E}$  is the result of a diffuse light source being reflected off a glass surface into the MSE lines of sight at the Brewster angle, i.e. such that the light received by the diagnostic is polarised parallel to the cross product of the vectors describing the optical paths of the two legs of the reflected light  $\vec{E} = \vec{s}_{\text{incident}} \times \vec{s}_{\text{reflected}}$  (orange and black in figure 4.13b). The paths were recorded using 3D-FARO measurements with a sub-mm accuracy, allowing an accurate reconstruction of  $\vec{E}$ . Due to time constraints, only 12 lines of sight were analysed this way, with each  $\vec{E}$  being arbitrarily chosen due to technical constraints.

The unexpected result is shown in figure 4.14. Instead of finding a linear relationship between the angle measured by the diagnostic and the angle modelled after the FARO-data with a slope of 1 (dashed line), the points exhibit a slope of 1.25 (solid line). To ensure that this was not caused by a wrong choice of coordinate systems, the measured angles are listed on the right. Even though the plot only includes one data point for every line of sight, the deviation from the expected slope is consistent with all measurements, whether they are taken on adjacent views or views further apart. If the choice of  $\vec{x}$  and  $\vec{y}$  had caused a systematic deviation, then adjacent views would be showing a similar

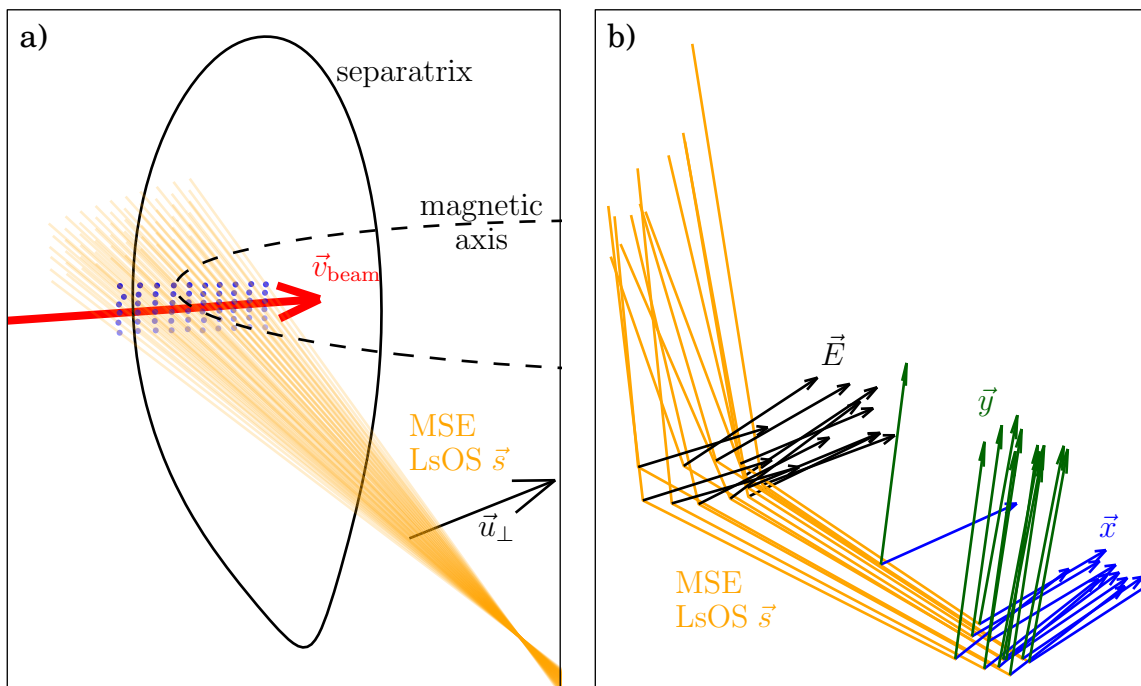


**Figure 4.13:** a) Simplified overview plot of the MSE observation geometry showing the MSE lines of sight  $\vec{s}$ . b) Selected MSE lines of sight  $\vec{s}$ , their coordinate systems  $(\vec{x}, \vec{y})$ , and the known polarisation  $\vec{E}$  generated through reflection under the Brewster angle. Compared to the lines of sight shown in a), the lines of sight shown in b) are interrupted where they intersect the mirror to generate the known polarisation.

deviation. Instead, channels with similar angles are grouped together, indicating that the effect is dominantly dependent on the input polarisation.

The magnitude of this non-linearity is in contradiction to the findings of [94] where only the protective glass was estimated to have a non-linear effect of 2%. This means that either the glass has changed its properties since the characterisation, or that another component in the optical relay system is responsible. For that explanation, two candidates have been identified. The vacuum window might become birefringent when experiencing stress and thus impose a retardation on one polarisation direction. The dielectric mirror, although originally chosen optimally for the wavelength and angle of incidence to retain the light's polarisation, might have aged and become diattenuating or even depolarising. These three physical phenomena, diattenuation, retardance and depolarisation are described using so-called Müller matrices [102], which describe the change of a Stokes vector through interaction with a medium.

To resolve this and obtain their Müller matrices, the components must be removed and analysed. If this is not possible, a  $180^\circ$  scan of the throughput polarisation with a ro-

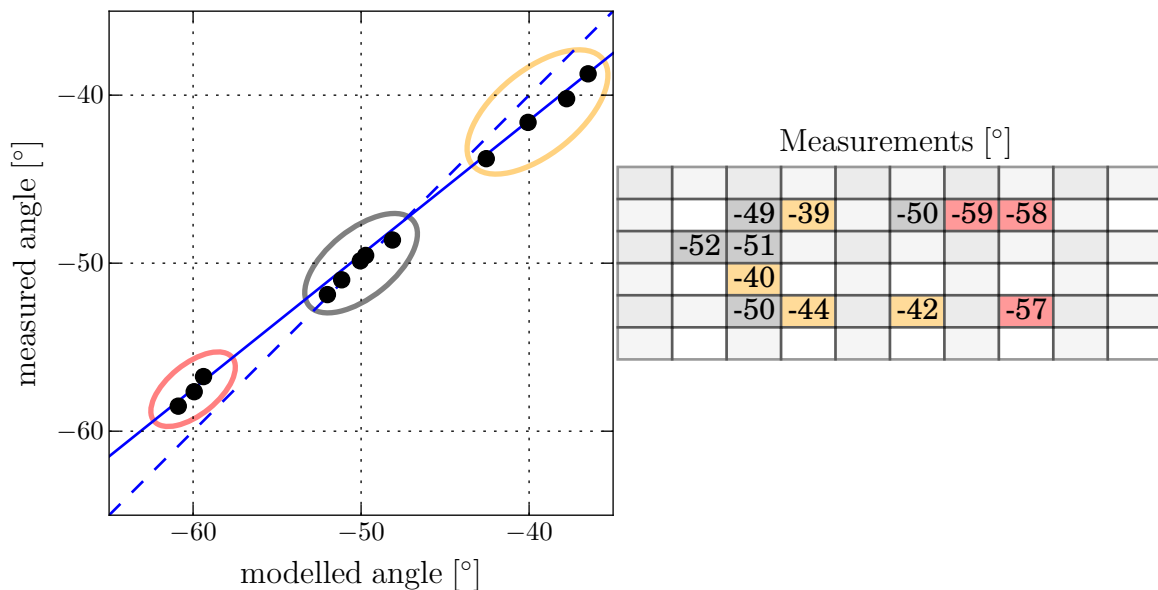


**Figure 4.14:** Plot: comparison between measured angle  $\gamma_m$  and modelled angle  $\gamma_{\text{torus}}$  (corrected by global offset  $\Delta\gamma$ ). Table:  $\gamma_m$  for each of the 12 analysed lines out of all  $6 \times 10$ . Coloured table entries correspond to plotted data points highlighted by an ellipse of the same colour.

tating polariser can be used for an empirical calibration, assuming that the optical components do not change their properties between opening and operating of the tokamak. This assumption is not met for an allegedly stress-sensitive vacuum window, although this could be somewhat corrected by measuring the three polarised light sources placed on the MSE's view dump during the evacuation and monitoring the vacuum window properties.

Due to narrow time constraints, neither the component's analysis, nor the mapping calibration could be completed during the 2015 opening. As a result, no first-principle absolute calibration of the MSE system is available.

However, a measurement taken in 2012 does exist. It is similar to the mapping calibration in that it also was performed using a rotating polariser, but it was not ensured that the polariser was perpendicular to each line of sight. Because of that, it cannot provide the absolute calibration as accurate as desired. This is because when the polariser is not perpendicular to the line of sight, then its rotation will not result in a linear progression of the measured polarisation angle but instead lead to sinusoidal artefacts similar to the ones found here (cf. figure 4.15). Nonetheless, it still gives a rough estimate of the systematic error incurred due to the non-linearity.

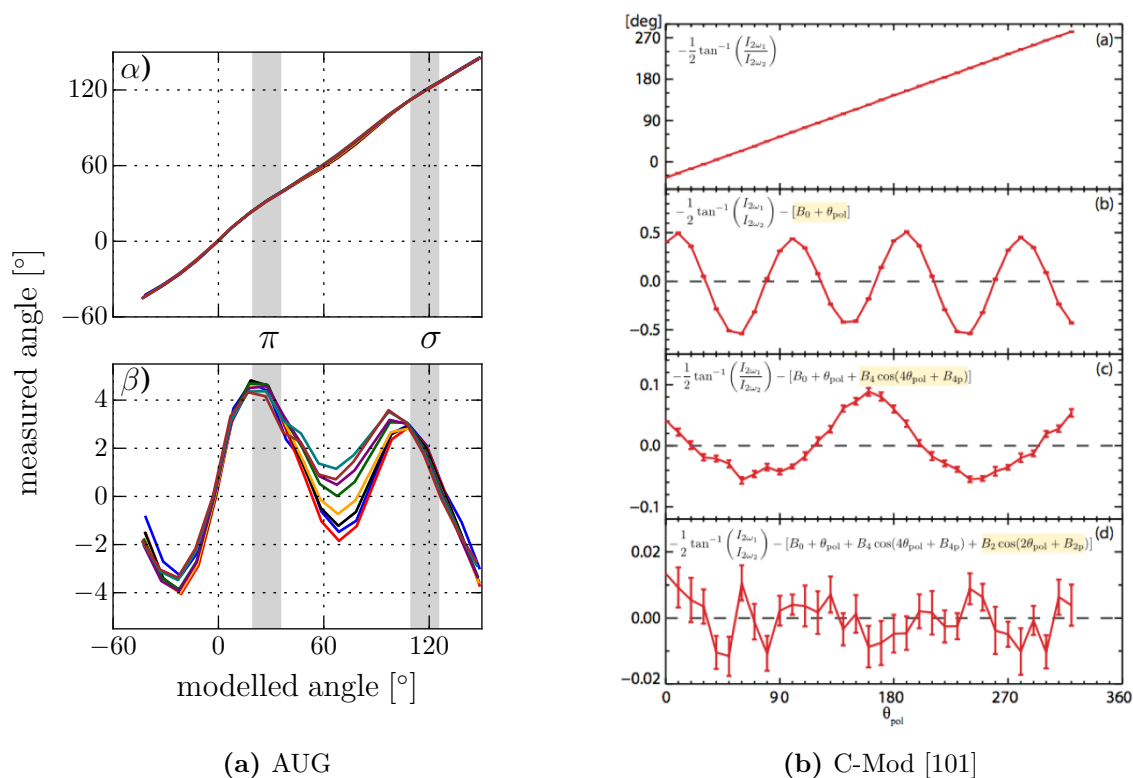


**Figure 4.15:** Non-linearity of the MSE diagnostic on a) ASDEX Upgrade and b) Alcator C-Mod. Shaded regions in a) indicate expected values of  $\pi$  and  $\sigma$ .  $a\alpha$ ) shows the measured angle,  $a\beta$ ) shows the residual of the the measured angle after fitting a straight line through it.

As is seen in figure 4.15a $\beta$ , the non-linearity appears to be up to  $\pm 4^\circ$ , although it must be stressed that part of that range will likely come from the non-perpendicularly aligned polariser. Subplot (b) shows the result of a proper measurement from C-Mod, where the same form of non-linearity has been found, but where it could be narrowed down to  $\pm 0.5^\circ$ . The non-linearity is composed of multiple components that have a  $2\gamma$  and  $4\gamma$  periodicity, originating in polarisation-affecting phenomena in the optical components.

To sum it up, a proper calibration is obtained by:

- Characterising the optical components and modelling the Stokes vector through them.
- Performing an empirical calibration.

Optimally, both approaches should be taken so that the results can be cross-checked.

In the absence of both, the MSE must be calibrated ad-hoc by comparing its measurements to synthetic MSE angles from a well-trusted equilibrium reconstruction, performed for example using localised MHD-markers like sawteeth or NTMs [103]. This does, how-

ever, yield only the absolute offset, but no non-linear corrections. To account for the non-linearity, the curves in figure 4.15a $\beta$  were linearised around the angles of the  $\pi$  and  $\sigma$  measurements. This results in a combined estimated correction factor:

$$\gamma' \approx 1.15 \cdot \gamma_m + \Delta\gamma \quad (4.8)$$

The factor 1.15 is effectively the inverse slope of the curve in the shaded areas of 4.15a $\alpha$ . It must be stressed that this correction is only a rough estimate since it is based on an imperfect measurement. Even with the correction a systematic error remains. If there is a variation of the MSE angles during an experiment of up to  $2^\circ$ , then based on the correction factor of 1.15 the systematic error will be of the order of  $0.3^\circ$ . This error is outside the statistical uncertainty of  $0.2^\circ$ , so it cannot be neglected. Its impact on the equilibrium reconstruction with MSE data is discussed in section 5.2.2.



# 5 Equilibrium Reconstruction

In section 2.1.1 the Grad-Shafranov-equation (GSE) was introduced:

$$-\Delta^*\psi = \mu_0 R^2 p'(\psi) + f f'(\psi) = \mu_0 R j_{\text{tor}}$$

Analytical solutions of the GSE for special cases are known. However, they can generally not be used to reconstruct the magnetic equilibria of experiments. Instead, an iterative approach is necessary to obtain a set of  $\psi$ ,  $p'$  and  $f f'$  that is compatible with the measurements.

## 5.1 General Approach

There are two different ways of approaching the equilibrium reconstruction problem:

**Predictive reconstruction** prescribes the equilibrium quantities.

**Interpretive reconstruction** fits the equilibrium quantities to experimental data.

Unless indicated otherwise, the explanation thereof will be based on [7].

### Predictive Equilibrium Reconstruction

A predictive reconstruction prescribes a set of  $p'$  and  $f f'$ , the axis position, the poloidal field coil currents, total plasma current and vessel geometry. Using the coordinates derived from an initial guess  $\psi = \psi_0$ , the aforementioned quantities are used to generate a new  $\psi$ . The process is repeated with the new  $\psi$ . This is done iteratively until convergence to generate an equilibrium.

The approach can be used to perform a Markov-Chain Monte-Carlo sampling the equilibrium probability distribution by comparing the generated equilibrium to the experimental data to judge its compatibility with the experiment. Due to the high dimensionality of the problem — all quantities listed above would have to be sampled against all experimental inputs — this is prohibitively expensive from a computational point of view and thus only used in rare cases or with reduced complexity.



For this thesis, the predictive approach was explored at first but later abandoned in favour of the faster interpretive equilibrium reconstruction with generalised error propagation to account for uncertainties.

### Interpretive Equilibrium Reconstruction

Interpretive reconstruction describes the process of fitting the fundamental equilibrium quantities to a set of experimental data. This also requires a forward model that is able to derive synthetic measurements akin to the experimental data from the equilibrium fundamentals. This model is represented by a response matrix  $R$ . The goal is to find an equilibrium state vector  $\vec{x}$  that, ideally, yields the experimental data in the measurement vector  $\vec{m}$ :

$$\vec{m} = R\vec{x} \quad (5.1)$$

Here,  $\vec{x}$  describes  $p'(\psi)$ ,  $ff'(\psi)$ , the vertical shift of the plasma  $z_{\text{shift}}$  and the external coil currents  $I_{\text{ext},i}$ . The coil currents and vertical shift are elements of  $\vec{x}$  themselves while the  $p'$ - and  $ff'$ -profiles must be parametrised using basis functions ( $\pi_i(\psi)$ ,  $\phi_j(\psi)$ ) like splines, whose coefficients  $a_i$ ,  $b_j$  become entries in  $\vec{x}$ .

$$\begin{aligned} p'(\psi) &= \sum_i a_i \pi_i(\psi) \\ ff'(\psi) &= \sum_j b_j \phi_j(\psi) \end{aligned} \quad (5.2)$$

The linear model represented by  $R$  links these quantities to the experimental data. For instance, the external magnetic measurements introduced in 3.2.1 directly relate to  $\psi$  at the position of measurement. Another example are measurements of the pressure, which are modelled by discrete integrals over  $p'$ :

$$p(\psi) = \sum_i p_i(\psi) = \sum_i \int_{\psi_{\text{wall}}}^{\psi} p'_i(\psi') d\psi' \quad (5.3)$$

Note that this includes all pressure contributions, i.e. thermal electron and ion pressure as well as fast ion pressure.

An iterative process is necessary to obtain an equilibrium. Starting with an initial guess of  $\psi = \psi_0$  and  $\vec{x} = \vec{x}_0$ , a self-consistent set of  $\vec{x}_0$  and  $\psi$  is generated using Picard iterations [104, 105]. Based on that  $\psi$ , an  $R$  is formulated, which is used in the linear regression to obtain a new, better-suited  $\vec{x}$  by minimising the residual sum of squares  $\chi^2$ :

$$\min \chi^2 = \min \left\{ [(\vec{m} - R\vec{x}) \cdot \vec{\Sigma}^{-1}]^2 \right\} \quad (5.4)$$

Here,  $\chi$  indicates the goodness of fit and should become as small as possible. Ideally,  $\chi$  will become approximately the number of degrees of freedom, so ideally the number of entries in  $\vec{x}$ .  $\vec{\Sigma}$  contains the inverse uncertainties of the data in  $\vec{m}$  (one standard deviation). After the initial cycle, Picard iterations and linear regressions alternate until  $\psi$  converges. The final set of  $\psi$  and  $\vec{x}$  describes the reconstructed equilibrium, while the final synthetic measurements are given by  $\vec{m}' = R\vec{x}$ .

This approach is common in equilibrium reconstruction software (e.g. CLISTE [8], EFIT [106]) and is also used in IDE [107], the software used for this thesis.

The last cycle's response matrix is also used to estimate the errors of  $\vec{x}$  [108] through generalised error propagation of the statistical errors of the input data. This is done by defining the Hessian matrix  $H$  and its inverse, the covariance matrix  $C$ :

$$\begin{aligned} H &= R^T \vec{\Sigma} R \\ C &= H^{-1} \end{aligned} \tag{5.5}$$

As the reconstruction is based on linear regression, the uncertainties (one standard deviation) are given by:

$$\sigma_x = \sqrt{(R\vec{x})^T C (R\vec{x})} \tag{5.6}$$

Here,  $\vec{x}$  can be any equilibrium quantity like  $p(\psi)$ , but also derived quantities. Note that this is only valid for linear relationships, so, for example, the asymmetric uncertainties of the  $q$ -profile must be evaluated for its inverse  $\iota/2\pi$ , the rotational transform, and then converted back to  $q$ .

Not all quantities that are used in  $R$  to generate an equilibrium are welcome in the error estimation. In general, the reconstruction is under-determined: there exists sufficient information at the plasma edge and beyond, but few diagnostics provide information on the bulk magnetic equilibrium. Those that do are usually not able to work routinely. As a result, to facilitate convergence, non-experimental quantities that serve as heuristics are added to  $\vec{m}$  and  $R$ .

These include regularisation in the form of curvature and amplitude constraints. Here,  $\vec{m}$  is extended with entries  $\vec{m}_{\text{reg}} = 0$  (i.e. bias towards smooth, flat profiles), whose weights  $\vec{\Sigma}_{\text{reg}}$  determine their impact on the reconstruction. To some extent, these regularisation entries can be justified physically: for one thing, pressure and current profiles cannot be arbitrarily steep, i.e. smooth profiles are more likely than jagged ones. For another thing, entropic arguments can be used to justify that flat profiles are more likely than steep ones. In any case, even if reasonable, regularisation still isn't based on experimental data or, strictly speaking, physical models. While useful in the reconstruction itself, if regularisation is also considered in the error propagation, it results in a seemingly accurate reconstruction when the real, experimentally derived error bars are actually large.

To reduce the influence of regularisation, IDE makes use of a current diffusion model [107]. While the reconstruction technique sketched above is independent of time, IDE uses the current distribution of the previous time point's equilibrium at  $t = t_{n-1}$  to guide its reconstruction of the equilibrium at  $t = t_n$ . Specifically, the toroidal current density at  $t = t_n$  is added as an entry in  $\vec{m}$  after diffusing the current density/poloidal flux as prescribed by the current/flux diffusion equation (CDE) [9, 109]:

$$\sigma_{\parallel} \frac{\partial \psi}{\partial t} = \frac{R_0 J^2}{\mu_0 \rho_{\text{tor}}} \frac{\partial}{\partial \rho_{\text{tor}}} \left( \frac{G_2}{J} \frac{\partial \psi}{\partial \rho_{\text{tor}}} \right) - \frac{V'}{2\pi \rho_{\text{tor}}} (j_{\text{bs}} + j_{\text{CD}}) \quad (5.7)$$

Here,  $\sigma_{\parallel}$  is the parallel conductivity,  $J$  describes the effect of poloidal currents,  $G_2$  and  $V'$  describe the geometry of a flux surface, while  $j_{\text{bs}}$  and  $j_{\text{CD}} = j_{\text{NBCD}} + j_{\text{ECCD}}$  are the non-inductive contributions to the plasma current density. IDE computes the bootstrap contribution self-consistently using its calculated equilibrium and experimentally obtained kinetic profiles and also generates self-consistent ECCD deposition by using TORBEAM. The neutral beam current drive must be supplied beforehand, e.g. using TRANSP. The current density profile evolved in this manner is used as another constraint on the equilibrium reconstruction, albeit with large error bars to not drown out any possible experimental data.

This allows reducing the regularisation for time points after  $t = t_0$  and thus yielding a more physics-based equilibrium reconstruction and more realistic uncertainties. Still, in the absence of internal information, the current diffusion model also leads to seemingly very accurate reconstructions whose error bars then simply reflect the uncertainties applied to the current diffusion model.

For that reason, all entries in  $R$  corresponding to the current diffusion model are weakened by several orders of magnitude before performing the generalised error propagation, so that the obtained uncertainties reflect the experimental information and not any biases imposed by the model. Note that the regularisation constraints (smoothness, amplitude) are still present, albeit weakened until no effect on the reconstruction is observed any more. At this point it is assumed that the regularisation does no longer distort the actual result, but also not lead to unreasonably large uncertainties due to seemingly limitless gradients.

In summary, the equilibrium reconstruction result itself is guided more by the CDE than the regularisation. In the error estimation, the CDE is not taken into account and the regularisation is weakened to reasonable levels, which are discussed in more detail in the next section.

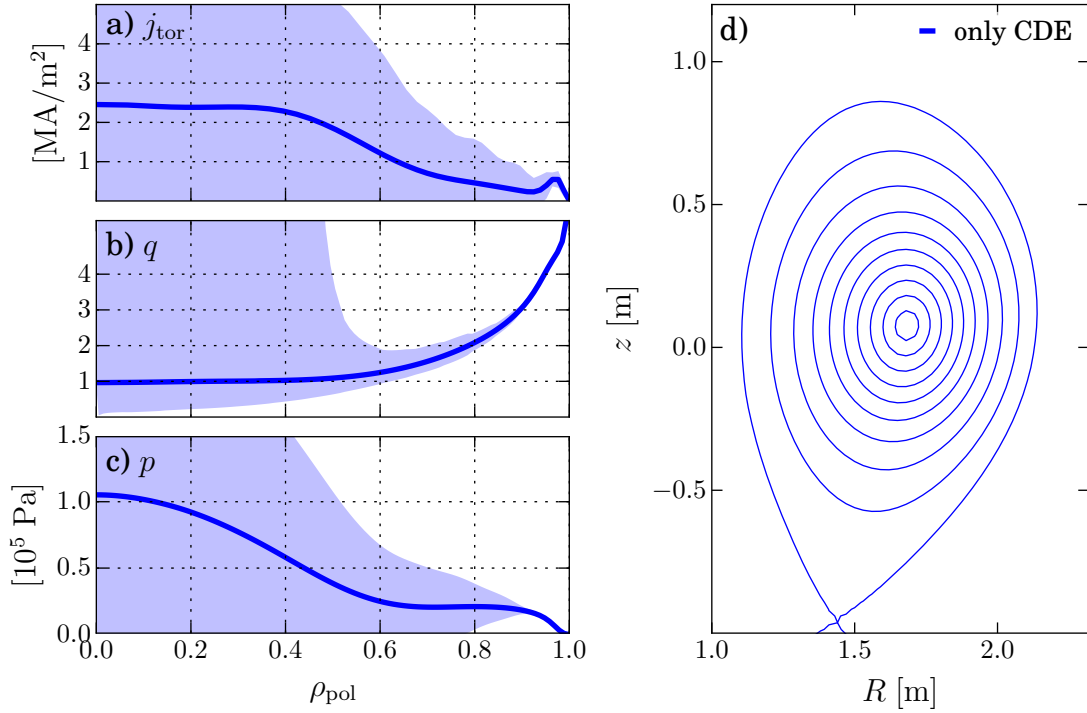


**Figure 5.1:** Left: a) toroidal current density, b)  $q$  and c) pressure profile reconstructed with magnetic data and edge pressure information. Shaded areas indicate one standard deviation of uncertainty. Right: corresponding flux surfaces. (#32232,  $t = 3.0$  s)

## 5.2 Accuracy and Internal Constraints

### 5.2.1 Statistical Errors

Without internal constraints, the error bars of equilibria in the core plasma are very large. This is shown in figure 5.1 for a case with data from external magnetic measurements and edge pressure information. The presence of edge pressure data is immediately evident from the pressure plot, where the uncertainty is small near the edge. The  $q$ -profile, too, is well known near the edge, and becomes progressively less certain towards the core. That is because  $q_{95} \approx (a/R)(B_{\text{tor}}/B_{\text{pol}}) \propto I_{\text{p}}^{-1}$  depends on well-known quantities that become progressively less certain towards the core, especially the enclosed current and thus  $B_{\text{pol}}$ .

Both current density and pressure have large error bars in the plasma core. This doesn't mean that any profile in the shaded areas is valid, but that the shape of the profiles can vary to a large extent as long as the overall integrals are maintained, i.e. total current or total stored energy.

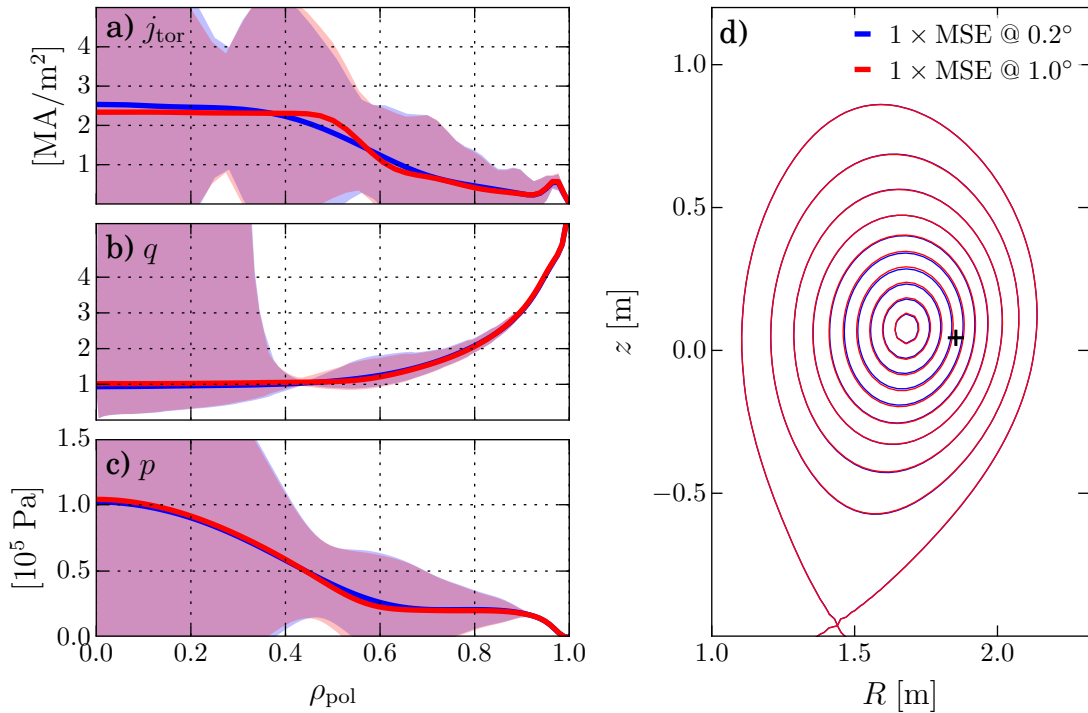


**Figure 5.2:** Same as figure 5.1, but with one MSE channel at the location indicated on the right-hand plot. The MSE data were applied with an uncertainty of  $\sigma_{\text{MSE}} = 0.2^\circ$  and  $\sigma_{\text{MSE}} = 1.0^\circ$  (blue and red, respectively).

$$I_p = \int j_{\text{tor}} \, dA \qquad W = \frac{3}{2} \int p \, dV \qquad (5.8)$$

The effect of a single channel of MSE data from the core is displayed in figure 5.2, with an uncertainty of the MSE data of  $\sigma_{\text{MSE}} = 0.2^\circ$  and  $\sigma_{\text{MSE}} = 1.0^\circ$ . To avoid confusion it has to be stressed that  $\sigma$  here refers to the uncertainty of the MSE data, not the  $\sigma$  component of the MSE spectrum. As discussed in section 4.1, the MSE diagnostic strongly constrains  $B_{\text{pol}}$ , which directly improves the accuracy of the  $q$ -profile through the additional data. The exact radial location of the MSE data can be seen by the contraction in the uncertainty band. Both pressure and current density profile are also less uncertain, although as an integral measurement, one MSE channel alone cannot properly constrain them.

Note that the  $q$ -profile and its uncertainty are virtually identical at  $\sigma_{\text{MSE}} = 0.2^\circ$  and at  $\sigma_{\text{MSE}} = 1.0^\circ$ . In either case it is a very strong constraint for  $q$  and it must therefore be ensured that systematic errors do not affect the measurement as this would have immediate consequences for the reconstruction. A discussion of the influence of systematic MSE errors is given below.

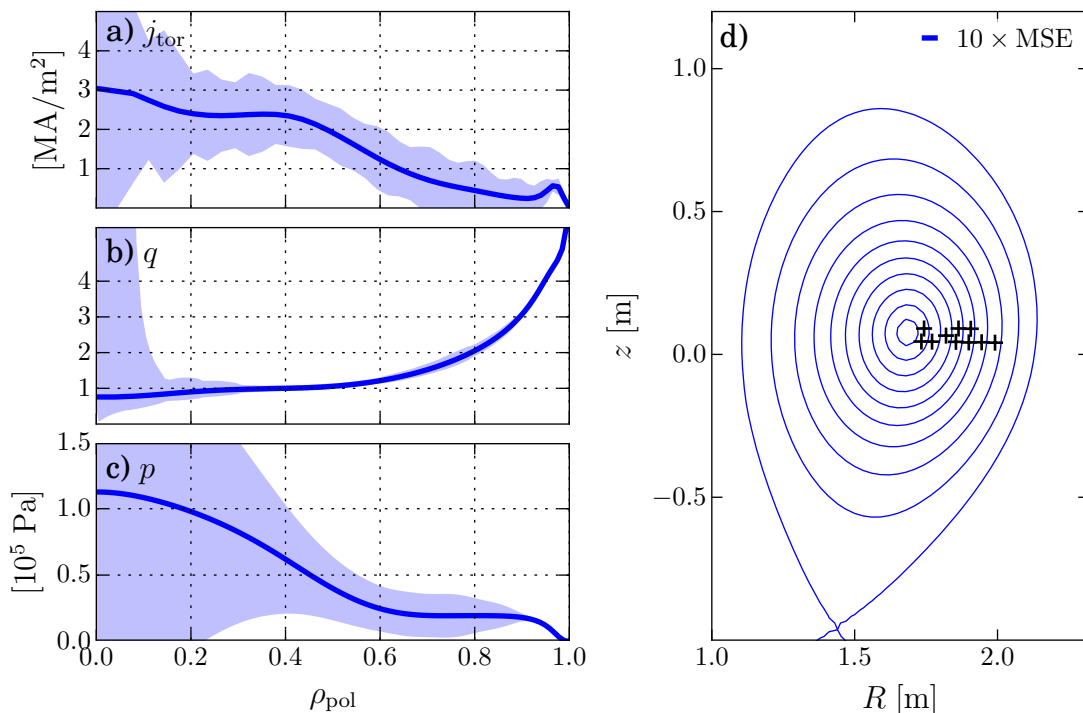


**Figure 5.3:** Same as figure 5.1, but with ten MSE channels at the locations indicated on the right-hand plot.

It should also be noted that DCN polarimetry produces similar results, but is not as radially resolved as MSE as it picks up contributions from several points along its line of sight.

Finally, using a full set of ten MSE channels yields the results shown in figure 5.3. The  $q$ -profile is now well-known along the whole minor radius with the exception of the volume right around the magnetic axis. The various integral current measurements of the MSE also help constrain the toroidal current density much more strongly. Even though a single measurement only yields the total current enclosed by a flux surface, the set of integral measurements combines to constrain the overall current density profile. The pressure profile, however, is still afflicted with large error bars. That is because even if the toroidal current profile is well-known, there still remains some leeway to shift current density between  $p'$  and  $ff'$ . This can be improved by supplying core pressure information, for example using the fast ion pressure calculated by TRANSP on top of the measured kinetic pressure.

As mentioned before, the correct values of regularisation through curvature and amplitude constraints are not clear-cut. In figure 5.4 on the following page the case with ten MSE channels is shown with varying strength of the regularisation. It is immediately clear that the black case with regularisation increased tenfold has little credibility: it suggests that the current and pressure profiles are known with less than about 15% of

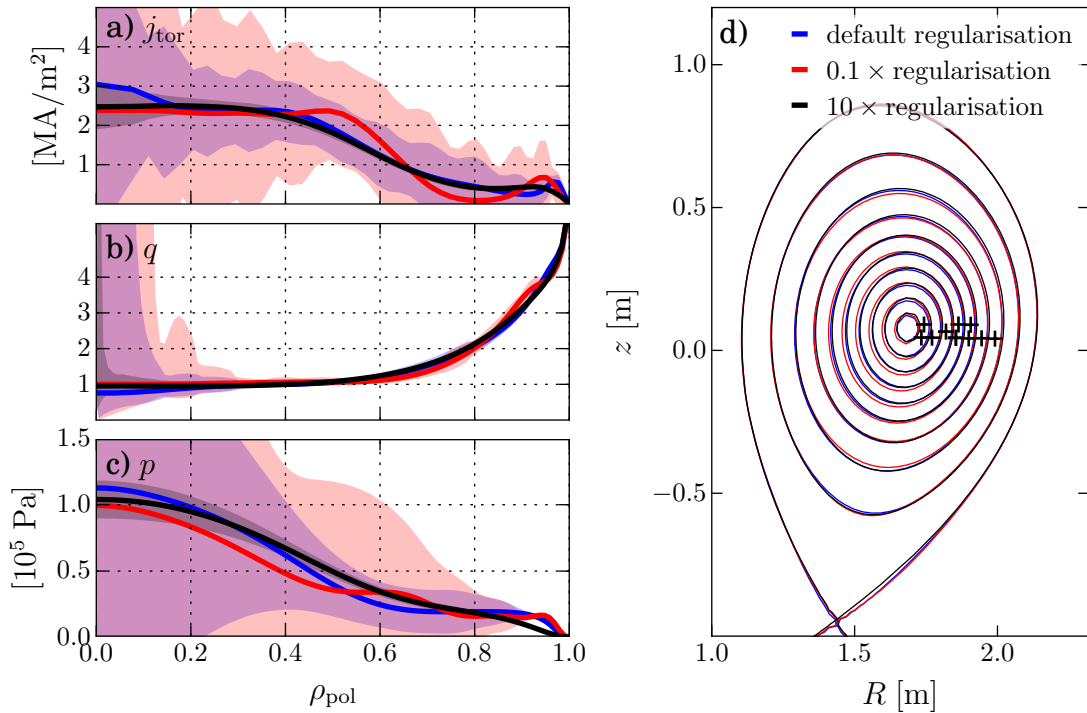


**Figure 5.4:** Same as figure 5.1, but with ten MSE channels at the locations indicated on the right-hand plot and different values of regularisation.

uncertainty on the magnetic axis and virtually no uncertainty outside mid-radius, even though none of the experimentally available information is constraining the equilibrium in that regard.

In contrast, the uncertainties of the red case where regularisation has been weakened by a factor of ten are significantly larger than in the blue reference case with default regularisation. Despite this, the resulting profiles are unchanged inside the uncertainty of the reference case. Only  $j_{\text{tor}}$  approaches the reference uncertainty at  $\rho_{\text{pol}} \approx 0.5$  as it starts oscillating compared to the reference case. The red pressure profile develops a step just outside mid-radius, but otherwise remains very close to the reference case. This step is not supported by any experimental evidence and simply an artefact of the reduced regularisation. In  $q$ , the uncertainties remain unchanged outside of  $\rho_{\text{pol}} \approx 0.3$  and the overall result is largely identical to the reference case — which is to be expected since it is strongly constrained by the MSE information. In summary, despite the profiles now having the option to be an order of magnitude steeper, the changes compared to the blue reference case are small.

Consequently, the regularisation of the blue case has been used for the subsequent analyses of this work. It is a reasonable compromise between artificially reducing the uncertainties towards unrealistic accuracy and increasing them needlessly without affecting the actual result, or even introducing baseless artefacts. It has to be noted that for

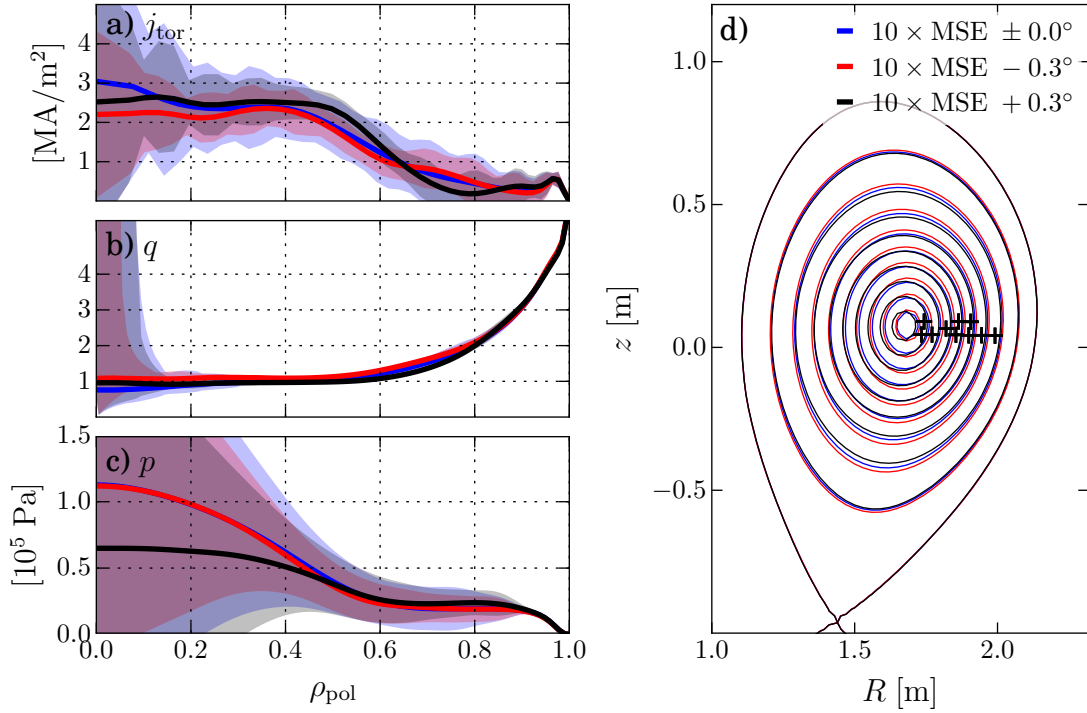


**Figure 5.5:** Same as figure 5.1, but with ten MSE channels shifted by  $\pm 0.3^\circ$  to gauge the impact of systematic errors.

analyses in the next chapter the  $q$ -profile is of main importance and, as shown here, it and its uncertainty does not change much due to the regularisation.

### 5.2.2 Systematic Errors

Systematic errors of the experimental data like e.g. offsets are not covered by the generalised error propagation as it assumes randomly distributed errors. Systematic errors must therefore be analysed on a case-by-case basis.

In section 4.3 the potential systematic error of the MSE diagnostic was estimated to be around  $\pm 0.3^\circ$ . In order to gauge the reliability of equilibrium reconstructions with MSE data, the effect of systematic shifts of said magnitude is investigated.

The results of an example case are displayed in figure 5.5. In the  $q$ -profile the location of, for example, the  $q = 3/2$  surface shifts by  $\Delta\rho \approx 0.1$  across the three cases. Such an offset is sufficient to lead to a failure of pre-emptive NTM-stabilisation as the ECCD deposition would not be directed towards the resonant flux surface. Another difference is that the blue and black case appear to fall below unity and thus would appear to be susceptible to sawteeth, whereas the red case stays slightly above unity.



In the current density profile, the changes are more pronounced. While the red and blue cases match relatively well, the black case differs by more than a standard deviation at mid-radius. In the pressure profiles, red and blue are also indistinguishable, while the black case deviates towards the plasma core. Here, supplying central pressure information may help decide which profile is more likely to be correct.

To summarise, the systematic errors of the MSE diagnostic are able to change the reconstructed  $q$ -profiles in subtle ways. On the one hand that means that the overall shape of the profiles will be correct, e.g. if analysis yields  $q_{\min} \approx 2$ , then it is unlikely that a  $q = 3/2$  surface or surfaces of even lower  $q$  were present. On the other hand, fine details of the profile cannot be resolved beyond any reasonable doubt. For example, the location of rational surfaces may shift by up to  $\Delta\rho \approx \pm 0.05$ . Larger uncertainties of the location occur in areas of low shear  $s \approx 0$ .

In conclusion, the achievable accuracy allows large features of the  $q$ -profile to be resolved reliably, so it can clearly discriminate between conventional scenarios with a monotonic  $q$ -profile ( $q_0 \approx 1$ ) and hybrid/advanced scenarios with  $1 < q_{\min} < 2$  and/or centrally reversed  $q$ -profiles. At the same time, features that lead to different behaviour in discharges of the same overall type may be too subtle to be accurately resolved with the currently achievable accuracy. Further improvements in the MSE calibration as suggested in section 4.3 as well as expanded DCN polarimetry should improve these capabilities for the next experimental campaign.

# 6 Experimental and Modelling Results

As described before, several physical improvements are expected due to flat/slightly reversed, elevated central  $q$ -profiles. They can be summarised as:

- Improved confinement, i.e.  $H_{98} > 1$ .
- Improved stability, i.e. no sawteeth, no lower-helicity NTMs.
- Increased bootstrap current fraction.

The general approach of all experiments in this work is the same: the  $q$ -profile is manipulated using external current drive from ECRH and NBI such that it becomes elevated and flattened/reversed in the region around the magnetic axis. To maximise current drive efficiency, the experiments were carried out at relatively low density (up to  $6 \cdot 10^{19} \text{ m}^{-3}$  line averaged central density).

For that to be possible, they took place, insofar as possible, shortly after one of the regular boronisations of ASDEX Upgrade. Boronisation refers to the coating of the tokamak's inner walls with boron, which increases the pumping of impurities away from the plasma by the walls [110]. On top of reducing unwanted radiative losses due to the impurities, this also allows operation at lower densities as less deuterium has to be injected to displace the impurities. In addition, the plasma scenario operates with large clearances to the wall to reduce the amount of gas received from wall recycling. Furthermore, to maximise the relative amount of driven current but also not increase  $q_{95}$  too much from reactor-relevant values [111], the discharges were all performed at a plasma current of 800 kA. At reduced current (and thus increased  $q_{95}$ ), the non-inductive contributions to the total current — bootstrap current, ECCD and NBCD — are relatively larger, which amounts to a higher non-inductive current fraction. At the same time, increased  $q_{95}$  will decrease the fusion power [112]. Future advanced reactors with high non-inductive current fraction may operate at a compromise value of  $q_{95} \approx 5$  [46], so the experiments of this thesis at  $I_p \approx 800 \text{ kA}$ ,  $B_{\text{tor}} \approx 2.5 \text{ T}$  (i.e.  $q_{95} \approx 5.3$ ) are relevant to the foreseen scenario.

The resulting  $q$ -profiles are reconstructed using IDE (cf. chapter 5) and all available data, including MSE and DCN polarimetry, thermal pressure data from IDA and modelled fast ion pressure from TRANSP. If the profiles are found to be flat and elevated as desired, then the neutral beam heating power is increased in subsequent experiments to

ensure that  $T_i/T_e$  remains favourable such that the ITG critical temperature gradient is maximised.

Two specific techniques were used to manipulate the  $q$ -profile. One aims to prevent/delay the relaxation of the initially hollow current profile during the ramp-up phase by means of early heating. This is the standard approach for such studies as described in section 2.6 on page 37 [46, 63–66]. The other approach allows the current profile to relax and become monotonic, and then applies external current drive and heating later on. This new approach reduces the dependence on the machine conditions in the start-up phase. The results of the early heating approach are presented in section 6.1. Section 6.2 on page 105 reports on the emergence of an ITB (cf. subsection 2.3.2) induced by narrow on-axis counter-ECCD and its transport modelling with TGLF while section 6.3 on page 114 focuses on the results of broad counter- and co-ECCD discharges with feedback-controlled  $\beta$ .

## 6.1 Early Heating

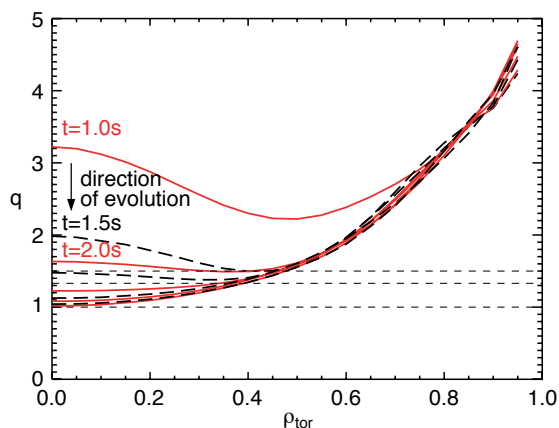


**Figure 6.1:** Evolution of an early heated  $q$ -profile in steps of 0.5 s as shown in [64]. Dashed horizontal lines indicate rational values of  $q$ .

of 1 MA, so it is to be expected that the elevated  $q$  will decay faster at 800 kA.

By heating the electrons early on, the duration of this diffusion is prolonged. Here, it is important to heat the plasma uniformly so that no central temperature peaking arises to prevent current peaking as discussed in section 2.6. In addition to early NBI heating, broad central ECRH/counter-ECCD is employed to delay the relaxation of  $q$  in these experiments.

The early heating scheme exploits the temperature dependence of the resistive timescale  $\tau_R \propto T_e^{3/2}$ . The current induced in the plasma through the ohmic coil must diffuse inwards, so the initial current profile is hollow. This behaviour is fundamentally the same as the skin effect. As a result of the initially hollow core current density, the initial  $q$ -profile is elevated and even reversed towards the magnetic axis. As current diffuses inwards, the central safety factor decreases and its profile takes on the usual monotonic shape. Previous experiments [64] suggest that this approach allows maintaining an elevated  $q$ -profile with  $q_{\min} > 1.5$  until at least 2.0 s as shown in figure 6.1. This was done at a plasma current of 1 MA, so it is to be expected that the elevated  $q$  will decay faster at 800 kA.

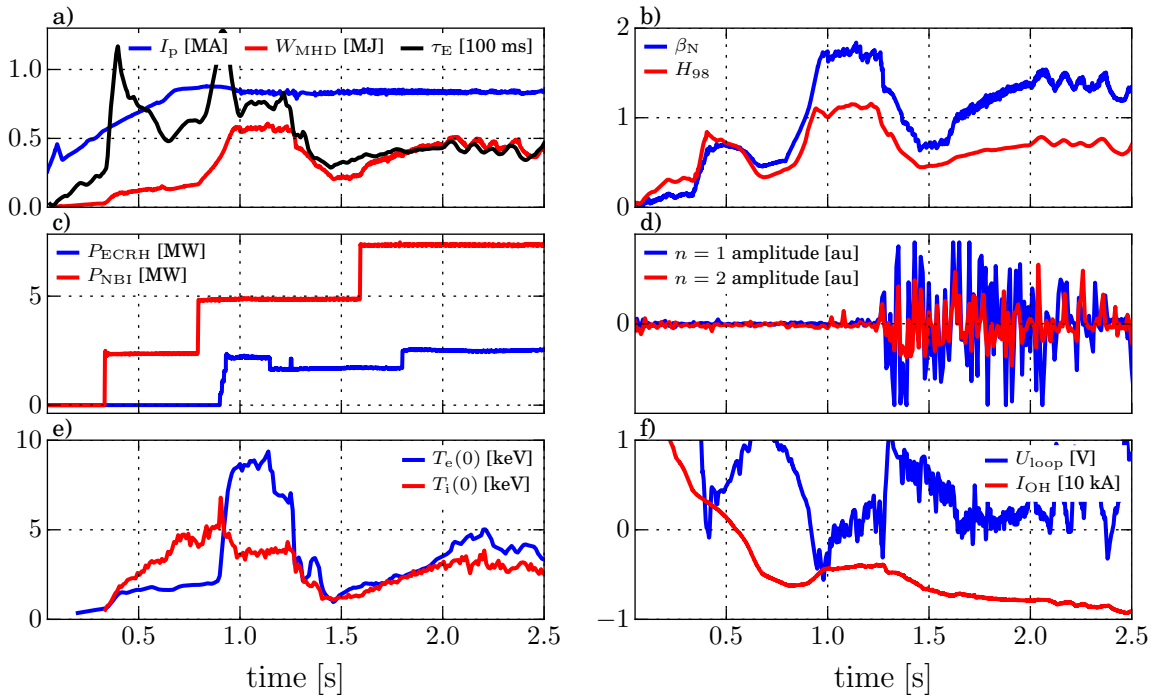


**Figure 6.2:** Temporal evolution of key plasma parameters in discharge #31163.

### 6.1.1 Starting Point

Figure 6.2 shows the temporal evolution of several plasma parameters at the starting point of the early heating scenario development experiments performed for this thesis (#31163). During the ramp-up of the current, the first neutral beam source is turned on at just after 0.3 s. Another source is added 500 ms later, the central counter ECCD is added after another 100 ms. As the ECRH is turned on, central  $T_e$  rises from around 2 to around 8 keV. Simultaneously and despite not removing any NBI heating, the central ion temperature falls from almost 6 to around 4 keV. Despite the reduction in ion temperature after 0.9 s, the H-factor remains steady at about 1.1 until a 3,1-NTM emerges at 1.26 s. The mode helicity is determined through phase analysis of magnetic probe data (cf. section 3.2.1).

The simultaneous decrease of the ion temperature as the electron temperature rises at about 900 ms is in line with the ITG mode's critical gradient parameter dependence, i.e. increasing  $T_e$  lowers it and thus increases ion heat transport. As such, the improved H-factor results from improved electron confinement while the ions remain comparably cold, which is not the desired outcome for a fusion reactor.

The ECCD deposition during the phase of improved confinement is shown in figure 6.3. It increases steadily from just outside of  $\rho_{\text{pol}} \approx 0.3$  until  $\rho_{\text{pol}} \approx 0.1$ , where the current drive reaches about  $-4 \text{ MA/m}^2$ . Inside 0.1, the current density increases strongly beyond

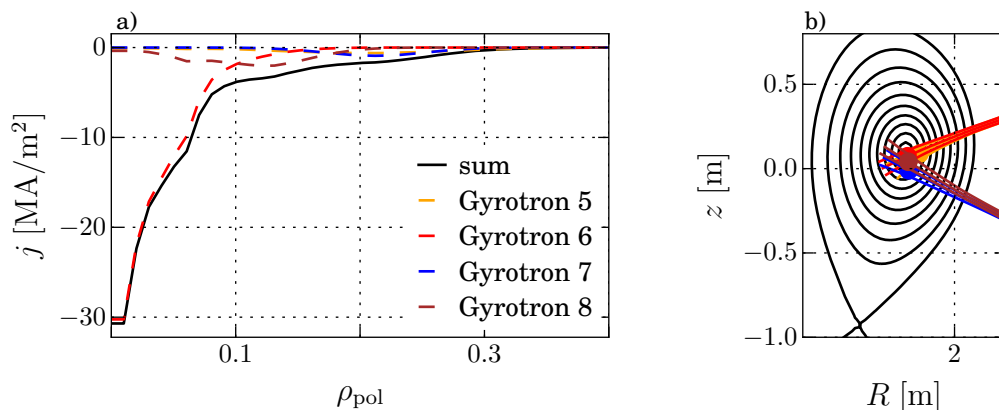


**Figure 6.3:** Current drive deposition through ECRH at 1.25 s in #31163 as calculated by TORBEAM.

$-30 \text{ MA/m}^2$ , which is an order of magnitude higher than the toroidal plasma current density. That means that a very strong reduction of the toroidal current density is to be expected near the axis, which would result in a region of reversed shear in its vicinity. In fact, since the expected toroidal plasma current density will be of the order of  $4 \text{ MA/m}^2$ , one might even expect a current hole to develop. Whether this is possible or not is unclear; results from section 6.2 where a reversed-shear ITB is further outside than expected (i.e. that the shear reversal is further outside than expected) suggest that the plasma current experiences an anomalous outward diffusion that might counteract the excessive counter-ECCD. IDE itself does not allow negative  $j_{\text{tor}}$  as this would make the resulting poloidal magnetic flux ambiguous.

The evolution of  $q$  is shown in figure 6.4.  $q$  is strongly elevated at first and drops slowly towards its usual monotonic shape. With the addition of central counter-ECCD at 0.9 s, the  $q$ -profile becomes more unsteady near the axis, occasionally dipping below unity. An immediate shear reversal near the axis is not observed. In fact, the profile is not particularly elevated nor flattened or reversed. This changes directly after the NTM appears, with  $q_0$  rising within 100 ms to up to 3 before collapsing again. This shear reversal repeats again for several times as the NTM disappears and reappears intermittently during the remainder of the discharge, making a steady state analysis impossible.

During the phase of improved confinement 0.9–1.26 s, the loop voltage (figure 6.2f) becomes negative and then rises slowly back up, suggesting that the discharge required very little inductive current to maintain the total plasma current. The bulk of the non-inductive current must be bootstrap current since two NBI sources and ECCD in the counter-current direction cannot explain the observation on their own. The current in the central transformer (OH current) itself makes this even clearer as it stops dropping and instead increases: from just before 1.0 s until the NTM’s appearance, the transformer

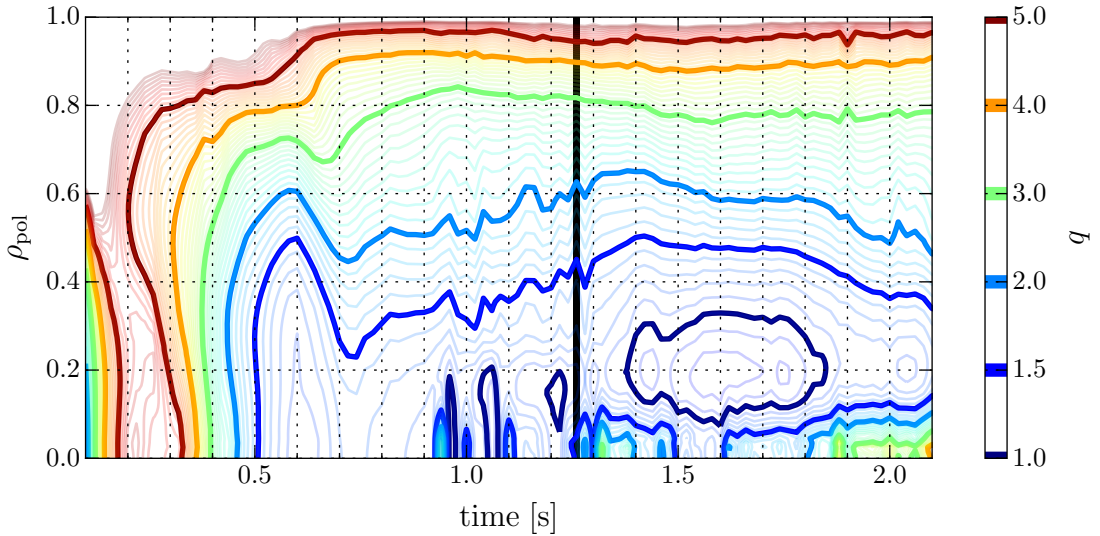


**Figure 6.4:** Contour plot showing the evolution of  $q$ -profile in #31163. Onset of the 3,1-NTM is highlighted by the vertical black bar at 1.26 s.

is not adding current to the plasma, but actually removing it. This is also apparent in the total current, which overshoots before 1 s and is reduced back to 800 kA afterwards. It must, however, be stressed that this 300 ms interval before the NTM — while much longer than the energy confinement time  $\tau_E \approx 50$  ms — is too short compared to the resistive timescale, which is of the order of seconds. The state is transient and a full decoupling from the central solenoid is not observed.

The appearance of a 3,1-NTM is unusual for conventional AUG discharges, where 3,2 and 2,1 are the most common NTM helicities. Its strong deleterious effect on the confinement is consistent with a position near the edge ( $\rho_{\text{pol}} \approx 0.8$  according to the equilibrium reconstruction), where the flattened temperature profile propagates inwards via profile stiffness. The estimated location also matches with a gap in the ECE's channels' location, which is why a localisation with the ECE-magnetics correlation scheme failed (cf. subsection 2.5.2).

This changes between 1.6 s and 1.7 s. During this time, the NTM localisation scheme finds a 2,1-NTM at  $\rho_{\text{pol}} \approx 0.54$ . It moves towards  $\rho_{\text{pol}} \approx 0.48$  by 1.8 s and then quickly towards the axis, vanishing before 1.87 s. The emergence is generally consistent with the reconstructed  $q = 2$  surface, but the ensuing behaviour cannot be properly reproduced by the  $q$ -profile, although the general trend also points towards the  $q = 2$  surface moving inwards. This is caused by an increase in the polarised background which corrupts the inner MSE measurements (see figure 4.6): while the outermost pair of channels maintains its  $90^\circ$  difference between  $\pi$  and  $\sigma$  during the NTM's existence, the innermost suffers a variation of up to  $0.9^\circ$ . This affects the accuracy of the reconstruction, particularly

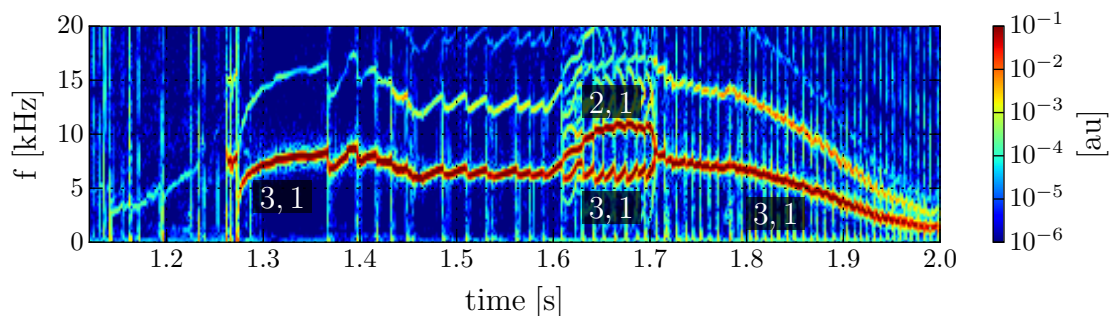


**Figure 6.5:** Spectrogram of a magnetic pickup coil’s signal showing the signature of NTMs. Broadband events in the form of vertical lines are ELMs. (#31163)

further inside the plasma, and explains why the mode’s motion is not properly described by the reconstructed  $q$ -profile.

An explanation for why the 2,1-NTM is not permanently localisable is given by figure 6.5: the 2,1-NTM becomes apparent after 1.6 s. It couples to the 3,1-NTM at 1.7 s seconds but remains localisable until it vanishes at 1.77 s. This coincides with momentary uptick in the mode frequency.

The general consistency between the NTM phenomenology and the reconstructed  $q$ -profile shows that the equilibrium reconstruction is reasonably accurate. This discharge is used as a basis for the development of the scenario. However, open questions remain about the reliability of the reconstruction near the magnetic axis, where the polarised background is stronger in comparison to the actual MSE signal.

### 6.1.2 Iterative Improvements

The development of the early heating scenario continued iteratively. For one, the heating scheme was optimised. In #31163, after the first neutral beam was turned on, the stored energy  $W_{\text{MHD}}$  and electron temperature saturated before the next beam was added, needlessly allowing the hollow current profile to decay without additional bootstrap current that could have compensated the process. Note that one also cannot ramp up the heating power too quickly as this would destabilise the plasma and increase the risk of disruption or, if applied too early when the density is still too low, simply not be absorbed and just heat the tokamak walls. The former was also observed in [64], with reference given therein [113] for more details of how high fast ion density may stabilise ITG turbulence and thus give rise to an ion-ITB (cf. subsection 6.3.2)

With the plasma stored energy and thus  $\beta$  rising earlier, the plasma column approached the outer wall faster, meaning that the feed-forward programmed positioning coil currents

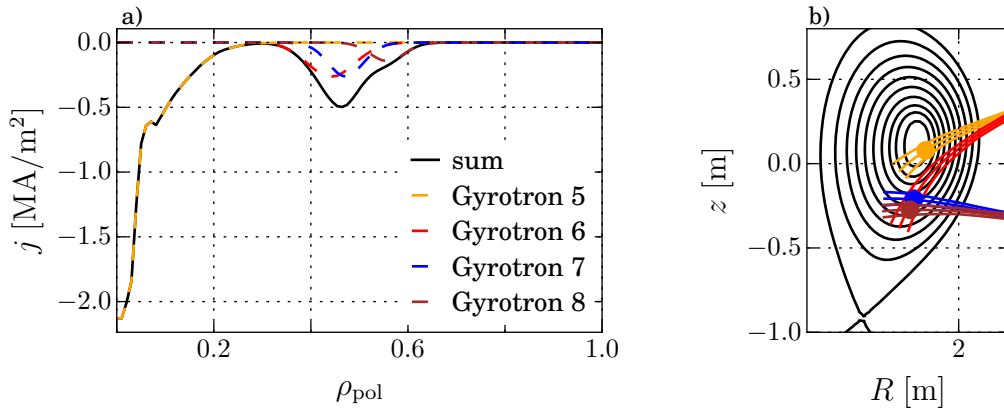


**Figure 6.6:** ECCD deposition in #32342 at 2.16 s.

had to be adapted to prevent the plasma from touching the wall and collecting unwanted impurities.

The faster rise in  $\beta$  lead to phases where ELMs became stable, causing the edge and thus overall density to rise quickly, increasing  $\beta$  even further until large MHD instabilities severely reduced the confinement again. To prevent this, further neutral gas had to be puffed during the ramp-up phase to maintain regular ELM crashes which expel particles and thus permit a lower density. Additional gas puffs will destabilise ELMs, but also lower the edge temperature and thus shift the core temperature profile down as well. A lower amount of gas can suffice to change the shape and height of pedestal temperature profiles just enough to trigger ELMs without negatively affecting the core temperatures noticeably. More details about this process are given in [52].

Experience gained from the late heating experiments that were conducted in parallel were also incorporated in the early heating scheme, particularly the counter-ECCD deposition. It was widened to flatten the  $q$ -profile over a larger radial extent rather than narrowly reverse it and to heat the electrons more uniformly and prevent the unwanted strong temperature peaking as much as possible.

Naturally, the points mentioned here also apply to the late heating experiments, although there the control system can handle most issues automatically via feedback control as the discharge is steadier than in the ramp-up phase where the plasma undergoes large changes in a short time.

### 6.1.3 Latest Result

In the final iteration of the early heating experiments for this work, the ECCD deposition was adjusted to be wider and avoid excessive current drive on axis as displayed in figure



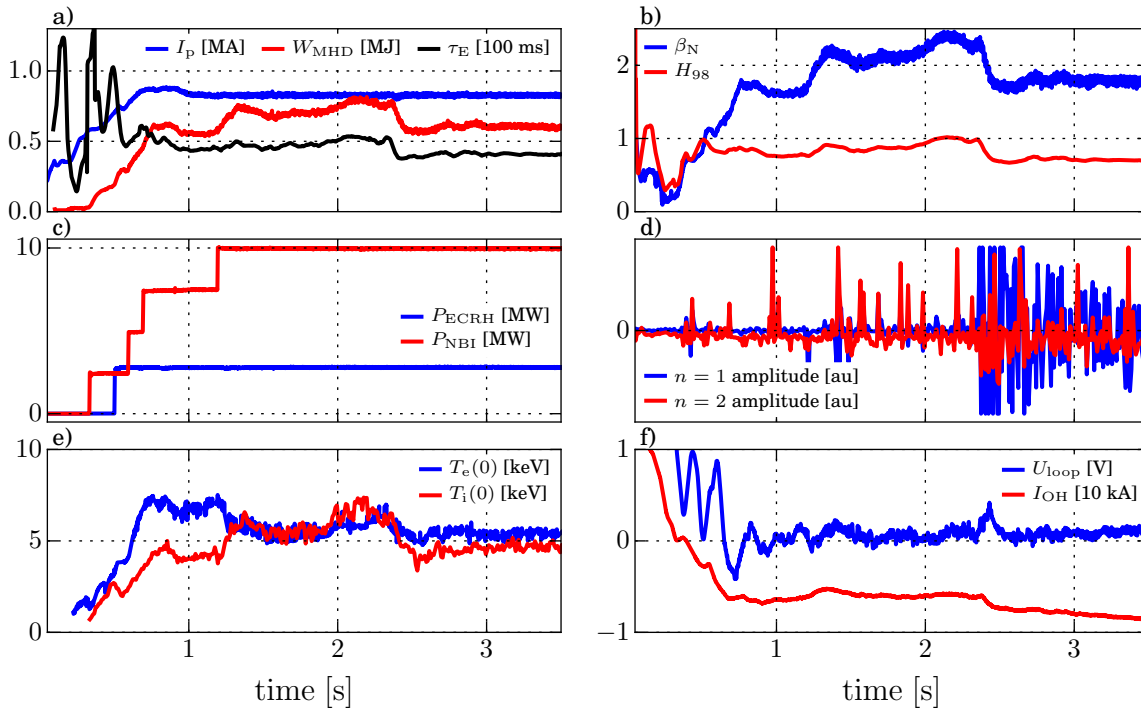


**Figure 6.7:** Temporal evolution of key plasma parameters in discharge #32342.

6.6. The contribution of gyrotron 6 was erroneously placed too far outside due to an unexpected density gradient which deflected the beam away from the centre.

The time evolution of plasma parameters of the latest early heating experiment (#32342) is shown in figure 6.7. Here, three NBI sources and ECRH were added in short succession from 300 ms until 700 ms, which resulted in a steady increase of the stored energy. A fourth NBI source was added at 1.2 s, pushing  $\beta_N$  to about 2.2. After a short drop to 2.0, it recovers and increases towards 2.4 at 2.2 s. A 2,1-NTM ends this phase at 2.3 s. Before its emergence, an interesting development is seen in the OH current: the transformer stops inducing current into the plasma at about 900 ms. From then until the performance degradation due to the NTM, the current in the OH coil remains stable, i.e. the non-inductive contributions from NBCD and bootstrap current suffice to compensate the resistive losses without inductive support. The loop voltage  $U_{\text{loop}}$ , however, is still slightly positive, so one cannot consider this phase to be in a stationary state — even without the NTM it is unlikely to have continued indefinitely (cf. figure 6.25 in subsection 6.3.1).

The individual contributions to the plasma current are shown in figure 6.8, both from IDE and TRANSP. Note that TRANSP is given the full current to place inside the separatrix whereas IDE is able to place currents in the scrape-off layer just outside the separatrix, which explains the slight difference in the total currents when integrating over the area inside the separatrix.  $I_{\text{NBCD}}$  is derived from NUBEAM in both cases.  $I_{\text{ECCD}}$

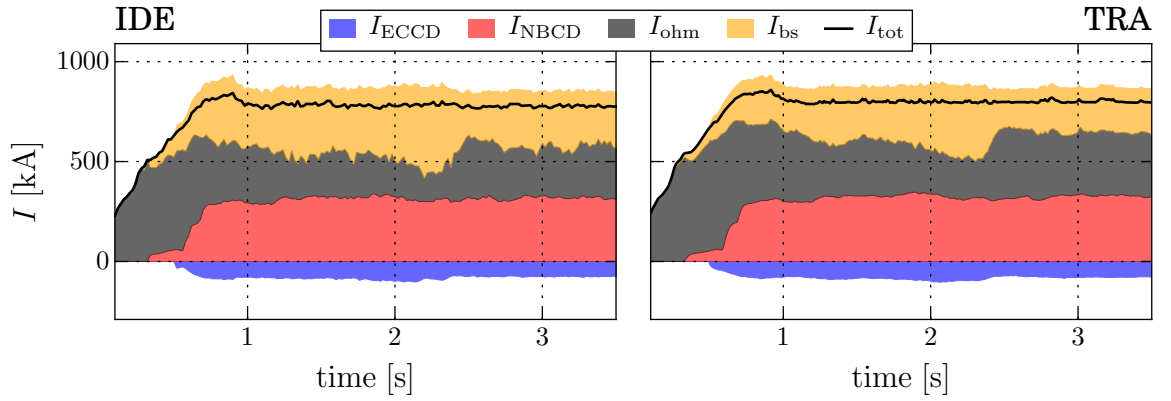


**Figure 6.8:** Composition of plasma current from IDE and TRANSP. (#32342)

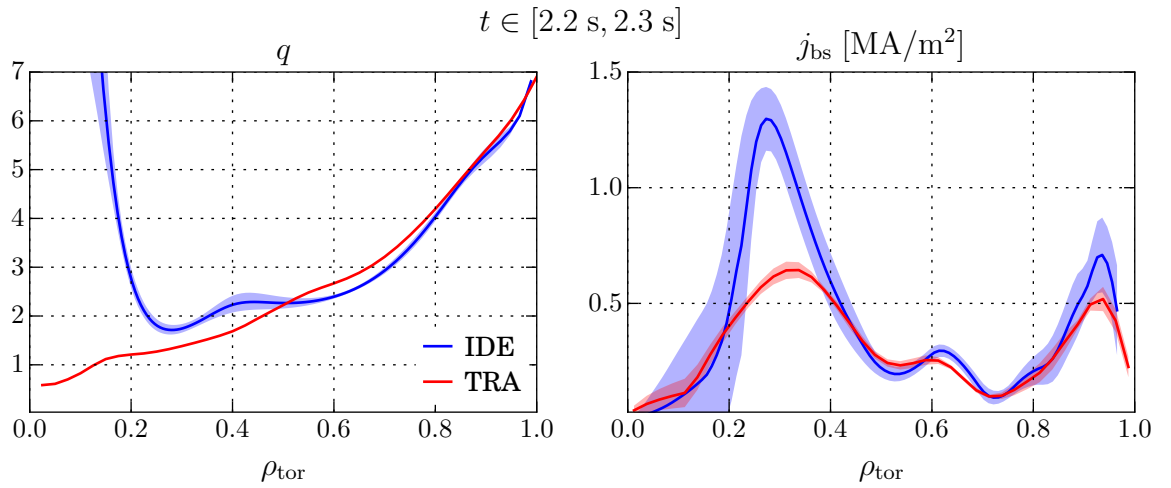


**Figure 6.9:**  $q$  and  $j_{bs}$  from IDE and TRANSP #32342. Solid lines represent averages, shaded areas indicate one standard deviation.

is from TORBEAM in IDE and TORAY in TRANSP; both contributions agree. The remaining current is divided between  $I_{bs}$  and  $I_{ohm}$ , with the latter being simply the total current with all non-inductive contributions subtracted. The general trends of these last two current components are the same in IDE and TRANSP, although the absolute value differs: at around 2.2 s, IDE estimates that  $I_{ohm} \approx 100$  kA, whereas TRANSP's calculations yield about twice as much ohmic current.

This discrepancy is resolved when comparing  $q$  in IDE and TRANSP (figure 6.9). IDE's bootstrap current density is substantially higher for  $0.2 < \rho_{pol} < 0.4$ . This region coincides with  $q_{IDE} > q_{TRANSP}$ , i.e. IDE predicts a lower poloidal field, which increases  $j_{bs}$ . Considering that no sawteeth were observed in the discharge and that IDE has additional information from MSE and DCN polarimetry that TRANSP lacks, one can confidently assess that TRANSP's forward model failed to accurately predict the equilibrium. The

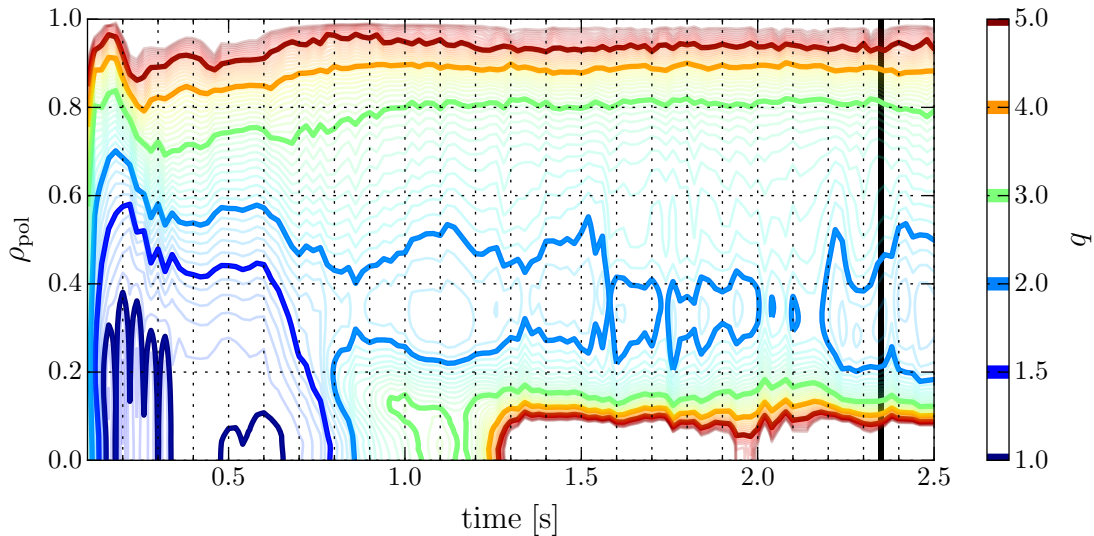


**Figure 6.10:** Contour plot showing the evolution of  $q$ -profile in #32342. Onset of the 2,1-NTM is highlighted by the vertical black bar at 2.35 s.

exact reasons leading to this discrepancy between the forward model and the fit are unclear. Possible reasons include differences in the forward model's starting point but also slight differences between TORBEAM and TORAY: experience gathered with many reconstructions of such equilibria suggests that the emergence of an axial current hole is a strongly non-linear process that causes a bifurcation when the on-axis counter-ECCD exceeds some threshold value. Note, however, that this process is not some kind of artefact unique to IDE, but can also be observed in TRANSP [107].

In any case, the bootstrap current is not sufficiently high to allow the discharge to enter a completely non-inductive regime, although this could possibly be corrected by adding a fifth NBI source and thus increasing  $\beta \propto j_{\text{bs}}$ .

Another aspect of interest is the 2,1-NTM at 2.35 s, which was located at  $\rho_{\text{tor}} \approx 0.6$ , which is in broad agreement with the reconstructed  $q$ -profile in figure 6.10. Two main differences are visible in the figure compared to the result of #31163 (figure 6.4): Firstly, in the very beginning of the discharge,  $q$  is reduced to values below unity very quickly. This is due to an artefact in the early temperature reconstruction from IDA (cf. subsection 3.2.4) that resulted in a peaked  $T_e$  profile that caused excessive inward current diffusion. The profile recovers back above  $q = 1$  as soon as MSE data is present (after 300 ms), i.e. when experimental information trumps the current diffusion model. Secondly, unlike in #31163, as the extra heating power is added,  $q$  increases further to stay above 1.5 and then even reverses after the fourth source is activated. From the fact that  $q$  has to recover back towards a hollow profile it is concluded that the early heating should be even earlier to prevent a current peaking. Since early NBI injection

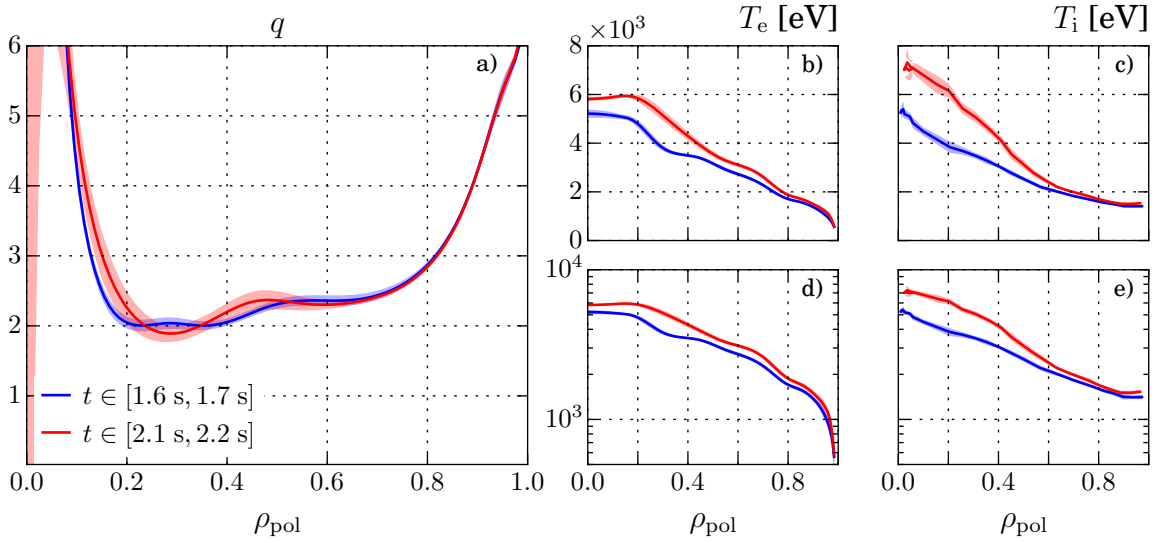


**Figure 6.11:** Safety factor, linear/logarithmic electron and ion temperatures. (#32342)

can be problematic as the thin plasma might not be able to absorb the beam, it could be necessary to begin with a modulated beam that mimics a slow, but earlier ramp-up.

What is peculiar about the NTM is that it emerges after a phase of seeming stability. Despite the external heating remaining constant, the stored energy slowly changes as described above, with the ion temperature in particular rising for no apparent reason at around 1.8 s (see figure 6.7e). This process occurs over several hundred ms, i.e. on a timescale comparable to the resistive timescale. It is therefore prudent to look for an explanation based on the current profile evolution.

The  $q$ -profiles as well as  $T_e$  and  $T_i$  for two time points in the seemingly steady phase are shown in figure 6.11. The ion temperature experiences the biggest change from the first to the second time point, which is very striking in figure 6.11c:  $T_i(0)$  rises from just over 5 keV to about 7 keV. The cause for this increase is best discerned from figure 6.11e: while there is a slight increase of the edge ion temperature, the biggest contribution to the higher core temperature is a steeper slope in the profile for  $0.4 < \rho_{\text{pol}} < 0.6$ . Inside and outside of that region, the slope is flatter, i.e. the critical gradient is increased locally.

This region of locally increased critical gradient matches broadly with a slight shear reversal in figure 6.11a: at the earlier time, the  $q$ -profile has a flattening around  $\rho_{\text{pol}} \approx 0.6$ , which turns into a region of slightly reversed shear for  $0.45 < \rho_{\text{pol}} < 0.6$  later on. Such a shear reversal would delay the onset of ITG modes and thus increase the critical gradient locally as shown in subsection 2.3.3. Note that the potential systematic errors affecting the MSE and thus equilibrium reconstruction do not permit an attribution of this weak

ITB to a change in the  $q$ -profile beyond any doubt. Still, the systematic errors can only cause the absolute values of  $q$  to be inaccurate, not their general trends and shape.

To summarise, the early heating scenario development has progressed steadily. The early heating scheme has to be optimised further to maintain elevated  $q$ -profiles without premature relaxation. Phases of high bootstrap current are reached, although fully non-inductive operation has not yet been possible; higher  $\beta$  may allow such operation. Intermittent phases of improved confinement with  $H_{98} > 1$  were observed, although no steady state has been achieved. The scenario remains susceptible to  $n = 1$  NTMs.

## 6.2 Late Heating with Narrow Counter-ECCD

A more unconventional technique than the early heating discussed in the previous section is the late heating approach. Here, the current profile is allowed to become monotonic before ECCD and NBCD are added to shape the current profile.

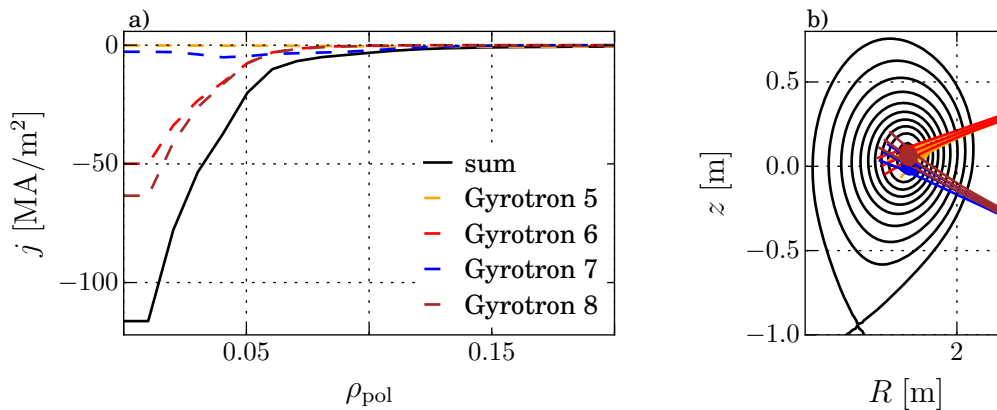


**Figure 6.12:** ECCD deposition in #31113 at 2.95 s.

In an early stage of the late heating scenario development, discharges with strong counter-ECCD on axis were performed. One example is discharge #31113, whose ECCD deposition profile is depicted in figure 6.12.

The temporal evolution of the discharge is plotted in figure 6.13. The first neutral beams are turned on after 1.2 s, with the ECCD being added at 1.5 s. The plasma is allowed to equilibrate until 3.0 s, at which point a third neutral beam is added. Until 3.2 s, confinement is high with  $H_{98} > 1.15$  in the steady phase before 3.0 s and rising to almost 1.4 before a 3,2-NTM undoes the improvement. With the exception of the short phases after NBI sources are turned on, the discharge is steadily consuming flux as its loop voltage is well above 0 and  $I_{\text{OH}}$  decreases steadily. This is in line with the observations reported in section 6.1.3, where even four NBI sources were insufficient to fully decouple the plasma from the ohmic transformer.

The 3,2-NTM is located at  $\rho_{\text{pol}} \approx 0.43$ . This is in agreement with the reconstructed  $q$ -profile shown in figure 6.14, which puts  $q = 1.5$  at  $\rho_{\text{pol}} \approx 0.4$ . According to the  $q$ -profile,  $q_{\text{min}}$  rises above unity just after ECCD is turned on, causing a gradual shear reversal near the axis which becomes stationary at about 2.0 s. From then on,  $q$  remains just above unity  $q_{\text{min}} > 1$  and the central safety factor approaches values of  $q_0 \geq 3$ .

Similar to the observation of section 6.1.3, one can expect improved confinement where  $s < 0$ , which is discussed in the following.

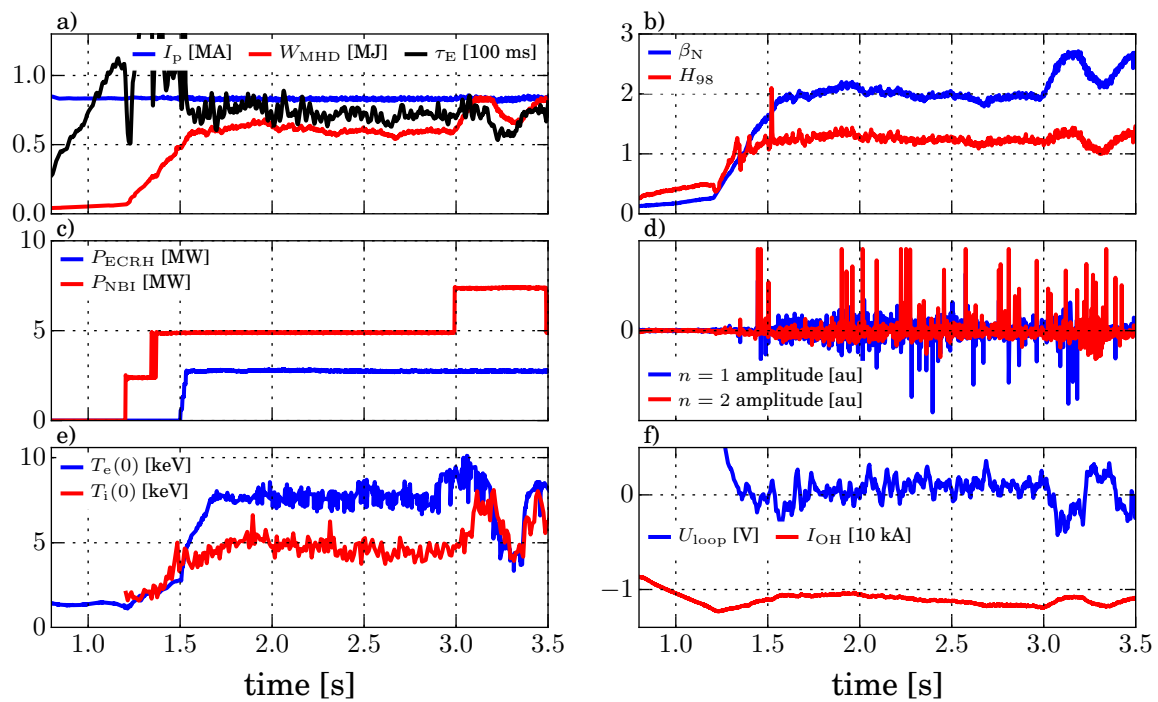


**Figure 6.13:** Temporal evolution of key plasma parameters in discharge #31113.

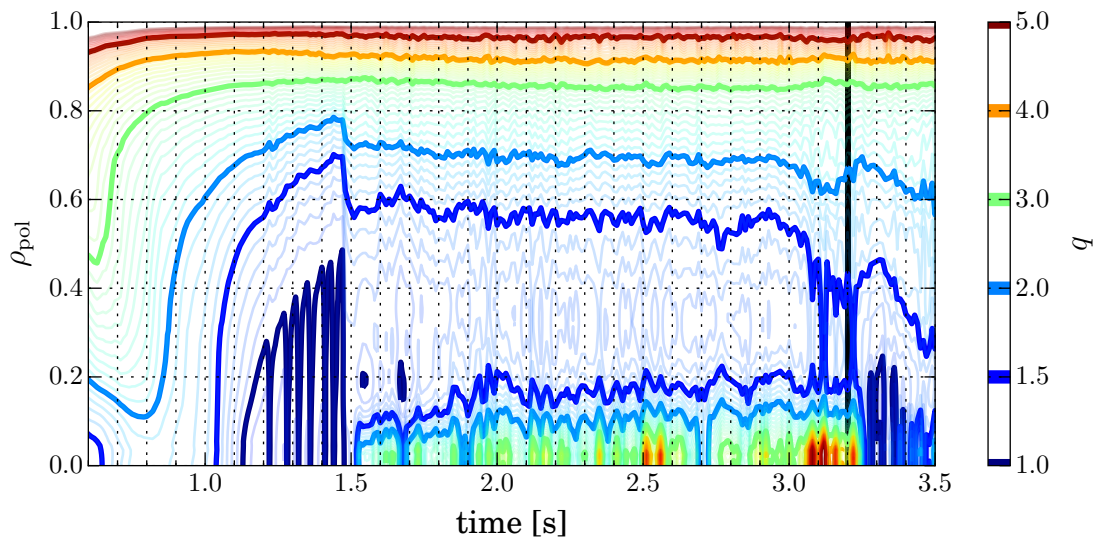


**Figure 6.14:** Contour plot showing the evolution of  $q$ -profile in #31113. Onset of the 3,2-NTM is highlighted by the vertical black bar at 3.2 s.

## 6.2.1 Steady State Internal Transport Barrier

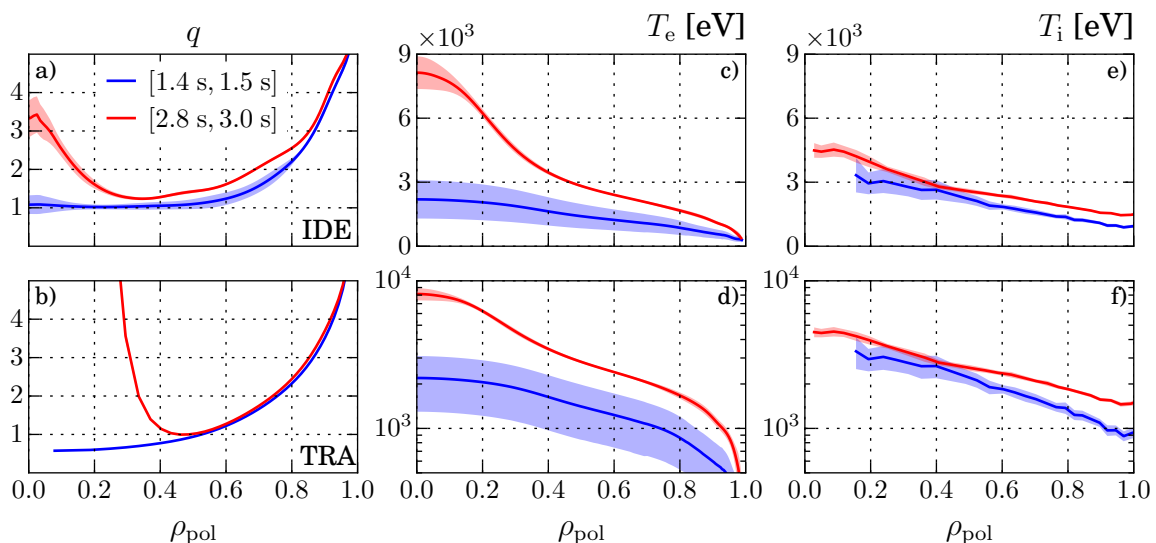


**Figure 6.15:** Safety factor calculated by IDE and TRANSP as well as linear and logarithmic electron and ion temperatures. Displayed are two time points of #31113, one at the start of ECCD (blue), one at the end of the steady state phase (red).

The temperature and  $q$ -profiles of two time points of #31113 are shown in figure 6.15. The curves in blue indicate the state at about 1.5 s, just before ECCD was added. The red curves represent the profiles in the final 200 ms of the steady state phase, from 2.8 s onward. Note that the red case has, at that point, already been stationary for several hundred ms, i.e. much longer than the energy confinement time  $\tau_E \approx 70$  ms. This means that from a transport perspective the plasma is in a steady state.

The addition of ECRH results in a slight increase of the ion temperature, particularly due to a higher edge temperature. From figure 6.15f it is also evident that the ion temperature gradient has decreased in the outer plasma  $\rho_{\text{pol}} > 0.4$  as the slope of the later profile has become flatter compared to the earlier one. This is because the electrons are significantly warmer in the red case, which drives ITG modes. Nonetheless, despite the high electron temperature, a slight increase of the slope is observed inside  $\rho_{\text{pol}} \approx 0.4$ , which points to another phenomenon affecting the transport. Despite being only a slight increase, it is outside the error bars. Without it,  $T_i(0)$  would be approximately 0.7 keV lower.

The electron temperature rises more strongly than the ion temperature ( $T_e(0) \approx 2 \rightarrow 8$  keV). Much of this stems from an increased edge temperature as visible in both figure 6.15c and figure 6.15d. Especially the latter, however, also shows a noticeable increase of the critical electron temperature gradient inside  $\rho_{\text{pol}} \approx 0.4$ .



Both the electron and ion temperature increase inside  $\rho_{\text{pol}} \approx 0.4$  coincide with the reversed shear shown in figures 6.15a and 6.15b. In this case, however, the  $q$ -profile from the TRANSP forward model seems more compatible with the kinetic observations since its region with  $s < 0$  extends inwards from  $\rho_{\text{pol}} \approx 0.5$ , whereas IDE's fit result only exhibits  $s < 0$  inside  $\rho_{\text{pol}} \approx 0.3$ .

Of course, for an authoritative analysis of plasma transport processes one cannot simply choose whichever equilibrium suits the desired outcome the most. In this case, however, the goal is to verify our ability to model transport even in the context of more exotic  $q$ -profiles. Considering that systematic errors affect the reconstruction particularly in the plasma centre, and that high amounts of counter-ECCD near the axis produce unusual equilibria, it is not unreasonable to allow some degree of freedom with respect to the  $q$ -profile as long as it is conducive to the goal of verifying the transport model. This is why in the analysis of the next subsection, the TRANSP  $q$ -profile was used. Even though it already has a wider region of reversed shear compared to IDE's result — which matches better with the observed kinetic profile — it will be seen that the modelling with TGLF is still only successful when shifting  $q_{\text{min}}$  even further outside.

To summarise, the resulting plasma shows a clear reduction of transport inside  $\rho_{\text{pol}} \approx 0.4$ , i.e. an ITB (cf. subsection 2.3.2). Although it affects both ions and electrons, the barrier is most evident in the electrons due to the high electron heating from the central ECRH. The phenomenology is similar to e.g. that of ITBs observed in JT-60U [66], i.e. an ITB caused by reversed shear inside of which confinement is degraded due to a reduced toroidal current density and thus reduced poloidal field. Several other examples with the same trends are summarised in [27].

Later experiments used an optimised ECCD configuration with broader deposition where confinement improvements are, for the most part, not limited to small regions. Still, the emergence of a clear ITB for several energy confinement times makes this discharge a suitable candidate to benchmark TGLF and test its sensitivity to shear-related transport effects. This will be discussed in the following.

### 6.2.2 Transport Modelling with TGLF

Successful modelling of the ITB should result in the simulated profile evolution matching the experimentally measured evolution. This means that in this steady state case the profiles should not change and that the transport coefficients calculated by TGLF match the ones derived from a power balance analysis.

The power balance results for #31113, 2.9 s  $\rightarrow$  3.0 s are shown in figure 6.16. It uses the experimentally obtained temperature profiles to derive  $\nabla T$  and has power deposition profiles for the NBI from TRANSP/NUBEAM and for ECRH from TORBEAM. Power radiated from the inside of the plasma is also taken into account using radiation profiles obtained via tomographic reconstruction of bolometric radiation measurements [114].

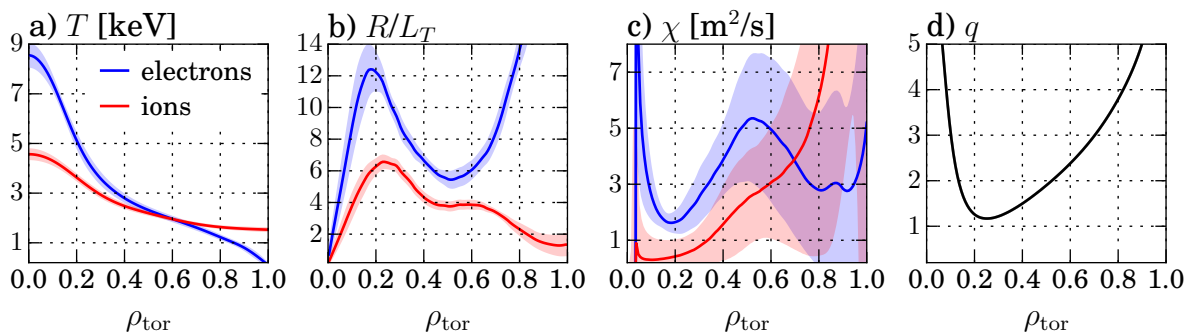


**Figure 6.16:** Results of an ASTRA power balance analysis, showing a) the electron/ion temperature, b) the normalised temperature gradients, c) the respective heat diffusion coefficients and d) the safety factor profile. Solid lines represent an average over the indicated time interval, shaded areas represent one standard deviation around the average. (#31113,  $t \in [2.9 \text{ s}, 3.0 \text{ s}]$ )

The average  $q$ -profile reconstructed for this time interval is shown in figure 6.16d for reference, but it is not used in the actual power balance analysis since it is not required to interpret the experimental profiles (cf. subsection 2.3.4 on page 29).

The normalised ion temperature gradient  $R/L_{T_i}$  in particular shows an increase inside of  $\rho_{\text{tor}} \approx 0.4$  compared to the flat trend just outside that location.  $R/L_{T_e}$  has a minimum at  $\rho_{\text{tor}} \approx 0.5$  and increases more strongly, peaking at  $R/L_{T_e} > 12$  at  $\rho_{\text{tor}} \approx 0.2$ . This is also reflected in the thermal diffusivities in figure 6.16c:  $\chi_i$  and  $\chi_e$  at  $\rho_{\text{tor}} \approx 0.2$  are less than half compared to their values at mid-radius. As such this observation also satisfies another definition of an ITB, namely a local reduction in the diffusion coefficients. It is striking, however, that the  $q$ -profile only reverses inside of  $\rho_{\text{tor}} \approx 0.25$ , i.e. well inside the region of improved confinement. This suggests that either there is a more complex explanation for the ITB or that the real  $q$ -profile has  $q_{\text{min}}$  further outside.

The TGLF simulations were performed with the experimental temperature profiles serving as boundary conditions at  $\rho_{\text{tor}} = 0.8$ , starting at 2.0 s until 3.0 s and using the initial temperature profiles as start values. Subsequent temperature profiles are the result of evolving the initial profiles using the transport coefficients calculated by TGLF. Throughout the time interval, the  $q$ -profile is kept constant. The density profile is taken from the experiment, i.e. electron density and ion density calculated using  $Z_{\text{eff}}$  from charge exchange measurements ( $Z_{\text{eff}} \approx 1.2$  for all analysed discharges), which also provided plasma rotation profiles. The latter are used to generate the radial electric field's main contribution  $\vec{v}_{\text{tor}} \times \vec{B}_{\text{pol}}$ . Fast ion densities are taken from TRANSP. In the following, the stationary results of the simulations are discussed using the profiles after 2.9 s.

At first, only the electron temperature profile was evolved. The results are summarised in figure 6.17. The final temperature profile in figure 6.17a indicates that the simulation

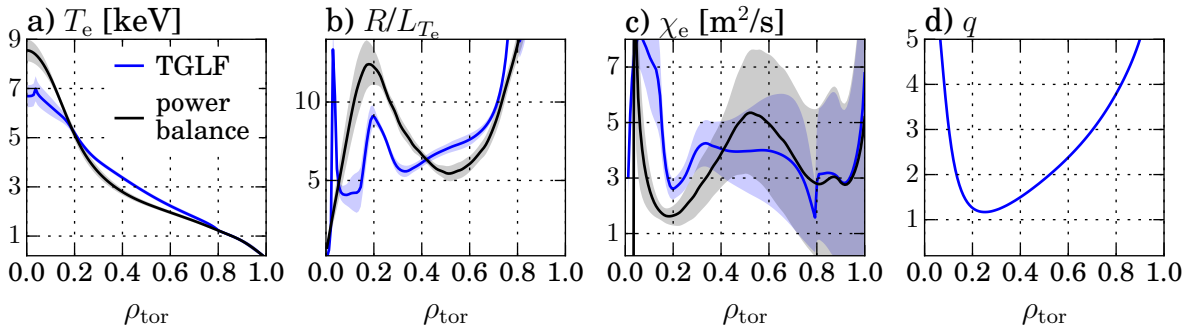


**Figure 6.17:** Evolution of electron temperature profile with TGLF (blue) compared to power balance (black). Individual subplots show same quantities as figure 6.16. (#31113,  $t \in [2.9 \text{ s}, 3.0 \text{ s}]$ )

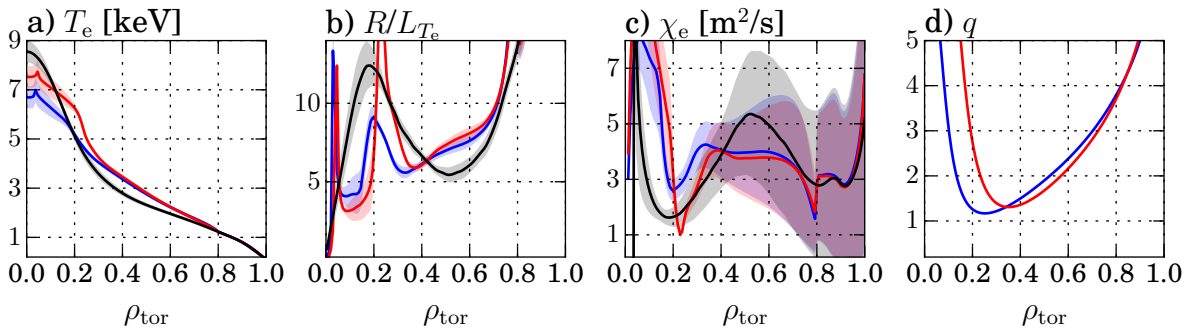


**Figure 6.18:** Evolution of electron temperature profile with TGLF with the original  $q$ -profile (blue) and with a shifted  $q$ -profile (red). Power balance results (black) are shown for comparison. Individual subplots show same quantities as figure 6.16. (#31113,  $t \in [2.9 \text{ s}, 3.0 \text{ s}]$ )

does not capture the transport barrier completely, although the normalised temperature gradient in figure 6.17b does show an increase at the expected location. This increase is, however, neither as pronounced nor as wide as necessary to reproduce the experimental results. The reason for this is the simulated transport coefficient shown in figure 6.17c: while it is slightly lower than the power balance result for  $\rho_{\text{tor}} > 0.4$ , it is also higher by a similar amount for  $\rho_{\text{tor}} < 0.4$ . The power balance estimates  $\chi_e < 2 \text{ m}^2\text{s}^{-1}$  at  $\rho_{\text{tor}} \approx 0.2$ , whereas TGLF calculates  $\chi_e \approx 2.8 \text{ m}^2\text{s}^{-1}$ . Moreover, the power balance estimates a reduction in  $\chi_e$  over a larger extent of the minor radius, i.e.  $0.1 \lesssim \rho_{\text{tor}} \lesssim 0.4$  — in contrast, TGLF’s noticeable reduction is limited to  $0.15 \lesssim \rho_{\text{tor}} \lesssim 0.3$ . This coincides with the onset of the negative shear since  $\rho_{\text{tor}}(q_{\text{min}}) \approx 0.25$ , so it the result may be caused by an incorrectly reconstructed  $q$ -profile.

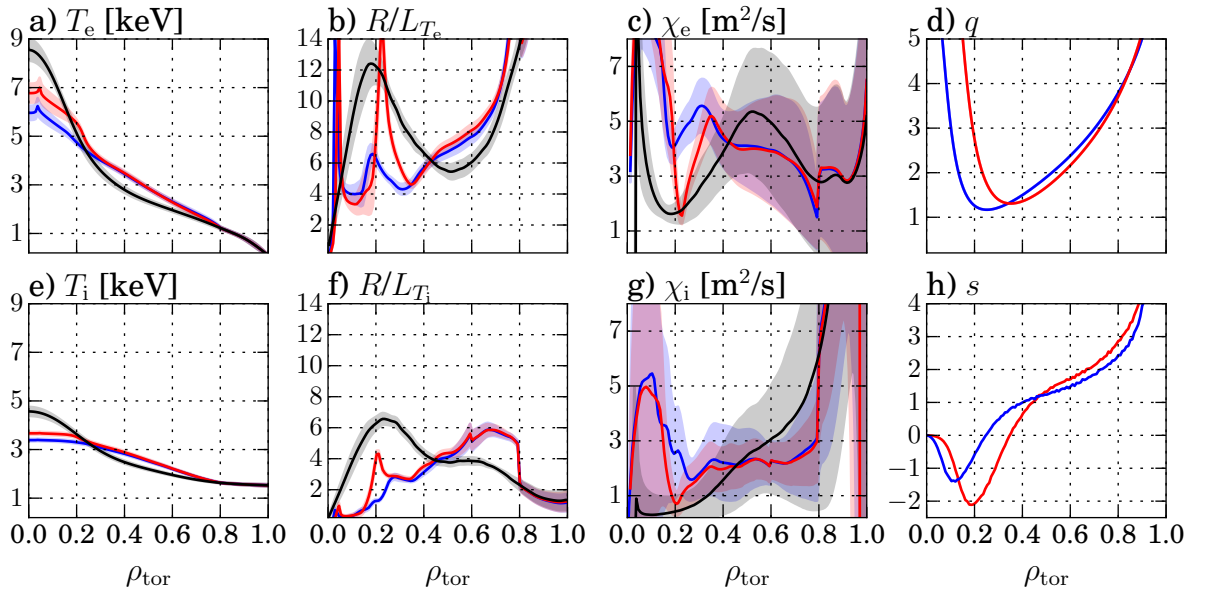


**Figure 6.19:** Evolution of electron/ion temperature profile with TGLF with the original  $q$ -profile (blue) and with a shifted  $q$ -profile (red). Power balance results (black) are shown for comparison. Individual subplots show same quantities as figure 6.16. (#31113,  $t \in [2.9 \text{ s}, 3.0 \text{ s}]$ )

In order to verify whether an inaccurate  $q$ -profile may be responsible for the result, an artificially shifted  $q$ -profile was used for an otherwise unchanged simulation. Its results are illustrated in figure 6.18. The shifted  $q$ -profile has its minimum further outside  $\rho_{\text{tor}}(q_{\text{min}}) \approx 0.25 \rightarrow 0.35$ , which is reflected in the newly obtained profiles:  $\chi_e$  in figure 6.18c now agrees well with the power balance analysis for  $0.2 \lesssim \rho_{\text{tor}} \lesssim 0.4$ , although it is still too low further outside and too high further inside. As a result,  $R/L_{T_e}$  is now significantly higher in the region of interest, although its radial extent has not increased significantly; the temperature gradient drops strongly inside  $\rho_{\text{tor}} \approx 0.2$ . Nonetheless, the resulting temperature profile in figure 6.18a is close to the experimentally obtained profile, reaching 7.5 keV at the axis compared to the experimental value of 8.5 keV. While the simulation matches the experimental values qualitatively, there still remain quantitative differences: the computed transport barrier is located further outside than the experimentally observed one, the peak of the profile is flatter and the outside of the profile is generally warmer than in the experiment. This leads to an artefact at the boundary since the heat flux inside of it must match the heat flux outside of it: since  $\nabla T_e$  is slightly higher,  $\chi_e$  is reduced to match the boundary heat flux.

In this discharge, a lot of axial electron heating was applied which made the ITB most noticeable in the electrons. This is why the initial simulations focussed on the electron temperature profile. As the fusion power depends on the ion temperature, it, too, must be properly simulated.

The result of the combined electron/ion temperature evolution with TGLF is shown in figure 6.19. The former is fundamentally the same as the previously described behaviour when only simulating electron heat transport, although the overall confinement is worse as the ITB's effect is less pronounced. This reduces the axial electron temperature by about 500 eV compared to the pure electron case. Outside the ITB, electron heat transport largely occurs as before.

The ion temperature profiles in figure 6.19e with original and shifted  $q$ -profile are very similar and only exhibit a noticeable albeit still small difference inside of  $\rho_{\text{tor}} \approx 0.3$ .  $T_i(0)$  from TGLF does not exceed 3.7 keV and falls short of the experimental value of 4.5 keV by almost 20%.

The lower electron temperature in the ion-electron case compared to the pure-electron case discussed before is due to an increase in the total electron-ion heat transfer by about 40% caused by the colder ions. As such it appears as if the electron heat transport is still correctly modelled as discussed before, but the seemingly cooler ions also affect the electrons.

The normalised ion temperature gradient in figure 6.19f only matches the power balance result on a very basic level, i.e. it is of the same order of magnitude. The trend, however, is reversed, showing a strong discontinuity at the boundary  $\rho_{\text{tor}} = 0.8$ . In  $\chi_i$  (figure 6.19g), some indications for an ITB are present, although not very pronounced and difficult to reconcile with the conventional understanding of how shear affects transport: there are two dips in  $\chi_i$ , one for the case with unshifted  $q$ -profile for  $0.2 \lesssim \rho_{\text{tor}} \lesssim 0.35$ , one for the shifted case for  $0.15 \lesssim \rho_{\text{tor}} \lesssim 0.35$ , i.e. the shift in  $\chi_i$  is only partial, and also in the opposite direction. This is in contradiction to the expected behaviour seen in the electron case, i.e. the region of low transport following the region of reversed shear.

A case where only  $T_i$  was evolved with TGLF while  $T_e$  was fixed to the experimental value is omitted as it merely reproduced the result of figure 6.19e with slightly increased  $T_i$ . This is because due to the fixed and thus now higher  $T_e$  more power could be exchanged from electrons to ions.

To summarise, the application of TGLF to this ITB case has revealed several things:

- It is possible to capture the effects of the  $q$  and  $s$  on electron transport with TGLF. It is fairly sensitive to changes in  $q$  and  $s$ . This means that an accurate reconstruction of the magnetic equilibrium is crucial for a proper modelling of the underlying transport processes.
- It is not possible to match the experimentally observed ion temperatures in the presence of unusual  $q$ -profiles with TGLF. There are indications of the reversed shear impeding ion heat transport, but they appear contradictory since they do not follow the reversed shear when it is shifted, whereas electron heat transport does react as expected.

Had both electron and ion heat transport been significantly different from the experimental observations then it could have been argued that incorrect TGLF inputs were responsible. Here however, only the ion result is very different from the experiment whereas the electron behaviour is largely captured by TGLF's model, in particular when fixing the ion temperatures to their experimental values. This does not definitively exclude an input error that might only affect ion transport, but it does also raise the question whether TGLF's approximations are as appropriate for ion heat transport as they are for electron heat transport, at least in such conditions with strong localised reversed shear.

### 6.3 Late Heating with Broad Counter-ECCD

This section reports on the latest iteration of late heating experiments where the ECCD deposition was broader and more neutral beam power was supplied in order to facilitate a potential  $\beta$ -stabilisation of the pedestal as well as a high bootstrap current fraction. The experiments are summarised as:

pulse number	ECCD configuration	feedback-controlled $\beta_N$	NBI 6/7 setting
32298	on-axis counter	2.0	maximum off-axis
32303	on-axis counter	2.7	maximum off-axis
32304	central heating only	2.7	standard off-axis
32305	off-axis co	2.7	standard off-axis

Discharges #32298 and #32303 use the same ECCD configuration, which is shown in figure 6.20 together with those from #32304 and #32305. In all of them the feedback-control changes the NBI heating power in real-time to maintain a target  $\beta$  [115].

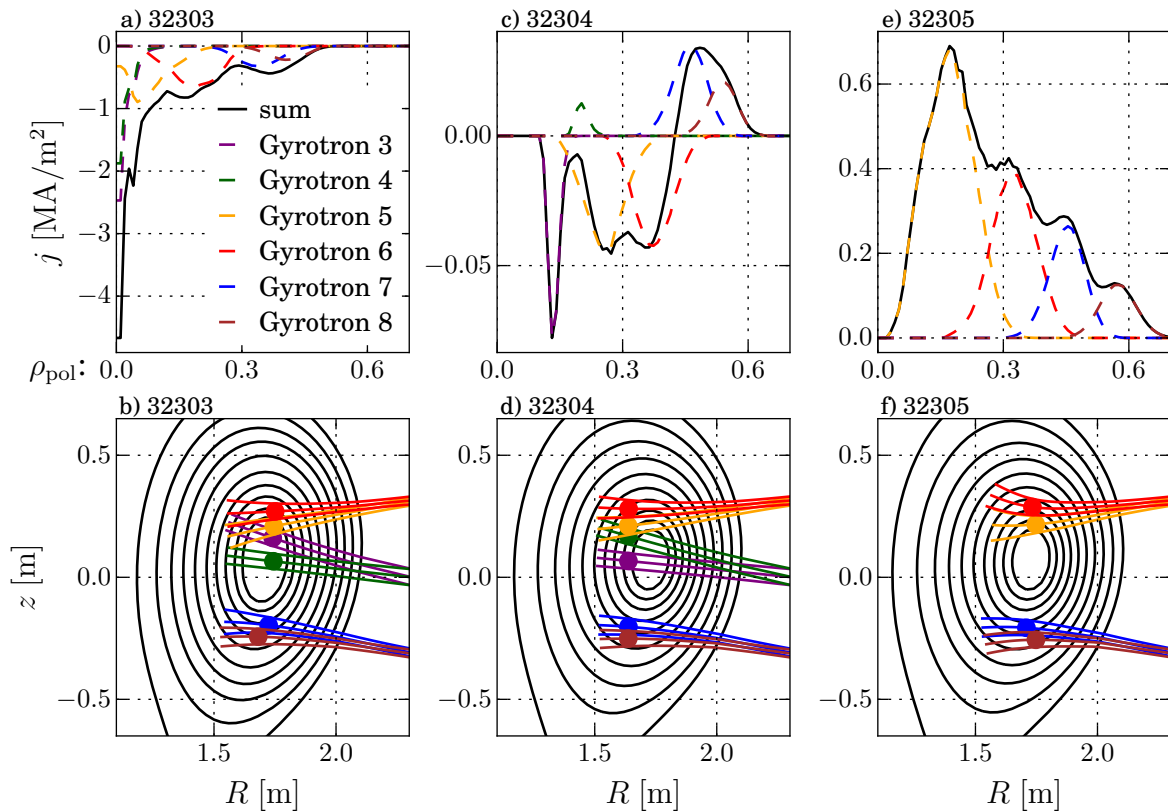


**Figure 6.20:** ECCD deposition for the steady high  $\beta$  phase ( $\sim t = 3.75$  s) in (#32298 and) #32303, #32304 and #32305.

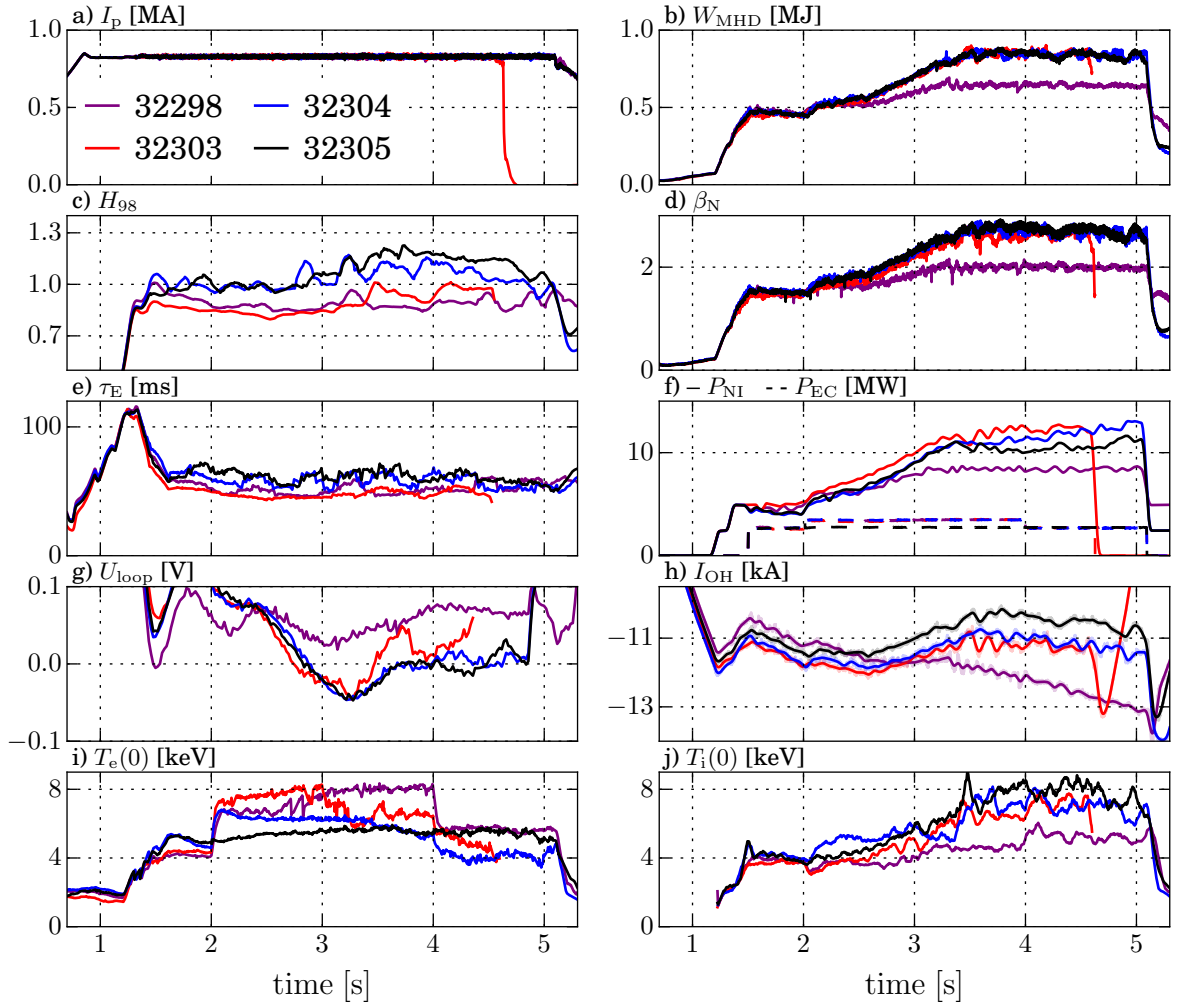


**Figure 6.21:** Temporal evolution of key plasma parameters in discharges #32298, #32303-32305.

Figures 6.20a and 6.20b (#32303) show the broad counter-ECCD that extends from  $\rho_{pol} \approx 0.5$  inwards, whose deposited current density would rise somewhat linearly to just over  $1 \text{ MA/m}^2$  at the axis if not for the divergence at the very centre, which only affects a small volume. The same deposition is applied in #32298, although with a lower  $\beta$ , which allows separating  $\beta$  and ECCD effects. As is shown in figures 6.20c and 6.20d, no current is driven by ECCD in #32304, which makes this a control discharge. In #32305 it is attempted to minimise the ohmic current rather than maximising the bootstrap current, which is why it features off-axis co-ECCD. In general, ECCD has to be done close to the axis where  $T_e$  is high as to maximise current drive efficiency. As a result of the central EC deposition, the electron temperatures in the two on-axis ECCD cases are the highest as shown in figure 6.21i, although in #32303 they drop at higher  $\beta$  since the warmer ions increase electron heat transport.



All discharges follow the same sequence, which is sketched in figure 6.21: two neutral beam sources are added just before 1.5 s, after which the four ECRH2 gyrotrons are turned on. Where applicable, two more ECRH1 gyrotrons are activated at 2.0 s for their maximum operation time of 2.0 s. Moreover, at 2.0 s the  $\beta$  feedback control assumes control and ramps up the neutral beam power to reach the preset target  $\beta$  as indicated in the table above. The target value is reached just before 3.5 s and kept stable until 5.0 s. In #32303, the lack of central electron heating after ECRH1 is shut off leads to central impurity accumulation, which causes a disruption at just after 4.6 s.

The feedback controlled phase between 3.5 s and 5.0 s (and in particular before 4.0 s when full ECRH was applied, where applicable) is of main interest as it allows studying the confinement properties and current profile at various external current drives and stored energies. In figure 6.21g one can immediately discern the  $\beta_N = 2$  case (purple, #32298) from the other three ( $\beta_N = 2.8$ ) since the latter all have their loop voltage dip into negative values at around 2.8 s. In contrast, the purple  $U_{\text{loop}}$  remains positive throughout the pulse, i.e. continues to require inductively driven current from the transformer. This is also reflected in 6.21h, where — after the  $\beta$ -ramp is finished — the transformer has to continue to increase  $I_{\text{OH}}$  in #32298 while it remains fairly constant in the other three for several hundred ms and more. This is discussed in detail in section 6.3.1.

Another important aspect of the feedback controlled phase is that the global confinement differs between the various cases. Specifically, the  $H$ -factor (figure 6.21c) is highest for #32305, closely followed by #32304, both well above unity. In contrast, the counter-ECCD cases exhibit a confinement degradation with  $H_{98} < 1$ , both at high and low  $\beta$ . Due to this confinement degradation, the feedback control is forced to add more NBI power in #32303 to maintain the desired  $\beta$  value. For instance, from 3.5 s to 4.0 s, #32303 requires approximately 2 MW of additional heating compared to #32305 to maintain the same stored energy (see figure 6.21b), which is why the  $H$ -factor also differs between these two discharges.

About 0.5 MW of the additional 2 MW are due to the maximum off-axis position of the off-axis neutral beams which, according to TRANSP/NUBEAM simulations, led to increased shine through, i.e. the beam not being absorbed by the plasma. The remaining, unaccounted 1.5 MW may be explained by variations of the  $q$ -profile during the high  $\beta$  phase, as discussed in the following.

The safety factor as well as the electron and ion temperatures are plotted in figure 6.22.  $T_e$  is similar in all four discharges over large extents of the minor radius.  $T_i$  differs strongly between the low  $\beta$  discharge #32298 and the others since the  $\beta$  control actuates with neutral beams that primarily heat the ions. As is evident from figure 6.22c<sub>log</sub>, the lower ion temperature in #32298 is based primarily on a reduced pedestal temperature, but also a locally reduced critical gradient for  $0.3 \lesssim \rho_{\text{pol}} \lesssim 0.7$ . Overall, ion heat confinement is worse since  $T_e/T_i > 1$ .

In #32303, however, ion temperatures are very similar to those from the best confinement case #32305. The main remaining difference is clearly shown in figure 6.22a:  $q$  is

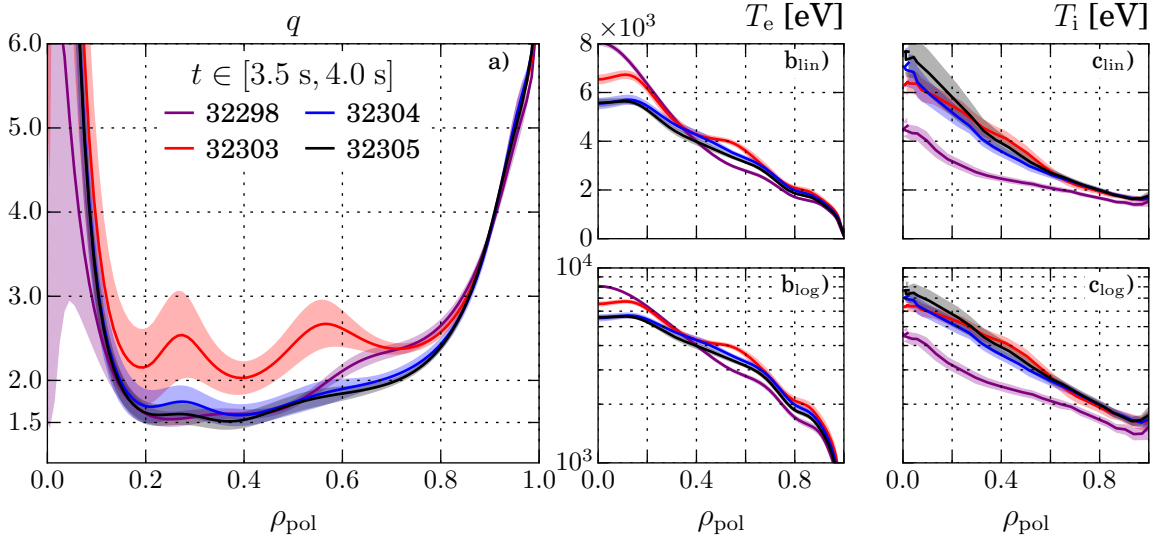


**Figure 6.22:** Comparison between  $q$ -profiles and temperatures in #32298, #32303-32305.

significantly higher over a large extent of the minor radius, which is linked to increased heat transport as described in subsection 2.3.3 on page 24: non-linear gyrokinetic simulations estimate that going from  $q = 1.5 \rightarrow 2$  raises  $\chi_i$  by up to 25% [30], which is of the order of the observed confinement degradation. Moreover, [30] finds a linear relationship between heat transport and  $q$ .

Note, however, that the uncertainty of  $q$  in #32303 is larger because the MSE diagnostic was intermittently impaired during the feedback-controlled phase due to an extra beam being active on box 1. As a result, the profile is less reliable closer to the magnetic axis.

If the confinement improvement due to an increase of  $\beta$  is linear in the observed range, then it is no surprise that an increase of  $\beta_N$  by 35% ( $2.0 \rightarrow 2.7$ ) can be almost entirely compensated by an increase of  $q$  by about 33% ( $\sim 1.5 \rightarrow \gtrsim 2$ ). Unfortunately the number of discharges is too small to derive some kind of empirical scaling from these observations. Consequently it cannot be established whether a confinement improvement which is supra-linear in  $\beta$  due to a feedback loop (see section 2.6) is observed.

Finally, the MHD activity of the discharges is illustrated in figure 6.23 on the next page. With the exception of #32303, which disrupted after loss of central ECRH and subsequent impurity accumulation, MHD activity in the four discharges was muted and did not lead to sudden performance degradation like in the early heating case discussed in subsection 6.1.3 on page 99. Such strong MHD activity appears with likelihoods of the order of 0.8 and above, which is the case several times in the observed intervals, albeit only in the very early or very late stages of the experiments, for short periods. In the

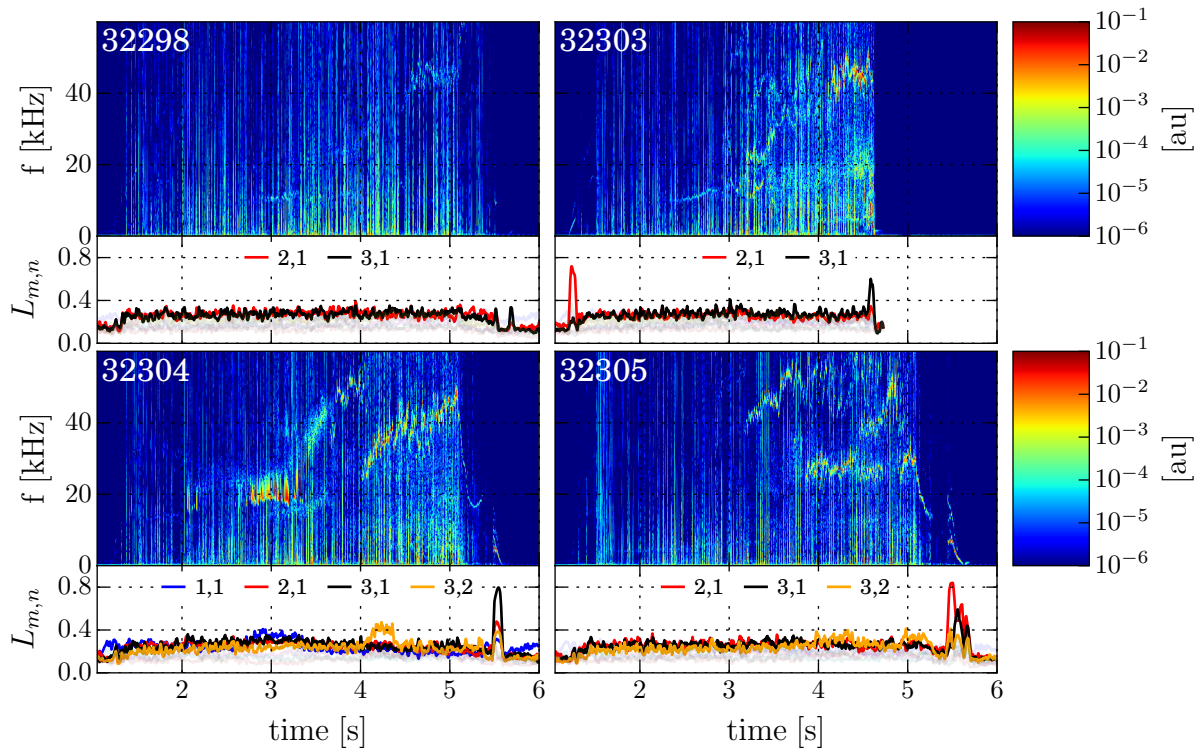


**Figure 6.23:** Spectrograms of a magnetic signal and likelihoods of different helicities as calculated by SVD analysis [70] for #32298, #32303-32305. The faint likelihood traces represent helicities up to 5,2 whose likelihood did not exceed 0.4 throughout the entire discharge.

feedback-controlled phases the spectrograms reveal several noticeable MHD phenomena for the high- $\beta$  discharges #32303-32305 at various frequencies. Only some of these MHD events are sufficiently clear to be characterised by the SVD analysis. In the no-ECCD case #32304 there is some indication of 1,1-activity during the NBI ramp-up at 3,0 s, which disappears shortly afterwards and is succeeded by a distinct 3,2-signature after 4.0 s. The 1,1-signature is absent in the co-ECCD case #32305, but a 3,2-signature also appears to become more prominent after 4.0 s. In both cases the events are not strong enough to noticeably degrade the confinement (cf. figure 6.21ce). In the counter-ECCD case #32303, no noticeable MHD activity appears until just before the disruption — the 2,1/3,1 signature is present throughout the discharges at approximately the same likelihood, so this level can be considered to be the baseline. In contrast to #32304/5, no 3,2 activity is observed here. Overall, the MHD activity is consistent with the reconstructed  $q$ -profiles (cf. figure 6.22a) and stored energies: in #32298  $\beta$  is too low for significant MHD activity, in #32303  $q$  is too high for the 3,2 instabilities that are present at lower  $q$  in #32304/5.

To summarise, the results partially meet the expectations. On the one hand, no performance-degrading MHD instabilities occurred. Particularly low-helicity MHD in-

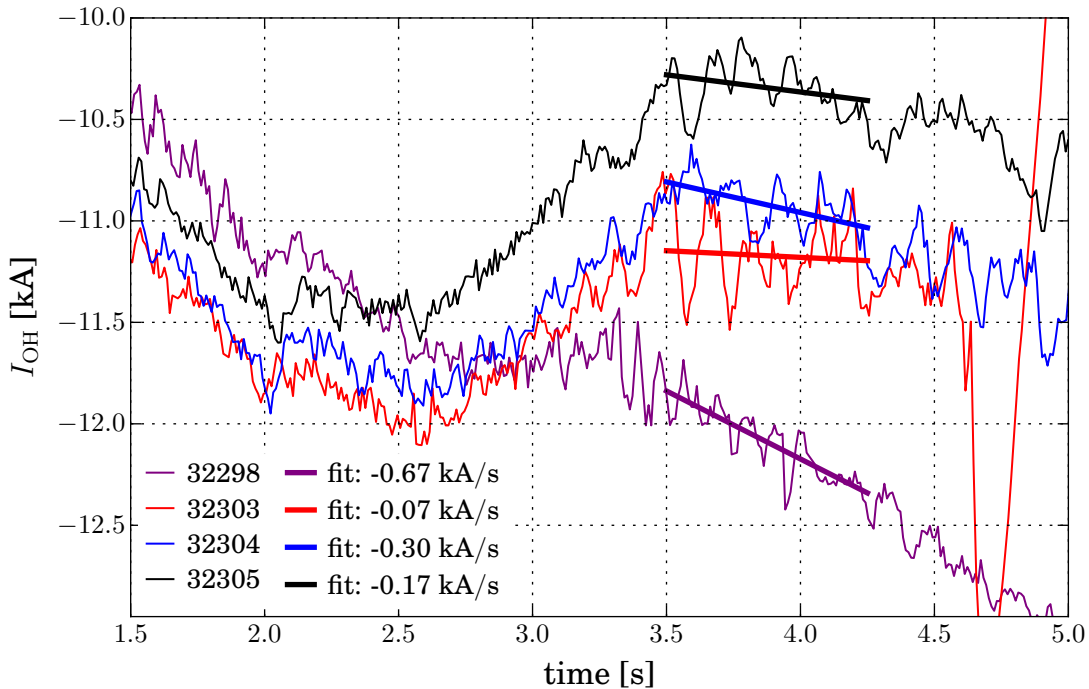


**Figure 6.24:** Current flowing in the central solenoid for #32298, #32303–32305. Thick straight lines represent a linear fit to the curves during the feedback-controlled phase. Fully non-inductive operation would result in a slope of 0 kA/s.

stabilities were not present, although light 3,2-activity was observed in the no- and co-ECCD cases. It is possible that the existing MHD activity may ultimately evolve into such instabilities, but they were not observed so far. This may occur once the equilibria are entirely converged, which they were not yet during these discharges (see next section). On the other hand, no particularly high global confinement was observed, which may be explained by the broader current profile and hence elevated  $q$ -profile. Furthermore, the high- $\beta$  discharges require little additional flux from the central solenoid, suggesting that they are either in or very close to a fully non-inductive state. This will be discussed in detail in the next section, while the transport modelling is discussed in section 6.3.2.

### 6.3.1 Steady State Operation with High Bootstrap Fraction

The different discharge scenarios do not vary only the confinement properties of the plasma, but also its ability to maintain the plasma current independent of inductive current drive. In figure 6.24 the current evolution in the central solenoid is plotted. In order to estimate the reliance on inductive current, the evolution from the beginning of the flat- $\beta$ -phase was fitted using linear least-squares regression. A decrease in the plotted current indicates inductive current drive (and ohmic heating, hence the abbreviation

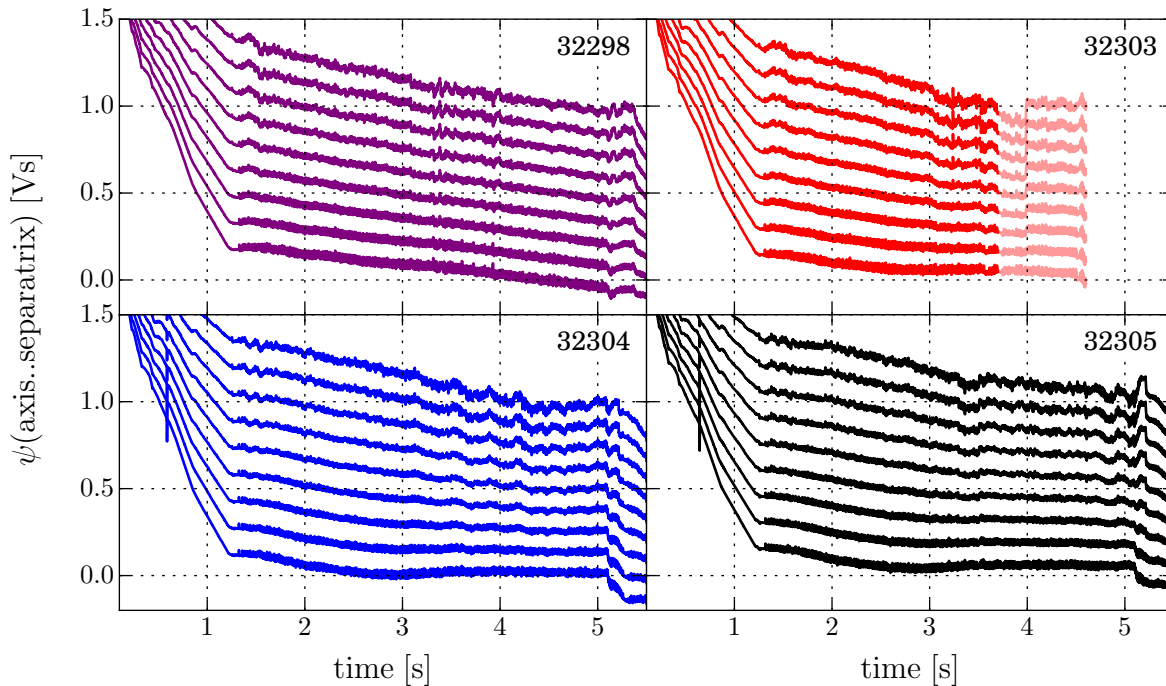


**Figure 6.25:** Temporal evolution of poloidal magnetic flux at selected minor radii. Top trace represent the axis flux, bottom trace the separatrix flux, traces in-between the flux at equidistant minor radii between axis and separatrix. Flat trend would indicate steady state, i.e.  $U_{\text{loop}} = \partial\psi/\partial t = 0$ . Faded traces for #32303 indicate increasingly faulty MSE data due to modulation of a second beam of NBI box 1.

OH), which is clear for the low  $\beta$  counter-ECCD case #32298. In contrast, the high  $\beta$  counter-ECCD case #32303 appears to use less inductive current by about one order of magnitude. The control case with high  $\beta$  and no ECCD also improves over #32298, but only by a factor of two, indicating that the counter-ECCD has a significant impact. The high  $\beta$  co-ECCD case #32305 appears similar to #32303 in that it, too, requires almost an order of magnitude less OH current, but appears to fall short of #32303's result. This is remarkable because it means that the counter-ECCD approach increases the bootstrap current enough to more than compensate the ECCD in the opposite direction.

It has to be noted, however, that  $I_{\text{oh}}$  in the feedback-controlled phase has large variations. As a result, the fit would change its slope if one were to shift the end point. The current extent of the fit was chosen as a compromise, although a proper analysis of this signal will require a longer stable period to assess whether the plasma remains stationary.

A more thorough investigation is based on the reconstructed equilibrium. If it is in a stationary state, the flux pumping by the OH coil will cease and the poloidal flux will freeze  $\partial\psi/\partial t = 0$ . This should happen at the separatrix, which will be in line with  $U_{\text{loop}}$  in figure 6.21g and the stationary  $I_{\text{oh}}$ , but also further inside up to the magnetic axis.

This is pictured in figure 6.25: it is immediately evident that #32298 was not stationary, which is in line with the non-zero loop voltage and continued flux pumping  $dI_{\text{oh}}/dt < 0$ . In the other three cases, the edge of the plasma appears to have become stationary, but further inside one still observes changes. In #32303 and #32304 the ECRH1 was turned off at 4.0 s, and before this the plasma does not appear to have entered a steady state. Note that the increasingly corrupt MSE data in #32303 does not allow a definitive assessment: from the evolution before 3.7 s it does appear as if the plasma approaches a steady state, but the corrupt MSE data and subsequent deactivation of ECRH1 make this unclear. In #32305 no ECRH1 was active and the MSE data was clean, so it is evident that the equilibrium and its current distribution still evolve near the axis. In conclusion, to analyse the final converged state the discharges have to be run for longer periods. This will become possible either by optimising the ECCD deposition to rely only on ECRH2 or, at the latest, once ECRH3 becomes available to provide ECCD for 10 rather than 2 seconds at a time like ECRH2 (cf. subsection 3.3.1 on page 55).

The composition of the plasma current from IDE and TRANSP in each discharge is shown in figure 6.26. Again in all discharges the current from NBCD is taken from NU-BEAM and is therefore identical in both codes. The ECCD from TORBEAM (IDE) and TORAY (TRANSP) also match reasonably well. The remaining current is partitioned between bootstrap current and the ohmic current, which is merely the total current with all non-inductive contributions subtracted. Like in section 6.1.3, TRANSP underestimates the bootstrap current when compared to IDE's result, which is again caused by the  $q$ -profile in TRANSP being lower than the one reconstructed by IDE.

In the phase between 3.5 s and 4.0 s, IDE calculates  $I_{\text{bs}}$  to approximately 0.4 MA for both #32303 and #32305 (and #32304), with the former having a slightly larger value than the latter. To complement this, IDE estimates approximately 50 kA of remaining  $I_{\text{ohm}}$  in #32305 but around 200 kA for #32303. Most of this additional current is found near the magnetic axis (see figure 6.27) such that it compensates the counter-ECCD in order to satisfy IDE's requirement of  $j_{\text{tor}} > 0$ . This is in contradiction to the observations made so far: both discharges appear to rely on similar levels of inductive current with #32303 even appearing slightly more independent of the central solenoid (see figure 6.24). Even if that were not the case, then both discharges would still have to be very similar, whereas according to IDE there is a discrepancy of up to 0.2 MA ( $\approx 50\%$  of  $I_{\text{bs}}$ ) during the interval in question. In that sense, IDE and TRANSP are in agreement as TRANSP estimates approximately the same  $I_{\text{bs}}$  for both #32303 and #32305, too, albeit overall less than IDE. Assuming that the used ECCD and NBCD models yield accurate results, then there could be three explanations:

- The reconstructed  $q$ -profile may be too low, which would result in a reduced  $I_{\text{bs}}$ . Moreover, the equilibrium may be inaccurate in some other way, e.g. by not allowing negative toroidal current density or because the MSE data was partially compromised in #32303.
- The stable phase was too short and the small  $dI_{\text{oh}}/dt$  is merely a transient artefact.

- The bootstrap current model (see equation 2.23) is not suitable for such conditions and underestimates the actual  $I_{bs}$ .

Upgrades to the MSE and DCN polarimetry will alleviate the first point. The second point can be investigated by performing discharges with longer stable phases. If the discrepancy cannot be resolved after implementing these two improvements, then it may be necessary to revisit the bootstrap current model.

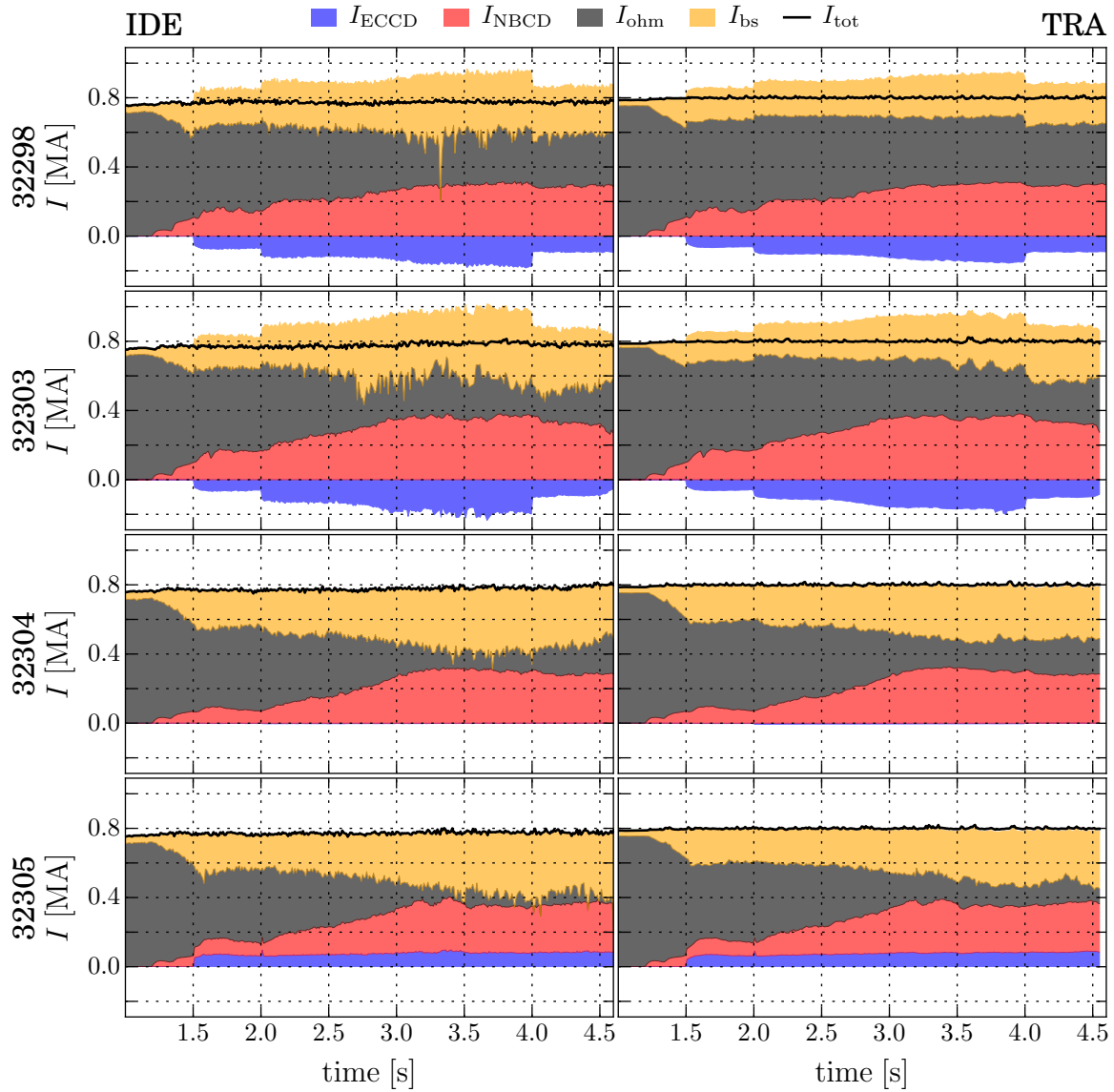


**Figure 6.26:** Composition of plasma current from IDE and TRANSP.

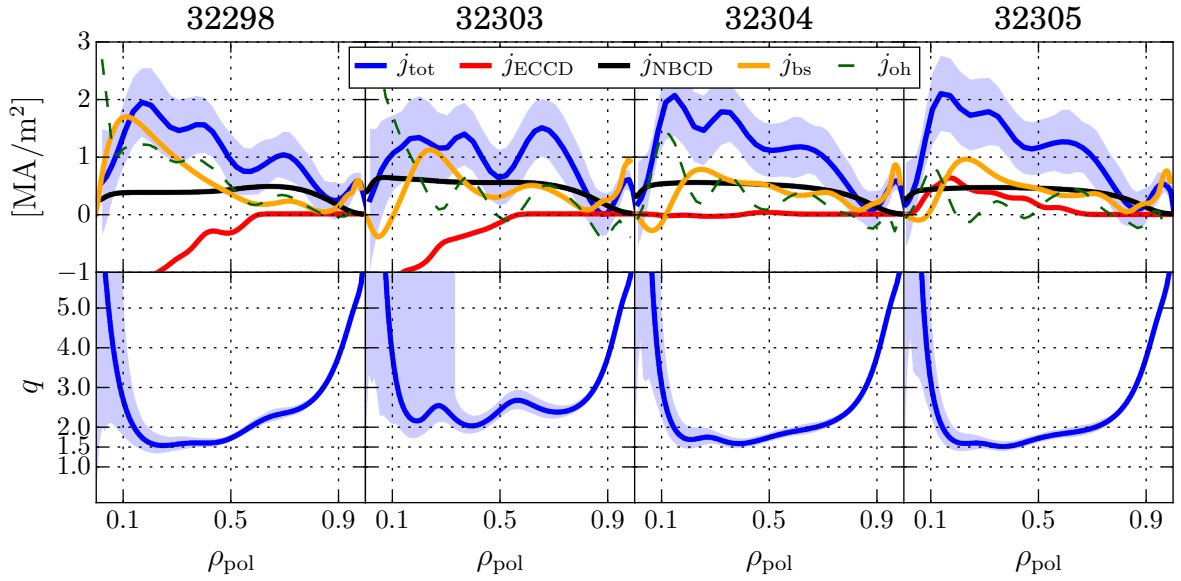


**Figure 6.27:** Composition of plasma current from IDE from 3.5 s to 4.0 s in each discharge.

The simplified plasma model used in section 2.6 on page 37 suggested that for  $T_e$  profiles like the ones here ( $R/L_{T_e} \approx 6$  in #32303–32305, cf. figure 6.29) the addition of central counter-ECCD would result in approximately 40–50% of additional bootstrap current compared to the no-ECCD case. Here, as mentioned above, both the counter-ECCD case #32303 and the no- and co-ECCD cases #32304/5 appear to have the similar amounts of bootstrap current. However, the discrepancy described above is, in fact, approximately 50%. So, while the simplified model appears unable to describe the current observations, it remains to be seen whether the improvements above will prove it right in the end.

In any case, the presented results suggest that quasi-non-inductive operation at  $B \approx 2.5$  T and  $q_{95} = 5.3$  with  $I_p = 800$  kA and  $\beta_N = 2.7$  is possible at ASDEX Upgrade, even if some questions regarding the plasma’s current composition and final converged state remain unanswered for the time being. For the co-ECCD pulse #32305 the reconstructed current composition is consistent with the low loop voltage  $U_{\text{loop}} \approx 0$  and also sums up to the total  $j_{\text{tor}}$  as shown in figure 6.27, i.e.  $j_{\text{oh}}$  remains within the confidence band of  $j_{\text{tor}}$ <sup>1</sup>. A significant lengthening of pulses is definitely possible. Moreover, tentatively, the counter-ECCD approach seems at least as useful for prolonging the pulse length as co-ECCD, although the latter also offers better confinement due to lower  $q$ .

<sup>1</sup>cf. the discussion on appropriate regularisation in subsection 5.2.1 on page 87. Even weaker regularisation and thus larger confidence bands would diminish this argument and make it less meaningful.



### 6.3.2 Transport Modelling with TGLF

A (quasi-)non-inductive operation scenario with indefinite (or at least very long) pulse length would be very attractive for a fusion power plant. This also requires an understanding of the confinement properties of the resulting plasma. The depth of understanding can be tested by modelling the plasma heat transport with numerical simulations like TGLF.

For this purpose, discharges #32298 and #32303 were modelled with TGLF. The same boundary conditions and data were supplied as described in section 6.2.2.

The modelling is done in two parts. First, one without TGLF taking effects from  $\vec{E} \times \vec{B}$ -shear into account, then one with such effects. The reason for this is that recent gyrokinetic studies have found discrepancies in the ion heat transport between GYRO (on which TGLF is based) and GENE (cf. 2.3.4 on page 29). These discrepancies seem to be due to GYRO/TGLF significantly overestimating the impact of the  $\vec{E} \times \vec{B}$ -shear on ion heat transport as described in [116] and references therein. The exact reason for this overestimation is, as of now, unclear. In contrast, GENE results do not reproduce such strong stabilisation due to  $\vec{E} \times \vec{B}$ -shear. Instead, GENE studies find a comparable level of stabilisation of turbulent ion heat transport when taking electromagnetic effects of fast ions into account [117, 118].

As mentioned before, due to their high computational costs, full gyrokinetic simulations with GYRO or GENE could not be performed for this thesis.

#### TGLF without $\vec{E} \times \vec{B}$ -shear

The initial result for the low- $\beta$ -case #32298 is shown in figure 6.28. For comparison, the power balance result is shown in blue. The displayed quantities are averages over the last 200 ms of the steady state phase, which is much longer than the energy confinement time  $\tau_E \approx 50$  ms.

The TGLF result underestimates  $\chi_e$  outside  $\rho_{\text{tor}} \approx 0.6$  and in turn overestimates it inside  $\rho_{\text{tor}} \approx 0.5$ . As a result, the electron temperature is slightly elevated outside of  $\rho_{\text{tor}} \approx 0.4$  and falls short of the power balance result inside of that minor radius. This leads to the TGLF result ultimately falling short of the experimental value by about 20% on axis.

The ion temperature profile in figure 6.28e, however, matches the experimental result well, with the exception of a slump for  $0.3 < \rho_{\text{tor}} < 0.6$  that barely exceeds the error bars. In short, the central ion temperature is reproduced, although the profile shape is slightly off. This is because  $\chi_i$  is only in qualitative agreement with the power balance result, as it is again underestimated outside of  $\rho_{\text{tor}} \approx 0.4$  and overestimated inside of that. As a result, the average  $R/L_{T_i}$  is about the same for TGLF and the power balance, which maintains the core ion temperature, despite its trend being reversed as shown in figure 6.28f.

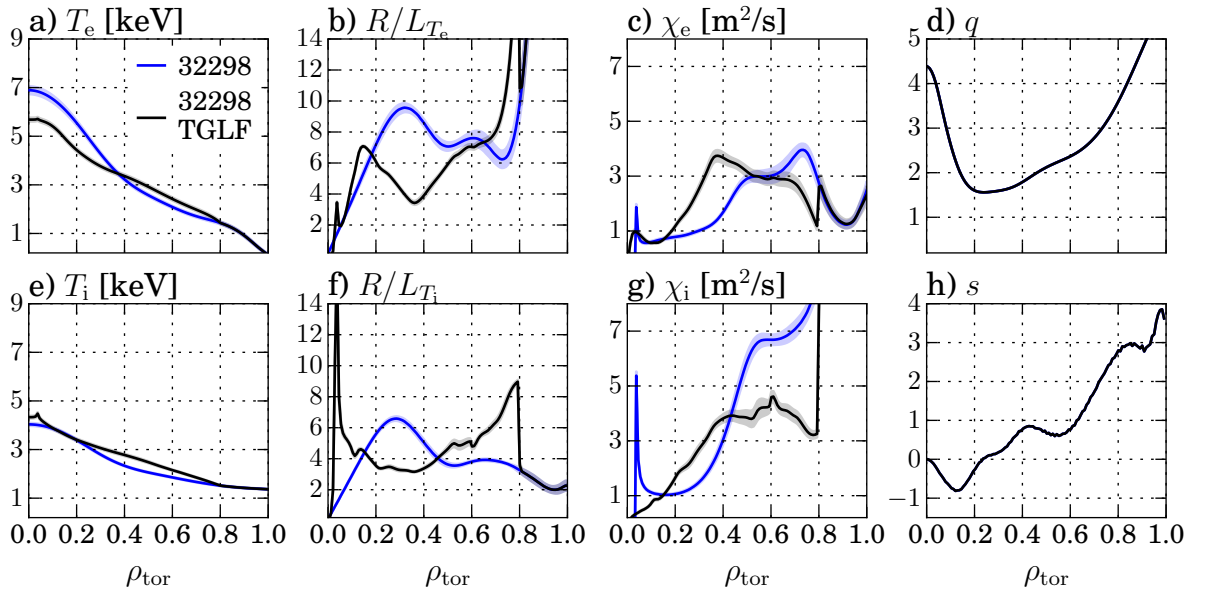


**Figure 6.28:** Power balance analysis and TGLF evolution results for the electron/ion temperature profiles in #32298. ( $t \in [3.8 \text{ s}, 4.0 \text{ s}]$ )

In summary, even though the core ion temperature can be reproduced with TGLF, some stabilising effect is missing inside of mid-radius. At the same time, some destabilising influence is not taken into account further outside. The same is observed for the electrons, although there the two errors do not cancel out.

Figure 6.29 shows the evolution of electron and ion heat transport as predicted by TGLF for the high- $\beta$  case #32303. Power balance results for #32298 as well as #32303 are also included for comparison. The electron temperature profile is very similar in both discharges, and TGLF's result for #32303 is in agreement with its power balance counterpart, with only slight deviations from the power balance result compared to the TGLF prediction for #32298. The situation is different for the ion heat transport: here evolving the  $T_i$  profile with TGLF's transport coefficient now leads to substantially lower profiles. Despite the additional ion heating, the resulting profile looks more like the one for #32298 than that of #32303. This is because the strong reduction in  $\chi_i$  just inside  $\rho_{\text{tor}} \approx 0.7$  is not reproduced. The transport coefficient remains at values close to those of #32298.

This behaviour, which is consistent with that described in section 6.2.2, suggests that there is some phenomenon that affects only ion heat transport and is not taken into account by TGLF. Do note that this effect is not negligible as evident from figure 6.30. Only when increasing the neutral beam power by 50% does the central ion temperature reach the experimentally observed value of about 6.5 keV.

At the same time TGLF is affected by a changing  $q$ -profile as shown in figure 6.31, although not to such a large extent that it could be used to explain the discrepancy. It does, however, highlight that TGLF is sensitive to the shear since  $\chi_i$  always exhibits

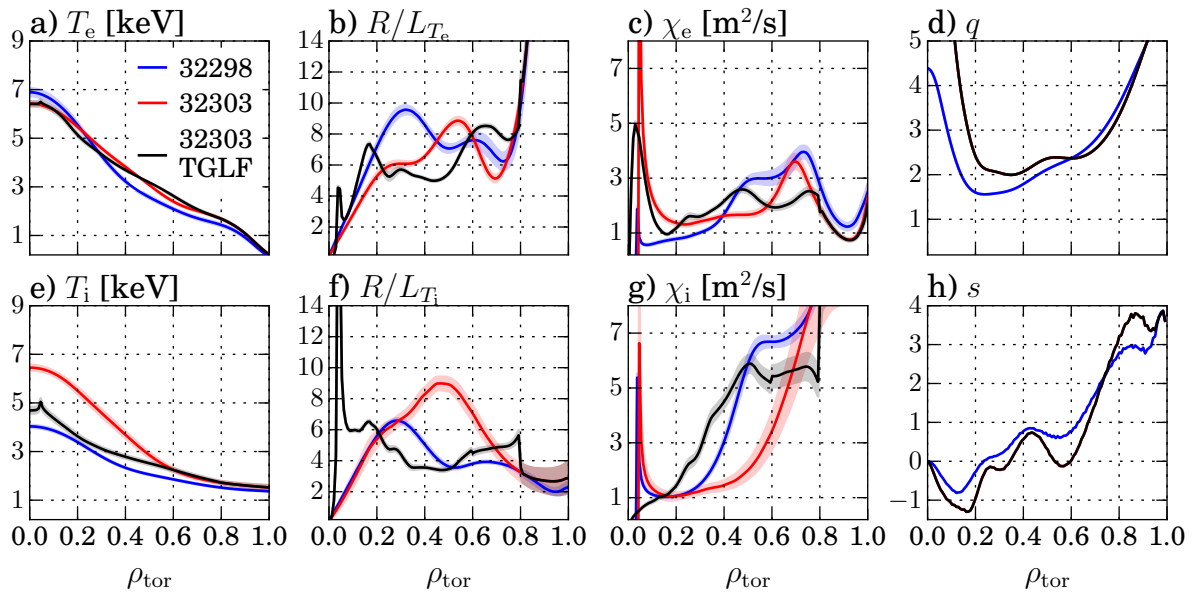


**Figure 6.29:** Power balance analysis (#32298 blue, #32303 red) and TGLF evolution results for #32303 (black) for the electron/ion temperature profiles. ( $t \in [3.8 \text{ s}, 4.0 \text{ s}]$ )

an increase when  $s \approx 0.5$  (see section 2.3.3), e.g. around  $\rho_{\text{tor}} \approx 0.45$  for the elevated  $q$ -profile, or around  $\rho_{\text{tor}} \approx 0.3$  for the monotonic case: in both cases  $\chi_i$  rises compared to the other one.

Finally, one quantity that varies between #32298 and #32303 is the fast ion density. Fast ions are thought to stabilise micro-instabilities in several ways. One is the so-called dilution effect [113]. It is assumed that the fastest growing micro-instability will outpace the other modes and drive turbulence. Any effect that weakens this fastest growing mode will therefore delay the turbulence and thus weaken turbulent transport. This weakening happens because impurities or fast ions do not participate in the main ions' modes since

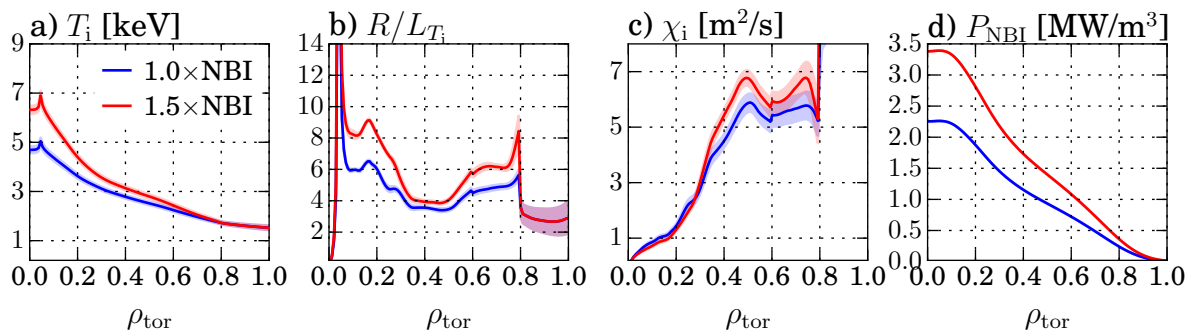


**Figure 6.30:** TGLF modelling results for the ion temperature profile with the actual neutral beam power and 50% additional power. (#32303,  $t \in [3.8 \text{ s}, 4.0 \text{ s}]$ )

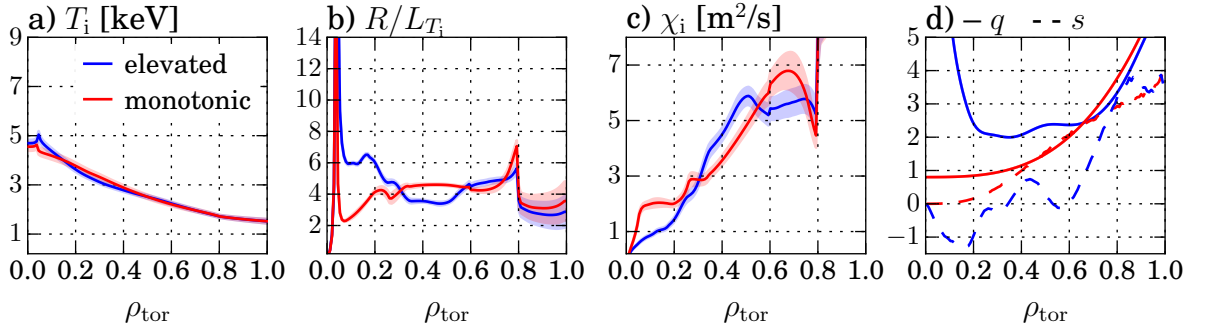


**Figure 6.31:** TGLF modelling results for the ion temperature profile with the actual  $q$ -profile and an artificially created monotonic one (both  $q$  and normalised shear  $s$  displayed in box d). (#32303,  $t \in [3.8 \text{ s}, 4.0 \text{ s}]$ )

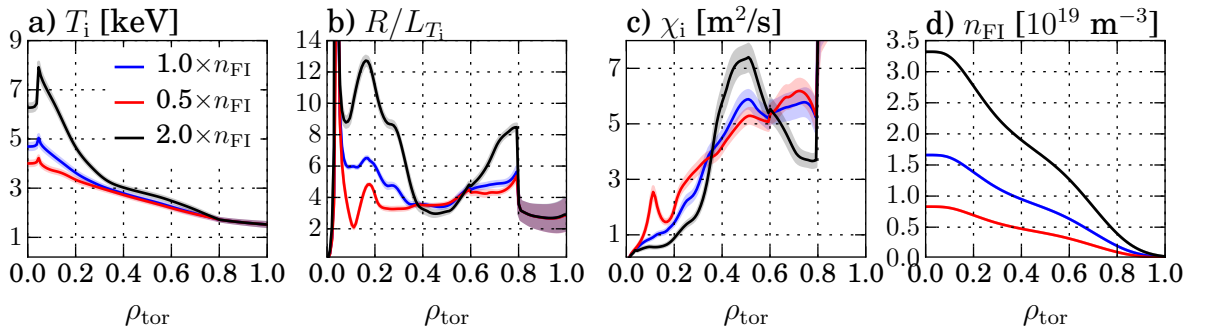


**Figure 6.32:** TGLF modelling results for the ion temperature profile with the actual fast ion density and artificially halved/doubled fast ion density (see box d). (#32303,  $t \in [3.8 \text{ s}, 4.0 \text{ s}]$ )

their drift velocity (see equation 2.18 on page 14) is different due to their different mass and/or energy. As long as the impurity/fast ion modes do not become dominant over the main ion modes, their diluting effect will result in a stabilisation.

Another effect that is limited to fast ions is due to their high energy. They can be considered to have  $T_{i,\text{fast}}/T_e \gg 1$ , which would allow them to respond to an initial perturbation faster than the main ions and at least partially shield the potential fluctuation (see section 2.3.3 on page 24).

Evidently, as seen in figure 6.32, the fast ions do affect the ion heat transport as calculated by TGLF. Still, even when doubling the fast ion density, TGLF can still not reproduce the experimentally observed profiles. A potential explanation for this may be the lack of electromagnetic fast ion effects in TGLF's model. Recent results [117, 118] from non-linear gyrokinetic analyses of JET discharges suggest that such effects can play a major role in stabilising micro-instabilities and thus reducing ion heat transport. In fact, [118]

also shows the result of a predictive numerical simulation of an ITER H-mode hybrid discharge where electromagnetic fast ion effects increase the core ion temperature by about 30% compared to a simulation without such effects. This is approximately the discrepancy between experiment and TGLF in figure 6.29e:

$$\frac{T_{i,\text{exp}}(0)}{T_{i,\text{TGLF}}(0)} \approx \frac{6.5 \text{ keV}}{5.0 \text{ keV}} \approx 1.3$$

Of course, the matching value may be a coincidence but it does show that the magnitude of this EM-effect may explain the observed mismatch between model and experiment.

In summary, even without effects of  $\vec{E} \times \vec{B}$ -shear and similar to the on-axis counter-ECCD case of subsection 6.2.2, TGLF is able to reproduce the experimentally observed electron transport well in the high- $\beta$  case with additional neutral beam heating with some discrepancies remaining in the low- $\beta$  case. In contrast, the ion transport is significantly over-estimated, which results in lower ion temperature profiles compared to the experiment. Since there is no reason for this to be different in the subsequent discharges #32304/5, their analysis has been omitted.

### **TGLF with $\vec{E} \times \vec{B}$ -shear**

The previous section explored effects not related to  $\vec{E} \times \vec{B}$ -shear, which is now taken into account.

The result of the TGLF-predicted  $T_e$  and  $T_i$  profiles for #32298 is shown in figure 6.33. For the electrons, the change due to the additional  $\vec{E} \times \vec{B}$ -shear pushes the result towards the experiment: inside  $\rho_{\text{tor}} \approx 0.5$   $\chi_e$  decreases from the non- $\vec{E} \times \vec{B}$ -shear case which increases  $R/L_{T_e}$  further inside, allowing the  $T_e$  profile to largely close the gap towards the experimentally obtained one. The difference is now less than 10%, which approaches the measurement accuracy.

For the ions in figure 6.33, the additional  $\vec{E} \times \vec{B}$ -shear decreases  $\chi_i$  everywhere compared to the non- $\vec{E} \times \vec{B}$ -shear case. Consequently,  $\chi_i$  now completely agrees with its power balance counterpart inside  $\rho_{\text{tor}} \approx 0.4$ . Outside of that, however, it is now even farther away from the experimentally obtained value. Altogether this now results in the modelled ion temperatures surpassing the experimentally ones with  $T_i(0)$  being more than 10% too high.

In summary, the inclusion of  $\vec{E} \times \vec{B}$ -shear has improved the electron heat transport modelling but leads to underestimated ion heat transport in the outer half of the plasma and thus overestimated ion temperatures.

In the high- $\beta$  case displayed in figure 6.34 the additional  $\vec{E} \times \vec{B}$ -shear leads to a substantial confinement improvements beyond the experimentally observed values. For  $0.3 < \rho_{\text{tor}} < 0.8$ ,  $\chi_e$  is reduced by up to 50% and more while  $\chi_i$  drops up to 80% in the same interval.

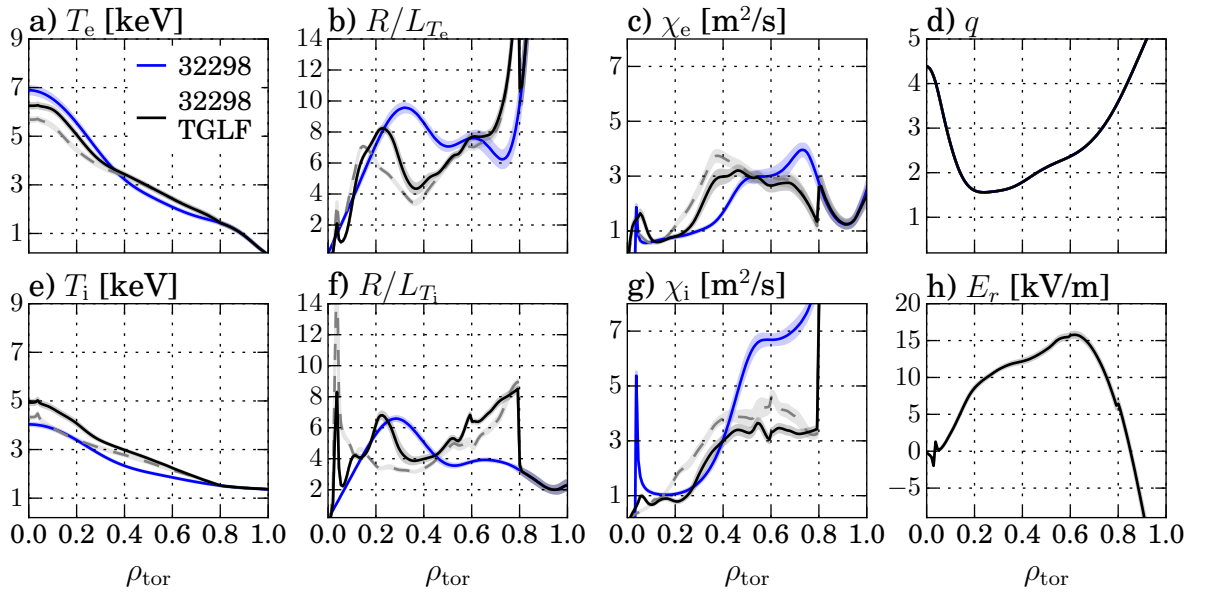


**Figure 6.33:** Power balance analysis and TGLF evolution results for the electron/ion temperature profile in #32298. Grey dashed curves indicate result without  $\vec{E} \times \vec{B}$ -shear. ( $t \in [3.8 \text{ s}, 4.0 \text{ s}]$ )

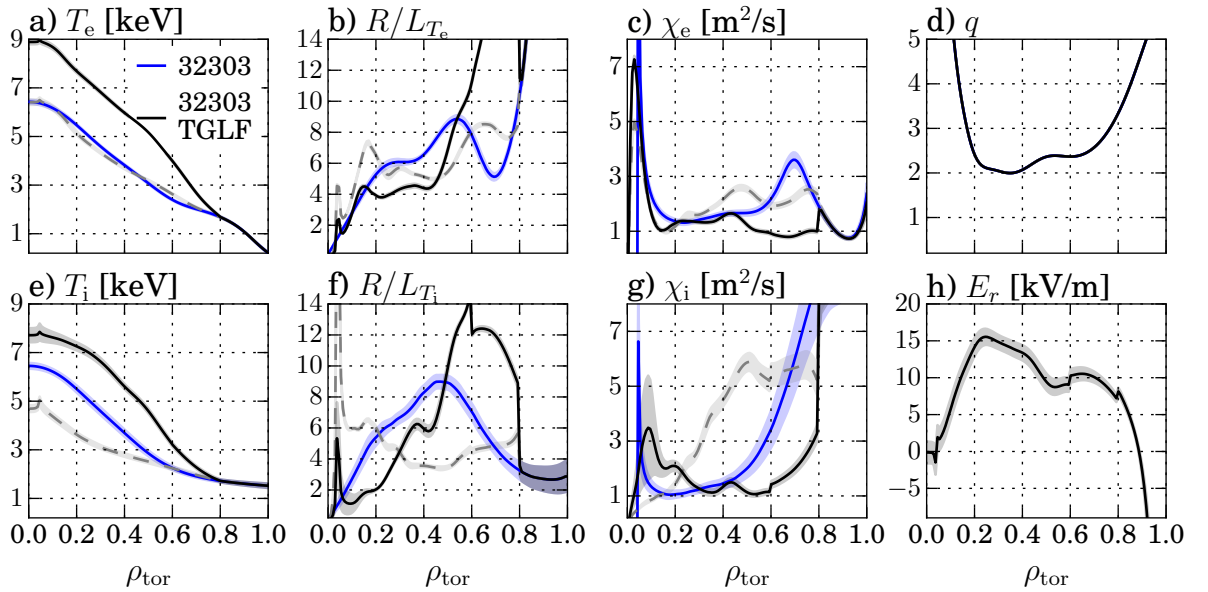


**Figure 6.34:** Power balance analysis and TGLF evolution results for the electron/ion temperature profile in #32303. Grey dashed curves indicate result without  $\vec{E} \times \vec{B}$ -shear. ( $t \in [3.8 \text{ s}, 4.0 \text{ s}]$ )

As a result, the electron and ion temperature profiles are now higher, well outside the

measurement accuracy.  $T_e(0)$  surpasses the experimental value by approximately 40% and  $T_i(0)$  still by over 15%.

For the high- $\beta$  case without  $\vec{E} \times \vec{B}$ -shear, the electron but not the ion temperature profile can be reproduced with TGLF. In contrast, for full  $\vec{E} \times \vec{B}$ -shear neither of them matches with the experiment. This is due to ion transport now being underestimated; the scale of  $\vec{E} \times \vec{B}$ -shear is larger than the ETG turbulence scale ( $\sim$  electron gyroradius) and has negligible effect on it. The ions, however, whose transport channel is affected by  $\vec{E} \times \vec{B}$ -shear, are now warmer and can transfer heat to the electrons.

It is known that the effect of the  $\vec{E} \times \vec{B}$ -shear is non-linear in TGLF [119], so it is possible that a slight variation of  $v_{\text{tor}}$  and thus  $E$  might be sufficient to reproduce the experimental values. This is shown in figure 6.35, where  $v_{\text{tor}}$  has been varied from zero to the full experimental value in order to scale  $E \approx v_{\text{tor}} B_{\text{pol}}$ . Reducing  $v_{\text{tor}}$  by about 40% would result in the core ion temperature matching the experimental values (green curves). This variation is well outside the experimental uncertainties, so it cannot explain the overall findings. Moreover, even with a 40% reduction the  $T_i$  profile shape itself would still be wrong, leading to overall higher ion temperatures across the minor radius, which in turn increases the electron temperature as well.

The mismatch is ultimately caused by the fact that the  $\vec{E} \times \vec{B}$ -shear is affecting the profiles across the whole minor radius. Thus,  $\chi_i$  is strongly reduced due to the additional shear flows everywhere, whereas in the experiment  $\chi_i$  increases strongly outside of  $\rho_{\text{tor}} \approx 0.5$ . Further inside, the TGLF  $\chi_i$  remains above the power balance  $\chi_i$ ; only at full  $\vec{E} \times \vec{B}$ -

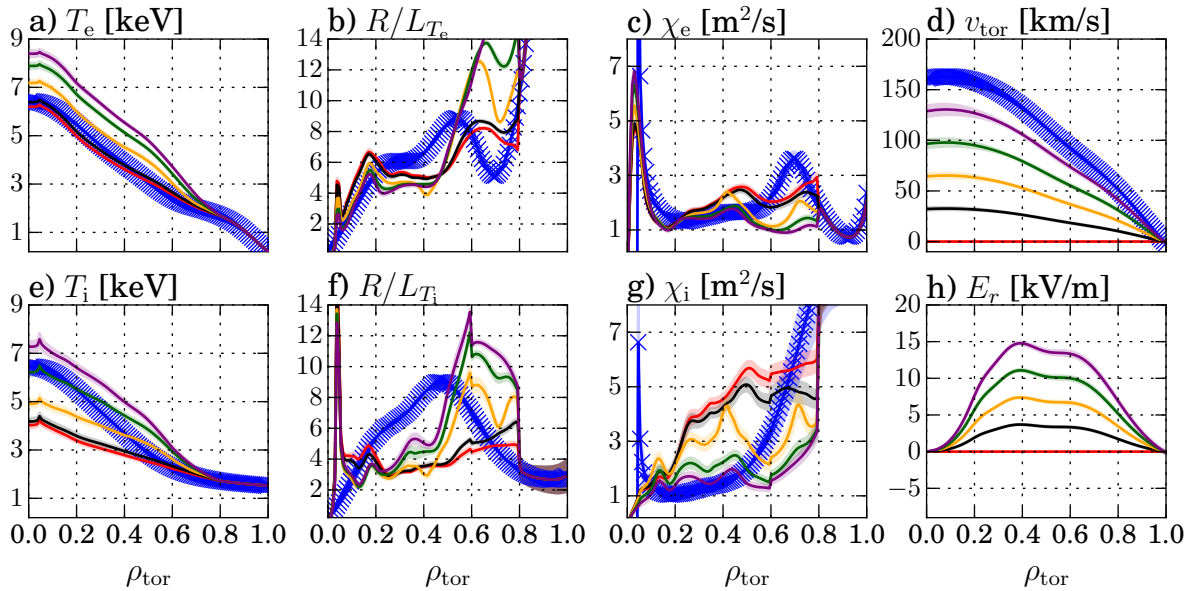


**Figure 6.35:** Impact of a variation of the radial electric field on the electron ion temperature profiles as calculated by TGLF. Experimental results from a power balance analysis are indicated by blue symbols. (#32303,  $t \in [3.8 \text{ s}, 4.0 \text{ s}]$ )

shear does the inner  $\chi_i$  match the power balance value, but then the outer values have already caused an overshoot of the ion temperature profile. In order to correct for the shape mismatch,  $v_{\text{tor}}$  and/or  $B_{\text{pol}} \propto 1/q$  would each have to differ from their apparent values by 20–40% at different radii, which exceeds the uncertainties of both  $v_{\text{tor}}$  and  $q$ .

To summarise, the order magnitude of the  $\vec{E} \times \vec{B}$ -stabilisation is consistent with the experimental results, but the exact location of its impact does not match with the experiment and thus distorts the evolved temperature profiles. This apparent weakness of TGLF's physics model may be due to an original overemphasis of the  $\vec{E} \times \vec{B}$ -stabilisation in GYRO. Further investigation is necessary to resolve this discrepancy and reconcile the effects of  $\vec{E} \times \vec{B}$ -stabilisation and fast ion stabilisation, and the experiment.





## 7 Summary and Outlook

MHD instabilities like sawteeth or NTMs threaten the performance of future tokamak fusion reactors and can ultimately damage them. Furthermore, pulsed operation can make reactors uneconomical. One way of dealing with these issues is to raise the  $q$ -profile inside the plasma such that instabilities like sawteeth or lower-helicity NTMs can no longer emerge. Simultaneously, an elevated  $q$ -profile is thought to increase the bootstrap current in the plasma and help prolong the pulse length or even enter a fully non-inductive state.

A new approach to study plasmas under these conditions is to elevate the  $q$ -profile using broad central counter-ECCD and investigate the resulting plasmas in steady state. To plan the counter-ECCD deposition, TORBEAM was updated such that it accurately deposits power on the axis.

There are two approaches to achieve elevated  $q$ -profiles. One is to heat the plasma early on, thereby delaying the relaxation process during which the initially elevated  $q$ -profile decays into a monotonic one. Aside from this early heating technique, the late heating approach allows the  $q$ -profile to relax before manipulating it with external current drive.

Both techniques were used. By optimising the ECCD deposition and the NBI heating sequence, the early heating scenario was improved to maintain  $q > 1.5$  and  $T_i \geq T_e$ . Lower helicity instabilities were no longer observed, although the scenario remains susceptible to 2,1-NTMs. The optimised ECCD deposition was also applied to late heating experiments, where a large non-inductive current fraction was observed at  $\beta_N = 2.7$  without noticeable core MHD-instabilities.

### Progress on the MSE Diagnostic

In order to study such plasma it is necessary to accurately reconstruct the  $q$ -profile and therefore the entire plasma equilibrium. This requires information from inside the plasma, which is gathered with the MSE diagnostic. Two sources of systematic errors have been identified. Potential solutions to both have been devised but could not be implemented in time.

For one, polarised background light has been identified as a cause for spurious MSE signals. One strong source of this light are neutral particles in the divertor, whose emissions are reflected by the specular tungsten surfaces of the plasma facing components.

These reflections polarise originally unpolarised light and allow it to disrupt the MSE measurement. A likely solution is to upgrade the MSE diagnostic with polychromators to measure on several wavelengths simultaneously such that both signal and background are recorded. The latter is then subtracted from the former to correct the measurement.

Another issue are non-linearities in the MSE's optical relay system. These non-linearities are caused by effects like birefringence, diattenuation or depolarisation. They rotate the input polarisation depending on the initial polarisation, corrupting the measurement. To account for this, a correction factor was applied for the analyses of this work. A proper solution is to perform a full 180° calibration of the MSE system that yields a mapping from diagnostic coordinates into plasma coordinates.

Despite these issues, the reconstructed equilibria were found to be largely consistent with several unrelated physical observations. Inconsistencies were limited to very central regions of the plasma where the emissions of the attenuated beam are more easily drowned out by background light, so the bulk of the plasma volume could be accurately described.

## **Non-inductive Operation**

The late heating scenario in particular resulted in quasi-non-inductive operation at  $B \approx 2.5$  T and  $q_{95} = 5.3$  with  $I_p = 800$  kA and  $\beta_N = 2.7$ . Both counter- and co-ECCD experiments allowed operation without additional inductive current for more than a second, which falls short of the resistive timescale. This is supported by equilibrium reconstruction which revealed that the plasma was in fact not yet in a stationary state and that extended discharges are necessary to assess the scenario's suitability for purely non-inductive operation. Both broad off-axis co-ECCD and broad on-axis counter-ECCD result in similar non-inductive current fractions which suggests that the elevated  $q$ -profile due to counter-ECCD results in at least as much additional bootstrap current as the EC current driven in opposite direction. Neither IDE nor TRANSP are able to reproduce this observation and instead yield only about the same bootstrap current for both ECCD configurations, i.e. about  $I_{bs} \approx I_p/2 \approx 400$  kA. This may be caused by inaccurate equilibrium reconstruction, too short analysis intervals or shortfalls in the bootstrap model.

## **Transport Modelling with TGLF**

TGLF modelling of late heating discharges was performed in order to validate its applicability to such scenarios. It was found that electron heat transport in an ITB created through strong shear reversal near the axis can be reproduced with TGLF as well as in the aforementioned quasi-non-inductive discharges where  $q$  was flattened and elevated over a larger extent of the minor radius.

---

In contrast, it was not possible to reproduce the experimentally observed ion temperatures in the ITB case with TGLF and, in particular, in the case with flat, elevated  $q$ -profiles. Without  $\vec{E} \times \vec{B}$ -shear, TGLF's transport coefficients are consistently above those obtained by power balance analysis by up to a factor of 2, which results in the central ion temperature being under-estimated by about the same amount. By increasing the neutral beam power by 50% or by increasing the fast ion density by 100% the experimentally observed core ion temperature could be achieved, although the profile shape remained inconsistent with the experiment. A possible reason for this may be electromagnetic effects of fast ions which are thought to have a stabilising influence on micro-instabilities according to recent gyrokinetic results.

Conversely, with  $\vec{E} \times \vec{B}$ -shear the transport coefficients calculated by TGLF lead to an overestimation of  $T_i$  at  $\beta_N = 2.0$  and to an overestimation of both electron and ion temperatures at  $\beta_N = 2.7$ . The difference between experimentally observed transport coefficients and predicted ones broadly matches with a possibly related difference between the gyrokinetic codes GYRO — on which TGLF is based — and GENE.

A silver lining of the case without  $\vec{E} \times \vec{B}$ -shear is that TGLF is *under*-estimating the ion heat transport, which means that similar scenarios predicted by TGLF may surpass expectations when experimentally implemented. This would be especially the case for future fusion reactors that intrinsically produce fast ions. On the other hand, predictions that relied on strong  $\vec{E} \times \vec{B}$ -stabilisation of turbulence may be too optimistic, although perhaps the aforementioned fast-ion-stabilisation may ultimately take its place.

## Outlook

The MSE diagnostic will be properly calibrated in the next opening of ASDEX Upgrade in mid-2016. Moreover, an upgrade to eliminate background interference is also foreseen to be in place by the next experimental campaign. On top of that, the DCN polarimetry is also being expanded and the imaging MSE system may also enter routine operation before the next campaign. This will allow equilibrium reconstruction with very high accuracy which will allow a far more reliable analysis of advanced scenarios.

The experiments described in this work should be extended towards longer feedback-controlled phases to investigate whether they reach a stationary, non-inductive state. To this end it may be necessary to further develop the early heating scenario such that the full pulse length of ASDEX Upgrade ( $\approx 10$  s) is available for the current profile to converge. The additional current drive capacities of the new ECRH3 system will facilitate this. Optimisations to the plasma shape could also be contemplated as they may permit higher values of  $\beta_N$  and hence more bootstrap current.

Considering that the experimental observations appear in line with gyrokinetic results from GENE, it may be appropriate to model the experiments using gyrokinetic codes and/or other numerical codes that make use of a more comprehensive physics model.



## 8 Bibliography

- [1] J Wesson and D J Campbell. *Tokamaks*. International series of monographs on physics. Clarendon Press, 3rd edition, 2004.
- [2] EFDA. Tokamak principle, 2011.
- [3] J P Freidberg. *Ideal magnetohydrodynamics*. Modern Perspectives in Energy Series. Plenum Publishing Company Limited, 1987.
- [4] T. Pütterich. Control and Diagnostic of High-Z Impurities in Fusion Plasmas, 2014.
- [5] Hartmut Zohm. *Magnetohydrodynamic Stability of Tokamaks*. Number 1. Wiley, 2015.
- [6] U. Stroth. *Plasmaphysik: Phänomene, Grundlagen, Anwendungen*. Studium (Vieweg + Teubner). Vieweg+Teubner Verlag, 1 edition, 2011.
- [7] P. J. McCarthy. *An Integrated Data Interpretation System for Tokamak Discharges*. Phd thesis, University College Cork, 1992.
- [8] P. J. McCarthy, P. Martin, and W. Schneider. The CLISTE Interpretive Equilibrium Code, IPP Report 5/85. Technical report, Max-Planck-Institut für Plasmaphysik, 1999.
- [9] G. V. Pereverzev and P. N. Yushmanov. Automated System for TRansport Analysis Automated System for TRansport Analysis. (February), 2002.
- [10] EuroFusion. EuroFusion Charged Particle Movements, 2005.
- [11] A. G. Peeters. The bootstrap current and its consequences. *Plasma Phys. Control. Fusion*, 42(00):231–242, 2000.
- [12] O. Sauter, C. Angioni, and Y. R. Lin-Liu. Neoclassical conductivity and bootstrap current formulas for general axisymmetric equilibria and arbitrary collisionality regime. *Physics of Plasmas*, 6(7):2834, 1999.
- [13] O. Sauter, C. Angioni, and Y. R. Lin-Liu. Erratum: Neoclassical conductivity and bootstrap current formulas for general axisymmetric equilibria and arbitrary collisionality regime (Physics of Plasmas (1999) 6 (2834)). *Physics of Plasmas*, 9(12):5140, 2002.

- [14] Paulett C. Liewer. Measurements of microturbulence in tokamaks and comparisons with theories of turbulence and anomalous transport. *Nuclear Fusion*, 25:543–621, 1985.
- [15] F. Romanelli. Models of plasma transport based on microturbulence. *Plasma Physics and Controlled Fusion*, 31(10):1535, 1989.
- [16] D. H. Sharp. An overview of Rayleigh-Taylor instability. *Physica D: Nonlinear Phenomena*, 12(1-3):3–18, 1984.
- [17] F. Jenko, W. Dorland, and G. W. Hammett. Critical gradient formula for toroidal electron temperature gradient modes. *Physics of Plasmas*, 8(9):4096–4104, 2001.
- [18] J Weiland. *Collective Modes in Inhomogeneous Plasmas: Kinetic and Advanced Fluid Theory*. Series in Plasma Physics and Fluid Dynamics. Taylor & Francis, 2000.
- [19] A. J. Wootton, et al. Fluctuations and anomalous transport in tokamaks. *Physics of Fluids B: Plasma Physics*, 2(12):2879, 1990.
- [20] A. E. White, et al. Measurements of the cross-phase angle between density and electron temperature fluctuations and comparison with gyrokinetic simulations. *Physics of Plasmas*, 17(5), 2010.
- [21] X. Garbet, et al. Physics of transport in tokamaks. *Plasma Physics and Controlled Fusion*, 46(12B):B557–B574, 2004.
- [22] E. J. Doyle, et al. Chapter 2: Plasma confinement and transport. *Nuclear Fusion*, 47(6):S18, jun 2007.
- [23] C. Angioni, et al. Particle transport in tokamak plasmas, theory and experiment. *Plasma Physics and Controlled Fusion*, 51:124017, 2009.
- [24] F. Ryter, et al. Electron heat transport in ASDEX Upgrade: experiment and modelling. *Nuclear Fusion*, 43:1396–1404, 2003.
- [25] C Gormezano, et al. Chapter 6: Steady state operation. *Nuclear Fusion*, 47(6):S285–S336, jun 2007.
- [26] W Suttrop, et al. Identification of plasma-edge-related operational regime boundaries and the effect of edge instability on confinement in ASDEX Upgrade. *Plasma Physics and Controlled Fusion*, 39(12):2051–2066, 1997.
- [27] R. C. Wolf. Internal transport barriers in tokamak plasmas. *Plasma Physics and Controlled Fusion*, 45(1):R1–R91, 2002.
- [28] G. M. Staebler, et al. Resolving the mystery of transport within internal transport barriers. *Physics of Plasmas*, 21(5):055902, may 2014.
- [29] S. C. Guo and F. Romanelli. The linear threshold of the ion-temperature-gradient-driven mode. *Physics of Fluids B: Plasma Physics*, 5(2):520, 1993.

- 
- [30] J. E. Kinsey, R. E. Waltz, and J. Candy. The effect of safety factor and magnetic shear on turbulent transport in nonlinear gyrokinetic simulations. *Physics of Plasmas*, 13(2):022305, 2006.
- [31] R. E. Waltz, G. D. Kerbel, J. Milovich, and G. W. Hammett. Advances in the simulation of toroidal gyro-Landau fluid model turbulence. *Physics of Plasmas*, 2(6):2408, 1995.
- [32] J. Candy, R. E. Waltz, and M. N. Rosenbluth. Smoothness of turbulent transport across a minimum-q surface. *Physics of Plasmas*, 11(5 PART 1):1879–1890, 2004.
- [33] A. G. Peeters, C. Angioni, M. Apostoliceanu, F. Jenko, and F. Ryter. Linear gyrokinetic stability calculations of electron heat dominated plasmas in ASDEX Upgrade. *Physics of Plasmas*, 12(2):022505, 2005.
- [34] T. Dannert and F. Jenko. Gyrokinetic simulation of collisionless trapped-electron mode turbulence. *Physics of Plasmas*, 12(7):1–8, 2005.
- [35] N. Bonanomi, et al. Trapped electron mode driven electron heat transport in JET: experimental investigation and gyro-kinetic theory validation. *Nuclear Fusion*, 55(11):113016, 2015.
- [36] P. Manz, M. Ramisch, and U. Stroth. Physical mechanism behind zonal-flow generation in drift-wave turbulence. *Physical Review Letters*, 103(16):1–4, 2009.
- [37] T M Antonsen, et al. Physical mechanism of enhanced stability from negative shear in tokamaks: Implications for edge transport and the L-H transition. *Physics of Plasmas*, 3(6):2221–2223, 1996.
- [38] P. J. McCarthy. Practical expressions for local magnetic shear, normal and geodesic curvatures in an axisymmetric plasma equilibrium of arbitrary cross-section. *Plasma Physics and Controlled Fusion*, 55(8):085011, 2013.
- [39] K H Burrell. Effects of  $E \times B$  velocity shear and magnetic shear on turbulence and transport in magnetic confinement devices. *Physics of Plasmas*, 4(5):1499, 1997.
- [40] G. M. Staebler, J. E. Kinsey, and R. E. Waltz. A theory-based transport model with comprehensive physics. *Physics of Plasmas*, 14(5):055909, 2007.
- [41] G. M. Staebler, J. E. Kinsey, and R. E. Waltz. Gyro-Landau fluid equations for trapped and passing particles. *Physics of Plasmas*, 12(10):1–24, 2005.
- [42] F. Jenko, W. Dorland, M Kotschenreuther, and B N Rogers. Electron temperature gradient driven turbulence. *Physics of Plasmas*, 7(5):1904, 2000.
- [43] T. Görler, et al. The global version of the gyrokinetic turbulence code GENE. *Journal of Computational Physics*, 230(18):7053–7071, 2011.
- [44] Jeff Candy and R. E. Waltz. An Eulerian gyrokinetic-Maxwell solver. *Journal of Computational Physics*, 186(2):545–581, 2003.



- [45] F. Sommer, et al. Transport properties of H-mode plasmas with dominant electron heating in comparison to dominant ion heating at ASDEX Upgrade. *Nuclear Fusion*, 55(3):033006, 2015.
- [46] C.C. Petty, et al. High-beta, steady-state hybrid scenario on DIII-D. *Nuclear Fusion*, 56(1):016016, 2016.
- [47] F. Wagner, et al. Regime of improved confinement and high beta in neutral-beam-heated divertor discharges of the ASDEX tokamak. *Physical Review Letters*, 49(19):1408–1412, 1982.
- [48] ASDEX Team. The H-Mode of ASDEX. *Nuclear Fusion*, 29(11):1959, 1989.
- [49] E Wolfrum, et al. Overview of recent pedestal studies at ASDEX Upgrade. *Nuclear Fusion*, 55(5):53017, 2015.
- [50] A. Burckhart. *Different ELM regimes at ASDEX Upgrade and their linear stability analysis*. PhD thesis, 2013.
- [51] C. D. Challis, et al. Improved Confinement in JET High  $\beta$  Plasmas with an ITER-Like Wall. *Nuclear Fusion*, 55(5):053031, 2015.
- [52] M.G. Dunne, et al. Global performance enhancements via pedestal optimisation on ASDEX Upgrade. *PPCF*, Submitted:1–26, 2016.
- [53] ITER physics basis. Chapter 2: Plasma confinement and transport, 2002.
- [54] F. Troyon, R. Gruber, H. Saurenmann, S. Semenzato, and S. Succi. MHD-Limits to Plasma Confinement. *Plasma Physics and Controlled Fusion*, 26(1A):209–215, 2002.
- [55] F. Perkins. Chapter 3: MHD stability, operational limits and disruptions. *Nuclear Fusion*, 39(12):2251–2389, 2002.
- [56] R. J. Hastie. Sawtooth instability in tokamak plasmas. *Astrophysics and space science*, 256(1-2):177–204, 1997.
- [57] F. Ryter, et al. Experimental study of trapped-electron-mode properties in tokamaks: Threshold and stabilization by collisions. *Physical Review Letters*, 95(8):1–4, 2005.
- [58] V. Igochine, et al. Structure and dynamics of sawteeth crashes in ASDEX Upgrade. *Physics of Plasmas*, 17(12):122506, 2010.
- [59] I Furno, et al. Understanding sawtooth activity during intense electron cyclotron heating experiments on TCV. *Nuclear Fusion*, 41(4):403, 2001.
- [60] V Igochine, et al. Stochastic sawtooth reconnection in ASDEX Upgrade. *Nuclear Fusion*, 47(1):23, 2007.

- 
- [61] M. Reich, A. Bock, M. Maraschek, and ASDEX Upgrade Team. NTM Localization by Correlation of Te and dB/dt. *Fusion Science and Technology*, 61(4):309–313, 2012.
- [62] A. Bock. Correlation analysis methods for real-time localisation of magnetic islands in fusion plasmas, 2012.
- [63] J. Hobirk, et al. Reaching High Poloidal Beta at Greenwald Density with Internal Transport Barrier Close to Full Noninductive Current Drive. *Physical Review Letters*, 87(8):085002, 2001.
- [64] J. Stober, et al. The role of the current profile in the improved H-mode scenario in ASDEX Upgrade. *Nuclear Fusion*, 47(8):728–737, aug 2007.
- [65] J. Hobirk, et al. Improved confinement in JET hybrid discharges. *Plasma Physics and Controlled Fusion*, 54(9):095001, sep 2012.
- [66] Y. Sakamoto, et al. Development of reversed shear plasmas with high bootstrap current fraction towards reactor relevant regime in JT-60U. *Nuclear Fusion*, 49(9):095017, sep 2009.
- [67] Rudolf Neu. Tungsten as a Plasma Facing Material, 2003.
- [68] L. J. Spitzer. The Stellarator Concept. *Physics of Fluids*, 1(1958):253–264, 1958.
- [69] A. D. Sanderson and P. E. Stott. A bundle divertor for a fusion reactor. *Journal of Nuclear Materials*, 76-77(C):530–535, sep 1978.
- [70] C Galperti, et al. Development of real-time MHD markers based on biorthogonal decomposition of signals from Mirnov coils. *Plasma Physics and Controlled Fusion*, 56(11):114012, 2014.
- [71] W. Suttrop and A G Peeters. Practical limitations to plasma edge electron temperature measurements by radiometry of electron cyclotron emission, IPP Report 1/306. Technical report, Max-Planck-Institut für Plasmaphysik, 1996.
- [72] W. Suttrop. Electron Cyclotron Emission Plasma Diagnostics. Technical report.
- [73] B. Kurzan and H. D. Murmann. Edge and core Thomson scattering systems and their calibration on the ASDEX Upgrade tokamak. *Review of Scientific Instruments*, 82(10):103501, 2011.
- [74] E. Viezzer, T. Pütterich, R. Dux, and R. M. McDermott. High-resolution charge exchange measurements at ASDEX Upgrade. *Review of Scientific Instruments*, 83(10):103501, 2012.
- [75] A. Mlynek, et al. Design of a digital multiradian phase detector and its application in fusion plasma interferometry. *Review of Scientific Instruments*, 81(3):033507, 2010.

- [76] T Akiyama, et al. Conceptual design of high resolution and reliable density measurement system on helical reactor FFHR-d1 and demonstration on LHD. *Nuclear Fusion*, 55(9):93032, 2015.
- [77] R. Fischer, C. J. Fuchs, B. Kurzan, W. Suttrop, and E. Wolfrum. Integrated data analysis of profile diagnostics at ASDEX upgrade. *Fusion Science and Technology*, 58(2):675–684, 2010.
- [78] R. Fischer, E. Wolfrum, and J. Schweinzer. Probabilistic lithium beam data analysis. *Plasma Physics and Controlled Fusion*, 50(8):085009, 2008.
- [79] I. Hutchinson. *Principles of Plasma Diagnostics*. Cambridge, 2nd edition, 2005.
- [80] A. Mlynek. Status of the new DCN polarimeter on ASDEX Upgrade Introduction, presentation at AUG programme seminar, 2015.
- [81] R. Prater. Heating and current drive by electron cyclotron waves. *Physics of Plasmas*, 11(5 PART 2):2349–2376, 2004.
- [82] T. Ohkawa. Steady-State Operation of Tokamaks by RF-Heating. Technical report, General Atomics, 1976.
- [83] N. J. Fisch and A. H. Boozer. Creating an asymmetric plasma resistivity with waves. *Physical Review Letters*, 45(9):720–722, 1980.
- [84] F. Leuterer, et al. The ECRH system of ASDEX Upgrade. *Fusion Engineering and Design*, 56-57:615–619, 2001.
- [85] D. Wagner, et al. Present status of the new multifrequency ECRH system for ASDEX upgrade. *IEEE Transactions on Plasma Science*, 36(2 PART 1):324–331, 2008.
- [86] E. Poli, A. G. Peeters, and G. V. Pereverzev. TORBEAM, a beam tracing code for electron-cyclotron waves in tokamak plasmas. *Computer Physics Communications*, 136(1-2):90–104, 2001.
- [87] V. D. Shafranov. Equilibrium of a toroidal pinch in a magnetic field. *Soviet Atomic Energy*, 13(6):1149–1158, 1963.
- [88] O. Vollmer, et al. Commissioning and Performance of the New ASDEX Upgrade Neutral Beam Injector. In *20. SOFT*, pages 449–452, 1998.
- [89] I. T. Chapman, et al. Modeling sawtooth stabilization by energetic ions from neutral beam injection. *Physics of Plasmas*, 14(7):1–4, 2007.
- [90] Y. J. Hu, Y. M. Hu, and Y. R. Lin-Liu. Electron shielding current in neutral beam current drive in general tokamak equilibria and arbitrary collisionality regime. *Physics of Plasmas*, 19(3):034505, 2012.
- [91] TRANSP home page, <http://w3.pppl.gov/transp>.

- 
- [92] Alexei Pankin, Douglas McCune, Robert Andre, Glenn Bateman, and Arnold Kritz. The tokamak Monte Carlo fast ion module NUBEAM in the national transport code collaboration library. *Computer Physics Communications*, 159(3):157–184, 2004.
- [93] F. M. Levinton, et al. Magnetic field pitch-angle measurements in the PBX-M tokamak using the motional Stark effect. *Physical Review Letters*, 63(19):2060–2063, 1989.
- [94] T. Löbhard. Kalibrierverfahren für die Motional Stark Effekt Diagnostik am Fusionsexperiment ASDEX Upgrade, 2011.
- [95] H. Yuh. *The Motional Stark Effect Diagnostic on Alcator C-Mod*. PhD thesis, Massachusetts Institute of Technology, 2005.
- [96] R. C. Wolf, et al. Motional Stark Effect measurements of the local magnetic field in high temperature fusion plasmas. *Journal of Instrumentation*, 10(10):P10008–P10008, 2015.
- [97] M. F M De Bock, N. J. Conway, M. J. Walsh, P. G. Carolan, and N. C. Hawkes. Ab initio modeling of the motional Stark effect on MAST. *Review of Scientific Instruments*, 79(10):9–13, 2008.
- [98] James C. Kemp. Polarized light and its interaction with modulating devices. Technical report, Hinds International, Inc., Hillsboro, OR, 1987.
- [99] O. P. Ford, J. Howard, and R. C. Wolf. The prototype imaging motional Stark effect diagnostic for ASDEX upgrade. *Review of Scientific Instruments*, 86(9):0–10, 2015.
- [100] R. T. Mumgaard. Lower Hybrid Current Drive on Alcator C-Mod : Measurements with an Upgraded MSE Diagnostic and Comparisons to Simulation by. 2015.
- [101] R. T. Mumgaard, S. D. Scott, and J. Ko. Robotic calibration of the motional Stark effect diagnostic on Alcator C-Mod. *Review of Scientific Instruments*, 85(5):053505, 2014.
- [102] A. Dinklage, et al. Forward Modeling of Motional Stark Effect Spectra. *Fusion Science and Technology*, 59(2):406–417, 2011.
- [103] M. Reich. Calibration methods for the MSE diagnostic at ASDEX Upgrade. In *34th EPS Conference on Plasma Physics*, 2007.
- [104] K. Lackner. Computation of ideal MHD equilibria. *Computer Physics Communications*, 12(1):33–44, 1976.
- [105] M. Rampp, R. Preuss, R. Fischer, and ASDEX Upgrade Team. GPEC, a real-time capable Tokamak equilibrium code. *arXiv.org*, pages 1–26, nov 2015.

- [106] L. L. Lao, H. St. John, R.D. Stambaugh, and W. Pfeiffer. Separation of  $\beta$  p and i in tokamaks of non-circular cross-section. *Nuclear Fusion*, 25(10):1421–1436, 1985.
- [107] R. Fischer, A. Bock, M. G. Dunne, C. J. Fuchs, and L. Giannone. Coupling of the flux diffusion equation with the equilibrium reconstruction at ASDEX Upgrade. *Fusion Science and Technology*, 2016.
- [108] P. H. Richter. Estimating Errors in Least-Squares Fitting. *TDA Progress Report*, pages 42–122, 1995.
- [109] F. Felici, et al. Real-time physics-model-based simulation of the current density profile in tokamak plasmas. *Nuclear Fusion*, 51(8):083052, 2011.
- [110] R. Neu, et al. Final steps to an all tungsten divertor tokamak. *Journal of Nuclear Materials*, 363-365(1-3):52–59, 2007.
- [111] H. Zohm, et al. On the physics guidelines for a tokamak DEMO. *Nuclear Fusion*, 53:073019, 2013.
- [112] T. C. Luce, et al. High performance stationary discharges in the DIII-D tokamak. *Physics of Plasmas*, 11(5):2627, 2004.
- [113] G. Tardini, et al. Ion ITB Dynamics in ASDEX Upgrade. In *32nd EPS Conference on Plasma Physics*, volume 29C, pages P–2.028, 2005.
- [114] M. Bernert. *Analysis of the H-mode density limit in the ASDEX Upgrade tokamak using bolometry*. PhD thesis, Ludwig-Maximilians-Universität München, 2013.
- [115] W. Treutterer, et al. Real-time diagnostic integration with the ASDEX upgrade control system. *Fusion Engineering and Design*, 84(7-11):1871–1874, 2009.
- [116] T. Görler, et al. A flux-matched gyrokinetic analysis of DIII-D L-mode turbulence. *Physics of Plasmas*, 21(12):0–12, 2014.
- [117] J. Citrin, et al. Nonlinear Stabilization of Tokamak Microturbulence by Fast Ions. *Physical Review Letters*, 111(15):155001, 2013.
- [118] J Citrin, et al. Electromagnetic stabilization of tokamak microturbulence in a high- $\beta$  regime. *Plasma Physics and Controlled Fusion*, 57(1):014032, 2015.
- [119] G. M. Staebler, J. Candy, R. E. Waltz, J.E. E Kinsey, and W.M. M Solomon. A new paradigm for  $E \times B$  velocity shear suppression of gyro-kinetic turbulence and the momentum pinch. *Nuclear Fusion*, 53(11):113017, 2013.

# Acknowledgements

There is a saying that is particularly fitting for a large experiment like ASDEX Upgrade as well as the larger fusion research effort itself: “If you want to go fast, go alone. If you want to go far, go together.” With this in mind I would like to extend my sincerest gratitude and appreciation to those who have supported me up to and throughout the completion of this dissertation. I could not have gone this far by myself.

Firstly, I would like to thank my academic supervisor Jörg Stober for his limitless support, helpful insights and discussions, and for always having my back. Not only was Jörg’s door always open to me, I always left smarter and more motivated after having walked through it, too.

I also want to extend my thanks to Hartmut Zohm, who not only supported my physics work, e.g. with his report estimating the bootstrap current that served as an impetus for section 2.6, but was also very supportive when I took a leave to dabble in federal politics for a few months.

For his support, input and hard work, I am incredibly grateful to Rainer Fischer. Without Rainer’s commitment, this study would have been nearly impossible to conclude. Also, many thanks go to Emiliano Fable, who guided me through the potential pitfalls of transport simulation.

I want to thank Matthias Reich not only for his invaluable help with the MSE diagnostic, but also for fruitful discussions and also for originally opening the door to this PhD work with his excellent supervision of my diploma thesis. Thanks also go to Stefan Eder for his technical support for the MSE. I am also thankful to David Rittich for his hands-on support with the MSE system and also for remembering to open the MSE’s shutter before some of my experiments, as well as to Benedikt Geiger, whose enthusiasm and curiosity stimulated several fruitful investigations. Many thanks go to Andreas Burckhart and Oliver Ford, whose work on the IMSE diagnostic also benefitted the conventional MSE a lot. Finally, I would also like to thank Robert Mumgaard, who took the long trip from Massachusetts to help us try out the MSE polychromator prototype he and his colleagues had constructed.

For their help with the ECRH system I must thank Martin Schubert and Dietmar Wagner. Similarly, Emanuele Poli’s help with TORBEAM was invaluable, and so was Christian Hopf’s help at the NBI. I am also grateful to Thomas Pütterich, whose support as an experiment and task force leader was crucial.

---

When it came to MHD questions, Anja Gude, Valentin Igochine and Marc Maraschek were always eager to help me. In the same vein I have to thank Louis Giannone and Patrick McCarthy for questions related to the plasma equilibrium. When it came to turbulence, Tim Happel's and Clemente Angioni's explanations were a lifesaver. I can only hope that my section on micro-instabilities will save you time in the future. Nothing works without computers, and for me they worked because of Karl Behler, David Coster, Sven Martinov, Michael Kraus and Christian Guggenberger. Thank you all for this.

Special thanks go to Bernhard Sieglin, Mike Dunne and Alexander Mlynek, not only for their helpful discussions and their friendship, but also for proof-reading this thesis.

My thanks for the nice time in Lisbon and Padova with the PhD network go to Livia Casali, Luís Guimaraes, Nicola Fomesu, Marco Barbisan and Chiara Piron.

Unfortunately, I cannot list every single person's contribution. So, for the help with the myriad of day-to-day problems, for the helpful discussions, for the experimental data from your diagnostics, for the friendship and patience, and, of course, for the laughter and fun at work and outside of it, I extend my thanks not just to the people named above, but also to Matthias Bernert, Vasil Bratanov, Marco Cavedon, Ivo Classen, Severin Denk, Michael Faitsch, Sina Fietz, Athina Kappatou, Alexander Lebschy, Rachael McDermott, Michael Oberparleiter, Tomasz Odstrčil, Steffen Potzel, Markus Rampp, Philip Schneider, Eleonora Viezzer, Martin Weidl, Markus Weiland, and Matthias Willensdorfer.

Finally, I want to thank my friends and family for their support and patience. In particular, I would like to thank my parents: without their courageous decision to leave everything behind and come to this country, or without their encouragement ever since, I would not be writing this today.